



TECHNISCHE  
UNIVERSITÄT  
DARMSTADT

*Four-Nucleon Forces in Ab Initio Nuclear Structure*  
*Vierteilchenkräfte in der Ab Initio Kernstrukturtheorie*

VOM FACHBEREICH PHYSIK  
DER TECHNISCHEN UNIVERSITÄT DARMSTADT

ZUR ERLANGUNG DES AKADEMISCHEN GRADES  
DOCTOR RERUM NATURALIUM  
(DR. RER. NAT.)

GENEHMIGTE DISSERTATION VON  
STEFAN SCHULZ, M.Sc.  
GEBOREN IN GIEßEN

REFERENT: PROF. DR. ROBERT ROTH  
KORREFERENT: PROF. DR. HANS-WERNER HAMMER

TAG DER EINREICHUNG: 6. FEBRUAR 2018  
TAG DER PRÜFUNG: 23. APRIL 2018

DARMSTADT 2018  
DI7

Four-Nucleon Forces in Ab Initio Nuclear Structure  
Vierteilchenkräfte in der Ab Initio Kernstrukturtheorie

Genehmigte Dissertation von Stefan Schulz, geboren in Gießen.

Referent: Prof. Dr. Robert Roth

Korreferent: Prof. Dr. Hans-Werner Hammer

Tag der Einreichung: 6. Februar 2018

Tag der Prüfung: 23. April 2018

2018 – Darmstadt – D17

Dieses Dokument wird bereitgestellt von tprints,  
E-Publishing-Service der TU Darmstadt  
<http://tprints.ulb.tu-darmstadt.de>

URN: urn:nbn:de:tuda-tprints-73842

URL: <http://tprints.ulb.tu-darmstadt.de/id/eprint/7384>

Veröffentlicht unter CC BY-NC-SA 4.0 International



Siehe <https://creativecommons.org/licenses/by-nc-sa/4.0> für mehr Informationen.

# *Four-Nucleon Forces in Ab Initio Nuclear Structure*

## ABSTRACT

In recent years, there has been tremendous progress in the construction and application of nuclear interactions from chiral effective field theory (EFT). Today, two- and three-nucleon interactions are routinely used in many-body calculations, reaching unprecedented quality in the ab initio description of nuclei. Although four-nucleon ( $4N$ ) forces have been constructed from chiral EFT, they have never been investigated systematically in finite nuclei.

This work aims at the inclusion of explicit  $4N$  forces in many-body nuclear structure calculations. We investigate two different interactions, a simple  $4N$  contact interaction and the complete leading order of the chiral  $4N$  interaction. To include these interactions, we develop a partial-wave decomposition (PWD) and represent the  $4N$  interactions in a basis of harmonic oscillator states using Jacobi coordinates. Especially the PWD for the chiral  $4N$  interaction requires significant effort, much more than its three-nucleon counterpart, and constitutes the main part of this work. However, the endeavor is worthwhile, as it makes the consistent inclusion of  $4N$  interaction in many-body calculations possible.

The inclusion of the  $4N$  contact interaction and its PWD is simpler than in the chiral case. It, nevertheless, yields valuable insights into the effect of  $4N$  interactions in nuclear structure calculations. Two- and three-body interactions from chiral EFT often predict an overbinding of nuclei, and root-mean-square radii are much smaller than the experimental results. We, therefore, focus on ground-state energies and charge radii with the contact interaction. Our results clearly show that the employed contact interaction is not able to mitigate this effect. It does have a sizable effect on radii, but improving the agreement of charge radii with experiment yields unphysical binding energies. Furthermore, the contact interaction is compared to the effect of neglected many-body contributions, which are induced by transforming the two- and three-body interactions using the similarity renormalization group. These neglected contributions scale strongly with the number of nucleons, and we find the contact interaction to have a far gentler scaling.

For the first time, we present ground-state energies calculated using a partial-wave decomposed representation of the chiral  $4N$  interaction. Although we cannot achieve model-space convergence due to the computational cost of the PWD, our analysis strongly indicates that the order of magnitude of the effect of the  $4N$  force is correctly reflected even in small model spaces. Overall, we find the effect of the chiral  $4N$  interaction to be extremely small in all investigated nuclei, yielding contributions below 1% of the binding energy in all cases and even smaller effects in light nuclei. We conclude that, in the foreseeable future, the chiral  $4N$  interaction has no relevance for ab initio descriptions of nuclei based on typical chiral interactions.



# *Vierteilchenkräfte in der Ab Initio Kernstrukturtheorie*

## ZUSAMMENFASSUNG

In den vergangenen Jahren gab es erhebliche Fortschritte bei der Konstruktion und Anwendung von Kernkräften, die aus der chiralen effektiven Feldtheorie (EFT) hergeleitet werden. Unter anderem werden heutzutage Zwei- und Drei-Teilchen-Kräfte routinemäßig in Vielteilchenrechnungen verwendet und die ab initio Beschreibung von Kerneigenschaften ist wesentlich präziser geworden. Obwohl eine Vier-Nukleonen-Wechselwirkung (4N-Wechselwirkung) im Rahmen der chiralen EFT konstruiert wurde, gibt es bis heute keine systematische Untersuchung von endlichen Kernen, welche diese Kräfte miteinbezieht.

Diese Arbeit hat die Verwendung von expliziten 4N-Wechselwirkung in Kernstrukturrechnungen zum Ziel, insbesondere die Anwendung in Vielteilchensystemen. Zum einen verwenden wir eine simple 4N-Kontaktwechselwirkung, zum anderen die komplette führende Ordnung der chiralen 4N-Wechselwirkung. In beiden Fällen wird eine Partialwellenzerlegung (PWZ) entwickelt. Der zentrale Aspekt dieser Arbeit ist die PWZ der chiralen 4N-Wechselwirkung, welche äußerst aufwendig ist, insbesondere im Vergleich mit der PWZ von Drei-Teilchen-Kräften. Der hohe Aufwand ist aber lohnenswert, da es konsistente Vielteilchenrechnungen unter Einbeziehung der 4N-Wechselwirkung überhaupt erst ermöglicht.

Für die 4N-Kontaktwechselwirkung ist die PWZ erheblich einfacher als für die chiralen Kräfte. Nichtsdestotrotz erhält man mit dieser einfachen Kraft nützliche Einsichten in den Effekt von 4N-Wechselwirkung in Kernstrukturrechnungen. Wir untersuchen vor allem den Effekt auf Grundzustandsenergien und Ladingsradien. Diesen vergleichen wir mit dem Effekt vernachlässigter Vielteilchenbeiträge, die durch die Verwendung der Similarity Renormalization Group induziert werden. Die Beiträge dieser induzierten Wechselwirkung skalieren aber sehr stark mit der Anzahl der Nukleonen, ganz im Gegensatz zur verwendeten Kontaktwechselwirkung, für die wir ein deutlich schwächeres Skalierungsverhalten finden. Außerdem zeigen schon Berechnungen, die auf chiralen Zwei- und Drei-Teilchen-Kräften beruhen, oft eine Überbindung der Atomkerne, also zu kleine Radien und Energien im Vergleich mit experimentellen Daten. Die verwendete Kontaktwechselwirkung führt aber zu unphysikalisch kleinen Bindungsenergien, wenn die Kraft stark genug sein soll um deutlich größere Radien vorherzusagen.

Im Rahmen dieser Arbeit wurden zum ersten Mal Grundzustandsenergien von Kernen mit Hilfe einer chiralen 4N-Wechselwirkung berechnet, die vorher in einzelne Partialwellen zerlegt wurde. Obwohl wir aufgrund des hohen Rechenaufwandes der PWZ keine Konvergenz bezüglich des 4N-Modellraums erhalten, zeigt die Analyse sehr deutlich, dass auch kleine Modellräume die Größenordnung des Effekts der 4N-Wechselwirkung gut wiedergeben. Insgesamt finden wir nur einen sehr kleinen Effekt der chiralen 4N-Wechselwirkung, mit Beiträgen die immer unterhalb von 1 % der Bindungsenergie liegen, wobei die Beiträge in leichten Kernen noch deutlich kleiner sind. Deshalb wird die chirale 4N-Wechselwirkung in absehbarer Zukunft keine Relevanz für typische ab initio Kernstrukturrechnungen haben.



# Contents

LIST OF ABBREVIATIONS	ix
1 INTRODUCTION	I
2 CHIRAL EFFECTIVE FIELD THEORY	5
2.1 Chiral Symmetry . . . . .	6
2.2 Effective Lagrangian . . . . .	8
2.3 Effective Interaction . . . . .	11
2.4 Regularization and Renormalization . . . . .	13
2.5 Chiral Forces . . . . .	14
3 ANGULAR MOMENTUM	17
3.1 Basic Concepts . . . . .	17
3.2 Spherical Tensors . . . . .	21
3.3 Transformations . . . . .	23
3.4 Recoupling Coefficients . . . . .	28
4 INTERACTION MATRIX ELEMENTS	31
4.1 Jacobi Harmonic Oscillator Basis . . . . .	32
4.2 Four-Nucleon Partial-Wave Decomposition . . . . .	37
4.3 Contact Interaction . . . . .	38
4.4 Chiral Four-Nucleon Interaction . . . . .	40
5 MANY-BODY CALCULATIONS	57
5.1 Similarity Renormalization Group . . . . .	58
5.2 JT-coupled scheme . . . . .	61
5.3 No-Core Shell Model . . . . .	64
5.4 Hartree-Fock Method . . . . .	66

6	RESULTS FOR A FOUR-BODY CONTACT INTERACTION	69
6.1	The EM/N500 Interaction . . . . .	70
6.2	The SMS/H500 Interaction . . . . .	77
7	EFFECTS OF THE CHIRAL 4N INTERACTION	87
7.1	Momentum Grids . . . . .	88
7.2	Model Space Convergence . . . . .	93
7.3	Interaction Classes . . . . .	95
7.4	Regulator Dependence . . . . .	97
7.5	Perturbative Inclusion . . . . .	101
7.6	Channel Structure . . . . .	102
7.7	Frequency Variation . . . . .	106
7.8	Relevance of the Four-Nucleon Force . . . . .	109
8	CONCLUSIONS	113
	APPENDICES	117
A	Partial-Wave Decomposition of the Chiral Four-Nucleon Interaction . . . . .	119
B	Four-Nucleon Extension of Spherical Hartree-Fock . . . . .	153
	REFERENCES	159



# List of Abbreviations

<b>3N</b>	three-nucleon
<b>4N</b>	four-nucleon
<b>CFP</b>	coefficient of fractional parentage
<b>CGC</b>	Clebsch-Gordan coefficient
<b>EFT</b>	effective field theory
<b>GFMC</b>	Green's function Monte Carlo
<b>HF</b>	Hartree-Fock
<b>HO</b>	harmonic oscillator
<b>HOB</b>	harmonic oscillator bracket
<b>IMSRG</b>	in-medium similarity renormalization group
<b>IT-NCSM</b>	importance-truncated no-core shell model
<b>LEC</b>	low-energy constant
<b>LO</b>	leading order
<b>QCD</b>	quantum chromodynamics
<b>QED</b>	quantum electrodynamics
<b>NCSM</b>	no-core shell model
<b>NLO</b>	next-to-leading order
<b>N<sup>2</sup>LO</b>	next-to-next-to-leading order

<b>NN</b>	nucleon-nucleon
<b>PWD</b>	partial-wave decomposition
$\pi$ <b>N</b>	pion-nucleon
<b>rms</b>	root-mean-square
<b>SRG</b>	similarity renormalization group
<b>UCOM</b>	unitary correlation operator method

*Der Mensch muß bei dem Glauben verharren,  
daß das Unbegreifliche begreiflich sei; er würde  
sonst nicht forschen.*

J.W. von Goethe, Wilhelm Meisters Wanderjahre

# 1

## Introduction

The ab initio description of nuclei has made tremendous progress in the past decade, solving multiple previously insurmountable problems in the process. We only interpret calculations as ab initio, if they are microscopic and all introduced approximations are controllable, that is, they are systematically improvable. A microscopic description of nuclei, modeling them as a collection of protons and neutrons, began after the seminal experiments by Chadwick that discovered the neutron [1]. Moreover, the microscopic description requires an interaction between nucleons. The first approach towards the modern understanding of nuclear interactions is the work by Yukawa [2], formulating an interaction based on the exchange of a massive boson. From the properties of the nuclear interaction, Yukawa also estimated the mass of these bosons to be about 100 MeV, predicting the pions that were discovered in 1947 [3]. This idea led to the development of increasingly complex and accurate meson exchange models, see ref. [4] and references therein. These models reached an unprecedented precision, for instance, the CD-Bonn potential [5] allows the description of the world nucleon-nucleon (NN) scattering data of 2000 with a  $\chi^2/\text{datum} \approx 1$ . The potential is still used frequently today [6–8]. However, it is not necessary to use a meson exchange model to obtain interactions at this level of precision, in fact, multiple more phenomenological NN interactions have been constructed. Well-known examples include the JISP16 [9] and Argonne  $v_{18}$  [10] interactions. These high-precision interactions, including the CD-Bonn potential, are known as realistic interactions.

Calculations based on these interactions soon revealed that three-nucleon (3N) interactions are necessary for the description of many-body systems, in fact, Fujita and Miyazawa already proposed a 3N interaction

based on a two-pion exchange with an intermediate  $\Delta$ -excitation in 1957 [11]. Over the years, multiple 3N forces have been developed [12], most of them using meson exchange and additional phenomenological contributions, but fail to provide a deeper understanding of the nuclear interaction. Nevertheless, they allow accurate calculations of binding energies for light nuclei [13].

Taking the idea of an ab initio description seriously, the actual microscopic description of nuclei should be based on quantum chromodynamics (QCD), which describes the fundamental interaction between quarks and gluons. Although QCD-based nuclear structure approaches exist [14–16], they do not yet allow for a quantitative description of nuclei. Quarks are confined to hadrons in the low-momentum regime of nuclear structure, and a description in terms of nucleons and mesons as effective degrees of freedom should be possible. However, a direct derivation of the force between the nucleons is hindered by the nonperturbative nature of QCD at low momenta, and calculations with that goal are currently far away from a high-precision description, although this option is investigated [17]. Due to pioneering work by Weinberg [18, 19], we are able to construct a low momentum expansion, which is known as chiral effective field theory (EFT). It uses a separation of scales to limit the effective degrees of freedom to nucleons and pions. At the low momenta relevant for nuclear structure, other contributions, like heavier mesons, can be excluded. It is based on the symmetries of QCD, promoting the use of chiral symmetry and providing a clear connection to the underlying theory. In accord with the ab initio idea, it allows systematic improvement by increasing the chiral order, and it allows the consistent construction of multi-nucleon forces in the same framework. Furthermore, chiral EFT directly yields a hierarchy of many-body forces, as four-nucleon (4N) forces only contribute at a higher chiral order than 3N ones, which in turn require a higher order than NN ones. However, currently the low-energy constants (LECs) that are introduced by chiral EFT are fit to data. In the future, these parameters may be calculated using QCD [20, 21], which would enable the construction of the nuclear interactions completely from the fundamental theory.

The construction of chiral interactions has made a tremendous progress over the last years, with multiple NN forces available at the fifth order of the chiral expansion or even beyond [22–26]. Calculations were often limited to the three-body contributions at next-to-next-to-leading order ( $N^2LO$ ), however, the three-body force has been derived up to  $N^3LO$  in 2011 [27, 28], and recently a computationally efficient approach for the partial-wave decomposition (PWD) of the three-body forces at  $N^3LO$  became available [29]. At the level of  $N^3LO$  we also have four-body forces, which have been derived over ten years ago [30, 31]. Recently the research focus shifted to calculations with consistent chiral interactions, which take all contributions at a fixed order into account, and a reliable uncertainty quantification of the chiral expansion, which requires calculations at different chiral orders. These goals warrant the inclusion of the chiral 4N interaction in many-body calculations, and so far, the calculations that include the 4N forces are limited to neutron and symmetric nuclear matter [32–35], or estimates for  ${}^4\text{He}$  [36]. We aim at a PWD of the chiral 4N interaction at  $N^3LO$  in this work.

Along with the development of nuclear interactions, we also require methods to efficiently solve the many-body problem. The first methods that allowed to solve the Schrödinger equation exactly can be ap-

plied to few-nucleon systems only, a well-known example dating back to 1960 for three- and later four-body systems is the Faddeev method, see ref. [37] and references therein. With the increase of available computational resources, methods that are able to handle more nucleons became available. In the 1980s Monte Carlo based approaches were introduced in nuclear structure, like variational Monte Carlo [38] and Green's function Monte Carlo (GFMC) [39]. The latter allows for an exact calculation of nuclear observables, and it is routinely used for the calculation binding energies and radii [40]. Similarly, the no-core shell model (NCSM) [41] allows the exact calculations of ground- and excited bound states. However, both GFMC and NCSM are limited to p-shell nuclei. The importance-truncated no-core shell model (IT-NCSM) [42, 43] extends the reach to lower sd-shell nuclei, but these (quasi-)exact methods all have at least an exponential scaling with the number of nucleons.

For the ab initio description of heavier nuclei, systematically improvable approximations have to be introduced. In doing so, the reach of many-body calculations has been tremendously expanded in the last two decades. Prominent examples include coupled-cluster theory [44], self-consistent Green's function [45, 46], in-medium similarity renormalization group (IMSRG) [47, 48], and many-body perturbation theory [49]. A recent overview of modern methods can be found in [50]. Today, a large number of ab initio methods for a wide range of nuclei are available and new methods are developed frequently [51, 52], increasing the range of applicability.

This increasing number of many-body methods and their successful application can partly be linked to advances in the treatment of nuclear interactions. For years the solution of the many-body problem was hindered by the structure of the realistic nuclear interaction. All of these interactions feature a strong short-range repulsion, which can be linked to the finite size of the nucleons. As nucleons are treated as point-like particles, such effects are encoded in the interaction. Additionally, these interactions feature strong tensor forces. Due to this, the description of nuclei requires highly correlated states, which is difficult for many-body methods. For instance, methods that rely on the construction of a many-body basis from uncorrelated states usually exhibit a poor convergence with the number of basis states. The use of chiral EFT typically yields slightly softer interactions than other realistic interactions. However, the relevant improvement is the use of efficient transformations of the Hamiltonian, for instance, reducing the strength of the repulsive core, and thereby softening the interaction. After applying a unitary transformation, all observables are, in principle, unchanged and the correlations of the wave function are shifted to the unitary operator. Such unitary operators can be constructed explicitly as done in the unitary correlation operator method (UCOM) [53]. Today, the similarity renormalization group (SRG) [54–57] is in widespread use, which is based on the solution of a flow equation that softens the Hamiltonian. Its main advantages are its flexibility, as the so-called generator of the flow equation can be tailored to the problem at hand, and it allows a straightforward extension to many-nucleon interactions. However, such unitary transformations induce many-body forces, even when only applied to a two-body interaction. This is another source of four-body forces, which can have significant impact when neglected [58–60]. Explicit inclusion of these forces is possible, but computationally expensive [60, 61]. The optimal solution would be an improved generator for the flow equation,

that reduces the induced contributions significantly. Despite searches for alternative generators [60, 62–67], currently no completely satisfying solution exists.

It might be possible to add a phenomenological  $4N$  interaction that mimics the neglected induced contributions. For this reason, and to test our methods on a simple interaction first, we investigate a four-body contact interaction. This allows for a much simpler PWD than the full chiral interaction. Furthermore, chiral interactions typically produce overbinding in heavier nuclei and predict a radius that is far too small. We also investigate if the contact interaction can mitigate this effect.

The main goal of this work is the inclusion of initial  $4N$  forces in (ab initio) many-body calculations and the investigation of their effects. We discuss all steps necessary for the calculation of nuclear observables using four-body forces, starting from the construction of the interaction from chiral EFT to selected many-body methods. We start with an introduction to chiral EFT in chapter 2. All two- and three-body forces, as well as the chiral  $4N$  force employed throughout this work are based on chiral EFT. In chapter 3, we revisit angular momentum theory and develop a diagrammatic notation for it. This is a necessary prerequisite for the remainder of the work. Afterwards, we are able to use this knowledge to obtain interaction matrix elements for the four-body interactions, which is presented in chapter 4. This is a nontrivial step, as the initial interactions are in a single-particle representation. However, we want to obtain matrix elements in a fully antisymmetrized Jacobi basis, which requires a coordinate change and a PWD. Especially for the chiral  $4N$  interaction this requires an involved derivation, which is discussed in detail. However, we also introduce a simple contact interaction, which is far easier to handle in a PWD. Afterwards, we want to perform many-body calculations using the four-body force, and all remaining steps necessary for that goal are discussed in chapter 5. This involves additional treatment of the matrix elements using the SRG evolution for two- and three-body interactions, and an additional transformation to the JT-coupled scheme. We use two many-body methods in this work, namely the Hartree-Fock (HF) method and the NCSM, or its extension, the IT-NCSM. Employing these methods, we analyze the effect of the four-body interactions, starting with an analysis of the changes to ground-state energies and radii when using the contact interaction in chapter 6. Chapter 7, provides a detailed investigation of the chiral  $4N$  interaction including the variation of relevant parameters. Finally, we present conclusions and an outlook on future research opportunities in chapter 8.

*The purpose of this work is not to improve our detailed picture of nuclear forces, which it is hardly likely could be accomplished with these methods [...].*

Steven Weinberg [19]

# 2

## Chiral Effective Field Theory

The overall goal this work contributes to, is the ab initio description of nuclei. Starting from first principles, all calculations should be based on quarks and gluons as degrees of freedom. This approach is hardly feasible, however, there have been investigations aiming at a QCD description of light nuclei [14, 15]. Fortunately, this approach is not necessary, nuclear structure can be explained quantitatively using nucleons as effective degrees of freedom. Of course, this approach directly prompts the question, what the interaction between nucleons is.

Constructing a realistic nuclear interaction directly from QCD is not yet possible, although there are investigations with that goal [17]. Such a construction is impeded by the non-perturbative nature of QCD at low momentum, which is the regime we are interested in for nuclear structure. To bridge this gap, chiral EFT has been developed – pioneering work has been done by Weinberg [18, 19]. Constructing an effective interaction for low momenta is made possible by a peculiarity in the hadron spectrum. There exists a large gap between the mass of the pions  $m_{\pi^0} \approx 135$  MeV and  $m_{\pi^\pm} \approx 140$  MeV [68] and all other mesons, the lightest of which is the  $\eta$ -meson with a mass of  $m_\eta \approx 775$  MeV [68]. The reason for this gap is tied to the approximate chiral symmetry of QCD, in fact, chiral symmetry turns out to be crucial for the construction of chiral EFT. The topic is discussed in more detail in section 2.1.

In case of nuclear structure, we are interested in low momenta. Therefore, we can ignore all heavier mesons, which also defines the so-called break-down scale  $\Lambda_\chi \approx m_\eta$ , at momenta larger than  $\Lambda_\chi$  our theory is bound to fail, as we ignore relevant degrees of freedom. Due to their small mass, pions have to be included explicitly. However, in case of phenomena that only probe extremely low momenta, it is possible to con-

struct a pionless EFT [69]. The final result is an expansion in  $Q/\Lambda_\chi$ , where  $Q$  is some low momentum or a pion mass. Being an expansion, chiral EFT allows for systematic improvement.

Using only pions and nucleons as degrees of freedom and relying on chiral symmetry, we can construct an effective Lagrangian. The general path has been laid out by Weinberg [70]:

*If one writes down the most general possible Lagrangian, including all terms consistent with assumed symmetry principles, and then calculates matrix elements with this Lagrangian to any given order of perturbation theory, the result will simply be the most general possible S-matrix consistent with analyticity, perturbative unitarity, cluster decomposition and the assumed symmetry principles.*

This approach allows to establish a clear connection between the effective and the underlying field theory via the involved symmetries. Moreover, in the case of chiral EFT, we are able to consistently construct multi-nucleon interactions in the same framework. More details on the construction of the Lagrangian are given in section 2.2.

Up to this point, we have pions as degrees of freedom in the theory, however, it is possible to construct a purely nucleonic effective interaction from chiral EFT, which is discussed in section 2.3. Finally, we discuss some aspects of regularization and renormalization in section 2.4 and give an overview on the chiral interactions used in this work in section 2.5.

This chapter is only a very brief introduction to chiral EFT omitting many of the mathematical details. For more details on the derivation of chiral interactions and their application, the reviews by Epelbaum *et al.* [71] and Machleidt *et al.* [72] are good starting points. Furthermore, the pedagogical introductions by Koch [73] and Phillips [74] are helpful and for those interested in the mathematical details, there exist very thorough primers by Scherer *et al.* [75] and Epelbaum [76] for chiral perturbation theory and chiral effective field theory, respectively. Note that the construction of the chiral interactions is not unique, and we mainly follow ref. [76] in this chapter.

## 2.1 CHIRAL SYMMETRY

As the name chiral EFT suggests, chiral symmetry plays a central role in the construction of an effective Lagrangian. The name stems from the representation of fermions in a relativistic quantum field theory, where the field can be separated in so-called left- and right-handed parts. In case of the quark field  $q$  we can write

$$q = q_R + q_L \quad \text{with} \quad q_R = P_R q \quad \text{and} \quad q_L = P_L q, \quad (2.1)$$



where the projection operators on the left- and right-handed parts,  $P_L$  and  $P_R$ , can be written as

$$P_R = \frac{1}{2}(1 + \gamma_5) \quad \text{and} \quad P_L = \frac{1}{2}(1 - \gamma_5), \quad (2.2)$$

where  $\gamma_\mu$  are the usual gamma matrices and  $\gamma_5 = -i\gamma_0\gamma_1\gamma_2\gamma_3$ . As expected from a chiral object, right- and left-handed parts transform into each other under parity transformation. Generally, Dirac fields transform as

$$q(t, \mathbf{x}) \rightarrow \gamma_0 q(t, -\mathbf{x}), \quad (2.3)$$

therefore a right-handed field changes in the following way under a parity transformation,

$$q_R(t, \mathbf{x}) = P_R q(t, \mathbf{x}) \rightarrow P_R \gamma_0 q(t, -\mathbf{x}) = \gamma_0 P_L q(t, -\mathbf{x}) = \gamma_0 q_L(t, -\mathbf{x}), \quad (2.4)$$

as  $\gamma_0$  and  $\gamma_5$  anticommute.

Using these fields, we can write the Lagrangian for QCD,

$$\mathcal{L}_{QCD} = \bar{q}_L i \not{D} q_L + \bar{q}_R i \not{D} q_R - \bar{q}_L \mathcal{M} q_R - \bar{q}_R \mathcal{M} q_L - \frac{1}{4} G_{\mu\nu}^a G^{a,\mu\nu}, \quad (2.5)$$

where  $D_\mu$  is the covariant derivative,  $G_{\mu\nu}^a$  is the gluon field strength tensor and  $\mathcal{M}$  is a diagonal matrix in flavor space defining the masses of the different flavors. Note that we used the Feynman slash notation, that is,  $\not{D} = \gamma^\mu D_\mu$ . Throughout this chapter we are only interested in the two lightest quarks, up and down quarks, we therefore have  $\mathcal{M} = \text{diag}(m_u, m_d)$ .

We can already see that only the mass connects the right- and left-handed fields. For now, we assume that the quark masses are zero. In this so-called chiral limit, we can perform the following two transformations,

$$q_L \rightarrow \underbrace{\exp\left(-\frac{i}{2} \boldsymbol{\theta}_L \cdot \boldsymbol{\tau}\right)}_{=:L} q_L \quad \text{and} \quad q_R \rightarrow \underbrace{\exp\left(-\frac{i}{2} \boldsymbol{\theta}_R \cdot \boldsymbol{\tau}\right)}_{=:R} q_R, \quad (2.6)$$

without changing the Lagrangian, which defines the chiral symmetry. The six angles,  $\boldsymbol{\theta}_R$  and  $\boldsymbol{\theta}_L$ , define a rotation in flavor space. The Pauli matrices,  $\boldsymbol{\tau} = (\tau_x, \tau_y, \tau_z)$ , act in isospin space, which is identical to the flavor space in our case, as we only consider up and down quarks. Note that we can rotate left- and right-handed fields independently from each other, as long as we assume massless quarks. In case of non-vanishing mass, the chiral symmetry is explicitly broken by the mass terms in the Lagrangian. However, the quark masses are small compared to masses of hadrons, therefore chiral symmetry is still a good approximation.

We now represent the symmetry in a slightly different way, using the following angles,

$$\boldsymbol{\theta}_V = \frac{1}{2}(\boldsymbol{\theta}_R + \boldsymbol{\theta}_L) \quad \text{and} \quad \boldsymbol{\theta}_A = \frac{1}{2}(\boldsymbol{\theta}_R - \boldsymbol{\theta}_L), \quad (2.7)$$

which are called the vector and axial-vector rotations, respectively, named after the transformation behavior of their corresponding Noether currents.

These transformations lend themselves more easily to a physical interpretation. In case of a vector rotation, we rotate both, left- and right-handed fields in exactly the same way. This yields isospin symmetry in the two-flavor case. There is ample evidence from the hadron spectrum that this symmetry is realized in the ground state. For instance, all  $\mathcal{N}$ -baryons have almost the same mass. Furthermore, the mass difference between protons and neutrons is small, and the masses of the  $\varrho$ -mesons are close to each other [68].

The axial-vector transformation, however, rotates left- and right-handed fields differently. Applying such a transformation can, for instance, change a state with positive parity to a negative one. If this symmetry were realized in the ground state, we would expect pairs of mesons with opposite parity and similar mass. Obviously, this is not the case. For instance, we do not find a counterpart with positive parity for the  $\varrho$ -meson, which has a mass of 775 MeV [68]. The best candidate would be the  $a_1$ -meson with a mass of 1230 MeV [68].

From that, we can conclude that chiral symmetry must be spontaneously broken, that is, the ground state does not exhibit the symmetry, even though it is a symmetry of the Lagrangian. Continuous symmetries that are spontaneously broken generate massless bosons [77], the so-called Goldstone bosons. In case of chiral symmetry, we can identify the pions as Goldstone bosons. They are not massless, as the chiral symmetry is only an approximation, but they are significantly lighter than other hadrons, which makes them so-called pseudo-Goldstone bosons.

## 2.2 EFFECTIVE LAGRANGIAN

As QCD is nonperturbative in the low-energy regime, we now construct an effective Lagrangian that uses the symmetries of the underlying theory. We also use chiral symmetry for the construction, but as it is explicitly broken, we have to correct for this approximation. In this sense, we are constructing a perturbative expansion around the chiral limit.

For the effective description we use nucleons and pions as degrees of freedom. Here, it is crucial that pions are pseudo-Goldstone bosons, as their low mass results in a separation of scales in the hadron spectrum. We start by constructing the pion Lagrangian, using all possible terms that fulfill the symmetries of QCD, including chiral symmetry. Additionally, we add terms that break chiral symmetry, that is, we expand around the chiral limit. This whole approach is called chiral perturbation theory, and the resulting pion Lagrangian can be written as [76]

$$\mathcal{L}_\pi = \mathcal{L}_\pi^{(-2)} + \mathcal{L}_\pi^{(0)} + \mathcal{L}_\pi^{(2)} + \dots \quad \text{with} \quad (2.8a)$$

$$\mathcal{L}_\pi^{(-2)} = \text{tr}(U^\dagger U), \quad (2.8b)$$

$$\mathcal{L}_\pi^{(0)} = \frac{F^2}{4} \text{tr}(\partial_\mu U^\dagger \partial^\mu U) + \frac{F^2 B}{2} \text{tr}(\mathcal{M}(U + U^\dagger)), \quad (2.8c)$$

$$\begin{aligned} \mathcal{L}_\pi^{(2)} = & l_1 \text{tr}(\partial_\mu U^\dagger \partial^\mu U)^2 + l_2 \text{tr}(\partial_\mu U^\dagger \partial_\nu U) \text{tr}(\partial^\mu U^\dagger \partial^\nu U) + \frac{l_3 B^2}{4} \text{tr}(\mathcal{M}(U + U^\dagger))^2 \\ & + \frac{l_7 B^2}{4} \text{tr}(\mathcal{M}(U - U^\dagger))^2 + \dots, \end{aligned} \quad (2.8d)$$

where the trace is performed in flavor space and  $l_i$ ,  $F$ , and  $B$  are so-called LECs. These have to be determined to fix the theory. This is done by fitting to experimental data, as they cannot be determined from QCD yet. The upper indices correspond to the exponent of the so-called soft scale,  $Q$ , of the effective Lagrangian, which is linked to the number of derivatives and pion-mass insertions. The unitary matrix in flavor space,  $U$ , is constructed to transform as

$$U \rightarrow LUR^\dagger, \quad (2.9)$$

which results in a representation in terms of pion fields as

$$U = \mathbb{1} + \frac{i}{F} \boldsymbol{\tau} \cdot \boldsymbol{\pi} - \frac{1}{2F^2} \boldsymbol{\pi}^2 - \frac{i\alpha}{F^3} \boldsymbol{\pi}^2 \boldsymbol{\tau} \cdot \boldsymbol{\pi} + \frac{8\alpha - 1}{8F^4} \boldsymbol{\pi}^4 + \mathcal{O}(\boldsymbol{\pi}^5). \quad (2.10)$$

Here we have the LEC  $F$  again, the Pauli matrices in isospin,  $\boldsymbol{\tau}$ , and the pion fields,  $\boldsymbol{\pi}$ . The additional parameter  $\alpha$  indicates a freedom in choosing the unitary matrix, as only the first few terms are fixed due to unitarity. No observable calculated using chiral EFT depends on the choice of  $\alpha$  [76]. Typical choices for  $U$  include,

$$U = \exp\left(\frac{i}{F} \boldsymbol{\pi} \cdot \boldsymbol{\tau}\right) \quad \Leftrightarrow \quad \alpha = \frac{1}{6}, \quad (2.11a)$$

$$U = \frac{1}{F} \left( \sqrt{F^2 - \boldsymbol{\pi}^2} \mathbb{1} + i \boldsymbol{\pi} \cdot \boldsymbol{\tau} \right) \quad \Leftrightarrow \quad \alpha = 0. \quad (2.11b)$$

As  $U$  is unitary, the lowest-order contribution to the Lagrangian,  $\mathcal{L}_\pi^{(-2)}$ , is only a constant and can therefore be removed.

Without the explicitly symmetry-breaking terms in eq. (2.8), we would have massless pion fields. Mass is added as a perturbation, in the first order we have a term

$$\frac{F^2 B}{2} \text{tr}(\mathcal{M}(U + U^\dagger)) = F^2 B(m_u + m_d) - \frac{B}{2} (m_u + m_d) \boldsymbol{\pi}^2 + \mathcal{O}(\boldsymbol{\pi}^4), \quad (2.12)$$

where we obtain a mass contribution for the pions with  $M^2 = B(m_u + m_d)$ . At this level all pions have the same mass, but higher-order corrections break this isospin symmetry, for instance

$$\frac{l_7 B^2}{4} \text{tr}(\mathcal{M}(U - U^\dagger))^2 = \frac{l_7 B^2}{F^2} (m_u - m_d)^2 \pi_0^2 + \mathcal{O}(\boldsymbol{\pi}^6). \quad (2.13)$$

We now continue with the nucleonic fields. One could again start by constructing the most general Lagrangian for nucleons and add all possible interactions with pions. However, this results in a description

of the nucleons as completely active degrees of freedom, including the creation and annihilation of nucleons and nucleon loops in Feynman diagrams. The nucleon, however, is heavier than the breakdown scale of our effective theory, and we therefore want to exclude such effects. Instead, we use the so-called heavy-baryon formalism, where we separate the four-momentum of the nucleons into a massive part,  $mv_\mu$ , and a small additional momentum,  $k_\mu$ ,

$$p_\mu \rightarrow mv_\mu + k_\mu, \quad (2.14)$$

with  $v_\mu v^\mu = 1$  and  $v_\mu k^\mu \ll m$ . We, thereby, constrain the nucleons in the theory to a small momentum on the order of the soft scale, making a non-relativistic approximation. Creation and annihilation of nucleons are not possible anymore, and we obtained the nucleon mass,  $m$ , as a separate hard scale of the theory.

Furthermore, the nucleon field  $\Psi$  can be separated into the so-called large and small component,

$$N := \exp\left(imv_\mu x^\mu\right) \frac{1+\not{v}}{2} \Psi \quad \text{and} \quad h := \exp\left(imv_\mu x^\mu\right) \frac{1-\not{v}}{2} \Psi. \quad (2.15)$$

The small component  $h$  can be removed from the Lagrangian using the equation-of-motion or path-integral formalism [78]. Note that for  $v_\mu = (1, 0, 0, 0)$  and Dirac representation, the large component is represented using only the upper components of the spinor. Therefore, only the spin degree of freedom is left, as expected for a non-relativistic description.

The resulting effective Lagrangian reads [76]

$$\mathcal{L}_{\text{eft}} = \mathcal{L}_\pi + \mathcal{L}_{\pi N}^{(0)} + \mathcal{L}_{\pi N}^{(1)} + \dots + \mathcal{L}_{\pi NN}^{(0)} + \mathcal{L}_{\pi NN}^{(1)} + \dots + \mathcal{L}_{\pi NNN}^{(1)} + \dots, \quad (2.16a)$$

$$\mathcal{L}_{\pi N}^{(0)} = \bar{N} \left[ i\not{v}^\mu D_\mu + g_A \not{v}^\mu S_\mu \right] N, \quad (2.16b)$$

$$\mathcal{L}_{\pi N}^{(1)} = \bar{N} \left[ c_1 \text{tr}(\chi_+) + c_2 \left( v^\mu u_\mu \right)^2 + c_3 \not{v}^\mu u_\mu + c_4 [S^\mu, S^\nu] u_\mu u_\nu + c_5 \left( \chi_+ - \frac{1}{2} \text{tr}(\chi_+) \right) \right] N, \quad (2.16c)$$

$$\mathcal{L}_{\pi NN}^{(0)} = -\frac{1}{2} C_S (\bar{N} N) (\bar{N} N) + 2C_T (\bar{N} S^\mu N) (\bar{N} S_\mu N), \quad (2.16d)$$

$$\mathcal{L}_{\pi NN}^{(1)} = \frac{1}{2} D (\bar{N} N) (\bar{N} S^\mu u_\mu N), \quad (2.16e)$$

$$\mathcal{L}_{\pi NNN}^{(1)} = -\frac{1}{2} E (\bar{N} N) (\bar{N} \boldsymbol{\tau} N) \cdot (\bar{N} \boldsymbol{\tau} N), \quad (2.16f)$$

where we used the covariant derivative of the nucleon field  $D_\mu := \partial_\mu + \frac{1}{2} \left( u^\dagger \partial_\mu u + u \partial_\mu u^\dagger \right)$ , the nucleon spin operator  $S_\mu := -\frac{1}{4} \gamma_5 \left[ \gamma_\mu, \gamma_\nu \right] v^\nu$ , the chiral symmetry breaking contribution  $\chi_+ := 2B \left( u^\dagger \mathcal{M} u^\dagger + u \mathcal{M} u \right)$ , the conjugate nucleon field  $\bar{N} := N^\dagger \gamma^0$ , and a set of LECs,  $g_A$ ,  $c_i$ ,  $C_S$ ,  $C_T$ ,  $D$ , and  $E$ . The parameter  $g_A$  is known as the axial coupling. Pions fields are inserted using

$$u = \sqrt{U} = \mathbb{1} + \frac{i}{2F} \boldsymbol{\tau} \cdot \boldsymbol{\pi} - \frac{1}{8F^2} \boldsymbol{\pi}^2 - \frac{i(8\alpha - 1)}{16F^3} \boldsymbol{\pi}^2 \boldsymbol{\tau} \cdot \boldsymbol{\pi} + \mathcal{O}(\boldsymbol{\pi}^4) \quad (2.17)$$

and its covariant derivative

$$u_\mu = iu^\dagger \left( \partial_\mu U \right) u^\dagger. \quad (2.18)$$

In case of the pure pion Lagrangian from eq. (2.8), we always have a trace over flavor space, but the nucleon field includes protons and neutrons, and many of the operators in eq. (2.16) act in isospin space. Superscripts of  $\mathcal{L}$  indicate the soft scale, as in the pion case, and the exponent of the soft scale is given by

$$\mathcal{A} := d + \frac{n}{2} - 2, \quad (2.19)$$

where  $d$  is the sum of derivatives and pion mass insertions, and  $n$  is the number of nucleon fields.

### 2.3 EFFECTIVE INTERACTION

Once we have constructed the effective Lagrangian, we need to obtain an effective interaction from it. In principle, we could start using perturbation theory at this point. This approach works well for the calculation of scattering observables with up to one nucleon. However, in the few-nucleon sector perturbation theory is hindered by the strength of the interaction, which results in bound states that cannot be treated perturbatively.

There exist various approaches to overcome this problem. The solution suggested by Weinberg [18, 19] is the use of time-ordered perturbation theory. This approach does have a few drawbacks, namely an effective interaction that depends explicitly on the energy and non-orthonormal states [79]. To overcome these difficulties, Epelbaum, Glöckle, and Meißner [79] proposed using the so-called method of unitary transformation. Its basic idea is simply to construct a unitary operator that decouples nucleonic states from all states that contain at least one pion. We can express the projected Hamiltonian as

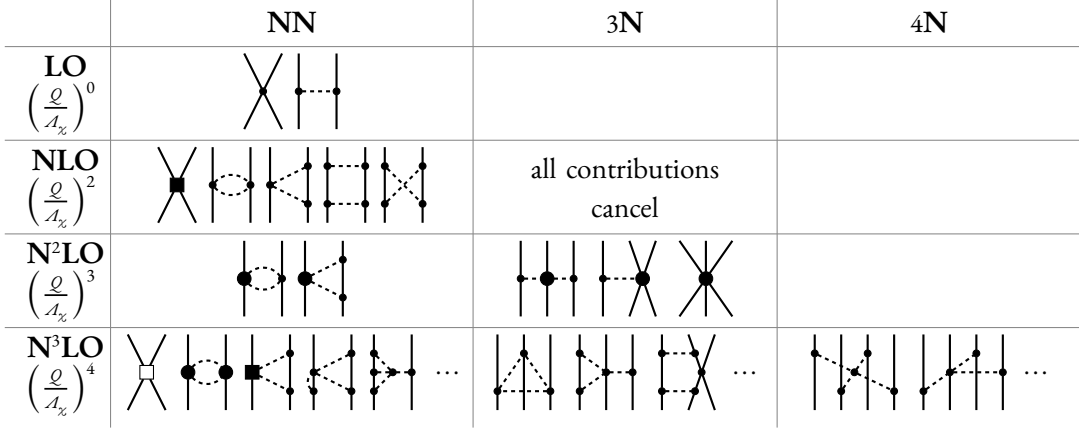
$$H_{\text{proj}} := U^\dagger H_{\text{EFT}} U = \begin{pmatrix} \eta H_{\text{proj}} \eta & 0 \\ 0 & \lambda H_{\text{proj}} \lambda \end{pmatrix}, \quad (2.20)$$

with a unitary transformation of [80]

$$U = \begin{pmatrix} \eta(1 + A^\dagger A)^{-\frac{1}{2}} & -A^\dagger(1 + AA^\dagger)^{-\frac{1}{2}} \\ A(1 + A^\dagger A)^{-\frac{1}{2}} & \lambda(1 + AA^\dagger)^{-\frac{1}{2}} \end{pmatrix}. \quad (2.21)$$

The operator  $\eta$  projects on a purely nucleonic state, while  $\lambda$  projects on a state with at least one pion. The operator  $A$  must fulfill  $A = \lambda A \eta$ . Constructing the Hamiltonian  $H_{\text{EFT}}$  is done by simply transforming the Lagrangian to a Hamiltonian density and integrating over space. Note that  $H_{\text{EFT}}$  contains infinitely many terms, just as the Lagrangian we constructed, and it contains pions as explicit degrees of freedom. Consequently, it cannot be used for calculating observables directly. Therefore, we have to obtain an effective interaction by solving the following decoupling equation, which follows from eqs. (2.20) and (2.21),

$$\lambda(H_{\text{EFT}} - [A, H_{\text{EFT}}] - AH_{\text{EFT}}A)\eta = 0. \quad (2.22)$$



**Figure 2.1:** Diagrammatic depiction of the chiral force at different orders. Solid lines indicate nucleons and dashed lines represent pions. Interactions are indicated by circles and squares, which correspond to  $\mathcal{A} = 0$  ( $\bullet$ ), 1 ( $\circ$ ), 2 ( $\blacksquare$ ), and 4 ( $\square$ ). No reducible, disconnected or vertex correction diagrams are shown. Each diagram represents all different time orderings.

Solving this equation can be done perturbatively, as shown in ref. [79]. For example, the first order yields,

$$V_{\text{eff}}^{(0)} = \eta H_{NN}^{(0)} \eta - \eta H_{\pi N}^{(0)} \frac{\lambda_1}{\omega} H_{\pi N}^{(0)} \eta, \quad (2.23)$$

where  $H_{NN}^{(0)}$  and  $H_{\pi N}^{(0)}$  correspond to the interaction parts of the Hamiltonian  $H_{\text{EFT}}$  at  $\mathcal{A} = 0$ . We also used  $\omega$  for the energy of the pion and  $\lambda_1$  for the projection operator on a state with exactly one pion and any number of nucleons.

The first part of eq. (2.23) corresponds to the lowest-order contact interaction, while the second part gives rise to the one-pion-exchange potential. The different contributions can be read from right to left. In the first case, we start with a nucleonic state, two of the nucleons interact, and we end up in a purely nucleonic state. This is obviously a contact interaction. The second part can be read as the creation, propagation and annihilation of a pion. This gives rise to the one-pion-exchange potential, however, creation and annihilation can also happen at the same nucleon.

Usually the different contributions are represented with Feynman-like diagrams, as shown in fig. 2.1. The contributions from eq. (2.23) make up the leading order (LO) of chiral EFT. For assigning an order to each contribution, the following power counting is used in case of the unitarity transformation method for fully connected diagrams, as given by eq. (5.138) in ref. [76],

$$v := 2(N + L - 2) + \sum_i \mathcal{A}_i \quad \text{with} \quad \mathcal{A}_i = d_i + \frac{n_i}{2} - 2, \quad (2.24)$$

where  $N$  is the number of nucleons,  $L$  the number of loops,  $d_i$  is the number of derivatives for the vertex  $i$ , and  $n_i$  is the number of nucleon lines at the vertex. The sum runs over all vertices.

Even though the diagrammatic representation is helpful to visualize the different contributions, in the

case of the unitary transformation, the contributions cannot be constructed from the diagrams alone, one has to solve eq. (2.22). Furthermore, there is no one-to-one correspondence between algebraic expressions and the individual diagrams. We can easily see that in case of the following second-order contributions, which give rise to multiple different diagrams,

$$-\eta H_{\pi N}^{(0)} \frac{\lambda_1}{\omega} H_{\pi N}^{(0)} \frac{\lambda_2}{\omega_1 + \omega_2} H_{\pi N}^{(0)} \frac{\lambda_1}{\omega} H_{\pi N}^{(0)} \eta \rightarrow \text{diagrams}, \dots \quad (2.25a)$$

$$\frac{1}{2} \eta H_{\pi N}^{(0)} \frac{\lambda_1}{\omega} H_{\pi N}^{(0)} \eta H_{\pi N}^{(0)} \frac{\lambda_1}{\omega} H_{\pi N}^{(0)} \eta \rightarrow \text{diagrams}, \dots \quad (2.25b)$$

In these diagrams, the vertices already have a time ordering. Note that both parts, eqs. (2.25a) and (2.25b), contribute to the box diagram as depicted in fig. 2.1 at next-to-leading order.

The final expressions can be worked out from the above contributions by inserting the interaction Hamiltonian and a straightforward calculation. More details and resulting expressions for the effective interaction are given in refs. [79, 81].

## 2.4 REGULARIZATION AND RENORMALIZATION

When constructing contributions at next-to-leading order (NLO), like the box diagram discussed in the previous section, we encounter loops in the diagrams. Such loops always imply a momentum we have to integrate over and, in general, the resulting expressions are not finite. There are various ways to regularize such integrals, for instance, simply cutting them off at a specific momentum or using dimensional regularization. This approach separates the infinities and by separating the constants in the Lagrangian into a renormalized part and counter terms, we can cancel the infinite contributions and obtain finite results. The renormalized constants can then be fixed by fitting to experimental data. This is so far the usual quantum-field-theory approach and details can be found in introductory literature, for instance in ref. [82].

However, when considering chiral EFT, we have an additional problem. The theory is not renormalizable in the usual sense, we need an infinite number of counter terms to cancel all the infinities that arise in this theory. This is not surprising for an effective theory, and, as it turns out, it does not pose a problem. It is possible to renormalize the theory order-by-order, that is, we can cancel all arising infinities up to the order we work at.

In principle the regularization of the loop integrals is sufficient to obtain finite expressions for the effective potential but this potential is still not physical. At this point arbitrary nucleon momenta are allowed in contrast to the preconditions for the use of a low-energy expansion. Furthermore, additional infinities would arise when inserting such a potential in a Lippmann-Schwinger equation. Therefore, external momenta are cut off at some point, usually by multiplying the potential with a Gaussian-like function. Usually, the function is chosen in such a way that a Taylor expansion of the regulator only introduces terms of order  $(Q/\Lambda)^\nu$ , where  $Q$  is some momentum that is cut off,  $\Lambda \neq \Lambda_\chi$  is the so-called cutoff momentum, and  $\nu$  is larger

than the order one works at. In principle, the theory should not depend on any of the high-momentum, that is, short-range contributions. In fact, a change of the coupling constants for the contact interactions should absorb the short-range physics up to excluded higher-order contributions.

Note that the cutoff  $\Lambda$  should still be much larger than typical momenta and can be of the order of the breakdown scale, that is  $Q \ll \Lambda \lesssim \Lambda_\chi$ . There is a practical advantage of choosing a smaller cutoff, as the resulting interaction is 'softer', that is, in a many-body calculation we need a smaller model space to achieve convergence. Therefore, most chiral interactions have a cutoff that is lower than the breakdown scale.

One can also use this approach for the regularization of the loops and simply skip renormalization, as done by Ordóñez *et al.* [83]. In this case, the neglected short-range physics is still captured in a redefinition of the LECs of the contact interactions.

After fixing the regularization completely, one can fit the undetermined LECs to data. Any observable calculated with such an interaction depends on  $\Lambda$ , but the dependence should decrease when using higher orders in chiral EFT. In fact, a reduced cutoff dependence is a necessary condition for a converging theory. However, a small cutoff dependence on its own is not sufficient to establish a convergence.

## 2.5 CHIRAL FORCES

This section is an overview of the different chiral interactions that play a role throughout this thesis. Note that there is a lot of freedom in the choice of regularization and fitting procedures, thus, a lot of different variants exist. This is only a small selection.

### NUCLEON-NUCLEON INTERACTION AT N<sup>3</sup>LO

The NN interaction we mainly use has been constructed by Entem and Machleidt [84]. It uses dimensional regularization for loop momenta [85] and, in addition, external momenta are multiplied with the regulator

$$\exp\left(-\left(\frac{p}{\Lambda_{2B}}\right)^{2n} - \left(\frac{p'}{\Lambda_{2B}}\right)^{2n}\right), \quad (2.26)$$

where  $p$  and  $p'$  are initial and final nucleon momenta in the center-of-mass frame. The cutoff used is  $\Lambda_{2B} = 500$  MeV and the exponents are chosen as to only generate contributions beyond  $Q^4$ , that is,  $n \geq 3$  for leading order and  $n \geq 2$  for higher-order contributions. The exact values for  $n$  vary between different contributions.

Fixing the LECs is done by fitting to pion-nucleon ( $\pi$ N) scattering phase shifts first. Then LECs introduced by contact terms, and a few additional LECs from the  $\pi$ N sector are fitted to NN scattering phase shifts. As a final optimization step, these LECs are adjusted by fitting to the same experimental data as the the CD-Bonn NN potential [5], however, only data up to a lab energy of 290 MeV is used.



SEMILOCAL MOMENTUM-SPACE REGULARIZED TWO-NUCLEON INTERACTION UP TO N<sup>4</sup>LO

This force is a recent construction of a two-body interaction by Reinert, Krebs, and Epelbaum [26]. For this interaction two different regularization approaches are combined. In case of the contact interactions, a simple nonlocal regulator is employed, that is

$$\exp\left(-\frac{p^2 + p'^2}{\Lambda_{2B}^2}\right), \quad (2.27)$$

where  $p$  and  $p'$  are initial and final nucleon momenta in the center-of-mass frame. The long-range parts of the interaction are regularized by modifying the pion propagator in momentum space, yielding a local regularization, for details see ref. [26].

The interaction is constructed for every order up to N<sup>4</sup>LO, which allows to investigate the order-by-order convergence of results obtained with a consistent set of interactions. Furthermore, for each order five different cutoffs are employed, namely 350, 400, 450, 500, and 550 MeV, allowing for a cutoff variation.

As in the previous case the LECs are first fitted to phase shifts and then optimized by fitting to  $\pi$ N and NN scattering data. The chosen data is based on the so-called 2013 Granada database [86, 87], see ref. [26] for details. Scattering data is included up to a lab energy of 260 MeV at N<sup>4</sup>LO, however, reduced datasets are used for lower orders. For instance, scattering data is only included up to 125 MeV at N<sup>2</sup>LO.

LOCAL THREE-NUCLEON INTERACTION AT N<sup>2</sup>LO

The 3N interaction by Navrátil [88] is designed to be local. As it only includes the first non-vanishing order of three-body interactions, there are no loops, and therefore no loop regularization is necessary. The nucleon momenta are regulated using

$$\exp\left(-\left(\frac{p'_2 - p_2}{\Lambda_{3B}}\right)^4\right) \exp\left(-\left(\frac{p'_3 - p_3}{\Lambda_{3B}}\right)^4\right), \quad (2.28)$$

where  $p_i$  and  $p'_i$  are the initial and final momenta of the  $i$ -th nucleon.

When using the interaction alongside the NN interaction by Entem and Machleidt [84], the original fit employs the same cutoff as the two-body interaction, that is  $\Lambda_{3B} = 500$  MeV. Two additional LECs appear at N<sup>2</sup>LO, namely  $c_D$  and  $c_E$ , they are fitted to the <sup>3</sup>H and <sup>3</sup>He binding energy, and to the triton half-life [89]. We will refer to this combination of two- and three-body interactions as EM/N500. Note that the two LECs are just a rescaling of the LECs from eqs. (2.16e) and (2.16f), that is

$$D = \frac{c_D}{F_\pi^2 \Lambda_\chi} \quad \text{and} \quad E = \frac{c_E}{F_\pi^4 \Lambda_\chi}. \quad (2.29)$$

However, Roth *et al.* [58] found that an interaction with a reduced three-body cutoff of  $\Lambda_{3B} = 400$  MeV, fixed by refitting  $c_E$  to the <sup>4</sup>He binding energy, is better suited when using the SRG to soften the interaction, inducing weaker many-body forces. This combination of two- and three-body forces is denoted as EM/N400 throughout this thesis.

SEMILOCAL MOMENTUM-SPACE REGULARIZED THREE-NUCLEON INTERACTION AT  $N^2LO$ 

When using the recent NN interactions by Reinert, Krebs, and Epelbaum [26], we combine them consistently with a three-body interaction. The PWD has been done by Hebeler [90], which is based on earlier work [29]. For consistency, the NN interaction is only included up to  $N^2LO$  as well. The regulator and cutoff is chosen to match the semilocal one from the two-body interaction.

There is no complete fitting procedure for this interaction yet, there only exist fits to the triton binding energy by Hütter [91], which correlates  $c_D$  and  $c_E$ , for calculations with this interaction we have to choose a value for one of the LECs. We will refer to this combination of two- and three-body interactions as SMS/H500, where the number indicates the cutoff momentum.

FOUR-NUCLEON INTERACTION AT  $N^3LO$ 

The leading 4N interaction has been derived by Epelbaum [30, 31]. As it does not contain any loop diagrams, no regularization scheme is necessary. A possible regulator for the external momenta is chosen in this work, and we perform the PWD, which is necessary to include the 4N contributions in a many-body calculation. Details can be found in section 4.4.

*Mach' dir keine Sorgen wegen deiner  
Schwierigkeiten mit der Mathematik.  
Ich kann dir versichern, dass meine  
noch größer sind.*

Albert Einstein

# 3

## Angular Momentum

The main part of this thesis addresses the partial-wave decomposition of the chiral 4N interactions, an effort that relies heavily on handling angular momenta and spherical tensors. In this chapter, the relevant relations of angular momentum in quantum mechanics are reviewed. As handling a large number of couplings of angular momenta is cumbersome in a purely algebraic fashion, this chapter also serves as an introduction to a diagrammatic approach. Especially for more complicated expressions, the diagrammatic approach allows a compact representation and it makes the structure clearly visible. All conventions used throughout this chapter are based on the excellent reference work by Varshalovich *et al.* [92] and the reader should refer to their work for a more thorough treatise on angular momentum in quantum mechanics. The diagrammatic representation is discussed thoroughly on pages 412-451 of ref. [92].

### 3.1 BASIC CONCEPTS

We start by expressing the essential elements of angular momentum theory using a diagrammatic notation. The diagrams are, in fact, graphs composed of different vertex and line types to distinguish the various elements relevant for the theory. Employing such graphs, we can represent states, operators and matrix elements. In general, the lines carry an angular momentum quantum number or coordinate label and vertices represent the different elements of the theory, which depend on the lines connected to them. Lines that connect multiple vertices always imply a summation or integration, depending on the type of line.

The most basic elements, bra and ket states are represented with one black dot and an attached line:

$$\begin{aligned} \hat{f}^{-1} |JM_J\rangle &:: \bullet \longrightarrow \xrightarrow{JM_J}, & \sqrt{4\pi} |\hat{r}\rangle &:: \bullet \dashrightarrow \xrightarrow{\hat{r}}, \\ \hat{f}^{-1} \langle JM_J| &:: \xrightarrow{JM_J} \longrightarrow \bullet, & \sqrt{4\pi} \langle \hat{r}| &:: \dashrightarrow \xrightarrow{\hat{r}} \bullet, \end{aligned}$$

where  $J$  is an arbitrary angular momentum quantum number,  $M_J$  the corresponding projection quantum number and  $\hat{r}$  is the unit vector in the direction of vector  $r$ . We also used the shorthand  $\hat{f} = \sqrt{2J+1}$ , which should not be confused with the previously established notation for a unit vector. All shown lines are so-called external lines, as they do not have a vertex at both ends. Hence, the ket states feature outgoing lines and the bra states incoming ones, which are denoted with a double arrow based on the convention from ref. [92].

The additional factors yield a slightly unusual normalization, which simplifies the transformation of diagrams, resulting in the following expressions for scalar products,

$$\xrightarrow{JM_J} \circ \xrightarrow{J'M'_J} = \frac{1}{\hat{f}^2} \langle JM_J | J'M'_J \rangle = \frac{\delta_{J,J'} \delta_{M_J,M'_J}}{\hat{f}^2}, \quad (3.1a)$$

$$\dashrightarrow \xrightarrow{\hat{r}} \circ \dashrightarrow \xrightarrow{\hat{r}'} = 4\pi \langle \hat{r} | \hat{r}' \rangle = 4\pi \delta^{(2)}(\hat{r} - \hat{r}'), \quad (3.1b)$$

$$\dashrightarrow \xrightarrow{\hat{r}} \circ \xrightarrow{LM_L} = \frac{\sqrt{4\pi}}{\hat{L}} \langle \hat{r} | JM_J \rangle = \frac{\sqrt{4\pi}}{\hat{L}} Y_{L,M_L}(\hat{r}) =: C_{L,M_L}(\hat{r}), \quad (3.1c)$$

$$\xrightarrow{LM_L} \circ \dashrightarrow \xrightarrow{\hat{r}} = \frac{\sqrt{4\pi}}{\hat{L}} \langle JM_J | \hat{r} \rangle = C_{L,M_L}^*(\hat{r}) = (-1)^{L-M_L} C_{L,-M_L}(-\hat{r}), \quad (3.1d)$$

where we used  $L$  to indicate an orbital angular momentum, and we introduced  $C_{L,M_L}$ , which is a different normalization of the spherical harmonics  $Y_{L,M_L}$ .

Coupled angular momenta are usually defined in terms of Clebsch-Gordan coefficients (CGCs),

$$|(j_1 j_2) JM_J\rangle := \sum_{m_1, m_2} \begin{pmatrix} j_1 & j_2 & J \\ m_1 & m_2 & M_J \end{pmatrix} |j_1 m_1, j_2 m_2\rangle, \quad (3.2)$$

however, for the diagrammatic approach 3j-symbols are better suited due to their symmetry properties. There are simple relations connecting these symbols,

$$\begin{pmatrix} j_1 & j_2 & J \\ m_1 & m_2 & M_J \end{pmatrix} = \hat{f} (-1)^{j_1 - j_2 + M} \begin{pmatrix} j_1 & j_2 & J \\ m_1 & m_2 & -M_J \end{pmatrix}, \quad (3.3a)$$

$$\begin{pmatrix} j_1 & j_2 & j_3 \\ m_1 & m_2 & m_3 \end{pmatrix} = \hat{f}_3^{-1} (-1)^{2j_1 + j_3 + m_3} \begin{pmatrix} j_1 & j_2 & j_3 \\ -m_1 & -m_2 & m_3 \end{pmatrix}. \quad (3.3b)$$

The 3j-symbol is only non-zero if the sum of the projection quantum numbers is zero and the triangular

relation is fulfilled, that is,

$$m_{j_1} + m_{j_2} + m_{j_3} = 0 \quad \text{and} \quad |j_1 - j_2| \leq j_3 \leq j_1 + j_2 \quad \text{and} \quad j_1 + j_2 + j_3 \text{ is an integer.} \quad (3.4)$$

These relations can be used to simplify and transform the phases in front of the 3j-symbols. Additionally, its value does not change for any cyclic permutation of the columns, which allows us to use the following diagrammatic notation,

$$\begin{pmatrix} j_1 & j_2 & j_3 \\ m_{j_1} & m_{j_2} & m_{j_3} \end{pmatrix} = \begin{array}{c} \nearrow j_1 m_{j_1} \\ + \bullet \xrightarrow{j_3 m_{j_3}} \\ \searrow j_2 m_{j_2} \end{array} = \begin{array}{c} \nearrow j_2 m_{j_2} \\ - \bullet \xrightarrow{j_3 m_{j_3}} \\ \searrow j_1 m_{j_1} \end{array}, \quad (3.5)$$

where a black dot connected to three lines represents a 3j-symbol. The plus or minus signs indicate the order of the lines, which is anti-clockwise and clockwise, respectively. If two of the lines are exchanged, the sign must be changed as well to not alter the expression. Note that it is often necessary to exchange lines of a 3j-symbol to reduce line crossings, which makes the graphs clearer and easier to read.

Incoming lines indicate a minus sign in front of the projection quantum number and an additional phase,

$$\begin{array}{c} \nearrow j_1 m_{j_1} \\ + \bullet \xrightarrow{j_3 m_{j_3}} \\ \nwarrow j_2 m_{j_2} \end{array} = (-1)^{j_2 - m_2} \begin{pmatrix} j_1 & j_2 & j_3 \\ m_{j_1} & -m_{j_2} & m_{j_3} \end{pmatrix}. \quad (3.6)$$

The  $(-1)^{-m}$  part of the phase ensures that the diagrammatic representation of a 3j-symbol behaves like a spherical tensor, which will be discussed in detail in the next section, and the  $(-1)^j$  is chosen to ensure a real-valued expression. Changing the sign of all projection quantum numbers or applying an odd permutation yields an additional factor of  $(-1)^{j_1+j_2+j_3}$ , which yields the following transformations of the diagrams,

$$\begin{array}{c} \nearrow j_1 m_{j_1} \\ + \bullet \xrightarrow{j_3 m_{j_3}} \\ \nwarrow j_2 m_{j_2} \end{array} = \begin{pmatrix} j_1 & j_2 & j_3 \\ m_{j_1} & m_{j_2} & m_{j_3} \end{pmatrix} = (-1)^{j_1+j_2+j_3} \begin{pmatrix} j_1 & j_2 & j_3 \\ -m_{j_1} & -m_{j_2} & -m_{j_3} \end{pmatrix} = \begin{array}{c} \nwarrow j_1 m_{j_1} \\ + \bullet \xrightarrow{j_3 m_{j_3}} \\ \nearrow j_2 m_{j_2} \end{array}, \quad (3.7a)$$

$$\begin{array}{c} \nearrow j_1 m_{j_1} \\ + \bullet \xrightarrow{j_3 m_{j_3}} \\ \nwarrow j_2 m_{j_2} \end{array} = (-1)^{2j_2} \begin{array}{c} \nearrow j_1 m_{j_1} \\ + \bullet \xleftarrow{j_3 m_{j_3}} \\ \nwarrow j_2 m_{j_2} \end{array}, \quad (3.7b)$$

$$\begin{array}{c} \nearrow j_1 m_{j_1} \\ + \bullet \xrightarrow{j_3 m_{j_3}} \\ \nwarrow j_2 m_{j_2} \end{array} = (-1)^{j_1+j_2+j_3} \begin{array}{c} \nwarrow j_1 m_{j_1} \\ - \bullet \xrightarrow{j_3 m_{j_3}} \\ \nearrow j_2 m_{j_2} \end{array}, \quad (3.7c)$$

where we used the properties from eq. (3.4) to simplify the factors in front of the diagrams.

We now return to the coupling expression from eq. (3.2) and express it using the diagrammatic approach,

$$\begin{aligned}
 |(j_1 j_2) J M_J\rangle &= \sum_{m_1, m_2} \hat{j}_1 \hat{j}_2 \hat{J} (-1)^{2j_1} \\
 &= \hat{j}_1 \hat{j}_2 \hat{J} (-1)^{2j_1}
 \end{aligned}$$
(3.8)

Disconnected diagrams, as seen in the first line, are simply multiplied. In the case above we have two states and a 3j-symbol, which implies a tensor product and normal multiplication.

In the last line we represent the sums over projection quantum numbers by connecting outgoing and incoming lines. Note that the final expression is more than a simple 3j-symbol. The  $j_1$  and  $j_2$  lines are internal lines and end in a black dot. Also note that we removed the projection numbers from the internal lines, as they are not free variables of the expression, similar to the way they are suppressed in the bra-ket notation on the left-hand side.

In case we sum over both quantum numbers, the angular momentum and its projection, we indicate the sum with a thick line,

$$\sum_{j, m_j} \hat{j}^2 \boxed{\mathcal{M}} \xrightarrow{j m_j} \xrightarrow{j m_j} \boxed{\mathcal{N}} = \sum_j \hat{j}^2 \boxed{\mathcal{M}} \xrightarrow{j} \boxed{\mathcal{N}} = \boxed{\mathcal{M}} \xrightarrow{j} \boxed{\mathcal{N}}, \quad (3.9)$$

where we represent subdiagrams with boxes. Note that we keep the  $j$ -label, as a single angular momentum line can appear in multiple places of a diagram. In this case all of the lines are thick but as long as they carry the same label, they still represent only one sum. Furthermore, non-diagrammatic parts of the formula may be part of the sum and depend on the same angular momentum.

In case of coordinate lines, internal lines indicate an integration over the solid angle,

$$\begin{aligned}
 \int \frac{d\Omega_r}{4\pi} C_{l', m'}^*(\hat{r}) C_{l, m}(\hat{r}) &= \xrightarrow{l' m'} \circ \hat{r} \circ \xrightarrow{l m} = \xrightarrow{l' m'} \circ \xrightarrow{l m}, \quad (3.10) \\
 \int \frac{d\Omega_r}{4\pi} C_{l_1, m_1}(\hat{r}) C_{l_2, m_2}(\hat{r}) C_{l_3, m_3}(\hat{r}) &= \xrightarrow{l_1 m_1} \circ \xrightarrow{l_2 m_2} \circ \hat{r} \circ \xrightarrow{l_3 m_3} = \xrightarrow{l_1 m_1} \circ \xrightarrow{l_2 m_2} \circ \xrightarrow{l_3 m_3} \\
 &= \begin{pmatrix} l_1 & l_2 & l_3 \\ 0 & 0 & 0 \end{pmatrix} \begin{pmatrix} l_1 & l_2 & l_3 \\ m_1 & m_2 & m_3 \end{pmatrix}, \quad (3.11)
 \end{aligned}$$

where we introduced a new vertex for the result of the second integral. Due to the properties of the 3j-symbol,

we know that  $l_1 + l_2 + l_3$  must be even for this vertex, otherwise it vanishes. Therefore no sign is necessary for this vertex, as the order of the columns is irrelevant.

### 3.2 SPHERICAL TENSORS

A spherical tensor  $\mathcal{M}_\lambda$  of rank  $\lambda$  is defined by the following commutator relation for its components  $\mathcal{M}_{\lambda\mu}$ , with  $\mu \in \{-\lambda, -\lambda + 1, \dots, \lambda\}$ ,

$$[J_\nu, \mathcal{M}_{\lambda\mu}] = \hat{\lambda} \begin{pmatrix} \lambda & 1 & \lambda \\ \mu & \nu & \mu + \nu \end{pmatrix} \mathcal{M}_{\lambda, \mu + \nu}, \quad (3.12)$$

where  $J_\nu$  are the components of the angular momentum operator in spherical representation with  $\nu \in \{-1, 0, 1\}$ , that is

$$J_{\pm 1} = \mp \frac{1}{\sqrt{2}} (J_x \pm iJ_y) \quad \text{and} \quad J_0 = J_z. \quad (3.13)$$

Typically, the phase of the tensor is chosen to satisfy

$$\mathcal{M}_{\lambda\mu}^\dagger = (-1)^{-\mu} \mathcal{M}_{\lambda, -\mu}. \quad (3.14)$$

As the angular momentum vector operator  $\mathbf{J}$  is the generator of rotations, eq. (3.12) determines the behaviour of  $\mathcal{M}_\lambda$  under rotations. It is, in fact, possible to separate matrix elements of the tensor into a part that is invariant under rotations, the reduced matrix element, and a second part that captures the general behavior of all spherical tensors, a 3j-symbol. This separation is known as the Wigner-Eckart theorem, see eq. (2) on page 475 of ref. [92]:

$$\langle jm_j | \mathcal{M}_{\lambda\mu} | j' m'_j \rangle = \langle j || \mathcal{M}_\lambda || j' \rangle (-1)^{j-m_j} \begin{pmatrix} j & \lambda & j' \\ -m_j & \mu & m'_j \end{pmatrix},$$

which can be translated into diagrammatic notation, yielding

$$\begin{array}{c} \text{Diagram 1: A box labeled } \mathcal{M} \text{ with three horizontal arrows entering from the right. The top arrow is labeled } jm_j \text{ (pointing left), the middle arrow is labeled } \lambda\mu \text{ (pointing right), and the bottom arrow is labeled } j'm'_j \text{ (pointing right).} \\ \\ \text{Diagram 2: A box labeled } \mathcal{M} \text{ with three horizontal arrows entering from the right. The top arrow is labeled } j \text{ (pointing left), the middle arrow is labeled } \lambda \text{ (pointing right), and the bottom arrow is labeled } j' \text{ (pointing right).} \\ \\ \text{Diagram 3: A vertex with three arrows meeting at a point. The top arrow is labeled } jm_j \text{ (pointing up-left), the bottom arrow is labeled } j'm'_j \text{ (pointing down-left), and the right arrow is labeled } \lambda\mu \text{ (pointing right).} \end{array} = (-1)^{2j} \underbrace{\text{Diagram 2}}_{= \langle j || \mathcal{M}_\lambda || j' \rangle} + \text{Diagram 3}, \quad (3.15)$$

where we represented the spherical tensor with a box in the diagrams. Note that the diagrammatic repre-





their components are operators. The scalar product can even be generalized to arbitrary rank,

$$\mathcal{M}_\lambda \cdot \mathcal{N}_\lambda := \sum_\mu \mathcal{M}_{\lambda,\mu} \mathcal{N}_{\lambda,\mu}^\dagger = \sum_\mu \mathcal{M}_{\lambda,\mu} (-1)^{-\mu} \mathcal{N}_{\lambda,-\mu} = (-1)^{-\lambda} \boxed{\mathcal{M}} \xrightarrow{\lambda} \boxed{\mathcal{N}}, \quad (3.18)$$

of course, both tensors must have the same rank.

### 3.3 TRANSFORMATIONS

When using the diagrammatic approach for evaluating quantum mechanical expressions, the main advantage lies in the simple rules for transforming diagrams. Applying these rules iteratively allows to simplify even extremely complicated expressions with relative ease, especially so, because their structure is clearly visible and an optimal scheme for simplifying the expression is apparent.

#### 3.3.1 BASIC TRANSFORMATIONS

We have already seen in eq. (3.7c) that we can invert the sign of a 3j-symbol, when introducing a factor of  $(-1)^{j_1+j_2+j_3}$ . In a similar fashion we can invert internal lines, which corresponds to renaming  $m_j$  to  $-m_j$  in the summation,

$$\boxed{\mathcal{M}} \xrightarrow{j} \boxed{\mathcal{N}} = \sum_{m_j} \mathcal{M}_{j,m_j} (-1)^{j-m_j} \mathcal{N}_{j,-m_j} = \sum_{m_j} (-1)^{j+m_j} \mathcal{M}_{j,-m_j} \mathcal{N}_{j,m_j} = (-1)^{2j} \boxed{\mathcal{M}} \xleftarrow{j} \boxed{\mathcal{N}}, \quad (3.19)$$

yielding a factor of  $(-1)^{2j}$ . These two transformations, changing signs and line direction, only result in phase factors. If we are only interested in the absolute value of an expression, we can safely omit all arrows and signs. In case of an integer angular momentum, the  $(-1)^{2j}$  factor is one, therefore, we will omit arrows in these cases. Special care has to be taken in the case of scalar products of half-integer angular momenta, in this case both lines must be inverted and only one factor is introduced,

$$\boxed{\mathcal{M}} \xrightarrow{j} \circ \xrightarrow{j'} \boxed{\mathcal{N}} = \frac{1}{\hat{j}^2} \sum_{m_j, m'_j} \mathcal{M}_{j,m_j} \delta_{j,j'} \delta_{m_j, m'_j} (-1)^{j'-m'_j} \mathcal{N}_{j,-m'_j} \quad (3.20)$$

$$= \frac{1}{\hat{j}^2} \sum_{m_j, m'_j} (-1)^{j+m_j} \mathcal{M}_{j,-m_j} \delta_{j,j'} \delta_{m_j, m'_j} \mathcal{N}_{j,m'_j} \quad (3.21)$$

$$= (-1)^{2j} \boxed{\mathcal{M}} \xleftarrow{j} \circ \xleftarrow{j'} \boxed{\mathcal{N}}. \quad (3.22)$$

We should especially consider that an inversion of only one of the lines yields scalar products with two incoming or two outgoing lines, which are ill-defined, as they correspond to two bra or two ket states. This also applies to single bra or ket states, that is, black dots with only a single line, as these become scalar products when combining diagrams. In case of a spherical harmonic, the inversion of an external coordinate line

corresponds to a parity transformation,

$$\boxed{\mathcal{M}} \xrightarrow{L} \circ \xrightarrow{\hat{r}} \cdots = \boxed{\mathcal{M}} \xrightarrow{L} \circ \xrightarrow{-\hat{r}} \cdots = (-1)^L \boxed{\mathcal{M}} \xrightarrow{L} \circ \xrightarrow{\hat{r}} \cdots. \quad (3.23)$$

We can express the scalar product with a 3j-symbol, which ensures that we can change line directions however we want,

$$\begin{array}{c} \xrightarrow{j m_j} + \xrightarrow{j' m'_j} \\ | \\ 0 \end{array} = \hat{j} \xrightarrow{j m_j} \circ \xrightarrow{j' m'_j} = \hat{j}^{-1} \delta_{j,j'} \delta_{m_j, m'_j}, \quad (3.24)$$

where we introduced a line with zero angular momentum. These lines have a few useful properties. As the sum over the projection quantum number is only one element, there is no difference between an internal and an external  $j = 0$  line. Therefore, two external  $j = 0$  lines can be joined together or an internal  $j = 0$  line can be separated in two external ones without changing the expression. They can also be inserted and removed from diagrams at any point, if the factors from eq. (3.24) are taken into account.

A tool that is helpful throughout all of quantum mechanics is the possibility to insert the identity operator in form of the completeness relation, which is done in diagrams by inserting a thick line,

$$\xrightarrow{j m_j} \circ \xrightarrow{l} \circ \xrightarrow{j' m'_j} = \xrightarrow{j m_j} \circ \xrightarrow{j' m'_j}, \quad (3.25a)$$

$$\xrightarrow{j m_j} \circ \xrightarrow{l} \circ \xrightarrow{j' m'_j} = \xrightarrow{j m_j} \circ \xrightarrow{j' m'_j}, \quad (3.25b)$$

$$\begin{array}{c} \swarrow j_1 m_{j_1} \quad \searrow j_1 m'_{j_1} \\ \xrightarrow{j_2 m_{j_2}} + \xrightarrow{l} \xrightarrow{j_2 m'_{j_2}} - \\ \swarrow \quad \searrow \end{array} = \hat{j}_1^2 \hat{j}_2^2 \begin{array}{c} \xrightarrow{j_1 m_{j_1}} \quad \xrightarrow{j_1 m'_{j_1}} \\ \xrightarrow{j_2 m_{j_2}} \quad \xrightarrow{j_2 m'_{j_2}} \end{array}. \quad (3.25c)$$

One has to be very careful when using this relations to remove an identity from the diagram, in such a case nothing else in the diagram should depend on the angular momentum to be removed and the line directions and signs must be exactly as given in the diagrams above.

The above relations can, for instance, be used to combine two spherical harmonics,

$$\begin{array}{c} \xrightarrow{\hat{r}} \circ \xrightarrow{j_1 m_{j_1}} \\ \xrightarrow{\hat{r}} \circ \xrightarrow{j_2 m_{j_2}} \end{array} = \xrightarrow{\hat{r}} \circ \xrightarrow{\hat{r}'} \begin{array}{c} \circ \xrightarrow{j_2 m_{j_2}} \\ \circ \xrightarrow{j_1 m_{j_1}} \end{array} = \xrightarrow{\hat{r}} \circ \xrightarrow{l} \circ \xrightarrow{\hat{r}'} \begin{array}{c} \circ \xrightarrow{j_2 m_{j_2}} \\ \circ \xrightarrow{j_1 m_{j_1}} \end{array} = \xrightarrow{\hat{r}} \circ \xrightarrow{l} \circ \begin{array}{c} \swarrow j_1 m_{j_1} \\ \searrow j_2 m_{j_2} \end{array}, \quad (3.26)$$

where we inserted an integral and a delta distribution in the first step, which does not change the expression. The integration has been performed using eq. (3.II).

### 3.3.2 CUTTING DIAGRAMS

When simplifying angular momentum diagrams, one often starts with a large connected diagram, which can then be cut into multiple simple parts. The main tool for this job is the Wigner-Eckart theorem (3.15). The diagrams are constructed in such a way that eq. (3.15) also works for any subdiagram  $\mathcal{M}$ , as they always have the properties of a spherical tensor matrix element. Furthermore, the Wigner-Eckart theorem is not constrained to external lines, it can just as well be applied for cutting internal ones,

$$(3.27)$$

However, there are a few requirements for cutting diagrams: At least one of the subdiagrams must have neither any external lines nor any unconnected bra or ket states. Furthermore, we have to cut all the lines connecting the two diagrams.

When cutting diagrams with less lines, we can insert a  $j = 0$  line in the diagram and remove it again. Starting from two subdiagrams connected by two lines,

where we used eq. (3.24) to insert two 3j-symbols, which also adds a factor. The dashed boxes correspond to the subdiagrams in eq. (3.27), and we use this equation to cut the diagram in the next step, yielding

At this point we start removing 3j-symbols using eq. (3.24) again, which results in

Note that we inverted two lines in the last step, the resulting factors cancel. We continue by removing the remaining 3j-symbols,

$$= \begin{array}{c} \boxed{\mathcal{M}} \\ \text{---} \end{array} \begin{array}{c} \curvearrowright \\ j_1 \end{array} \begin{array}{c} \boxed{\mathcal{N}} \\ \text{---} \\ \text{---} \\ \text{---} \end{array} \quad (3.28)$$

Note that a sign inversion was necessary to apply eq. (3.24) in the last step, which cancels the factor in front of the diagram.

The same trick can be applied for a single connecting line, which directly proves that the single angular momentum must be zero,

$$\begin{aligned} \boxed{\mathcal{M}} \begin{array}{c} \text{---} \\ j \end{array} \boxed{\mathcal{N}} \begin{array}{c} \text{---} \\ \text{---} \end{array} &= \overset{\circlearrowleft}{\int} \boxed{\mathcal{M}} \begin{array}{c} \text{---} \\ j \end{array} \begin{array}{c} \text{---} \\ + \end{array} \begin{array}{c} \text{---} \\ j \end{array} \begin{array}{c} \text{---} \\ + \end{array} \begin{array}{c} \text{---} \\ j \end{array} \boxed{\mathcal{N}} \begin{array}{c} \text{---} \\ \text{---} \end{array} \\ &= \overset{\circlearrowleft}{\int} \boxed{\mathcal{M}} \begin{array}{c} \text{---} \\ j \end{array} \begin{array}{c} \text{---} \\ 0 \end{array} \begin{array}{c} \text{---} \\ j \end{array} \begin{array}{c} \text{---} \\ + \end{array} \begin{array}{c} \text{---} \\ j \end{array} \boxed{\mathcal{N}} \begin{array}{c} \text{---} \\ \text{---} \end{array} \\ &= \delta_{j,0} \boxed{\mathcal{M}} \begin{array}{c} \text{---} \\ 0 \end{array} \begin{array}{c} \text{---} \\ 0 \end{array} \boxed{\mathcal{N}} \begin{array}{c} \text{---} \\ \text{---} \end{array} \end{aligned} \quad (3.29)$$

As in the previous case we used eq. (3.24) to insert and remove 3j-symbols that contain a zero angular momentum line in the first and last step, respectively. We cut the diagram using eq. (3.28) in the second step.

In case of four or even more lines, we have to apply the completeness relation from eq. (3.25c) to reduce the number of lines,

$$\begin{array}{c} \boxed{\mathcal{M}} \\ \text{---} \\ \text{---} \\ \text{---} \\ \text{---} \end{array} \begin{array}{c} \text{---} \\ j_1 \\ \text{---} \\ j_2 \\ \text{---} \\ j_3 \\ \text{---} \\ j_4 \end{array} \boxed{\mathcal{N}} \begin{array}{c} \text{---} \\ \text{---} \\ \text{---} \end{array} = \begin{array}{c} \boxed{\mathcal{M}} \\ \text{---} \\ \text{---} \\ \text{---} \\ \text{---} \end{array} \begin{array}{c} \text{---} \\ j_1 \\ \text{---} \\ + \\ \text{---} \\ J \\ \text{---} \\ - \\ \text{---} \\ j_1 \\ \text{---} \\ j_2 \\ \text{---} \\ j_3 \\ \text{---} \\ j_2 \\ \text{---} \\ j_4 \end{array} \boxed{\mathcal{N}} \begin{array}{c} \text{---} \\ \text{---} \\ \text{---} \end{array} = \begin{array}{c} \boxed{\mathcal{M}} \\ \text{---} \\ \text{---} \\ \text{---} \\ \text{---} \end{array} \begin{array}{c} \text{---} \\ j_1 \\ \text{---} \\ + \\ \text{---} \\ J \\ \text{---} \\ + \\ \text{---} \\ j_1 \\ \text{---} \\ j_2 \\ \text{---} \\ j_3 \\ \text{---} \\ j_4 \end{array} \boxed{\mathcal{N}} \begin{array}{c} \text{---} \\ \text{---} \\ \text{---} \end{array}, \quad (3.30)$$

where we cut three lines using eq. (3.27) in the last step. This procedure can be extended to additional lines, however, each additional line introduces another sum over an intermediate angular momentum, making the resulting diagram more complicated. When cutting diagrams it is therefore beneficial to cut as few lines as possible in each cut and only introduce additional sums when absolutely necessary. Note that all the cutting relations have been given in a form that does not introduce additional factors. If any of the line directions differ from the equations given above, the line has to be inverted before cutting.

### 3.3.3 COORDINATE CHANGES

One of the more involved tasks when using expressions in a spherical basis are coordinate changes. For this work, we need to be able to represent some coordinate  $\mathbf{R}$  in terms of two other coordinates, that is  $\mathbf{R} = \mathbf{r}_1 + \mathbf{r}_2$ . We start with the angular part, assuming we have only one spherical harmonic that depends on  $\hat{\mathbf{R}}$ . In case

of multiple spherical harmonics, they need to be combined into one by using eq. (3.26) first.

$$\begin{array}{c} \hat{R} \\ \circ \end{array} \xrightarrow{LM_L} = \begin{array}{c} \hat{r}_1 \\ \circ \end{array} \xrightarrow{l_1} \begin{array}{c} \circ \\ \circ \end{array} \xrightarrow{l_2} \begin{array}{c} \circ \\ \circ \end{array} \xrightarrow{LM_L} \times D_{l_1 l_2}^L \frac{r_1^{l_1} r_2^{l_2}}{R^L} \quad \text{with} \quad \mathbf{R} = r_1 + r_2 \quad (3.31)$$

$$D_{l_1 l_2}^L = \delta_{l_1+l_2, L} \sqrt{\frac{(2L+1)!}{(2l_1)!(2l_2)!}} \frac{1}{\hat{l}_1^2 \hat{l}_2^2}.$$

This formula is a diagrammatic representation of eq. (35) on page 167 of ref. [92], that is,

$$R^L Y_{L, M}(\hat{R}) = \sum_{l_1, l_2} \delta_{l_1+l_2, L} r_1^{l_1} r_2^{l_2} \sqrt{\frac{4\pi(2L+1)!}{(2l_1+1)!(2l_2+1)!}} \sum_{m_1, m_2} Y_{l_1, m_1}(\hat{r}_1) Y_{l_2, m_2}(\hat{r}_2) \begin{pmatrix} l_1 & l_2 & L \\ m_1 & m_2 & M \end{pmatrix}.$$

Note that the right-hand side of eq. (3.31) depends on the absolute value of  $R$ , thus the typical next step is representing  $R$  in terms of  $r_1$  and  $r_2$ , which can be done using Legendre polynomials. A function depending on  $\cos \vartheta$ , where  $\vartheta$  is the angle between  $r_1$  and  $r_2$ , can be expanded in terms of Legendre polynomials,

$$g(\cos \vartheta) = \sum_{l=0}^{\infty} c_l P_l(\cos \vartheta),$$

where the coefficient  $c_l$  is defined as

$$c_l := \frac{\hat{l}^2}{2} \int_{-1}^1 du P_l(u) g(u).$$

Additionally, a Legendre polynomial that depends on  $\cos \vartheta$  can be expanded in spherical harmonics,

$$P_l(\cos \vartheta) = \begin{array}{c} \hat{r}_1 \\ \circ \end{array} \xrightarrow{l} \begin{array}{c} \circ \\ \circ \end{array} \xrightarrow{\hat{r}_2} \begin{array}{c} \circ \\ \circ \end{array}.$$

This is known as the addition theorem, which is discussed as eq. (9) on page 164 of ref. [92] in an algebraic representation, that is,

$$P_l(\cos \vartheta) = \frac{4\pi}{\hat{l}^2} \sum_m Y_{l, m}(\hat{r}_1) Y_{l, m}^*(\hat{r}_2).$$

Combining the above equations for a function  $f$  that depends on the absolute value of  $R$ , we obtain

$$f(R) = \begin{array}{c} \hat{r}_1 \\ \circ \end{array} \xrightarrow{l} \begin{array}{c} \circ \\ \circ \end{array} \xrightarrow{\hat{r}_2} \begin{array}{c} \circ \\ \circ \end{array} \times \frac{1}{2} \int_{-1}^1 du P_l(u) f(R(r_1, r_2, u)), \quad (3.32)$$

with

$$R(r_1, r_2, u) = \sqrt{r_1^2 + r_2^2 + 2r_1 r_2 u}.$$

The integral over  $u$  can be interpreted as an integration over the angle  $\hat{r}_1 \cdot \hat{r}_2$ . When using the above equations with a minus sign, that is  $\mathbf{r} = \mathbf{r}_1 - \mathbf{r}_2$ , we need slight modifications. For eq. (3.31) we obtain an additional factor of  $(-1)^{l_2}$ , the expression is otherwise unchanged. In eq. (3.32), the expression for  $R$  is replaced with

$$r(r_1, r_2, u) = \sqrt{r_1^2 + r_2^2 - 2r_1 r_2 u}.$$

In cases with multiple coordinates that depend on the same angle, we still have only one integral, for instance, if we have coordinates  $\mathbf{R} = \mathbf{r}_1 + \mathbf{r}_2$  and  $\mathbf{r} = \mathbf{r}_1 - \mathbf{r}_2$ , we would obtain

$$f(R, r) = \sum_l \frac{1}{2} \int_{-1}^1 du P_l(u) f(R(r_1, r_2, u), r(r_1, r_2, u)).$$

Also note that the sum over  $l$  is, in principle, infinite. However, if one integrates over  $\hat{r}_1$  or  $\hat{r}_2$ , one gets limits for  $l$  from the solution of the integral. Even in more complicated situations, we always find a limit for  $l$  and the number of summands is finite in all cases throughout this work.

### 3.4 RECOUPLING COEFFICIENTS

When cutting diagrams, the goal is to reduce them to a product of well-known coefficients that do not depend on any external projection quantum number. These coefficients are defined with respect to the (re-)coupling behavior of states with multiple angular momenta. The simplest diagram is related to two coupled angular momenta, without changing the coupling order. We can calculate the overlap of such a state diagrammatically, using the coupled state from eq. (3.2).

$$\begin{aligned} \langle (j_1 j_2) J M_J | (j'_1 j'_2) J' M'_J \rangle &= \hat{j}_1 \hat{j}_2 \hat{J} (-1)^{2j_2} \begin{array}{c} \text{---} JM_J \text{---} \text{---} \text{---} \\ \text{---} j_1 \text{---} \text{---} \text{---} \\ \text{---} j_2 \text{---} \text{---} \text{---} \end{array} \times \hat{j}'_1 \hat{j}'_2 \hat{J}' (-1)^{2j'_1} \begin{array}{c} \text{---} j'_1 \text{---} \text{---} \text{---} \\ \text{---} j'_2 \text{---} \text{---} \text{---} \\ \text{---} J' M'_J \text{---} \end{array} \\ &= \hat{j}_1 \hat{j}'_1 \hat{j}_2 \hat{j}'_2 \hat{J} \hat{J}' (-1)^{2j'_1 + 2j_2} \begin{array}{c} \text{---} JM_J \text{---} \text{---} \text{---} \\ \text{---} j_1 \text{---} \text{---} \text{---} \\ \text{---} j_2 \text{---} \text{---} \text{---} \\ \text{---} j'_1 \text{---} \text{---} \text{---} \\ \text{---} j'_2 \text{---} \text{---} \text{---} \\ \text{---} J' M'_J \text{---} \end{array} \\ &= \delta_{J, J'} \delta_{M_J, M'_J} \delta_{j_1 j'_1} \delta_{j_2 j'_2} + \underbrace{\begin{array}{c} \text{---} j_1 \text{---} \text{---} \text{---} \\ \text{---} J \text{---} \text{---} \text{---} \\ \text{---} j_2 \text{---} \text{---} \text{---} \end{array}}_{=:\{j_1 j_2 J\}}, \end{aligned} \tag{3.33}$$

where we connected the bra and ket states in the first step. In the second step we cut the diagram using eq. (3.28), inverted the  $J$ -line and removed all scalar products. Usually one would expect the expression to just yield the Kronecker deltas, without any diagram or symbol. This diagram is, in fact, just a representation

of the triangular condition for  $j_1, j_2$ , and  $J$ , which is taken for granted when using the algebraic expression on the left-hand side. Any 3j-symbol already enforces the triangular condition, therefore this diagram can be removed completely if there is any 3j-symbol in the remaining diagram that connects the same three angular momenta. This calculation also displays a subtle issue with the diagrams when calculating a scalar product. In case of the bra-ket notation, the quantum numbers are ordered and it is clear which quantum number in the bra corresponds to a specific quantum number in the ket. This information is lost when using diagrams, one has to be careful which lines to connect. Note that the calculation above is usually discussed as the orthogonality relation for the CGCs.

We obtain a definition for a recoupling symbol, the 6j-symbol, when calculating the scalar product of states with three angular momenta in a different coupling order,

$$\begin{aligned}
 & \langle [j_1(j_2j_3)J_{23}]JM_J | [(j'_1j'_2)J_{12}j'_3]J'M'_J \rangle \\
 &= \text{Diagram} \times \hat{j}_1 \hat{j}'_1 \hat{j}_2 \hat{j}'_2 \hat{j}_3 \hat{j}'_3 \hat{J}_{12} \hat{J}_{23} \hat{J} \hat{J}' \\
 & \quad \times (-1)^{2j'_1+2j_3+2J_{12}+2J_{23}} \\
 &= \underbrace{\text{Diagram}}_{\begin{Bmatrix} j_1 & j_2 & J_{12} \\ j_3 & J & J_{23} \end{Bmatrix}} \times \hat{J}_{12} \hat{J}_{23} (-1)^{j_1+j_2+j_3+J} \delta_{j_1j'_1} \delta_{j_2j'_2} \delta_{j_3j'_3} \delta_{J,J'} . \quad (3.34)
 \end{aligned}$$

In the second line of the derivation we introduced a compact notation, where we have a large diagram on the left-hand side and multiple lines on the right-hand side. In such cases, the whole diagram, including all disconnected pieces, if any, are in front of all the algebraic expressions on the right-hand side. This is especially important when the diagram contains sums that act on the right-hand side as well. The right-hand side is then read in the usual order, that is, from top to bottom.

The 6j-symbol is invariant under permutations of its columns and under exchange of two angular momenta of the upper row with the momenta directly beneath them. Both symmetries can be seen easily in the diagrammatic expression by exchanging the position of two 3j-symbols, for example

$$\left\{ \begin{matrix} a & b & c \\ A & B & C \end{matrix} \right\} = \text{Diagram 1} = \text{Diagram 2} = \text{Diagram 3} = \left\{ \begin{matrix} B & A & c \\ b & a & C \end{matrix} \right\} . \quad (3.35)$$

Note that all phase factors, which appear when inverting signs and line directions in the third step, cancel each other.

We obtain a 9j-symbol, when calculating the scalar product of states with four angular momenta in a different coupling order,

$$\begin{aligned}
 & \left\langle [(j_1 j_2) J_{12} (j_3 j_4) J_{34}] J M_J \left| [(j'_1 j'_3) J_{13} (j'_2 j'_4) J_{24}] J' M'_J \right\rangle \\
 &= \begin{array}{c} \text{Diagram 1: A 9j-symbol diagram with four vertices and four external lines. The top vertex is labeled $j_1$ and $j'_1$, the right vertex $j_3$ and $j'_3$, the bottom vertex $j_4$ and $j'_4$, and the left vertex $j_2$ and $j'_2$. Internal lines are labeled $J_{12}, J_{13}, J_{24}, J_{34}$. Signs $+$ and $-$ are placed at vertices. External lines are labeled $JM_J$ and $J'M'_J$. } \end{array} \times \hat{j}_1 \hat{j}'_1 \hat{j}_2 \hat{j}'_2 \hat{j}_3 \hat{j}'_3 \hat{j}_4 \hat{j}'_4 \hat{J}_{12} \hat{J}_{34} \hat{J}_{13} \hat{J}_{24} \hat{J} \hat{J}' \\
 & \quad \times (-1)^{2j'_1 + 2j_2 + 2j'_2 + 2j_3 + 2j_4 + 2J_{13} + 2J_{34}} \\
 &= \begin{array}{c} \text{Diagram 2: A 9j-symbol diagram with four vertices and four external lines. The top vertex is labeled $j_1$ and $j'_1$, the right vertex $j_3$ and $j'_3$, the bottom vertex $j_4$ and $j'_4$, and the left vertex $j_2$ and $j'_2$. Internal lines are labeled $J_{12}, J_{13}, J_{24}, J_{34}$. Signs $+$ and $-$ are placed at vertices. External lines are labeled $JM_J$ and $J'M'_J$. } \end{array} \times \hat{J}_{12} \hat{J}_{34} \hat{J}_{13} \hat{J}_{24} \delta_{j_1 j'_1} \delta_{j_2 j'_2} \delta_{j_3 j'_3} \delta_{j_4 j'_4} \delta_{J, J'} \delta_{M_J, M'_J} \cdot \tag{3.36} \\
 & \quad \underbrace{\left\{ \begin{array}{ccc} j_1 & j_2 & J_{12} \\ j_3 & j_4 & J_{34} \\ J_{13} & J_{24} & J \end{array} \right\}}
 \end{aligned}$$

It is straightforward to verify that exchanging two rows or two columns of the 9j-symbol yields a factor of  $(-1)^{j_1 + j_2 + j_3 + j_4 + J_{12} + J_{34} + J_{13} + J_{24} + J}$ . The exponent of this factor must be an integer, therefore even permutations of rows or columns do not yield a factor. Furthermore, the 9j-symbol is invariant when flipping it along either of the diagonals.



*We have a habit in writing articles published in scientific journals to make the work as finished as possible, to cover all the tracks, [...]. So there isn't any place to publish, in a dignified manner, what you actually did in order to get to do the work.*

Richard Feynman

# 4

## Interaction Matrix Elements

The main challenge when including a four-body interaction in many-body calculations is the sheer number of matrix elements that need to be considered. It is, therefore, important to always work in a basis that uses the symmetries of the Hamiltonian to keep the number of matrix elements manageable while not impeding the actual calculation.

While working in the few-body sector, we use a coupled Jacobi harmonic oscillator (HO) basis that is completely antisymmetric with respect to particle exchange: As nucleons are fermions, we only need to consider antisymmetric states, and ignoring all states that are not completely antisymmetric drastically reduces the model-space size. The angular momenta and isospin quantum numbers are coupled to a total angular momentum and isospin to exploit rotational invariance and isospin symmetry, respectively. Note that isospin symmetry is broken by the Coulomb and nuclear interaction, and therefore, we cannot exploit it in the two-body sector, however, isospin breaking is negligible for interactions with a higher particle rank. We use the Jacobi coordinates to decouple the center-of-mass part, as we are only interested in intrinsic degrees of freedom, further reducing the size of the model space. Finally, we employ the HO basis, as it is widely used in many-body calculations, which makes further transformations unnecessary. In many-body calculations single-particle coordinates are employed, as it is not computationally feasible to construct a completely antisymmetric many-body Jacobi basis.

The main challenge of this work is deriving and implementing the calculation of matrix elements in the aforementioned bases, using the representation of the four-body interaction in single-particle momenta. The first sections discuss the details of the utilized model spaces, followed by the general transformation of

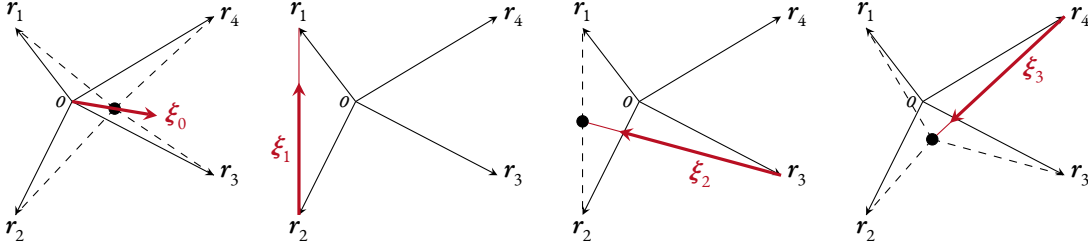
the single-particle momentum representation of the 4N interaction to the Jacobi HO basis. We discuss two specific four-body interactions in this chapter, a simple contact interaction with a nonlocal regulator and the chiral 4N interaction at N<sup>3</sup>LO.

## 4.1 JACOBI HARMONIC OSCILLATOR BASIS

The Jacobi HO basis we employ is defined using the following coordinates,

$$\begin{aligned}\xi_0 &= \sqrt{\frac{1}{A}}(r_1 + \dots + r_A), \\ \xi_1 &= \sqrt{\frac{1}{2}}(r_1 - r_2), \\ \xi_k &= \sqrt{\frac{k}{k+1}} \left[ \frac{1}{k}(r_1 + \dots + r_k) - r_{k+1} \right] \quad \text{with } k < A,\end{aligned}\tag{4.1}$$

where  $r_1, \dots, r_A$  are single-particle coordinates and we assume equal masses for all particles. This specific choice of coordinates implies  $A$  particles with identical mass. The coordinates are an extension of two-particle relative coordinates to an arbitrary number of particles, they also have an explicit center-of-mass coordinate,  $\xi_0$ , which allows the separation of the intrinsic degrees of freedom in this basis. Apart from a factor, the two-particle relative coordinate is equal to  $\xi_1$ . All additional Jacobi coordinates are defined relative to the center-of-mass of the previously included single-particle coordinates, a visualization is shown in fig. 4.1. Note that the Jacobi coordinates  $\xi_1, \dots, \xi_{A-1}$  do not change when adding the  $(A + 1)$ -st particle.



**Figure 4.1:** Construction of the four-body Jacobi coordinates  $\xi_0, \xi_1, \xi_2,$  and  $\xi_3$  from single-particle coordinates  $r_1, r_2, r_3,$  and  $r_4$ . Filled circles represent the center-of-mass of the particles indicated by dashed lines and the origin is marked by  $o$ .

These coordinates have a few desirable properties. First of all, transforming single-particle momenta  $p_1, \dots, p_A$  to Jacobi momenta  $\pi_1, \dots, \pi_A$  is done in exactly the same way as the coordinates. Furthermore, the transformation always has a Jacobian determinant of 1 and, especially important for using these coordinates in conjunction with the HO basis, the HO Hamiltonian has the same form,

$$H_{\text{HO}} = \sum_{i=1}^A \frac{p_i^2}{2m} + \frac{1}{2} m \omega^2 r_i^2 = \sum_{i=0}^{A-1} \frac{\pi_i^2}{2m} + \frac{1}{2} m \omega^2 \xi_i^2.$$

## TWO-BODY CASE

Using Jacobi coordinates we construct a two-body HO state,

$$\left| N_{\text{cm}} L_{\text{cm}} \mathcal{M}_{L_{\text{cm}}} \right\rangle \otimes \left| N_1, (L_1 S_1) J_1 \mathcal{M}_{J_1}, T_1 \mathcal{M}_{T_1} \right\rangle,$$

where  $N_{\text{cm}}$ ,  $L_{\text{cm}}$  and  $\mathcal{M}_{L_{\text{cm}}}$  are the radial, orbital angular momentum and projection quantum number corresponding to the center-of-mass part, respectively, which are defined with respect to  $\xi_0$  and  $\pi_0$ . The quantum numbers  $N_1$  and  $L_1$  correspond to a HO state that is defined with respect to  $\xi_1$  and  $\pi_1$ . Additionally, we define the quantum numbers  $S_1$  and  $T_1$ , which are the total spin and isospin of the first two particles, respectively, and we couple the relative part of the state to a total angular momentum  $J_1$ . The total energy quantum number of the state is given by the radial and the orbital angular momentum quantum numbers,

$$E = E_{\text{cm}} + E_1 \quad \text{with} \quad E_{\text{cm}} = 2N_{\text{cm}} + L_{\text{cm}} \quad \text{and} \quad E_1 = 2N_1 + L_1.$$

We are only interested in completely antisymmetric states. As the center-of-mass part must be symmetric when exchanging two particles, the relative part must be antisymmetric. Explicitly applying the particle-exchange operator  $P_{1,2}$  yields

$$P_{1,2} \left| N_1, (L_1 S_1) J_1 \mathcal{M}_{J_1}, T_1 \mathcal{M}_{T_1} \right\rangle = (-1)^{L_1 + S_1 + T_1} \left| N_1, (L_1 S_1) J_1 \mathcal{M}_{J_1}, T_1 \mathcal{M}_{T_1} \right\rangle,$$

which means that only states fulfilling

$$(-1)^{L_1 + S_1 + T_1} = -1 \tag{4.2}$$

are relevant. The  $(-1)^{L_1}$  part stems from the parity of the relative two-body wavefunction, as parity inversion and particle exchange in coordinate space are the same for the two-body relative part. Exchanging the coupling order of the spin and isospin, which corresponds to exchanging columns in CGCs, yields the remaining factors.

## THREE-BODY CASE

The three-body state is built upon the two-body one,

$$\begin{aligned} & \left| N_{\text{cm}} L_{\text{cm}} \mathcal{M}_{L_{\text{cm}}} \right\rangle \otimes \left| E_{12} k_{12} J_{12} \mathcal{M}_{J_{12}} T_{12} \mathcal{M}_{T_{12}} \right\rangle \\ & = \left| N_{\text{cm}} L_{\text{cm}} \mathcal{M}_{L_{\text{cm}}} \right\rangle \otimes \left| N_1 N_2, \left[ (L_1 S_1) J_1 \left( L_2 \frac{1}{2} \right) J_2 \right] J_{12} \mathcal{M}_{J_{12}}, \left( T_{12} \frac{1}{2} \right) T_{12} \mathcal{M}_{T_{12}} \right\rangle, \end{aligned}$$

where the left-hand side is an abbreviation using the intrinsic HO energy  $E_{12} = 2N_1 + L_1 + 2N_2 + L_2$ , and an index  $k_{12} = \{N_1, L_1, S_1, J_1, T_1, N_2, L_2, J_2\}$  that collects the remaining quantum numbers. Note that the center-of-mass part now corresponds to three particles and the parity of the intrinsic three-body state is given

by  $(-1)^{L_1+L_2} = (-1)^{E_{12}}$ . When enforcing eq. (4.2), the state is already antisymmetric under exchange of the first two particles, as the two-body relative part does not change when adding the third particle. The construction of a completely antisymmetric basis requires an explicit diagonalization of the antisymmetrization operator. As in the two-body case, the intrinsic part must be completely antisymmetric, and the antisymmetrizer does not depend on the projection quantum numbers, therefore, those parts are suppressed in the following formulae. An explicit calculation of the antisymmetrizer matrix elements yields

$$\begin{aligned} & \langle E'_{12} k'_{12} J'_{12} T'_{12} | \mathcal{A} | E_{12} k_{12} J_{12} T_{12} \rangle \\ &= \delta_{E_{12}, E'_{12}} \delta_{J_{12}, J'_{12}} \delta_{T_{12}, T'_{12}} \left( \frac{1}{3} \delta_{k_{12}, k'_{12}} - \frac{2}{3} \sum_{L, S} (-1)^{S_1+S'_1+T_1+T'_1} \hat{L}^2 \hat{S}^2 \hat{J}_1 \hat{J}'_1 \hat{J}_2 \hat{J}'_2 \hat{S}_1 \hat{S}'_1 \hat{T}_1 \hat{T}'_1 \langle \langle N'_1 L'_1, N'_2 L'_2 | N_1 L_1, N_2 L_2; L \rangle \rangle_{\frac{1}{3}} \right. \\ & \quad \left. \left\{ \begin{matrix} \frac{1}{2} & \frac{1}{2} & S'_1 \\ \frac{1}{2} & \frac{1}{2} & S_1 \end{matrix} \right\} \left\{ \begin{matrix} \frac{1}{2} & \frac{1}{2} & T'_1 \\ \frac{1}{2} & \frac{1}{2} & T_1 \end{matrix} \right\} \left\{ \begin{matrix} L_1 & S_1 & J_1 \\ L_2 & \frac{1}{2} & J_2 \\ L & S & J_{12} \end{matrix} \right\} \left\{ \begin{matrix} L'_1 & S'_1 & J'_1 \\ L'_2 & \frac{1}{2} & J'_2 \\ L & S & J_{12} \end{matrix} \right\} \right), \quad (4.3) \end{aligned}$$

where we used a harmonic oscillator bracket (HOB), which is related to coordinate transformations of HO states. We use the HOB as defined by Kamuntavičius *et al.* [93]. This formula is discussed in ref. [94], and a very detailed derivation can be found on pages 138-143 of ref. [95].

The antisymmetrizer is clearly block diagonal in  $T_{12}$ ,  $J_{12}$  and  $E_{12}$  and each block can be diagonalized separately. As we want to construct antisymmetric states, we are interested in all eigenstates of the antisymmetrizer that have an eigenvalue of one. All other eigenstates have a spurious symmetry, indicated by an eigenvalue of zero, and can be discarded. The entries of the eigenvectors obtained from a numerical diagonalization of each block are the so-called coefficients of fractional parentage (CFPs), which allow to construct an antisymmetrized basis from the partly antisymmetric one,

$$|E_{12} i_{12} J_{12} T_{12} \rangle_a = \sum_{k_{12}} c_{i_{12}, k_{12}}^{E_{12}, J_{12}, T_{12}} |E_{12} k_{12} J_{12} T_{12} \rangle,$$

where we labeled the completely antisymmetric state using a subscript  $a$ . The CFP depends on the  $TJE$ -block and the two indices  $i_{12}$  and  $k_{12}$ . We already introduced the index  $k_{12}$ , which corresponds to a set of quantum numbers in the partially antisymmetric state. The index  $i_{12}$  just labels the  $i_{12}$ -th eigenvector of the antisymmetrizer with an eigenvalue of one and does not correspond to any physical quantum numbers. In fact, there is a freedom in choosing CFPs, as the eigenvectors all have an eigenvalue of one and any linear combination of these eigenvectors is still an eigenvector with the same eigenvalue. It is advantageous to choose a set of CFPs that defines an orthonormal basis, but this does not eliminate the ambiguity in choosing the basis.

#### FOUR-BODY CASE

The same approach as in the three-body case can be used for constructing the four-body basis. Again, we define a partially antisymmetric basis, which is based on the fully antisymmetric three-body basis,

$$\begin{aligned}
& \left| E_{123} k_{123} J_{123} \mathcal{M}_{J_{123}} T_{123} \mathcal{M}_{T_{123}} \right\rangle \\
&= \left| E_{12} i_{12} \mathcal{N}_3, \left[ J_{12} \left( L_3 \frac{1}{2} \right) J_3 \right] J_{123} \mathcal{M}_{J_{123}}, \left( T_{12} \frac{1}{2} \right) T_{123} \mathcal{M}_{T_{123}} \right\rangle \\
&= \sum_{k_{12}} c_{i_{12}, k_{12}}^{E_{12}, J_{12}, T_{12}} \left| E_{12} k_{12} \mathcal{N}_3, \left[ J_{12} \left( L_3 \frac{1}{2} \right) J_3 \right] J_{123} \mathcal{M}_{J_{123}}, \left( T_{12} \frac{1}{2} \right) T_{123} \mathcal{M}_{T_{123}} \right\rangle \\
&= \sum_{k_{12}} c_{i_{12}, k_{12}}^{E_{12}, J_{12}, T_{12}} \left| E_{123} J_{123} \mathcal{M}_{J_{123}} \beta_{123}, \left[ \left( T_{12} \frac{1}{2} \right) T_{12} \frac{1}{2} \right] T_{123} \mathcal{M}_{T_{123}} \right\rangle,
\end{aligned}$$

where we introduced two additional shorthands using the indices

$$\begin{aligned}
\beta_{123} &= \{ N_1, L_1, S_1, J_1, N_2, L_2, J_2, N_3, L_3, J_3, J_{12} \} \quad \text{and} \\
k_{123} &= \{ E_{12}, i_{12}, J_{12}, T_{12}, N_3, L_3, J_3 \}.
\end{aligned}$$

The former indicates the spatial part of a four-body state that is partially antisymmetric in the first two particles and the latter is a collection of quantum numbers for the partially antisymmetric four-body basis. Furthermore, we introduced the intrinsic four-body energy quantum number  $E_{123} = E_{12} + 2N_3 + L_3$ . We suppressed the center-of-mass part in the expressions above and introduced quantum numbers corresponding to the additional Jacobi coordinate. The first and second Jacobi coordinate do not change when adding a particle, and the state we constructed is, therefore, antisymmetric in the first three particles.

Again we calculate the matrix elements of the antisymmetrizer to construct a fully antisymmetric basis,

$$\begin{aligned}
& \left\langle E'_{123} k'_{123} J'_{123} T'_{123} \left| \mathcal{A} \right| E_{123} k_{123} J_{123} T_{123} \right\rangle \\
&= \delta_{E_{123}, E'_{123}} \delta_{J_{123}, J'_{123}} \delta_{T_{123}, T'_{123}} \left( \frac{1}{4} \delta_{k_{123}, k'_{123}} - \frac{3}{4} \sum_{k_{12}, k'_{12}} \sum_{L_{23}, K} c_{i_{12}, k_{12}}^{E_{12}, J_{12}, T_{12}} c_{i'_{12}, k'_{12}}^{E'_{12}, J'_{12}, T'_{12}} \hat{J}_{12} \hat{T}_{12} \hat{J}_2 \hat{J}_3 \hat{J}'_{12} \hat{T}'_{12} \hat{J}'_2 \hat{J}'_3 \hat{L}_{23} \hat{K}^2 \right. \\
&\quad \left. (-1)^{T_{12} + T'_{12} + L_2 + L'_2 + J_2 + J'_2} \delta_{N_1, N'_1} \delta_{L_1, L'_1} \delta_{S_1, S'_1} \delta_{J_1, J'_1} \delta_{T_1, T'_1} \right. \\
&\quad \left. \begin{Bmatrix} J_1 & J_2 & J_{12} \\ J'_2 & K & J_3 \\ J'_{12} & J'_3 & J_{123} \end{Bmatrix} \begin{Bmatrix} J_3 & \frac{1}{2} & L_3 \\ L'_2 & K & J'_2 \end{Bmatrix} \begin{Bmatrix} L_3 & L'_2 & K \\ L'_3 & L_2 & L_{23} \end{Bmatrix} \begin{Bmatrix} L'_3 & L_2 & K \\ J_2 & J'_3 & \frac{1}{2} \end{Bmatrix} \right. \\
&\quad \left. \begin{Bmatrix} \frac{1}{2} & T_{123} & T_{12} \\ \frac{1}{2} & T_1 & T'_{12} \end{Bmatrix} \left\langle \left\langle N'_2 L'_2, N'_3 L'_3 \left| N_2 L_2, N_3 L_3; L_{23} \right\rangle \right\rangle_{\frac{1}{8}} \right), \quad (4.4)
\end{aligned}$$

see pages 52-56 of reference [61] for a detailed derivation of the formula. The calculation of the antisymmetrizer matrix elements can also be generalized to an  $A$ -body system, for details see ref. [94].

As in the three-body case, the antisymmetrizer is block-diagonal in the total angular momentum and isospin, as well as the total intrinsic HO energy. Diagonalization of the individual blocks yields a completely antisymmetric four-body basis,

$$\left| E_{123} i_{123} J_{123} T_{123} \right\rangle_a = \sum_{k_{123}} \tilde{c}_{i_{123}, k_{123}}^{E_{123}, J_{123}, T_{123}} \left| E_{123} k_{123} J_{123} T_{123} \right\rangle,$$

where we introduced another index,  $i_{123}$ , to label the different antisymmetric states.

In principle, this iterative scheme of adding one particle and antisymmetrizing the basis can be extended

to many-body systems. However, the necessary calculation and diagonalization of the antisymmetrizer are the main problems in using such a basis for an actual many-body calculation. With each new particle, the basis becomes larger, and at some point, the computational cost of antisymmetrization outweighs the possible gains of a Jacobi basis.

#### EMBEDDING

For performing calculations using the Jacobi HO basis it is often necessary to represent an irreducible  $N$ -body operator in a many-body space using  $N$ -body matrix elements. For instance, we can represent an irreducible two-body Hamiltonian in a three-body Jacobi HO basis using the two-body matrix elements,

$${}_a \langle E'_{12} i'_{12} J_{12} T_{12} | H^{[2]} | E_{12} i_{12} J_{12} T_{12} \rangle_a = 3 \sum_{k_{12}} \sum_{k'_{12}} \delta_{J_1, J'_1} \delta_{T_1, T'_1} \delta_{N_2, N'_2} \delta_{L_2, L'_2} \delta_{J_2, J'_2} c_{i_{12}, k_{12}}^{E_{12}, J_{12}, T_{12}} c_{i'_{12}, k'_{12}}^{E'_{12}, J'_{12}, T'_{12}} \\ {}_a \langle N'_1, (L'_1 S'_1) J_1, T_1 | H^{[2]} | N_1, (L_1 S_1) J_1, T_1 \rangle_a .$$

This formula can be derived by expressing the completely antisymmetric state in a partially antisymmetric one and decouple the additional particle. Details on the derivation can be found in ref. [61]. The case of embedding the matrix elements of a two-body Hamiltonian in a three-body space has one peculiarity. We assume all representations of the Hamiltonian in a three- or four-body basis to be independent of the isospin projection. This is not the case for the two-body representation, as the Coulomb and nuclear interaction break the isospin symmetry substantially. Therefore the two-body matrix element in the formula above is assumed to be the arithmetic mean of the possible isospin projections.

Formulae for the other transformations, that is, obtaining four-body matrix elements from two-body and three-body ones, are similar,

$${}_a \langle E'_{123} i'_{123} J_{123} T_{123} | H^{[3]} | E_{123} i_{123} J_{123} T_{123} \rangle_a = 4 \sum_{k_{123}} \sum_{k'_{123}} \delta_{J_{12}, J'_{12}} \delta_{T_{12}, T'_{12}} \delta_{N_3, N'_3} \delta_{L_3, L'_3} \delta_{J_3, J'_3} \tilde{c}_{i_{123}, k_{123}}^{E_{123}, J_{123}, T_{123}} \tilde{c}_{i'_{123}, k'_{123}}^{E'_{123}, J'_{123}, T'_{123}} \\ {}_a \langle N'_1, (L'_1 S'_1) J_1, T_1 | H^{[3]} | N_1, (L_1 S_1) J_1, T_1 \rangle_a ,$$

$${}_a \langle E'_{123} i'_{123} J_{123} T_{123} | H^{[2]} | E_{123} i_{123} J_{123} T_{123} \rangle_a = 6 \sum_{k_{123}} \sum_{k'_{123}} \sum_{k_{12}} \sum_{k'_{12}} \delta_{J_{12}, J'_{12}} \delta_{T_{12}, T'_{12}} \delta_{J_1, J'_1} \delta_{T_1, T'_1} \delta_{N_2, N'_2} \delta_{L_2, L'_2} \delta_{J_2, J'_2} \delta_{N_3, N'_3} \delta_{L_3, L'_3} \delta_{J_3, J'_3} \\ c_{i_{12}, k_{12}}^{E_{12}, J_{12}, T_{12}} c_{i'_{12}, k'_{12}}^{E'_{12}, J'_{12}, T'_{12}} \tilde{c}_{i_{123}, k_{123}}^{E_{123}, J_{123}, T_{123}} \tilde{c}_{i'_{123}, k'_{123}}^{E'_{123}, J'_{123}, T'_{123}} \\ {}_a \langle N'_1, (L'_1 S'_1) J_1, T_1 | H^{[2]} | N_1, (L_1 S_1) J_1, T_1 \rangle_a .$$

Note that in all cases there is a combinatorial factor, given by the binomial coefficient  $\binom{A}{N}$ , when transforming  $N$ -body matrix elements of an irreducible  $N$ -body operator in an  $A$ -body space. This also implies that three-body matrix elements of irreducible two-body operators must be treated differently from the matrix elements of irreducible three-body operators. A simple example would be to start with two-body matrix elements of an irreducible two-body operator, embed them in three-body space and afterwards transform

them to four-body space using the formulae above. We clearly obtain a factor of twelve instead of the expected factor of six. The same problem arises when performing a many-body calculation and representing few-body operators in many-body space. Therefore, the few-body matrix elements for operators of different particle ranks must be kept separate, if we want to use the same matrix elements for many-body calculations with varying particle numbers.

## 4.2 FOUR-NUCLEON PARTIAL-WAVE DECOMPOSITION

All interactions we cover in this chapter are defined in terms of single-particle momenta and uncoupled spin and isospin operators. However, the Jacobi basis we want to use has explicit orbital angular momentum defined with respect to Jacobi coordinates, thus we need to perform a 4N partial-wave decomposition (PWD).

Our final goal is the calculation of the following matrix element,

$$\begin{aligned} & \left\langle N'_{\text{cm}} L'_{\text{cm}} \mathcal{M}'_{L'_{\text{cm}}}; E'_{123} i'_{123} J'_{123} T'_{123} \left| V \right| N_{\text{cm}} L_{\text{cm}} \mathcal{M}_{L_{\text{cm}}}; E_{123} i_{123} J_{123} T_{123} \right\rangle_a \\ &= \sum_{\substack{k'_{123} \\ k'_{12} \\ k'_{123} \\ k'_{12}}} \sum_{\substack{c'_{123}, J'_{123}, T'_{123} \\ c'_{123}, k'_{123} \\ c'_{123}, k'_{123} \\ c'_{123}, k'_{12}}} \sum_{\substack{c'_{123}, J'_{123}, T'_{123} \\ c'_{123}, k'_{123} \\ c'_{123}, k'_{12}}} \left\langle \left[ \left( T'_{12} \frac{1}{2} \right) T'_{12} \frac{1}{2} \right] T'_{123} \mathcal{M}'_{T'_{123}} \left| V^{(T)} \right| \left[ \left( T_{12} \frac{1}{2} \right) T_{12} \frac{1}{2} \right] T_{123} \mathcal{M}_{T_{123}} \right\rangle \\ & \quad \left\langle N'_{\text{cm}} L'_{\text{cm}} \mathcal{M}'_{L'_{\text{cm}}}, E'_{123} J'_{123} \mathcal{M}'_{J'_{123}}, \beta'_{123} \left| V^{(S)} \right| N_{\text{cm}} L_{\text{cm}} \mathcal{M}_{L_{\text{cm}}}, E_{123} J_{123} \mathcal{M}_{J_{123}}, \beta_{123} \right\rangle, \end{aligned} \quad (4.5)$$

where we used that the interaction,  $V$ , can always be factorized in a spatial part,  $V^{(S)}$ , and an isospin part,  $V^{(T)}$ . The latter can usually be evaluated in a straightforward way, the former requires a PWD. All matrix elements we are going to use are defined in a single-particle momentum basis and are not coupled. The first step is decoupling the states and transform the expression to a Jacobi momentum basis by inserting two completeness relations,

$$\begin{aligned} & \left\langle N'_{\text{cm}} L'_{\text{cm}} \mathcal{M}'_{L'_{\text{cm}}}, E'_{123} J'_{123} \mathcal{M}'_{J'_{123}}, \beta'_{123} \left| V^{(S)} \right| N_{\text{cm}} L_{\text{cm}} \mathcal{M}_{L_{\text{cm}}}, E_{123} J_{123} \mathcal{M}_{J_{123}}, \beta_{123} \right\rangle \\ &= \iiint d^3 \pi_0 d^3 \pi_1 d^3 \pi_2 d^3 \pi_3 \iiint d^3 \pi'_0 d^3 \pi'_1 d^3 \pi'_2 d^3 \pi'_3 \sum_{\substack{m'_a, m'_b, m'_c, m'_d \\ m'_a, m'_b, m'_c, m'_d \\ m'_a, m'_b, m'_c, m'_d \\ m'_a, m'_b, m'_c, m'_d \\ m'_a, m'_b, m'_c, m'_d}} \sum_{\substack{M'_{L_1}, M'_{L_1} \\ M'_{L_2}, M'_{L_2} \\ M'_{L_3}, M'_{L_3} \\ M'_{J_1}, M'_{J_1} \\ M'_{J_2}, M'_{J_2} \\ M'_{J_3}, M'_{J_3}}} \sum_{\substack{M'_{L_1}, M'_{L_1} \\ M'_{L_2}, M'_{L_2} \\ M'_{L_3}, M'_{L_3} \\ M'_{J_1}, M'_{J_1} \\ M'_{J_2}, M'_{J_2} \\ M'_{J_3}, M'_{J_3}}} \sum_{\substack{M'_{L_1}, M'_{L_1} \\ M'_{L_2}, M'_{L_2} \\ M'_{L_3}, M'_{L_3} \\ M'_{J_1}, M'_{J_1} \\ M'_{J_2}, M'_{J_2} \\ M'_{J_3}, M'_{J_3}}} \sum_{\substack{M'_{L_1}, M'_{L_1} \\ M'_{L_2}, M'_{L_2} \\ M'_{L_3}, M'_{L_3} \\ M'_{J_1}, M'_{J_1} \\ M'_{J_2}, M'_{J_2} \\ M'_{J_3}, M'_{J_3}}} \sum_{\substack{M'_{L_1}, M'_{L_1} \\ M'_{L_2}, M'_{L_2} \\ M'_{L_3}, M'_{L_3} \\ M'_{J_1}, M'_{J_1} \\ M'_{J_2}, M'_{J_2} \\ M'_{J_3}, M'_{J_3}}} \\ & \quad \left( \begin{array}{c} \frac{1}{2} \quad \frac{1}{2} \\ m'_a \quad m'_b \end{array} \left| \begin{array}{c} S_1 \\ M_{J_2} \end{array} \right. \right) \left( \begin{array}{c} \frac{1}{2} \quad \frac{1}{2} \\ m'_c \quad m'_d \end{array} \left| \begin{array}{c} S'_1 \\ M'_{J_2} \end{array} \right. \right) \left( \begin{array}{c} L_1 \quad S_1 \\ M_{L_1} \quad M_{S_1} \end{array} \left| \begin{array}{c} J_1 \\ M_{J_1} \end{array} \right. \right) \left( \begin{array}{c} L'_1 \quad S'_1 \\ M'_{L_1} \quad M'_{S_1} \end{array} \left| \begin{array}{c} J'_1 \\ M'_{J_1} \end{array} \right. \right) \\ & \quad \left( \begin{array}{c} L_2 \quad \frac{1}{2} \\ M_{L_2} \quad m_{s_c} \end{array} \left| \begin{array}{c} J_2 \\ M_{J_2} \end{array} \right. \right) \left( \begin{array}{c} L'_2 \quad \frac{1}{2} \\ M'_{L_2} \quad m'_{s_c} \end{array} \left| \begin{array}{c} J'_2 \\ M'_{J_2} \end{array} \right. \right) \left( \begin{array}{c} L_3 \quad \frac{1}{2} \\ M_{L_3} \quad m_{s_c} \end{array} \left| \begin{array}{c} J_3 \\ M_{J_3} \end{array} \right. \right) \left( \begin{array}{c} L'_3 \quad \frac{1}{2} \\ M'_{L_3} \quad m'_{s_c} \end{array} \left| \begin{array}{c} J'_3 \\ M'_{J_3} \end{array} \right. \right) \\ & \quad \left( \begin{array}{c} J_1 \quad J_2 \\ M_{J_1} \quad M_{J_2} \end{array} \left| \begin{array}{c} J_{12} \\ M_{J_{12}} \end{array} \right. \right) \left( \begin{array}{c} J'_1 \quad J'_2 \\ M'_{J_1} \quad M'_{J_2} \end{array} \left| \begin{array}{c} J'_{12} \\ M'_{J_{12}} \end{array} \right. \right) \left( \begin{array}{c} J_{12} \quad J_3 \\ M_{J_{12}} \quad M_{J_3} \end{array} \left| \begin{array}{c} J_{123} \\ M_{J_{123}} \end{array} \right. \right) \left( \begin{array}{c} J'_{12} \quad J'_3 \\ M'_{J_{12}} \quad M'_{J_3} \end{array} \left| \begin{array}{c} J'_{123} \\ M'_{J_{123}} \end{array} \right. \right) \\ & \quad R_{N_{\text{cm}} L_{\text{cm}}}(\pi_0) R_{N'_{\text{cm}} L'_{\text{cm}}}^*(\pi'_0) R_{N_1 L_1}(\pi_1) R_{N'_1 L'_1}^*(\pi'_1) R_{N_2 L_2}(\pi_2) R_{N'_2 L'_2}^*(\pi'_2) R_{N_3 L_3}(\pi_3) R_{N'_3 L'_3}^*(\pi'_3) \\ & \quad Y_{L_{\text{cm}} M_{L_{\text{cm}}}}(\hat{\pi}_0) Y_{L'_{\text{cm}} M'_{L'_{\text{cm}}}}^*(\hat{\pi}'_0) Y_{L_1 M_{L_1}}(\hat{\pi}_1) Y_{L'_1 M'_{L'_1}}^*(\hat{\pi}'_1) Y_{L_2 M_{L_2}}(\hat{\pi}_2) Y_{L'_2 M'_{L'_2}}^*(\hat{\pi}'_2) Y_{L_3 M_{L_3}}(\hat{\pi}_3) Y_{L'_3 M'_{L'_3}}^*(\hat{\pi}'_3) \\ & \quad \left\langle m'_{s_a} m'_{s_b} m'_{s_c} m'_{s_d}, \pi'_1 \pi'_2 \pi'_3 \left| V^{(S)} \right| m_{s_a} m_{s_b} m_{s_c} m_{s_d}, \pi_1 \pi_2 \pi_3 \right\rangle \frac{1}{8} \delta^{(3)}(\pi'_0 - \pi_0) \end{aligned}$$

$$\begin{aligned}
& = \delta_{N_{cm}, N'_{cm}} \delta_{L_{cm}, L'_{cm}} \delta_{M_{L_{cm}}, M'_{L_{cm}}} \iiint d^3 \pi_1 d^3 \pi_2 d^3 \pi_3 \iiint d^3 \pi'_1 d^3 \pi'_2 d^3 \pi'_3 \sum_{\substack{m_{s_a}, m'_{s_a} \\ m_{s_b}, m'_{s_b}}} \sum_{\substack{M_{L_1}, M'_{L_1} \\ M_{S_1}, M'_{S_1}}} \sum_{\substack{M_{L_2}, M'_{L_2} \\ m_{s_c}, m'_{s_c}}} \sum_{\substack{M_{L_3}, M'_{L_3} \\ m_{s_d}, m'_{s_d}}} \sum_{\substack{M_{J_1}, M'_{J_1} \\ M_{J_2}, M'_{J_2}}} \sum_{\substack{M_{J_3}, M'_{J_3} \\ M_{J_{12}}, M'_{J_{12}}}} \\
& \left( \begin{array}{cc|c} \frac{1}{2} & \frac{1}{2} & S_1 \\ m_{s_a} & m_{s_b} & M_{J_2} \end{array} \right) \left( \begin{array}{cc|c} \frac{1}{2} & \frac{1}{2} & S'_1 \\ m'_{s_a} & m'_{s_b} & M'_{J_2} \end{array} \right) \left( \begin{array}{cc|c} L_1 & S_1 & J_1 \\ M_{L_1} & M_{S_1} & M_{J_1} \end{array} \right) \left( \begin{array}{cc|c} L'_1 & S'_1 & J'_1 \\ M'_{L_1} & M'_{S_1} & M'_{J_1} \end{array} \right) \\
& \left( \begin{array}{cc|c} L_2 & \frac{1}{2} & J_2 \\ M_{L_2} & m_{s_c} & M_{J_2} \end{array} \right) \left( \begin{array}{cc|c} L'_2 & \frac{1}{2} & J'_2 \\ M'_{L_2} & m'_{s_c} & M'_{J_2} \end{array} \right) \left( \begin{array}{cc|c} L_3 & \frac{1}{2} & J_3 \\ M_{L_3} & m_{s_d} & M_{J_3} \end{array} \right) \left( \begin{array}{cc|c} L'_3 & \frac{1}{2} & J'_3 \\ M'_{L_3} & m'_{s_d} & M'_{J_3} \end{array} \right) \\
& \left( \begin{array}{cc|c} J_1 & J_2 & J_{12} \\ M_{J_1} & M_{J_2} & M_{J_{12}} \end{array} \right) \left( \begin{array}{cc|c} J'_1 & J'_2 & J'_{12} \\ M'_{J_1} & M'_{J_2} & M'_{J_{12}} \end{array} \right) \left( \begin{array}{cc|c} J_{12} & J_3 & J_{123} \\ M_{J_{12}} & M_{J_3} & M_{J_{123}} \end{array} \right) \left( \begin{array}{cc|c} J'_{12} & J'_3 & J'_{123} \\ M'_{J_{12}} & M'_{J_3} & M'_{J_{123}} \end{array} \right) \\
& R_{N_1 L_1}(\pi_1) R_{N'_1 L'_1}^*(\pi'_1) R_{N_2 L_2}(\pi_2) R_{N'_2 L'_2}^*(\pi'_2) R_{N_3 L_3}(\pi_3) R_{N'_3 L'_3}^*(\pi'_3) \\
& Y_{L_1, M_{L_1}}(\hat{\pi}_1) Y_{L'_1, M'_{L_1}}^*(\hat{\pi}'_1) Y_{L_2, M_{L_2}}(\hat{\pi}_2) Y_{L'_2, M'_{L_2}}^*(\hat{\pi}'_2) Y_{L_2, M_{L_2}}(\hat{\pi}_2) Y_{L'_2, M'_{L_2}}^*(\hat{\pi}'_2) \\
& \frac{1}{8} \left\langle m'_{s_a} m'_{s_b} m'_{s_c} m'_{s_d}, \pi'_1 \pi'_2 \pi'_3 \left| V^{(s)} \right| m_{s_a} m_{s_b} m_{s_c} m_{s_d}, \pi_1 \pi_2 \pi_3 \right\rangle, \tag{4.6}
\end{aligned}$$

where  $R_{NL}$  is the radial HO wave function in Jacobi-momentum representation, which is orthonormal. Furthermore, we used that the interaction conserves total momentum, thus making the integration over the center-of-mass momentum simple. The factor of  $\frac{1}{8}$  originates from transforming the momentum conservation from a single-particle expression to Jacobi momenta, that is

$$\delta^{(3)}(\mathbf{p}'_1 + \mathbf{p}'_2 + \mathbf{p}'_3 + \mathbf{p}'_4 - \mathbf{p}_1 - \mathbf{p}_2 - \mathbf{p}_3 - \mathbf{p}_4) = \delta^{(3)}(2(\boldsymbol{\pi}'_0 - \boldsymbol{\pi}_0)) = \frac{1}{8} \delta^{(3)}(\boldsymbol{\pi}'_0 - \boldsymbol{\pi}_0).$$

For an interaction that depends on single-particle momenta, these momenta can easily be expressed in terms of Jacobi momenta. One can then insert such an interaction in eq. (4.6) and calculate the matrix elements. However, this approach requires the evaluation of an 18-dimensional integral and 24 nested sums, which limits the number matrix elements that can be computed in this way in a reasonable timeframe. Therefore, further simplification is necessary, depending on the type of interaction we use. Nevertheless, the naive approach employed in eq. (4.6) is an excellent tool for cross-checking the results of a more involved derivation. In the following sections, we discuss the contact and the chiral 4N interaction and specialize eq. (4.6) for each interaction.

### 4.3 CONTACT INTERACTION

A pure contact interaction for four particles could be modeled in the following way,

$$V = C \delta^{(3)}(\mathbf{r}_1 - \mathbf{r}_2) \delta^{(3)}(\mathbf{r}_2 - \mathbf{r}_3) \delta^{(3)}(\mathbf{r}_3 - \mathbf{r}_4),$$

however, a pure contact interaction is impossible to use in a many-body method. We therefore "smear out" the delta distributions by transforming the interaction to the momentum basis and multiplying with a reg-



ulator, yielding

$$\begin{aligned}
& \langle \mathbf{p}'_1 \mathbf{p}'_2 \mathbf{p}'_3 \mathbf{p}'_4 | V | \mathbf{p}_1 \mathbf{p}_2 \mathbf{p}_3 \mathbf{p}_4 \rangle \\
&= C \frac{1}{(2\pi)^{12}} \iiint d^3 r_1 d^3 r_2 d^3 r_3 d^3 r_4 \delta^{(3)}(\mathbf{r}_1 - \mathbf{r}_2) \delta^{(3)}(\mathbf{r}_2 - \mathbf{r}_3) \delta^{(3)}(\mathbf{r}_3 - \mathbf{r}_4) \exp\left(i \sum_i \mathbf{r}_i \cdot (\mathbf{p}'_i - \mathbf{p}_i)\right) \\
&= C \frac{1}{(2\pi)^9} \delta^{(3)}(\mathbf{p}'_1 + \mathbf{p}'_2 + \mathbf{p}'_3 + \mathbf{p}'_4 - \mathbf{p}_1 - \mathbf{p}_2 - \mathbf{p}_3 - \mathbf{p}_4) \\
&= \underbrace{C \frac{1}{8 (2\pi)^9}}_{c_{4B}} \delta^{(3)}(\boldsymbol{\pi}'_0 - \boldsymbol{\pi}_0) \\
&\rightarrow c_{4B} \delta^{(3)}(\boldsymbol{\pi}'_0 - \boldsymbol{\pi}_0) F(\boldsymbol{\pi}'_1, \boldsymbol{\pi}'_2, \boldsymbol{\pi}'_3, \mathcal{A}) F(\boldsymbol{\pi}_1, \boldsymbol{\pi}_2, \boldsymbol{\pi}_3, \mathcal{A}),
\end{aligned}$$

with the regulator

$$F(\boldsymbol{\pi}_1, \boldsymbol{\pi}_2, \boldsymbol{\pi}_3, \mathcal{A}) := \exp\left(-\left(\frac{\pi_1^2 + \pi_2^2 + \pi_3^2}{3\mathcal{A}^2}\right)^{n_{\text{exp}}}\right).$$

The regulator we use here is a nonlocal one, as the inverse Fourier transformation of the final expression would result in a nonlocal expression in coordinate space. With the regulator we have introduced two additional parameters, the cutoff  $\mathcal{A}$  and an exponent  $n_{\text{exp}}$ .

The final expression can be inserted in eq. (4.6) and drastically simplified. We can integrate over all solid angles and evaluate all sums by using the orthogonality relation of the CGCs (3.33). This leaves us with a spatial part of

$$\begin{aligned}
& \left\langle N'_{\text{cm}} L'_{\text{cm}} M'_{L_{\text{cm}}}, E'_{123} J'_{123} M'_{J_{123}} \beta'_{123} \middle| V^{(S)} \middle| N_{\text{cm}} L_{\text{cm}} M_{L_{\text{cm}}}, E_{123} J_{123} M_{J_{123}} \beta_{123} \right\rangle \\
&= c_{4B} \delta_{N'_{\text{cm}}, N_{\text{cm}}} \delta_{L'_{\text{cm}}, L_{\text{cm}}} \delta_{M'_{L_{\text{cm}}}, M_{L_{\text{cm}}}} \delta_{L'_{1,0}, L_{1,0}} \delta_{L'_{2,0}, L_{2,0}} \delta_{L'_{3,0}, L_{3,0}} \delta_{S_1, S_1} \delta_{J_1, J_1} \delta_{J_2, J_2} \delta_{J_3, J_3} \delta_{M'_{J_{123}}, M_{J_{123}}} \\
&\quad \iiint d\pi_1 d\pi_2 d\pi_3 \pi_1^2 \pi_2^2 \pi_3^2 R_{N_1 L_1}(\pi_1) R_{N_2 L_2}(\pi_2) R_{N_3 L_3}(\pi_3) F(\pi_1, \pi_2, \pi_3, \mathcal{A}) \\
&\quad \iiint d\pi'_1 d\pi'_2 d\pi'_3 \pi_1'^2 \pi_2'^2 \pi_3'^2 R_{N'_1 L'_1}^*(\pi'_1) R_{N'_2 L'_2}^*(\pi'_2) R_{N'_3 L'_3}^*(\pi'_3) F(\pi'_1, \pi'_2, \pi'_3, \mathcal{A}), \tag{4.7}
\end{aligned}$$

where the integration over the absolute values of the initial and final Jacobi momenta factorize. Therefore, we only have to perform a three-dimensional numerical integration over the Jacobi momenta. Furthermore, all orbital quantum numbers must be zero, which is expected of a contact interaction, as the centrifugal barrier prevents any contacts. However, it is also a consequence of the chosen regulator. If the regulator depends on an angle between the Jacobi coordinates, as would be the case for a local regulator, the contact interaction can act even in channels with nonzero angular momentum. Finally, the interaction is diagonal in many quantum numbers, including the complete isospin space, as we did not include any isospin operator. In fact, antisymmetrization ensures that this interaction is only nonzero in the  $J_{123}^{\pi_{123}} = 0^+$  channel with a total isospin of  $T_{123} = 0$ . These properties ensure that a lot of matrix elements need not be calculated and the nonzero ones do not require much computing power.

## 4.4 CHIRAL FOUR-NUCLEON INTERACTION

The chiral 4N interaction at N<sup>3</sup>LO has been derived by Epelbaum [30, 31] in a single-particle momentum basis. It is usually divided into eight different classes that correspond to specific combinations of coupling constants. Within these classes there are several operator structures. For applying the PWD, we require an interaction that can be factorized into an isospin and a spatial part, therefore, we have to handle every structure separately when transforming them to the Jacobi basis. The different classes are [31]

$$V_I := -\frac{2g_A^6}{(2F_\pi)^6} \frac{\boldsymbol{\sigma}_1 \cdot \mathbf{q}_1 \boldsymbol{\sigma}_4 \cdot \mathbf{q}_4}{[q_1^2 + M_\pi^2][q_{12}^2 + M_\pi^2]^2[q_4^2 + M_\pi^2]} \left[ (\boldsymbol{\tau}_1 \cdot \boldsymbol{\tau}_4 \boldsymbol{\tau}_2 \cdot \boldsymbol{\tau}_3 - \boldsymbol{\tau}_1 \cdot \boldsymbol{\tau}_3 \boldsymbol{\tau}_2 \cdot \boldsymbol{\tau}_4) \mathbf{q}_1 \cdot \mathbf{q}_{12} \mathbf{q}_4 \cdot \mathbf{q}_{12} \right] \quad (\text{Ia})$$

$$+ (\boldsymbol{\tau}_1 \times \boldsymbol{\tau}_2) \cdot \boldsymbol{\tau}_4 \mathbf{q}_1 \cdot \mathbf{q}_{12} (\mathbf{q}_{12} \times \mathbf{q}_4) \cdot \boldsymbol{\sigma}_3 \quad (\text{Ib})$$

$$+ (\boldsymbol{\tau}_1 \times \boldsymbol{\tau}_3) \cdot \boldsymbol{\tau}_4 \mathbf{q}_4 \cdot \mathbf{q}_{12} (\mathbf{q}_1 \times \mathbf{q}_{12}) \cdot \boldsymbol{\sigma}_2 \quad (\text{Ic})$$

$$+ \boldsymbol{\tau}_1 \cdot \boldsymbol{\tau}_4 (\mathbf{q}_{12} \times \mathbf{q}_1) \cdot \boldsymbol{\sigma}_2 (\mathbf{q}_{12} \times \mathbf{q}_4) \cdot \boldsymbol{\sigma}_3 \quad (\text{Id})$$

+ all permutations,

$$V_{II} := \frac{2g_A^4}{(2F_\pi)^6} \frac{\boldsymbol{\sigma}_1 \cdot \mathbf{q}_1 \boldsymbol{\sigma}_4 \cdot \mathbf{q}_4}{[q_1^2 + M_\pi^2][q_{12}^2 + M_\pi^2][q_4^2 + M_\pi^2]} \left[ (\boldsymbol{\tau}_1 \cdot \boldsymbol{\tau}_4 \boldsymbol{\tau}_2 \cdot \boldsymbol{\tau}_3 - \boldsymbol{\tau}_1 \cdot \boldsymbol{\tau}_3 \boldsymbol{\tau}_2 \cdot \boldsymbol{\tau}_4) \mathbf{q}_{12} \cdot \mathbf{q}_4 \right] \quad (\text{IIa})$$

$$+ (\boldsymbol{\tau}_1 \times \boldsymbol{\tau}_2) \cdot \boldsymbol{\tau}_4 (\mathbf{q}_{12} \times \mathbf{q}_4) \cdot \boldsymbol{\sigma}_3 \quad (\text{IIb})$$

$$- \frac{g_A^4}{(2F_\pi)^6} \frac{\boldsymbol{\sigma}_2 \cdot \mathbf{q}_2 \boldsymbol{\sigma}_3 \cdot \mathbf{q}_3 \boldsymbol{\sigma}_4 \cdot \mathbf{q}_4}{[q_2^2 + M_\pi^2][q_3^2 + M_\pi^2][q_4^2 + M_\pi^2]} [\boldsymbol{\tau}_1 \cdot \boldsymbol{\tau}_2 \boldsymbol{\tau}_3 \cdot \boldsymbol{\tau}_4 \boldsymbol{\sigma}_1 \cdot \mathbf{q}_{12}] \quad (\text{IIc})$$

$$- \frac{g_A^4}{2(2F_\pi)^6} \frac{\boldsymbol{\sigma}_1 \cdot \mathbf{q}_1 \boldsymbol{\sigma}_2 \cdot \mathbf{q}_2 \boldsymbol{\sigma}_3 \cdot \mathbf{q}_3 \boldsymbol{\sigma}_4 \cdot \mathbf{q}_4 [q_{12}^2 + M_\pi^2]}{[q_1^2 + M_\pi^2][q_2^2 + M_\pi^2][q_3^2 + M_\pi^2][q_4^2 + M_\pi^2]} [\boldsymbol{\tau}_1 \cdot \boldsymbol{\tau}_2 \boldsymbol{\tau}_3 \cdot \boldsymbol{\tau}_4] \quad (\text{IId})$$

+ all permutations,

$$V_{IV} := C_T \frac{4g_A^4}{(2F_\pi)^4} \frac{\boldsymbol{\sigma}_1 \cdot \mathbf{q}_1 (\boldsymbol{\sigma}_3 \times \boldsymbol{\sigma}_4) \cdot \mathbf{q}_{12}}{[q_1^2 + M_\pi^2][q_{12}^2 + M_\pi^2]^2} \left[ \boldsymbol{\tau}_1 \cdot \boldsymbol{\tau}_3 (\mathbf{q}_1 \times \mathbf{q}_{12}) \cdot \boldsymbol{\sigma}_2 \right] \quad (\text{IVa})$$

$$- (\boldsymbol{\tau}_1 \times \boldsymbol{\tau}_2) \cdot \boldsymbol{\tau}_3 \mathbf{q}_1 \cdot \mathbf{q}_{12} \quad (\text{IVb})$$

+ all permutations,

$$V_V := C_T \frac{2g_A^2}{(2F_\pi)^4} \frac{\boldsymbol{\sigma}_1 \cdot \mathbf{q}_1 (\boldsymbol{\sigma}_3 \times \boldsymbol{\sigma}_4) \cdot \mathbf{q}_{12}}{[q_1^2 + M_\pi^2][q_{12}^2 + M_\pi^2]} [(\boldsymbol{\tau}_1 \times \boldsymbol{\tau}_2) \cdot \boldsymbol{\tau}_3] \quad (\text{V})$$

+ all permutations,

$$V_{VII} := C_T^2 \frac{2g_A^2}{(2F_\pi)^2} \frac{(\boldsymbol{\sigma}_1 \times \boldsymbol{\sigma}_2) \cdot \mathbf{q}_{12} (\boldsymbol{\sigma}_3 \times \boldsymbol{\sigma}_4) \cdot \mathbf{q}_{12}}{[q_{12}^2 + M_\pi^2]^2} \boldsymbol{\tau}_2 \cdot \boldsymbol{\tau}_3 \quad (\text{VII})$$

+ all permutations.



that all expressions are diagonal in isospin. Keep in mind that we omit arrows on lines with integer quantum numbers. Every isospin structure is now expressed in diagrams, inserted in eq. (4.8) and simplified by cutting the diagram.

The easiest structure we have is a simple scalar product, as used in structure (IVa),

$$\begin{aligned}
& \left\langle \frac{1}{2} m'_{t_1}, \frac{1}{2} m'_{t_2}, \frac{1}{2} m'_{t_3}, \frac{1}{2} m'_{t_4} \left| \tau_1 \cdot \tau_3 \right| \frac{1}{2} m_{t_1}, \frac{1}{2} m_{t_2}, \frac{1}{2} m_{t_3}, \frac{1}{2} m_{t_4} \right\rangle \\
&= -\delta_{m_{t_2}, m'_{t_2}} \delta_{m_{t_4}, m'_{t_4}} \sum_{\mu} (-1)^{1-\mu} \left\langle \frac{1}{2} m'_{t_1} \left| \tau_{1,\mu} \right| \frac{1}{2} m_{t_1} \right\rangle \left\langle \frac{1}{2} m'_{t_3} \left| \tau_{3,-\mu} \right| \frac{1}{2} m_{t_3} \right\rangle \\
&= -6 \delta_{m_{t_2}, m'_{t_2}} \delta_{m_{t_4}, m'_{t_4}} \sum_{\mu} (-1)^{-\mu - m'_{t_1} - m'_{t_3}} \begin{pmatrix} \frac{1}{2} & 1 & \frac{1}{2} \\ -m'_{t_1} & \mu & m_{t_1} \end{pmatrix} \begin{pmatrix} \frac{1}{2} & 1 & \frac{1}{2} \\ -m'_{t_3} & -\mu & m_{t_3} \end{pmatrix} \\
&= -6 \delta_{m_{t_2}, m'_{t_2}} \delta_{m_{t_4}, m'_{t_4}} \begin{array}{c} \begin{array}{ccc} \swarrow & \frac{1}{2}, m'_{t_1} & \frac{1}{2}, m'_{t_3} \\ \downarrow & & \downarrow \\ \oplus & 1 & \oplus \\ \uparrow & & \uparrow \\ \searrow & \frac{1}{2}, m_{t_1} & \frac{1}{2}, m_{t_3} \end{array} \end{array},
\end{aligned}$$

where we used the scalar product for spherical tensors, as shown in eq. (3.16), and applied the Wigner-Eckart theorem (3.15) to obtain a representation in terms of 3j-symbols. Inserting this expression in eq. (4.8) is a simple matter of connecting the outgoing and incoming lines correctly, which yields

$$\begin{aligned}
& \left\langle \left[ \left( T_1 \frac{1}{2} \right) T_{12} \frac{1}{2} \right] T_{123} \mathcal{M}'_{T_{123}} \left| \tau_1 \cdot \tau_3 \right| \left[ \left( T_1 \frac{1}{2} \right) T_{12} \frac{1}{2} \right] T_{123} \mathcal{M}_{T_{123}} \right\rangle \\
&= \begin{array}{c} \begin{array}{c} \begin{array}{ccc} \begin{array}{c} \text{---} \oplus \text{---} \\ \downarrow \frac{1}{2} \\ \oplus \\ \uparrow \frac{1}{2} \\ \text{---} \oplus \text{---} \end{array} & \begin{array}{c} \begin{array}{c} \text{---} \oplus \text{---} \\ \downarrow \frac{1}{2} \\ \oplus \\ \uparrow \frac{1}{2} \\ \text{---} \oplus \text{---} \end{array} \\ \times \delta_{T_{123}, T'_{123}} \delta_{\mathcal{M}_{T_{123}}, \mathcal{M}'_{T_{123}}} \\ \times 6 \hat{T}_1 \hat{T}'_1 \hat{T}_{12} \hat{T}'_{12} \end{array} \\ \oplus \\ \begin{array}{c} \begin{array}{ccc} \begin{array}{c} \text{---} \oplus \text{---} \\ \downarrow \frac{1}{2} \\ \oplus \\ \uparrow \frac{1}{2} \\ \text{---} \oplus \text{---} \end{array} & \begin{array}{c} \begin{array}{c} \text{---} \oplus \text{---} \\ \downarrow \frac{1}{2} \\ \oplus \\ \uparrow \frac{1}{2} \\ \text{---} \oplus \text{---} \end{array} \\ \times \delta_{T_{12}, T'_{12}} \delta_{T_{123}, T'_{123}} \delta_{\mathcal{M}_{T_{123}}, \mathcal{M}'_{T_{123}}} \\ \times 6 \hat{T}_1 \hat{T}'_1 \end{array} \end{array} \\ = 6(-1)^{\frac{1}{2} + T_{12}} \hat{T}_1 \hat{T}'_1 \delta_{T_{12}, T'_{12}} \delta_{T_{123}, T'_{123}} \delta_{\mathcal{M}_{T_{123}}, \mathcal{M}'_{T_{123}}} \left\{ T_{12}, \frac{1}{2}, T_{123} \right\} \left\{ \begin{array}{ccc} T_1 & T'_1 & 1 \\ \frac{1}{2} & \frac{1}{2} & T_{12} \end{array} \right\} \left\{ \begin{array}{ccc} T_1 & T'_1 & 1 \\ \frac{1}{2} & \frac{1}{2} & \frac{1}{2} \end{array} \right\},
\end{array}$$

where the red lines indicate cuts, turquoise lines are new lines obtained from cutting two lines using eq. (3.28), and turquoise colored 3j-symbols have been inserted by cutting three lines using eq. (3.27). Note that line and sign inversions are necessary to obtain the standard representation of the 6j-symbols, yielding the additional factor of  $(-1)^{\frac{1}{2} + T_{12}}$ .

We can use the previous result to obtain an expression for  $\tau_2 \cdot \tau_3$ , which is relevant for structure (VII). The latter can be constructed from the former by exchanging the first two particles in isospin space. Exchanging the first two particles in the coupled state corresponds to a simple change in the coupling order, resulting in

a factor of  $(-1)^{1+T_1}$ . Rewriting  $\tau_2 \cdot \tau_3$  by using particle exchange operators  $P_{1,2}^{(T)}$ , acting only in isospin space, we obtain

$$\begin{aligned} & \left\langle \left[ \left( T_{1\frac{1}{2}} \right) T_{12\frac{1}{2}} \right] T'_{123} \mathcal{M}'_{T_{123}} \left| \tau_2 \cdot \tau_3 \right| \left[ \left( T_{1\frac{1}{2}} \right) T_{12\frac{1}{2}} \right] T_{123} \mathcal{M}_{T_{123}} \right\rangle \\ &= \left\langle \left[ \left( T_{1\frac{1}{2}} \right) T_{12\frac{1}{2}} \right] T'_{123} \mathcal{M}'_{T_{123}} \left| P_{1,2}^{(T)} \tau_1 \cdot \tau_3 P_{1,2}^{(T)} \right| \left[ \left( T_{1\frac{1}{2}} \right) T_{12\frac{1}{2}} \right] T_{123} \mathcal{M}_{T_{123}} \right\rangle \\ &= (-1)^{T_1+T'_1} \left\langle \left[ \left( T_{1\frac{1}{2}} \right) T_{12\frac{1}{2}} \right] T'_{123} \mathcal{M}'_{T_{123}} \left| \tau_1 \cdot \tau_3 \right| \left[ \left( T_{1\frac{1}{2}} \right) T_{12\frac{1}{2}} \right] T_{123} \mathcal{M}_{T_{123}} \right\rangle. \end{aligned}$$

The isospin expressions for structure (Id), the last one that only has a single scalar product, is straightforward to calculate,

$$\begin{aligned} & \left\langle \left[ \left( T_{1\frac{1}{2}} \right) T_{12\frac{1}{2}} \right] T'_{123} \mathcal{M}'_{T_{123}} \left| \tau_1 \cdot \tau_4 \right| \left[ \left( T_{1\frac{1}{2}} \right) T_{12\frac{1}{2}} \right] T_{123} \mathcal{M}_{T_{123}} \right\rangle \\ &= \begin{array}{c} \begin{array}{c} T_{123} \\ \begin{array}{c} \frac{1}{2} \quad \frac{1}{2} \\ \hline \frac{1}{2} \quad \frac{1}{2} \end{array} \\ \begin{array}{c} - \quad \rightarrow \quad \rightarrow \quad \rightarrow \quad + \\ \begin{array}{c} T'_{12} \quad \frac{1}{2} \quad \frac{1}{2} \quad T_{12} \\ \hline - \quad \rightarrow \quad \rightarrow \quad \rightarrow \quad + \\ T'_1 \quad \frac{1}{2} \quad 1 \quad T_1 \\ \hline \frac{1}{2} \quad \frac{1}{2} \end{array} \end{array} \end{array} \times \delta_{T_{123}, T'_{123}} \delta_{\mathcal{M}_{T_{123}}, \mathcal{M}'_{T_{123}}} \\ \times 6 \hat{T}_1 \hat{T}'_1 \hat{T}_{12} \hat{T}'_{12} \\ \begin{array}{c} \begin{array}{c} T'_{12} \quad T_{12} \\ \begin{array}{c} \frac{1}{2} \quad \frac{1}{2} \\ \hline \frac{1}{2} \quad \frac{1}{2} \end{array} \\ \begin{array}{c} + \quad \rightarrow \quad \rightarrow \quad \rightarrow \quad + \\ \begin{array}{c} T'_{12} \quad 1 \quad T_{12} \\ \hline T'_1 \quad T_1 \\ \hline \frac{1}{2} \quad \frac{1}{2} \end{array} \end{array} \end{array} \end{array} \times \delta_{T_{123}, T'_{123}} \delta_{\mathcal{M}_{T_{123}}, \mathcal{M}'_{T_{123}}} \\ \times 6(-1)^{2T_{12}} \hat{T}_1 \hat{T}'_1 \hat{T}_{12} \hat{T}'_{12} \\ \end{array} \\ &= 6(-1)^{1+T_1+T'_1+T_{123}} \hat{T}_1 \hat{T}'_1 \hat{T}_{12} \hat{T}'_{12} \delta_{T_{123}, T'_{123}} \delta_{\mathcal{M}_{T_{123}}, \mathcal{M}'_{T_{123}}} \begin{Bmatrix} \frac{1}{2} & \frac{1}{2} & 1 \\ T_{12} & T_{12} & T_{123} \end{Bmatrix} \begin{Bmatrix} T_1 & T'_1 & 1 \\ T'_{12} & T_{12} & \frac{1}{2} \end{Bmatrix} \begin{Bmatrix} T_1 & T'_1 & 1 \\ \frac{1}{2} & \frac{1}{2} & \frac{1}{2} \end{Bmatrix}. \end{aligned}$$

In this case one has to be careful when cutting the diagram, as the line directions do not fit to eq. (3.27), which introduces an additional factor. To indicate the necessary factor, the  $T_{12}$ -line has been colored red.

We continue with operators that contain two scalar products. The construction of the diagrams is straightforward, cutting them can be more involved due to additional lines. The following matrix element appears in operator structures (IIc) and (IIId),

$$\begin{aligned} & \left\langle \left[ \left( T_{1\frac{1}{2}} \right) T_{12\frac{1}{2}} \right] T'_{123} \mathcal{M}'_{T_{123}} \left| \tau_1 \cdot \tau_2 \tau_3 \cdot \tau_4 \right| \left[ \left( T_{1\frac{1}{2}} \right) T_{12\frac{1}{2}} \right] T_{123} \mathcal{M}_{T_{123}} \right\rangle \\ &= \begin{array}{c} \begin{array}{c} T_{123} \\ \begin{array}{c} \frac{1}{2} \quad \frac{1}{2} \\ \hline \frac{1}{2} \quad \frac{1}{2} \end{array} \\ \begin{array}{c} - \quad \rightarrow \quad \rightarrow \quad \rightarrow \quad + \\ \begin{array}{c} T'_{12} \quad \frac{1}{2} \quad 1 \quad \frac{1}{2} \quad T_{12} \\ \hline - \quad \rightarrow \quad \rightarrow \quad \rightarrow \quad + \\ T'_1 \quad \frac{1}{2} \quad \frac{1}{2} \quad T_1 \\ \hline \frac{1}{2} \quad \frac{1}{2} \end{array} \end{array} \end{array} \times \delta_{T_{123}, T'_{123}} \delta_{\mathcal{M}_{T_{123}}, \mathcal{M}'_{T_{123}}} \\ \times (-36) \hat{T}_1 \hat{T}'_1 \hat{T}_{12} \hat{T}'_{12} \\ \end{array}$$

$$\begin{aligned}
&= \begin{array}{c} \begin{array}{c} + \\ \uparrow \\ T'_{12} \quad 1 \quad T_{12} \\ \downarrow \\ T_{123} \end{array} \quad \begin{array}{c} + \\ \uparrow \\ T'_{12} \quad 1 \quad T_{12} \\ \downarrow \\ T_1 \end{array} \quad \begin{array}{c} + \\ \uparrow \\ \frac{1}{2} \quad 1 \quad \frac{1}{2} \\ \downarrow \\ T_1 \end{array} \\ + \quad - \quad + \end{array} \times \delta_{T_1, T_1'} \delta_{T_{123}, T_{123}'} \delta_{M_{T_{123}}, M_{T_{123}}'} \\
&= 36(-1)^{1+T_{12}+T_{12}'+T_{123}} \hat{T}_{12} \hat{T}'_{12} \delta_{T_1, T_1'} \delta_{T_{123}, T_{123}'} \delta_{M_{T_{123}}, M_{T_{123}}'} \left\{ \begin{array}{c} \frac{1}{2} \quad \frac{1}{2} \quad 1 \\ T_{12} \quad T'_{12} \quad T_{123} \end{array} \right\} \left\{ \begin{array}{c} \frac{1}{2} \quad \frac{1}{2} \quad 1 \\ T_{12} \quad T'_{12} \quad T_1 \end{array} \right\} \left\{ \begin{array}{c} \frac{1}{2} \quad \frac{1}{2} \quad 1 \\ \frac{1}{2} \quad \frac{1}{2} \quad T_1 \end{array} \right\}.
\end{aligned}$$

Furthermore, the structures (Ia) and (IIa) require the following matrix element,

$$\begin{aligned}
&\left\langle \left[ \left( T_1' \frac{1}{2} \right) T_{12}' \frac{1}{2} \right] T_{123}' M_{T_{123}}' \left| \tau_1 \cdot \tau_4 \quad \tau_2 \cdot \tau_3 \right| \left[ \left( T_1 \frac{1}{2} \right) T_{12} \frac{1}{2} \right] T_{123} M_{T_{123}} \right\rangle \\
&= \begin{array}{c} \begin{array}{c} T_{123} \\ \frac{1}{2} \quad \frac{1}{2} \\ \downarrow \\ - \quad + \\ \uparrow \\ T'_{12} \quad 1 \quad T_{12} \\ \downarrow \\ - \quad + \\ \uparrow \\ T_1 \quad 1 \quad T_1 \\ \downarrow \\ - \quad + \\ \frac{1}{2} \quad \frac{1}{2} \end{array} \\ + \quad - \end{array} \times \delta_{T_{123}, T_{123}'} \delta_{M_{T_{123}}, M_{T_{123}}'} \\
&\quad \times (-36) \hat{T}_1 \hat{T}'_1 \hat{T}_{12} \hat{T}'_{12} \\
&= \begin{array}{c} \begin{array}{c} + \\ \uparrow \\ T'_{12} \quad 1 \quad T_{12} \\ \downarrow \\ T_{123} \end{array} \quad \begin{array}{c} \frac{1}{2} \quad \frac{1}{2} \\ \downarrow \\ + \quad + \\ \uparrow \\ T_1 \quad 1 \quad T_1 \\ \downarrow \\ \frac{1}{2} \quad \frac{1}{2} \end{array} \quad \begin{array}{c} \frac{1}{2} \quad \frac{1}{2} \\ \downarrow \\ - \quad - \\ \uparrow \\ T_{12} \quad 1 \quad T_{12} \\ \downarrow \\ \frac{1}{2} \quad \frac{1}{2} \end{array} \\ + \quad + \quad - \end{array} \times \delta_{T_{123}, T_{123}'} \delta_{M_{T_{123}}, M_{T_{123}}'} \\
&\quad \times 36(-1)^{2T_{12}+2T_{12}'} \hat{T}_1 \hat{T}'_1 \hat{T}_{12} \hat{T}'_{12} \\
&= \begin{array}{c} \begin{array}{c} + \\ \uparrow \\ T'_{12} \quad 1 \quad T_{12} \\ \downarrow \\ T_{123} \end{array} \quad \begin{array}{c} \frac{1}{2} \quad \frac{1}{2} \\ \downarrow \\ + \quad + \\ \uparrow \\ T_1 \quad 1 \quad T_1 \\ \downarrow \\ \frac{1}{2} \quad \frac{1}{2} \end{array} \quad \begin{array}{c} \frac{1}{2} \quad \frac{1}{2} \\ \downarrow \\ - \quad - \\ \uparrow \\ T_{12} \quad 1 \quad T_{12} \\ \downarrow \\ \frac{1}{2} \quad \frac{1}{2} \end{array} \\ + \quad + \quad - \quad + \quad - \end{array} \\
&\quad \times 36(-1)^{2T_{12}+2T_{12}'} \hat{T}_1 \hat{T}'_1 \hat{T}_{12} \hat{T}'_{12} \delta_{T_{123}, T_{123}'} \delta_{M_{T_{123}}, M_{T_{123}}'} \\
&= \sum_K \left\{ \begin{array}{c} \frac{1}{2} \quad \frac{1}{2} \quad 1 \\ T_{12} \quad T'_{12} \quad T_{123} \end{array} \right\} \left\{ \begin{array}{c} \frac{1}{2} \quad \frac{1}{2} \quad 1 \\ \frac{1}{2} \quad \frac{1}{2} \quad K \end{array} \right\} \left\{ \begin{array}{c} \frac{1}{2} \quad \frac{1}{2} \quad T_1 \\ \frac{1}{2} \quad T_{12} \quad K \end{array} \right\} \left\{ \begin{array}{c} \frac{1}{2} \quad \frac{1}{2} \quad 1 \\ T_{12} \quad T'_{12} \quad K \end{array} \right\} \left\{ \begin{array}{c} \frac{1}{2} \quad \frac{1}{2} \quad T_1 \\ \frac{1}{2} \quad T_{12} \quad K \end{array} \right\} \\
&\quad 36(-1)^{1+T_{12}+T_{12}'+T_{123}} K^2 \hat{T}_1 \hat{T}'_1 \hat{T}_{12} \hat{T}'_{12} \delta_{T_{123}, T_{123}'} \delta_{M_{T_{123}}, M_{T_{123}}'},
\end{aligned}$$

which is the first isospin expression that requires the use of eq. (3.30) to cut four lines, inserting an additional sum in the process. In such a case, the newly created thick line, as well as the additional 3j-symbols are colored turquoise. For the above derivation, there are multiple possible ways to cut four lines and inserting the necessary additional sum. Choosing to insert it between two  $t = \frac{1}{2}$  lines ensures that  $K$  can only be 0 or 1, reducing the number of summands. We can again exchange the first two particles to obtain the last









Note that we obtained a few additional factors, as we inverted some coordinate lines to make use of eqs. (3.II) and (3.26). We now cut the diagram, yielding

$$\begin{aligned}
 &= \text{Diagram} \times \frac{1}{2} \hat{L}_i \hat{L}'_i (-1)^{Y_i+V'_i+X_i+V_i+Z_i} D_{Y_i, Y'_i}^{L'_i} D_{V_i, V'_i}^{L_i} \\
 &\times \iint d\Sigma_i d u_i P_{X_i}(u_i) Q_{N_i, L_i, V_i, V'_i}^{N'_i, L'_i, Y_i, Y'_i}(\mathcal{A}_i, \Sigma_i, u_i). \quad (4.9) \\
 &\underbrace{\hspace{15em}}_{=:\tilde{R}_{N_i, L_i, N'_i, L'_i}^{\mathcal{A}_i}(\mathcal{A}_i)}
 \end{aligned}$$

When inverting all signs of a 9j-symbol, the expression does not change. Applying the inversion to the equation above, we can show that  $L_i + L'_i + \Delta L_i$  must be even. Expressing the 9j-symbol in a traditional form and using the Kronecker deltas, we obtain

$$\begin{aligned}
 \tilde{R}_{N_i, L_i, N'_i, L'_i}^{\mathcal{A}_i} &= \iint d\Sigma_i d u_i \sum_{V_i=0}^{L_i} \sum_{Y_i=0}^{L'_i} \sum_{X_i} \sum_{Z_i} \widehat{V_i^2 L_i - V_i^2 Y_i^2 L'_i - Y_i^2 X_i^2 Z_i^2 L_i L'_i} \frac{1}{2} (-1)^{L'_i+X_i+V_i+Z_i} D_{Y_i, L'_i-Y_i}^{L'_i} D_{V_i, L_i-V_i}^{L_i} \\
 &\times P_{X_i}(u_i) Q_{N_i, L_i, V_i, L_i-V_i}^{N'_i, L'_i, Y_i, L'_i-Y_i}(\mathcal{A}_i, \Sigma_i, u_i) \begin{Bmatrix} Y_i & L'_i - Y_i & L'_i \\ V_i & L_i - V_i & L_i \\ Z_i & X_i & \Delta L_i \end{Bmatrix} \\
 &\begin{pmatrix} V_i & Y_i & Z_i \\ 0 & 0 & 0 \end{pmatrix} \begin{pmatrix} X_i & Z_i & \Delta L_i \\ 0 & 0 & 0 \end{pmatrix} \begin{pmatrix} L'_i - Y_i & L_i - V_i & X_i \\ 0 & 0 & 0 \end{pmatrix}, \quad (4.10)
 \end{aligned}$$

which we call the basis part, as it includes all information from the HO basis. Although this expression might look more complicated than the original integral, it is completely separated from the rest of the interaction, if the regulator does not depend on  $\Sigma_i$ .

We can now insert eq. (4.9) in eq. (4.6) and express it diagrammatically. We also cut the two external lines,  $J_{123}$  and  $J'_{123}$ , yielding a Kronecker delta. Furthermore, we add a regulator  $F$  that depends on momentum transfer. This results in a spatial part of

$$\begin{aligned}
 &\left\langle N'_{\text{cm}} L'_{\text{cm}} M'_{L_{\text{cm}}}, E'_{123} J'_{123} M'_{J_{123}} \beta'_{123} \middle| V_X^{(S)} \middle| N_{\text{cm}} L_{\text{cm}} M_{L_{\text{cm}}}, E_{123} J_{123} M_{J_{123}} \beta_{123} \right\rangle \\
 &= \delta_{N_{\text{cm}}, N'_{\text{cm}}} \delta_{L_{\text{cm}}, L'_{\text{cm}}} \delta_{M_{L_{\text{cm}}}, M'_{L_{\text{cm}}}} \delta_{J_{123}, J'_{123}} \delta_{M_{J_{123}}, M'_{J_{123}}} \iiint d\mathcal{A}_1 d\mathcal{A}_2 d\mathcal{A}_3 \mathcal{A}_1^2 \mathcal{A}_2^2 \mathcal{A}_3^2 \\
 &\text{Diagram} \times (-1)^{4+2S'_1+2J'_2+2J'_3+2L_1+2L_2+2L_3+2J_1+2J_{12}} \\
 &\times \frac{24(4\pi)^3}{8(2\pi)^9} \hat{S}'_1 \hat{S}'_1 \hat{J}'_1 \hat{J}'_1 \hat{J}'_2 \hat{J}'_2 \hat{J}'_3 \hat{J}'_3 \hat{J}'_{12} \hat{J}'_{12} \\
 &\times F(\mathcal{A}_1, \mathcal{A}_2, \mathcal{A}_3, \mathcal{A}) \\
 &\times \tilde{R}_{N_1, L_1, N'_1, L'_1}^{\mathcal{A}_1}(\mathcal{A}_1) \tilde{R}_{N_2, L_2, N'_2, L'_2}^{\mathcal{A}_2}(\mathcal{A}_2) \\
 &\times \tilde{R}_{N_3, L_3, N'_3, L'_3}^{\mathcal{A}_3}(\mathcal{A}_3), \quad (4.II)
 \end{aligned}$$



where we used eq. (3.15), the Wigner-Eckart theorem, to represent the the spin part in terms of a reduced matrix element, which is a simple factor, and a 3j-symbol. The momentum parts were simply expressed in a spherical basis, which results in an absolute value and a spherical harmonic. Furthermore, the scalar products result in a connecting line, both is shown in eq. (3.16). We continue by combining coordinate lines using eq. (3.26). This requires some lines to be inverted, but all phase factors cancel in this case, yielding

$$= \times \delta_{m_b, m'_b} \delta_{m_c, m'_c} \frac{-12g_A^6}{(2F_\pi)^6} \frac{q_1^2}{q_1^2 + M_\pi^2} \frac{q_4^2}{q_4^2 + M_\pi^2} \frac{q_{12}^2}{[q_{12}^2 + M_\pi^2]^2}.$$

We now express  $q_1$  by  $\Delta_1$  and  $q_{12}$ , replacing the angular part as well as the absolute value  $q_1$ . This transformation uses eqs. (3.31) and (3.32), in that order. The latter equation introduces an additional integral that can be interpreted as an integration over the angle  $\hat{\Delta}_1 \cdot \hat{q}_{12}$ . Afterwards we have multiple  $\Delta_1$  and  $q_{12}$  coordinate lines that we have to combine using eq. (3.26) again.

$$\times \delta_{m_b, m'_b} \delta_{m_c, m'_c} \int du_4 P_{X_4}(u_4) D_{K_1, K'_1}^{k_1} \sqrt{2^{-2K_1 - K'_1}} \frac{-6g_A^6}{(2F_\pi)^6}$$

$$\times \frac{q_1(\Delta_1, q_{12}, u_4)^{2-k_1}}{q_1(\Delta_1, q_{12}, u_4)^2 + M_\pi^2} \frac{q_4^2}{q_4^2 + M_\pi^2} \frac{q_{12}^{2+K_1}}{[q_{12}^2 + M_\pi^2]^2} \Delta_1^{K'_1}$$

$$\times \delta_{m_b, m'_b} \delta_{m_c, m'_c} \int du_4 P_{X_4}(u_4) D_{K_1, K'_1}^{k_1}$$

$$\times \sqrt{2^{-2K_1 - K'_1}} (-1)^{1+X_4+k_{12}} \frac{6g_A^6}{(2F_\pi)^6}$$

$$\times \frac{q_1(\Delta_1, q_{12}, u_4)^{2-k_1}}{q_1(\Delta_1, q_{12}, u_4)^2 + M_\pi^2} \frac{q_4^2}{q_4^2 + M_\pi^2} \frac{q_{12}^{2+K_1}}{[q_{12}^2 + M_\pi^2]^2} \Delta_1^{K'_1}.$$

Note that combining the coordinate lines requires line inversions that result in additional phase factors. We now express  $q_{12}$  and  $q_4$  in Jacobi momenta and separate a 6j-symbol from the diagram, as already indicated by the red line in the diagram above,

$$\begin{aligned}
& \times \delta_{m_b, m'_b} \delta_{m_c, m'_c} \int du_4 P_{X_4}(u_4) \int du_5 P_{X_5}(u_5) D_{K_1, K'_1}^{k_1} D_{K_{12}, K'_{12}}^{k'_{12}} \\
& \times \sqrt{2^{K_{12}-2K_1-K'_1}} \sqrt{3^{-K_{12}-K'_{12}}} (-1)^{1+X_4+k_{12}+k_4} \\
& \times \frac{3g_A^6}{(2F_\pi)^6} \frac{q_1(\mathcal{A}_1, q_{12}(\mathcal{A}_2, \mathcal{A}_3, u_5), u_4)^{2-k_1}}{q_1(\mathcal{A}_1, q_{12}(\mathcal{A}_2, \mathcal{A}_3, u_5), u_4)^2 + M_\pi^2} \\
& \times \frac{\frac{3}{4}\mathcal{A}_3^{2+K'_{12}}}{\frac{3}{4}\mathcal{A}_3^2 + M_\pi^2} \frac{q_{12}(\mathcal{A}_2, \mathcal{A}_3, u_5)^{2+K_1-k''_{12}}}{[q_{12}(\mathcal{A}_2, \mathcal{A}_3, u_5)^2 + M_\pi^2]^2} \mathcal{A}_1^{K'_1} \mathcal{A}_2^{K_{12}}.
\end{aligned}$$

At this point all single-particle momenta are replaced. We just have to simplify the expression, starting by combining coordinate lines again and separating an additional 6j-symbol, resulting in

$$\begin{aligned}
& \times \delta_{m_b, m'_b} \delta_{m_c, m'_c} \int du_4 P_{X_4}(u_4) \int du_5 P_{X_5}(u_5) D_{K_1, K'_1}^{k_1} D_{K_{12}, K'_{12}}^{k'_{12}} \\
& \times \sqrt{2^{K_{12}-2K_1-K'_1}} \sqrt{3^{-K_{12}-K'_{12}}} (-1)^{1+X_4+X_5+k_{12}+k_4+k'_4} \\
& \times \frac{3g_A^6}{(2F_\pi)^6} \frac{q_1(\mathcal{A}_1, q_{12}(\mathcal{A}_2, \mathcal{A}_3, u_5), u_4)^{2-k_1}}{q_1(\mathcal{A}_1, q_{12}(\mathcal{A}_2, \mathcal{A}_3, u_5), u_4)^2 + M_\pi^2} \\
& \times \frac{\frac{3}{4}\mathcal{A}_3^{2+K'_{12}}}{\frac{3}{4}\mathcal{A}_3^2 + M_\pi^2} \frac{q_{12}(\mathcal{A}_2, \mathcal{A}_3, u_5)^{2+K_1-k''_{12}}}{[q_{12}(\mathcal{A}_2, \mathcal{A}_3, u_5)^2 + M_\pi^2]^2} \mathcal{A}_1^{K'_1} \mathcal{A}_2^{K_{12}} \\
& \times \delta_{m_b, m'_b} \delta_{m_c, m'_c} \int du_4 P_{X_4}(u_4) \int du_5 P_{X_5}(u_5) \\
& \times D_{K_1, K'_1}^{k_1} D_{K_{12}, K'_{12}}^{k'_{12}} \sqrt{2^{K_{12}-2K_1-K'_1}} \sqrt{3^{-K_{12}-K'_{12}}} \\
& \times (-1)^{1+X_4+X_5+k_{12}+k_4+k'_4} \frac{3g_A^6}{(2F_\pi)^6} \mathcal{A}_1^{K'_1} \mathcal{A}_2^{K_{12}} \\
& \times \frac{q_1(\mathcal{A}_1, q_{12}(\mathcal{A}_2, \mathcal{A}_3, u_5), u_4)^{2-k_1}}{q_1(\mathcal{A}_1, q_{12}(\mathcal{A}_2, \mathcal{A}_3, u_5), u_4)^2 + M_\pi^2} \\
& \times \frac{\frac{3}{4}\mathcal{A}_3^{2+K'_{12}}}{\frac{3}{4}\mathcal{A}_3^2 + M_\pi^2} \frac{q_{12}(\mathcal{A}_2, \mathcal{A}_3, u_5)^{2+K_1-k''_{12}}}{[q_{12}(\mathcal{A}_2, \mathcal{A}_3, u_5)^2 + M_\pi^2]^2}.
\end{aligned} \tag{4.15}$$

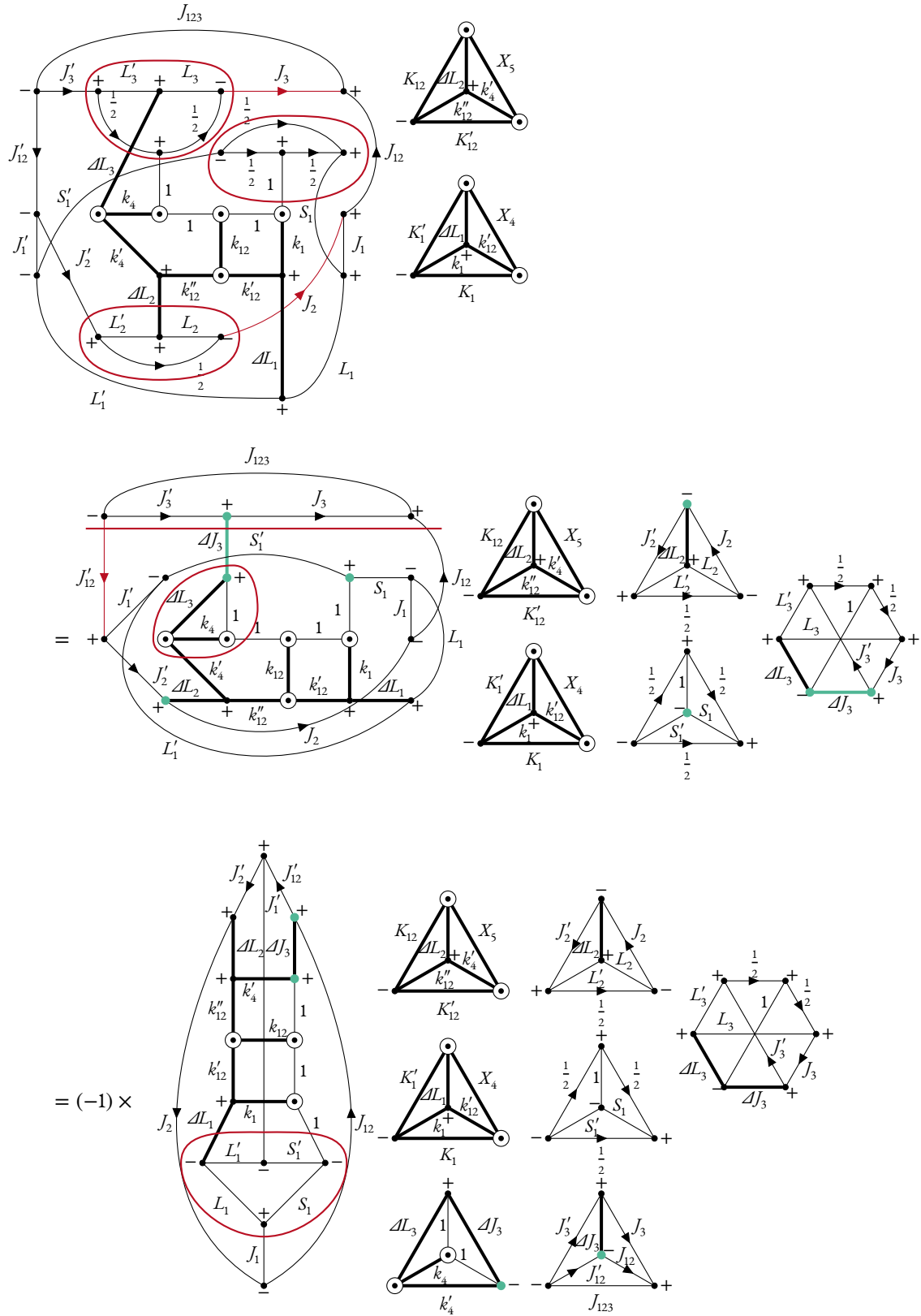
We can now insert the expression in eq. (4.11). To simplify the derivation, we will first completely simplify the diagrammatic part and then add the remaining part of the formula.

As there are only two spherical harmonics for each coordinate line, we can use eq. (3.10) to remove the coordinate lines, which enforces

$$\Delta L'_1 = \Delta L_1, \quad \Delta L'_2 = \Delta L_2 \quad \text{and} \quad \Delta L'_3 = \Delta L_3.$$

We end up with the a combined diagram for class (Ia), which we can simplify by cutting it into 6j-symbols

and 9j-symbols. As we have done for the isospin case in section 4.4.1, we indicate cuts by red lines and all newly added lines and 3j-symbols are colored turquoise. We obtain,



$= (-1) \times$

$= (-1) \times$

We can express the above diagram in a traditional form and add the remaining non-diagrammatic part of eqs. (4.11) and (4.15), yielding

$$\begin{aligned}
& \left\langle N'_{\text{cm}} L'_{\text{cm}} M'_{L_{\text{cm}}}, E'_{123} J'_{123} \mathcal{M}'_{J_{123}}, \beta'_{123} \left| V_{\text{Ia}}^{(S)} \right| N_{\text{cm}} L_{\text{cm}} \mathcal{M}_{L_{\text{cm}}}, E_{123} J_{123} \mathcal{M}_{J_{123}}, \beta_{123} \right\rangle \\
&= \delta_{N'_{\text{cm}}, N_{\text{cm}}} \delta_{L'_{\text{cm}}, L_{\text{cm}}} \delta_{M'_{L_{\text{cm}}}, M_{L_{\text{cm}}}} \delta_{J'_{123}, J_{123}} \delta_{\mathcal{M}'_{J_{123}}, \mathcal{M}_{J_{123}}} \iiint d\mathcal{A}_1 d\mathcal{A}_2 d\mathcal{A}_3 \mathcal{A}_1^2 \mathcal{A}_2^2 \mathcal{A}_3^2 \sum_{\mathcal{A}_1} \sum_{\mathcal{A}_2} \sum_{\mathcal{A}_3} \widehat{\mathcal{A}}_1^2 \widehat{\mathcal{A}}_2^2 \widehat{\mathcal{A}}_3^2 \\
& \frac{(-3)}{8\pi^6} \tilde{R}_{N_1, L_1, N'_1, L'_1}^{\mathcal{A}_1}(\mathcal{A}_1) \tilde{R}_{N_2, L_2, N'_2, L'_2}^{\mathcal{A}_2}(\mathcal{A}_2) \tilde{R}_{N_3, L_3, N'_3, L'_3}^{\mathcal{A}_3}(\mathcal{A}_3) F(\mathcal{A}_1, \mathcal{A}_2, \mathcal{A}_3, \mathcal{A}) \\
& I_{\text{Ia}}^{L'_1, L'_2, L'_3, S'_1, J'_1, J'_2, J'_3, J'_{12}, J'_{123}}(L_1, L_2, L_3, S_1, J_1, J_2, J_3, J_{12}, J_{123}; \mathcal{A}_1, \mathcal{A}_2, \mathcal{A}_3), \tag{4.16}
\end{aligned}$$





for our regulator. The number of grid points is investigated in detail in chapter 7, a typical number is 20 points in each dimension.

2. *Calculating the basis part for all necessary combinations of quantum numbers*

Note that all three basis parts in eq. (4.16) are identical. We only have to calculate it for the first Jacobi coordinate and we can then reuse it for the other two. As it depends on  $\mathcal{A}_1$ , we obtain a one-dimensional grid. We use the same maximum momentum as for the interaction grid but we can calculate much more grid points for the single dimension. Again, a detailed investigation is presented in chapter 7 with a typical number of 250 points.

3. *Combining interaction and basis grids*

In this step we actually calculate eq. (4.16), integrating over  $\mathcal{A}_1$ ,  $\mathcal{A}_2$ , and  $\mathcal{A}_3$  using the predefined grids. As the integration requires momenta that do not correspond to a specific grid point, we interpolate the grids using

$$I_{L_1, L_2, L_3, S_1, J_1, J_2, J_3, J_{123}; \mathcal{A}_1, \mathcal{A}_2, \mathcal{A}_3}^{L'_1, L'_2, L'_3, S'_1, J'_1, J'_2, J'_3, J'_{123}}(\mathcal{A}_1, \mathcal{A}_2, \mathcal{A}_3) = \sum_{i,j,k=0}^X c_{i,j,k} \mathcal{A}_1^i \mathcal{A}_2^j \mathcal{A}_3^k,$$

with  $X = 1$ , which is a linear interpolation, or  $X = 3$ , yielding a cubic interpolation. The 8 ( $X = 1$ ) or 64 ( $X = 3$ ) coefficients  $c_{i,j,k}$  are determined by the 8 or 64 grid points surrounding the required value. The basis parts are interpolated as well, using the same interpolation scheme, just reduced to one dimension.

The integration is performed using the Cubature library [96], which implements two algorithm for a fast multi-dimensional integration. For the creation of the basis grid, the so-called h-adaptive integration is used, which partitions the integration domain into subdomains recursively. The creation of the interaction grid relies on the so-called p-adaptive integration. In this case the degree of the Clenshaw-Curtis quadrature is doubled until convergence. The combination of the grids is a difficult task for both algorithms, frequently yielding innaccurate results. To mitigate the effect, both algorithms are employed and the results are compared. In case of differences, the integration is repeated while enforcing a minimum of 300000 sampling points.

The final matrix elements are calculated using eq. (4.5). This formula also requires the isospin parts that have been derived in section 4.4.1. Furthermore it uses the precalculated CFPs to antisymmetrize the representation, yielding matrix elements in the completely antisymmetric Jacobi HO basis.



# 5

## Many-Body Calculations

After constructing the Hamiltonian in the Jacobi HO basis, our goal is to include the two-, three- and four-body interaction in many-body calculations. However, there are some intermediate steps necessary to achieve this goal, all of which will be discussed within this chapter.

Typically, when using an interaction as constructed from chiral EFT, the so-called bare interaction, we struggle with the model-space convergence of the many-body method. This can be linked to properties of the interaction, for instance, a strong repulsion at short distances. Therefore, the interaction is first "softened" by using the SRG, yielding enhanced convergence in many-body calculations, which is discussed in section 5.1.

The SRG is performed in relative or Jacobi coordinates but the construction of an antisymmetrized many-body basis in these coordinates is difficult, as previously discussed in section 4.1. For this reason, the interaction is transformed to a single-particle basis, which makes it almost trivial to embed it in many-body space. Details of this basis are discussed in section 5.2

Finally, we can use the interaction in a many-body method of choice, in this work we focus on ground-state energies calculated in the NCSM as an exact many-body method in section 5.3 and HF calculations in section 5.4, which allows a simple approximation of ground-state energies in heavier nuclei.

## 5.1 SIMILARITY RENORMALIZATION GROUP

We have already discussed chiral interactions in great detail (chapter 2), and in principle, we would like to perform many-body calculations based directly on these interactions. However, including the bare interaction is very difficult due to its properties. For instance, the NN interactions feature a strong short-range repulsion and tensor forces, properties that the chiral forces share with all realistic NN interactions. Regardless of the nucleus in question, solving the Schrödinger equation with such an interaction must yield a highly correlated state. Using a many-body method that describes correlations by using superpositions of uncorrelated states, such a highly correlated state requires a large model space, that is, the convergence of the many-body calculation with respect to the size of the model space is very slow.

To improve the convergence, one constructs a Hamiltonian that reproduces all low-energy observables of the bare interaction without requiring such large model spaces. It is advantageous to construct such an interaction using a unitary transformation, an idea already implemented for realistic NN interactions in the UCOM [53]. A unitary transformation does not change any of the eigenvalues of the Hamiltonian and the unitary transformation can be applied to all other operators, which allows for the consistent description of observables. In the case of UCOM the unitary operator is constructed explicitly in a way as to reduce the correlation content of the wave function.

The SRG [54, 55] is built upon similar ideas and was, in fact, proposed before UCOM, yet it was not applied to NN interactions until about ten years ago [97]. Its approach, as applied in this work, differs from UCOM as it directly targets a matrix representation of the Hamiltonian. When representing the bare interaction in a basis of uncorrelated states, the correlations result in strong off-diagonal matrix elements that connect low-lying and high-lying basis states. For the transformed interaction these matrix elements should, ideally, vanish. For this reason, the SRG aims at a pre-diagonalization of the interaction, resulting in an interaction that, in a relative two-body coordinate representation, does not exhibit a strong repulsion anymore.

The SRG is in widespread use in nuclear structure theory today, which can be explained by the advantages of this framework [57]. It is conceptually simple and can easily be used for multi-nucleon forces, yet it allows for great flexibility and it can be tailored for specific use cases, for instance, specific many-body methods. The concept is powerful enough to be extended to a many-body method in its own right, the IMSRG [47, 48], which employs the SRG framework to decouple a specific reference state from its excitations in the  $A$ -body system under consideration.

This section only provides a brief overview of the SRG. In-depth information on details of the SRG and its many applications can be found in one of the excellent reviews on this topic [56, 57].

## 5.1.1 CONCEPT

The basic concept of the SRG is the continuous transformation of the Hamiltonian based upon the flow-equation,

$$\frac{d}{d\alpha} H_\alpha = [\eta_\alpha, H_\alpha], \quad (5.1)$$

where  $H_0$  is the initial Hamiltonian,  $\eta_\alpha$  is called the generator of the transformation and  $\alpha$  is the flow-parameter. The generator has to be anti-hermitian, aside from that it can be chosen freely, which allows for great flexibility within the SRG framework. Possible choices for the generator are discussed in the next section. It is a crucial property of the SRG that the flow-equation results in a unitary transformation of the Hamiltonian,

$$H_\alpha = U_\alpha^\dagger H_0 U_\alpha,$$

where the operator  $U_\alpha$  can be related to the generator,

$$\eta_\alpha = -U_\alpha^\dagger \frac{dU_\alpha}{d\alpha} \Leftrightarrow \frac{dU_\alpha}{d\alpha} = -U_\alpha \eta_\alpha. \quad (5.2)$$

The integration of eq. (5.1), which is often called SRG evolution, to a specific value of  $\alpha$  yields a transformed Hamiltonian that has exactly the same eigenvalues as before. Integrating eq. (5.2) allows for the explicit construction of the unitary transformation from the generator. Note that the generator usually depends on the Hamiltonian, therefore, eq. (5.1) has to be integrated simultaneously with eq. (5.2).

In principle, the SRG transformation is unitary and does not change the eigenvalues of the Hamiltonian nor any other observable. However, for a solution of the flow equation we have to represent the Hamiltonian and the generator in some basis, which leads to two truncations. Any basis we choose is truncated at some point, defining the model space we are working in. For instance, we truncate the Jacobi HO basis discussed in section 4.1 by limiting the maximum harmonic-oscillator energy quantum number. The effect of such a truncation can easily be investigated by varying the model-space size.

Furthermore, any basis we choose throughout this work has a fixed number of particles. However, during the SRG flow many-body interactions are induced with a higher particle rank than the bare interaction. Performing the SRG in a specific few-body basis, therefore, neglects all induced contributions beyond the particle number of the chosen basis. We are not able to include all these many-body contributions. Throughout this work we will always neglect 4N and higher contributions. Note that the explicit inclusion of induced four-body forces is possible but computationally expensive [60]. To investigate the effect of the induced contributions, one can vary  $\alpha$ . As higher values of  $\alpha$  should lead to additional induced forces, this allows to estimate the effect of the neglected contributions.

### 5.1.2 GENERATOR

As our goal is a pre-diagonalization of the Hamiltonian, we have to choose the generator accordingly. A simple choice, as proposed by Wegner [55, 98], is the following generator,

$$\eta_\alpha = [H_\alpha^{(d)}, H_\alpha],$$

where  $H_\alpha^{(d)}$  is the diagonal part of the Hamiltonian in a chosen basis. This yields a trivial fixed point when the Hamiltonian is completely diagonal. In fact, the fixed point is attractive and during the SRG evolution the Hamiltonian is driven towards a diagonal form.

A widespread choice in nuclear theory is

$$\eta_\alpha = m_N^2 [T_{\text{int}}, H_\alpha],$$

where  $T_{\text{int}}$  is the intrinsic kinetic energy and  $m_N$  is the mass of a nucleon. The kinetic energy is also a diagonal matrix in a relative two-body momentum representation and a tridiagonal one in case of a relative HO basis. Apart from improved convergence of many-body calculations, this definition is independent of the basis choice and was already used for the first application to NN interactions [97]. In this work we only use this generator based on the intrinsic kinetic energy.

Over the years many different generators have been investigated, aiming for reduced many-body contributions while keeping the improved convergence [60, 62–67]. This is still a very active field of research, but even though some of the generators seem to strike a slightly better balance than the kinetic energy, the changes are not drastic and the kinetic energy is still a very viable and well-tested choice for the SRG generator.

### 5.1.3 MANY-BODY CONTRIBUTIONS

Performing the SRG in two-body space is simple. The Hamiltonian consists of two parts, the intrinsic kinetic energy and a NN interaction. The evolution is performed in two-body momentum basis,

$$T_{\text{int}} + V_{\text{NN}}^{[2]} \xrightarrow{\text{SRG(2B)}} T_{\text{int}} + T_{\text{int},\alpha}^{[2]} + V_{\text{NN},\alpha}^{[2]},$$

where we indicate irreducible two-body contributions with an upper index of [2]. Note that the intrinsic kinetic energy is not a two-body operator, but an  $A$ -body operator, as it involves the center-of-mass motion. However, it can be expressed using momenta of two particles,

$$\begin{aligned} T_{\text{int}} &= T - T_{\text{cm}} \\ &= \frac{1}{2Am_N} \sum_{i < j} (\mathbf{p}_i - \mathbf{p}_j)^2. \end{aligned}$$

Due to the factor  $1/A$ , the intrinsic kinetic energy has to be handled separately when embedding it in a many-body space. We, therefore, subtract the kinetic energy after the evolution and the induced two-body part of the kinetic energy is absorbed in the interaction part, which are both irreducible two-body contributions and can be handled in the same way.

Obtaining the evolved irreducible three-body part requires a few additional technical steps, conceptually the evolution works analogously to the two-body case. Evolving the interaction in three-body space yields

$$T_{\text{int}} + V_{\text{NN}}^{[2]} + V_{\text{3N}}^{[3]} \xrightarrow{\text{SRG(3B)}} T_{\text{int}} + T_{\text{int},\alpha}^{[2]} + T_{\text{int},\alpha}^{[3]} + V_{\text{NN},\alpha}^{[2]} + V_{\text{NN},\alpha}^{[3]} + V_{\text{3N},\alpha}^{[3]}.$$

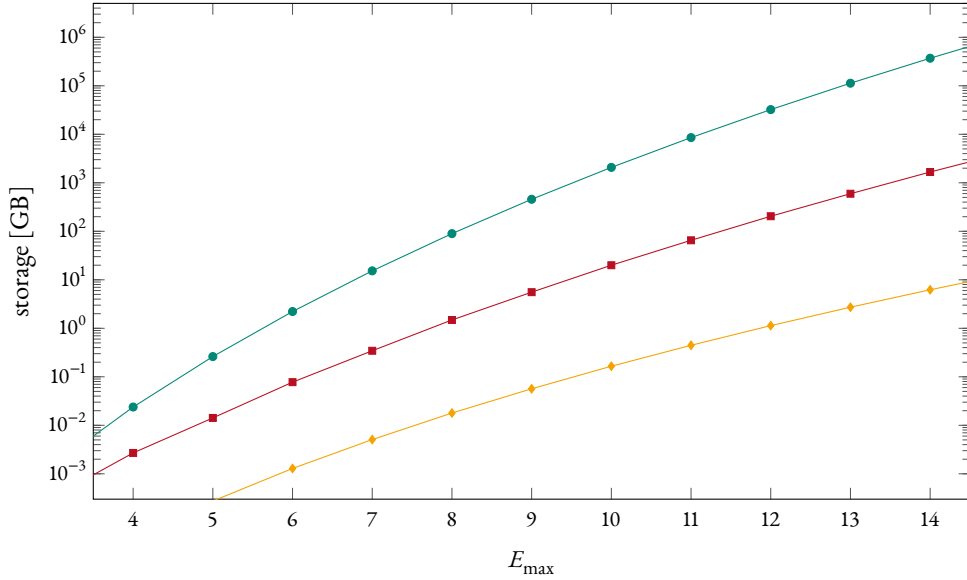
The result contains the intrinsic kinetic energy, which we directly subtract, as well as irreducible two- and three-body contributions. We can obtain the irreducible three-body part by subtracting the result from a two-body SRG evolution. However, the three-body evolution differs in details from the two-body one. For instance, we do not resolve the dependence on the isospin-projection quantum number in three-body space, and we always use the three-body Jacobi HO basis (see section 4.1), which might differ from the two-body basis. For this reasons we have to repeat the two-body evolution with matrix elements that are averaged over the projection quantum number and are represented in a two-body Jacobi HO basis. In principle, this allows a consistent subtraction from the result of the three-body evolution, yielding the irreducible three-body contributions. Note that the truncations of the two- and three-body Jacobi basis differ slightly, even if the same maximum HO energy quantum number is chosen, that is  $E_1 = E_{12}$ . Thus, the subtraction is only consistent, if the model space is sufficiently large.

In principle, this scheme can be extended to four-body space, as described in detail in refs. [60, 61]. However, in this work we only use the SRG up to the three-body level, as it is computationally too demanding to achieve convergence with respect to the model-space size in a four-body SRG evolution. A thorough investigation of the inclusion of induced 4N contributions can be found in ref. [60].

## 5.2 JT-COUPLED SCHEME

While it is helpful to perform the SRG in a Jacobi HO basis, as far less non-zero matrix elements have to be considered, it is not computationally feasible to extend such a basis to a many-body calculation beyond very light nuclei. The main problem is the complicated antisymmetrization of such a basis. When using a single-particle basis, however, antisymmetrization is almost trivial. In our case the single-particle states are HO states, that is,

$$|a\rangle = \left| n_a, \left( l_a \frac{1}{2} \right) j_a m_{j_a}, \frac{1}{2} m_{t_a} \right\rangle,$$



**Figure 5.1:** Storage space needed to store a four-body Hamiltonian for a given maximum HO energy quantum number in three different representations. Each matrix element requires 8 byte and the energy truncation in case of the Jacobi HO representation only applies to the intrinsic energy. The basis representations are the m-scheme ( $\bullet$ ), the JT-coupled scheme ( $\blacksquare$ ) and the Jacobi HO basis ( $\blacklozenge$ ). Lines are only included to guide the eye.

where the orbital angular momentum and spin is coupled. The many-body state in the m-scheme is a simple Slater determinant of these single-particle states. For example, in the four-body case we have

$$|abcd\rangle_a = \sqrt{4!} \mathcal{A} |a\rangle \otimes |b\rangle \otimes |c\rangle \otimes |d\rangle .$$

As the basis states are antisymmetric, only states that fulfill

$$a < b < c < d$$

are part of the basis. The ordering ensures an orthogonal basis set. We truncate the basis to a given maximum HO energy quantum number,

$$2n_a + l_a + 2n_b + l_b + 2n_c + l_c + 2n_d + l_d \leq E_{4,\max} .$$

The downside is the large number of non-zero matrix elements when expressing the interaction in this basis. We can, however, still use that the interaction is diagonal in parity, as well as, the sum of the angular momentum and the sum of the isospin projection quantum numbers, hence the name 'm-scheme'. The construction of a matrix in this many-body basis from few-body matrix elements is done using Slater-Condon rules [99, 100].

When storing the Hamiltonian in a few-body basis, we reduce the number of matrix elements we have to store by using the so-called JT-coupled scheme. As the Hamiltonian is diagonal in total angular momentum



and isospin, we can use these symmetries to reduce the number of relevant matrix elements. Due to spherical symmetry, the Hamiltonian is also independent of the total angular momentum projection quantum number. In the three- and four-body matrix elements we also assume independence of the total isospin projection, which is a small approximation, but it further reduces the necessary storage space. Naturally, we require a basis that is coupled to total angular momentum and total isospin in such a case. For the construction we simply apply the coupling to an antisymmetric m-scheme state to obtain an antisymmetric JT-coupled state, for example, in case of four particles,

$$\begin{aligned}
& \left| E J M_J T M_T \bar{\alpha}_{abcd} \right\rangle_a \\
&= \left| n_a n_b n_c n_d; \left( \left\{ \left[ \left( l_a \frac{1}{2} \right) j_a \left( l_b \frac{1}{2} \right) j_b \right] J_{ab} \left( l_c \frac{1}{2} \right) j_c \right\} J_{abc} \left( l_d \frac{1}{2} \right) j_d \right) J M_J; \left\{ \left[ \left( \frac{1}{2} \frac{1}{2} \right) T_{ab} \frac{1}{2} \right] T_{abc} \right\} T M_T \right\rangle_a \\
&= \sum_{m_a, m_b, m_c, m_d} \sum_{m_{j_a}, m_{j_b}, m_{j_c}, m_{j_d}} \sum_{M_{J_{ab}}, M_{J_{abc}}, M_{J_{abcd}}} \sum_{M_{T_{ab}}, M_{T_{abc}}, M_{T_{abcd}}} \left( \begin{array}{cc|c} j_a & j_b & J_{ab} \\ m_{j_a} & m_{j_b} & M_{J_{ab}} \end{array} \right) \left( \begin{array}{cc|c} J_{ab} & j_c & J_{abc} \\ M_{J_{ab}} & m_{j_c} & M_{J_{abc}} \end{array} \right) \left( \begin{array}{cc|c} J_{abc} & j_d & J \\ M_{J_{abc}} & m_{j_d} & M_J \end{array} \right) \\
&\quad \left( \begin{array}{cc|c} \frac{1}{2} & \frac{1}{2} & T_{ab} \\ m_{t_a} & m_{t_b} & M_{T_{ab}} \end{array} \right) \left( \begin{array}{cc|c} T_{ab} & \frac{1}{2} & T \\ M_{T_{ab}} & m_{t_c} & M_T \end{array} \right) \left( \begin{array}{cc|c} T_{abc} & \frac{1}{2} & T \\ M_{T_{abc}} & m_{t_d} & M_T \end{array} \right) |abcd\rangle_a, \tag{5.3}
\end{aligned}$$

where we introduced another index,  $\bar{\alpha}_{abcd} = \{\tilde{a}, \tilde{b}, \tilde{c}, \tilde{d}, J_{ab}, J_{abc}, T_{ab}, T_{abc}\}$ , with  $\tilde{a} = \{n_a, l_a, j_a\}$ . Again we order the single-particle indices by using

$$\tilde{a} \leq \tilde{b} \leq \tilde{c} \leq \tilde{d}.$$

This reduces the relevant matrix elements and ensures orthogonality of the basis. Note that with such a definition the coupled basis states are not normalized. However, by simply decoupling the matrix elements we retrieve the orthonormal m-scheme states again.

Converting a Hamiltonian given in Jacobi coordinates to the JT-coupled scheme is a non-trivial task and the formulae and derivations for the conversion in two- and three-body space are discussed in detail in ref. [101]. The derivation for four-body space can be found in ref. [61], yielding:

$$\begin{aligned}
& \left\langle E' J' M'_J T' M'_T \bar{\alpha}'_{abcd} \left| V_{4N} \right| E J M_J T M_T \bar{\alpha}_{abcd} \right\rangle_a \\
&= 4! \delta_{J, J'} \delta_{M_J, M'_J} \delta_{T, T'} \delta_{M_T, M'_T} \sum_{N_{cm}, L_{cm}} \sum_{E_{123}} \sum_{J_{123}} \sum_{T_{123}} \sum_{i_{123}} \sum_{E'_{123}} \sum_{i'_{123}} \\
&\quad \tilde{T}_{N_{cm}, L_{cm}, E, J, \bar{\alpha}_{abcd}}^{E_{123}, J_{123}, T_{123}, i_{123}} \tilde{T}_{N_{cm}, L_{cm}, E', J, \bar{\alpha}'_{abcd}}^{E'_{123}, J'_{123}, T'_{123}, i'_{123}} \delta_{T_{123}, T'} \left\langle E'_{123} i'_{123} J_{123} T_{123} \left| V_{4N} \right| E_{123} i_{123} J_{123} T_{123} \right\rangle_a, \tag{5.4}
\end{aligned}$$

with the transformation coefficient  $\tilde{T}$  given by

$$\begin{aligned}
\tilde{T}_{N_{cm}, L_{cm}, E, J, \bar{\alpha}_{abcd}}^{E_{123}, J_{123}, T_{123}, i_{123}} &= \sum_{k_{123}} \sum_{k_{12}} \sum_{L_{ab}} \sum_{K, P} \sum_{Q, R} \sum_{N_{cm}^{ab}, L_{cm}^{ab}} \sum_{N_{cm}^{abc}, L_{cm}^{abc}} \delta_{T_1, T_{ab}} \delta_{T_{12}, T_{abc}} \hat{j}_a \hat{j}_b \hat{j}_c \hat{j}_d \hat{L}_{ab}^2 \hat{S}_1 \hat{J}_{ab} \hat{J}_{abc} \hat{J}_1 \hat{K}^2 \hat{P}^2 \hat{J}_2 \hat{J}_2 \hat{Q}^2 \hat{R}^2 \hat{J}_{123} \hat{J}_3 \\
&(-1)^{1+L_{cm}^{ab}+L_{cm}^{abc}+L_{cm}+L_1+S_1+J_{ab}+J_{abc}+J_{12}+J+J_1+J_2+J_3} \langle\langle N_{cm}^{ab} L_{cm}^{ab}, N_1 L_1 | n_a l_a, n_b l_b; L_{ab} \rangle\rangle_1
\end{aligned}$$

$$\begin{aligned}
& \langle\langle N_{\text{cm}}^{abc} L_{\text{cm}}^{abc}, N_2, L_2 | N_{\text{cm}}^{ab} L_{\text{cm}}^{ab}, n_c l_c; K \rangle\rangle_2 \langle\langle N_{\text{cm}} L_{\text{cm}}, N_3 L_3 | N_{\text{cm}}^{abc} L_{\text{cm}}^{abc}, n_d l_d; Q \rangle\rangle_3 \\
& \left\{ \begin{matrix} l_a & \frac{1}{2} & j_a \\ l_b & \frac{1}{2} & j_b \\ L_{ab} & S_1 & J_{ab} \end{matrix} \right\} \left\{ \begin{matrix} L_{\text{cm}}^{ab} & J_1 & J_{ab} \\ l_c & \frac{1}{2} & j_c \\ K & P & J_{abc} \end{matrix} \right\} \left\{ \begin{matrix} L_{\text{cm}}^{abc} & J_{12} & J_{abc} \\ l_d & \frac{1}{2} & j_d \\ Q & R & J \end{matrix} \right\} \left\{ \begin{matrix} L_{\text{cm}}^{ab} & L_1 & L_{ab} \\ S_1 & J_{ab} & J_1 \end{matrix} \right\} \left\{ \begin{matrix} L_{\text{cm}}^{abc} & L_2 & K \\ P & J_{abc} & J_{12} \end{matrix} \right\} \\
& \left\{ \begin{matrix} L_2 & \frac{1}{2} & J_2 \\ J_1 & J_{12} & P \end{matrix} \right\} \left\{ \begin{matrix} L_{\text{cm}} & L_3 & Q \\ R & J & J_{123} \end{matrix} \right\} \left\{ \begin{matrix} L_3 & \frac{1}{2} & J_3 \\ J_{12} & J_{123} & R \end{matrix} \right\} c_{i_{12}, k_{12}}^{E_{12}, J_{12}, T_{12}} c_{i_{123}, k_{123}}^{E_{123}, J_{123}, T_{123}}. \quad (5.5)
\end{aligned}$$

A comparison of the storage space needed for a Hamiltonian in m-scheme, JT-coupled scheme, and Jacobi HO basis is shown in fig. 5.1. The storage space needed for different basis choices differs by orders of magnitude, which is a compelling argument to use the Jacobi HO basis as long as possible. Furthermore, we still use much less space when using the JT-coupled scheme compared to the decoupled version. As it is simple to perform the decoupling, we can obtain m-scheme matrix elements by decoupling them on the fly.

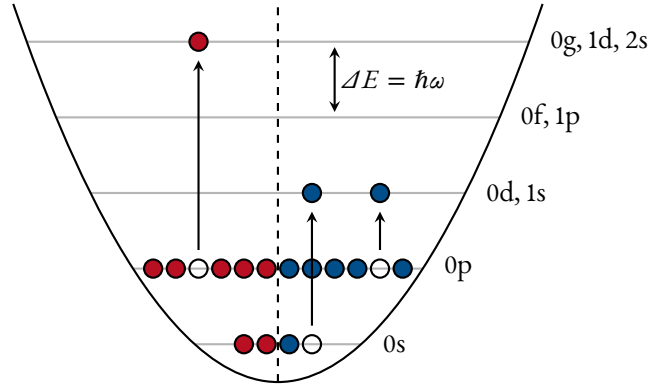
### 5.3 NO-CORE SHELL MODEL

The NCSM [41, 102–104] is a conceptually simple, yet exact many-body method that relies on the solution of a large-scale eigenvalue problem. Already its name suggests its origin from the shell-model, but calculations are performed without assuming a static core, thus, all nucleons are active degrees of freedom in this method. In its simplest formulation, it uses the m-scheme to construct an A-body basis and searches for the lowest-lying eigenvalues and corresponding eigenstates of the Hamiltonian in that basis.

The basis is truncated by limiting the HO excitation quanta to  $N_{\text{max}}$ . Note that this differs from the  $E_{\text{max}}$  truncation discussed in section 5.2. As an illustration, let us focus on the model space for  $^{16}\text{O}$ , of which one configuration is depicted in fig. 5.2. The  $N_{\text{max}} = 0$  space consists of exactly one configuration, the unperturbed HO state with, both, s- and p-shell filled completely. This corresponds to  $E_{16, \text{max}} = 12$  in a 16-body space. In case of open-shell nuclei, we get multiple configurations already at the  $N_{\text{max}} = 0$  level, which all have the same minimum  $E_{\text{max}}$ .

On top of this unperturbed configuration we add excitations in HO shells. These are truncated at  $N_{\text{max}}$ , yielding  $E_{16, \text{max}} = 12 + N_{\text{max}}$  in 16-body space. It follows that we need  $E_{2, \text{max}} = N_{\text{max}} + 2$  for a two-body and  $E_{4, \text{max}} = N_{\text{max}} + 4$  for a four-body interaction to fully cover the 16-body space, as only 2 and 4 particles are relevant, respectively. While this is not a problem for the two- or three-body interaction, with a typical truncation of  $E_{3, \text{max}} \approx 14$  in the three-body case, the four-body case must be truncated at lower  $E_{4, \text{max}}$ . This is an additional truncation whose effect has to be investigated.

The eigenvalue problem itself is solved using the Lanczos algorithm [105], which efficiently yields the lowest eigenvalues and corresponding eigenstates. With a set of eigenstates further operators can be evaluated, for instance the root-mean-square (rms) radius. An advantageous feature of the NCSM is that the calculated energies obey the variational principle, in other words, the NCSM yields a strict upper bound of the exact energies. Increasing  $N_{\text{max}}$  can only reduce the energies, therefore, the NCSM converges monoton-



**Figure 5.2:** Configuration for  $^{16}\text{O}$  with an excitation energy of  $6\hbar\omega$ . Neutrons and protons are depicted as blue and red dots, respectively.

ically to the exact energies.

Using the above formulation, the NCSM is restricted to p-shell nuclei, due to the factorial growth of the model-space size with the number of nucleons. Furthermore, the NCSM is computationally expensive and  $N_{\text{max}}$  is limited. Various extensions of the NCSM exist that aim to lighten the computational burden. One way to adapt the NCSM is the use of a different basis. For instance, we obtain exactly the same result by using the Jacobi HO basis instead of the single-particle one, which is called the Jacobi NCSM [94]. As the antisymmetrization of the Jacobi basis becomes increasingly expensive with a higher number of nucleons, this approach is only useful for  $A \lesssim 6$ , limiting the Jacobi NCSM to very light nuclei. However, the number of matrix elements is greatly reduced compared to the single-particle case and one can reach higher values of  $N_{\text{max}}$  in this formulation, at least for the lightest nuclei, that is  $A \lesssim 4$ . The Jacobi NCSM is used extensively throughout this work for solving the eigenvalue problem in four-body space, targeting  $^4\text{He}$ .

There are numerous other adaptations, for instance, as the HO is not well suited to describe loosely bound or scattering states, it is advantageous to incorporate continuum physics in such a case. Possible choices include the Berggren basis, as in the no-core Gamow shell model [106], or adding continuum states to the existing HO basis which leads to the no-core shell model with continuum [107, 108].

A different approach is to optimize the basis to the nucleus and interaction in question, for instance by using natural orbitals [109]. Alternatively, we can reduce the model-space size by identifying less important configurations and removing them from the model-space. This approach leads to the IT-NCSM [42, 43], which is also used in this work. For employing the importance truncation we need a reference state  $|\Psi_{\text{ref}}\rangle$ , which should be an approximation of the target state. We can then construct a model space by taking a full NCSM space and calculating an importance measure for each configuration  $|\Phi_v\rangle$ ,

$$x_v = \frac{\langle \Phi_v | H | \Psi_{\text{ref}} \rangle}{\epsilon_v - \epsilon_{\text{ref}}}.$$

For the denominator we use Møller-Plesset partitioning, where the difference between the energies is given

as the HO excitation energy, that is

$$\epsilon_\nu - \epsilon_{\text{ref}} = N\hbar\omega,$$

where  $N$  is the number of HO excitation quanta. Using this measure, we only include states that fulfill  $|\kappa_\nu| > \kappa_{\text{min}}$ , where  $\kappa_{\text{min}}$  is the importance threshold, an additional parameter in an IT-NCSM calculation.

In practice, the importance truncation is applied iteratively. We start with a full NCSM calculation, for example at  $N_{\text{max}} = 4$ . From the solution of the eigenvalue problem we obtain an eigenstate for the truncated Hamiltonian, which we use as a reference state in the next step. Afterwards we construct an importance-truncated model space in  $N_{\text{max}} = 6$ , using the resulting state from the  $N_{\text{max}} = 4$  calculation as an approximation of the target state. Applying the Lanczos algorithm to the Hamiltonian in the newly constructed space yields another eigenstate, which we can use as a reference state again. This procedure is continued until a sufficiently high value of  $N_{\text{max}}$  is reached.

Note that the removal of configurations slightly changes the results and for obtaining the energy of a targeted state or any other observable, therefore, we perform multiple calculations with different importance thresholds. Afterwards the results are extrapolated to vanishing importance threshold to regain the original NCSM result. This scheme yields a significant reduction of matrix sizes so that larger values of  $N_{\text{max}}$  can be reached and it extends the applicability of the NCSM to the lower sd-shell. A detailed description of the IT-NCSM and its application has been given by Roth [43].

## 5.4 HARTREE-FOCK METHOD

The HF method yields an approximate solution to the time-independent Schrödinger equation. Its central assumption is that the many-body wave function can be expressed using a single Slater determinant, thus, neglecting correlations between nucleons. The problem is then reduced to the determination of the optimal single-particle states, which is accomplished using a variational ansatz. Details of the derivation can be found in standard text books, for instance see ref. [110], and will not be discussed here.

The result is an eigenvalue problem for the so-called Fock operator  $f$ ,

$$f[g] |\xi_i\rangle = \epsilon_i |\xi_i\rangle, \quad (5.6)$$

$$\sum_a \langle a' | f[g] | a \rangle \langle a | \xi_i \rangle = \epsilon_i \langle a' | \xi_i \rangle, \quad (5.7)$$

where the Fock operator depends on the one-body density matrix  $g$ . The solution of the eigenvalue problem yields single-particle energies  $\epsilon_i$  and corresponding HF states  $|\xi_i\rangle$ . In eq. (5.7), the equation is expressed in terms of a basis, which will be the HO basis in our case, that is,

$$|a\rangle = \left| n_a, \left( l_a \frac{1}{2} \right) j_a m_{j_a}, \frac{1}{2} m_{i_a} \right\rangle.$$

Note that we use a spherical formulation of HF, targeting closed-shell nuclei. The HF states do not mix different angular momenta, their projections or particle types. In the HO basis, the Fock operator can be expressed as,

$$\begin{aligned}
 \langle a' | f[\xi] | a \rangle = & \underbrace{\langle a' | H^{[1]} | a \rangle}_{\langle a' | f[\xi]^{[1]} | a \rangle} + \underbrace{\sum_{b,b'} \langle a' b' | H^{[2]} | ab \rangle \xi_{b,b'}}_{\langle a' | f[\xi]^{[2]} | a \rangle} + \underbrace{\frac{1}{2} \sum_{b,b'} \sum_{c,c'} \langle a' b' c' | H^{[3]} | abc \rangle \xi_{b,b'} \xi_{c,c'}}_{\langle a' | f[\xi]^{[3]} | a \rangle} \\
 & + \underbrace{\frac{1}{6} \sum_{b,b'} \sum_{c,c'} \sum_{d',d} \langle a' b' c' d' | H^{[4]} | abcd \rangle \xi_{b,b'} \xi_{c,c'} \xi_{d,d'}}_{\langle a' | f[\xi]^{[4]} | a \rangle}, \tag{5.8}
 \end{aligned}$$

where we used the one-body density matrix of the system and the Hamiltonian. The one-body density matrix in terms of the HO states is given as

$$\xi_{a,a'} = \sum_{i=1}^A \langle a' | \xi_i \rangle \langle \xi_i | a \rangle,$$

where we only sum over the  $A$  occupied HF single-particle states, which are the states with the lowest single-particle energies  $\epsilon_i$ . From eqs. (5.6) and (5.8) it is apparent that HF is a mean-field method. The interaction between nucleons is simulated by a mean field, the Fock operator.

As we used the HO basis, the matrix elements required in eq. (5.8) are all given in m-scheme representation. However, as we store the matrix elements in a JT-coupled scheme, we can gain a tremendous speedup by performing the construction of the Fock operator directly in the coupled scheme. In case of the three-body part, the relevant formulae have been derived by Wirth [III]. The derivation for the four-body part of the Fock operator is discussed in appendix B.

As the Fock operator in the eigenvalue problem depends on the one-body density matrix, which in turn depends on the solution of the eigenvalue problem, eq. (5.6) has to be solved in a self-consistent way. The usual implementation is an iterative scheme. We start with the assumption that the single-particle HF states  $|\xi_i\rangle$  are HO states, thus the density matrix is diagonal. We construct the Fock operator using that density and then solve eq. (5.6) with it. From the solution of the eigenvalue problem we get a new set of states, from which we can construct a new density matrix, and so on. This is repeated until convergence is achieved. While the iterative scheme is simple, numerical stability is not guaranteed.



# 6

## Results for a Four-Body Contact Interaction

The first four-body interaction we use is the contact interaction, as defined in section 4.3. In this case, the PWD is simple and computationally cheap. The only parameters of the four-body interaction we can vary are the regulator and the strength  $c_{4B}$ . As described in section 4.3, we are using a nonlocal regulator, which ensures that the contact interaction only acts in the  $J^\pi = 0^+$  channel with isospin  $T = 0$ , which further reduces computational requirements.

In this chapter, we analyze the effect of the interaction for two different two- and three-body interactions, namely the EM/N500 interaction in section 6.1 and the SMS/H500 interaction in section 6.2, see section 2.5 for details on these interactions. In both cases the interaction has been transformed using the SRG and all contributions up to the three-body level are included. The four-body interaction has not been transformed. One question of interest is if the simple contact interaction can be used to mimic the omitted SRG-induced four-body forces. Furthermore, the two- and three-body interactions yield charge radii that are too small compared to experimental results for heavier nuclei. We therefore also investigate the contact interaction's effect on radii and whether the interaction can improve on the description of the chiral interactions. Before judging that, the effect of the regulator parameters and the convergence behavior is investigated for both sets of two- and three-body interactions in  ${}^4\text{He}$ . Afterwards, we investigate the effect of the contact interaction in heavier nuclei, especially the effect on the ground-state energies and charge radii and the scaling with the number of nucleons.

As the PWD is computationally simple, we include the 4N interaction at  $E_{4,\text{max}} = 20$  in Jacobi NCSM calculations of  ${}^4\text{He}$  and we use  $E_{4,\text{max}} = 10$  for HF calculations and for NCSM calculations of nuclei heavier

than  ${}^4\text{He}$ , as the four-body interaction requires a lot of storage space when represented in the JT-coupled scheme, as discussed in section 5.2. For all comparisons with experimental data, we use ground-state energies taken from refs. [112, 113], and charge radii listed in ref. [114].

## 6.1 THE EM/N500 INTERACTION

We first use the SRG-evolved EM/N500 interaction as a testbed for the contact interaction. This interaction has already been studied extensively for light and medium-mass nuclei [58, 115, 116]. It provides a good agreement with experimental ground-state energies for light nuclei. However, throughout the p-shell the effect of the missing SRG-induced four-body contributions becomes apparent. Additionally, charge radii are systematically predicted too small, which is most likely not only an effect of the SRG transformation but a deficiency of the initial interaction. We will use the interaction at two different flow parameters,  $\alpha = 0.04 \text{ fm}^4$ , and  $\alpha = 0.08 \text{ fm}^4$ , to capture the influence, if any, of the SRG evolution on the effect of the contact interaction.

We first investigate the behavior of the contact interaction for different regulator parameters. To that end, we can see the effect of the 4N interaction on the ground-state energy, that is, the difference between the ground-state energy of a calculation with and without four-body forces in fig. 6.1 for various regulator exponents and cutoffs. Furthermore, we investigate the convergence behavior and the perturbative inclusion of the interaction, as shown in fig. 6.2, and for the latter we employ first-order perturbation theory. To that end we calculate a ground state  $|\Psi_0\rangle$  without the 4N interaction and approximate the 4N contribution to the ground-state energy by calculating the first-order correction,

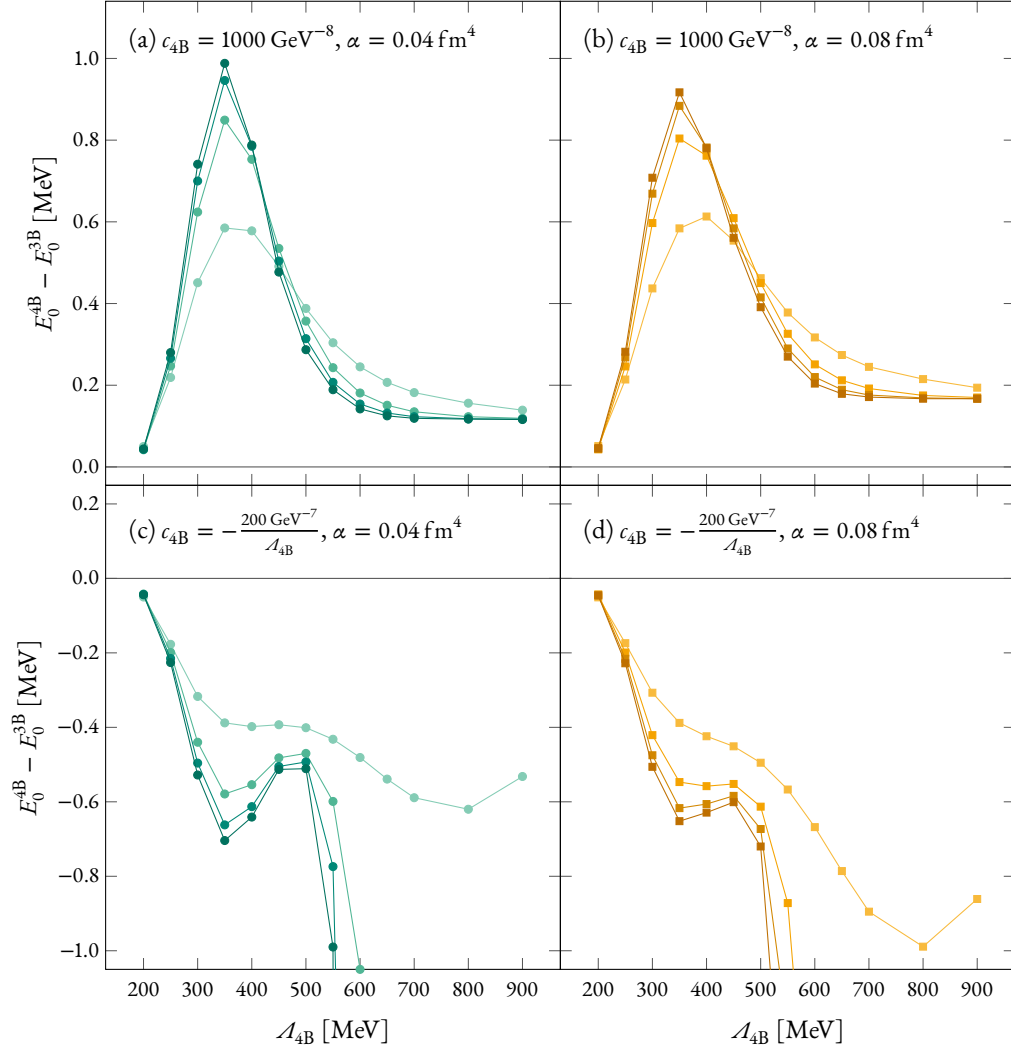
$$\langle \Psi_0 | V_{4N} | \Psi_0 \rangle . \quad (6.1)$$

The general behavior we observe for the contact interaction strongly depends on the sign of the interaction.

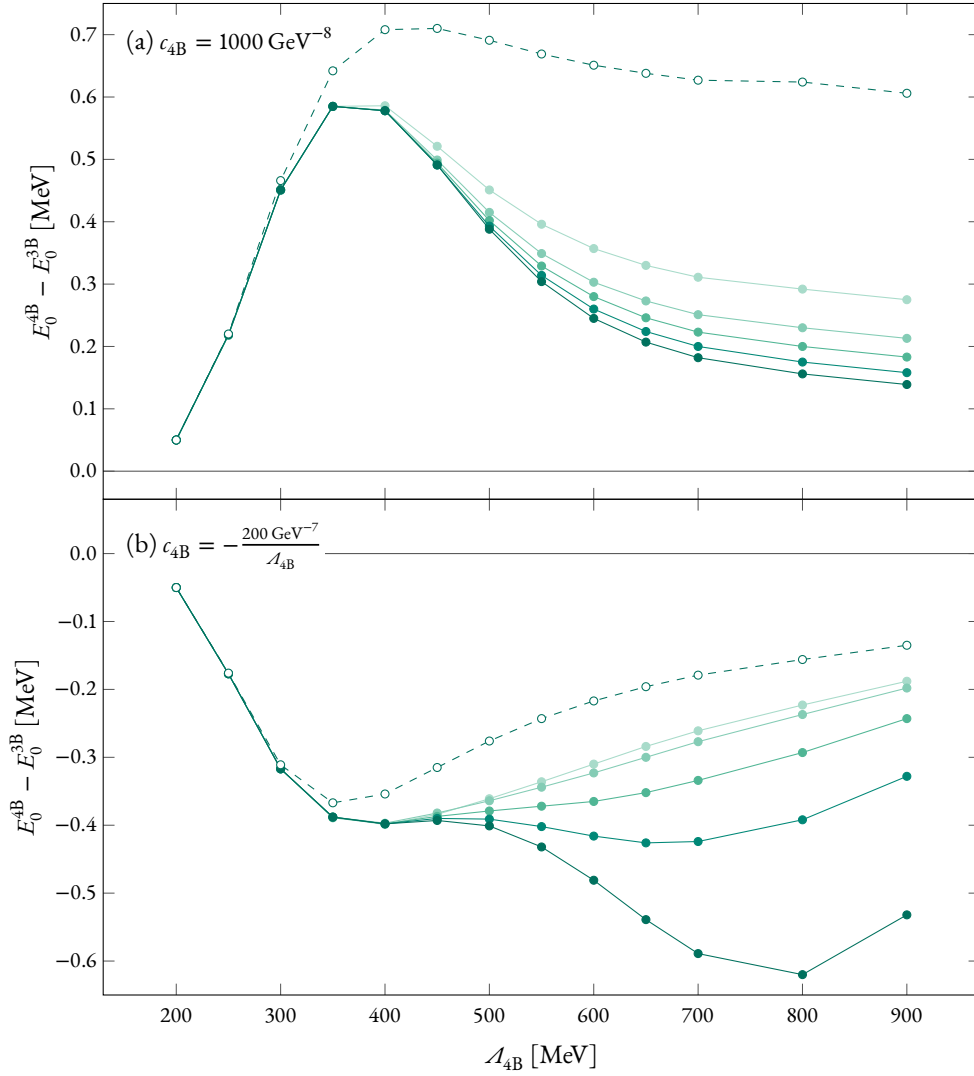
In case of a repulsive contact interaction, as depicted in figs. 6.1(a) and 6.1(b), we always see the same trend. At low cutoffs, its effect vanishes. This is not surprising, as we keep the factor  $c_{4B}$  constant, we simply cut away relevant parts of the integrals reducing the strength of the interaction. Increasing the cutoff, the strength peaks at some point and then reduces again. At these higher cutoffs, the contact interaction becomes increasingly short-ranged. We can interpret the reduced effect as the many-body method rearranging the ground state in such a way as to reduce the probability of four nucleons being extremely close to each other. This becomes easier for an extremely short-ranged interaction, reducing the effect the contact interaction has on the ground-state energy.

Note that this interpretation is consistent with the perturbative calculation, which cannot reproduce the weakening effect at larger cutoffs, as seen in fig. 6.2(a). Furthermore, we observe that convergence deteriorates rapidly at higher cutoffs. Up to  $\Lambda_{4B} = 300 \text{ MeV}$  the perturbative 4N contributions agree well with the full calculation, and at  $\Lambda_{4B} = 500 \text{ MeV}$  we still see a good convergence in an NCSM calculation at





**Figure 6.1:** Effect of the four-body contact interaction on the ground-state energy of  ${}^4\text{He}$  in Jacobi-NCSM calculations for different cutoffs and regulator exponents. The calculations are performed at  $N_{\text{max}} = 20$  and  $\hbar\omega = 20$  MeV with the EM/N500 interaction in the two- and three-body sector. The different regulator exponents  $n_{\text{exp}}$  shown are 2 (lightest line), 4, 6, and 8 (darkest line). The two- and three-body interactions have been SRG-evolved to flow-parameters of  $\alpha = 0.04 \text{ fm}^4$  (left side), and  $\alpha = 0.08 \text{ fm}^4$  (right side). Figures (a) and (b) depict a repulsive force with  $c_{4B} = 1000 \text{ GeV}^{-8}$  and in figures (c) and (d) the attraction of the interaction is scaled by using  $c_{4B} = -\frac{200 \text{ GeV}^{-7}}{A_{4B}}$ .



**Figure 6.2:** Convergence of the ground-state energy of  ${}^4\text{He}$  in Jacobi-NCSM calculations with 4N contact interactions using different cutoffs. The calculations are performed at  $N_{\text{max}} = 12$  ( $\circ$ ),  $N_{\text{max}} = 14$  ( $\bullet$ ),  $N_{\text{max}} = 16$  ( $\circ$ ),  $N_{\text{max}} = 18$  ( $\bullet$ ) and  $N_{\text{max}} = 20$  ( $\bullet$ ). Additionally a calculation without four-body interaction at  $N_{\text{max}} = 20$  is shown, estimating the four-body contribution using first-order perturbation theory ( $\circ$ ). All calculations employ a regulator exponent of  $n_{\text{exp}} = 2$  and a HO basis with a frequency of  $\hbar\omega = 20$  MeV, and for the two- and three-body sector the EM/N500 interaction has been SRG-evolved to a flow parameter of  $\alpha = 0.04$  fm $^4$ . Figure (a) depicts a repulsive force with  $c_{4B} = 1000$  GeV $^{-8}$  and in figure (b) the attraction of the interaction is scaled by using  $c_{4B} = -\frac{200 \text{ GeV}^{-7}}{\mathcal{A}_{4B}}$ .

$N_{\max} = 20$ . Beyond that point, however, results at  $N_{\max} = 20$  are less reliable and should be considered as an upper bound. This convergence behavior is not unexpected, as the NCSM is not well suited to capture extremely short-ranged or high-momenta physics.

When increasing the regulator exponent the general trend is identical, but the maximum of the peak increases while its width decreases. An increased exponent changes the regulator from an almost Gaussian shape to one that is similar to a step function, dropping off sharply at a given cutoff. At a fixed, low cutoff we, therefore, obtain a stronger effect of the contact interaction for larger exponents, as a step function includes more of the relevant low momenta. The inverse is true for higher cutoffs, the step-like functions seem to have the smallest effect. Note that the difference at larger cutoffs might be a convergence effect, as a Gaussian-like regulator extends to higher momenta which deteriorates convergence of the many-body calculation.

The behavior in case of an attractive contact interaction is different. For this case, the strength is reduced with increasing cutoff, as the larger cutoff increases the attraction and we obtain completely unphysical deeply-bound states. To this end we employ the scaling

$$c_{4B} = -\frac{200 \text{ GeV}^{-7}}{\mathcal{A}_{4B}}, \quad (6.2)$$

which matches the strength used in the repulsive case for  $\mathcal{A}_{4B} = 200 \text{ MeV}$ , but it is reduced for higher cutoffs. Note that this scaling is fine-tuned to suppress deeply-bound states for a regulator with  $n_{\text{exp}} = 2$ . Other exponents still exhibit unphysical behavior at larger cutoffs, as apparent from figs. 6.1(c) and 6.1(d). For the regulator exponent of  $n_{\text{exp}} = 2$  we can see increased attraction for larger cutoffs, even though  $c_{4B}$  is reduced. Increasing the regulator exponent introduces a sharp drop at  $\mathcal{A}_{4B} = 500 - 600 \text{ MeV}$ .

For the very low cutoffs, that is,  $\mathcal{A}_{4B} \leq 300 \text{ MeV}$ , the perturbative inclusion of the 4N contributions matches the full calculation and, therefore, we obtain exactly the same result as in the repulsive case. Bear in mind that the perturbative calculations in fig. 6.2(b) give the same results as the ones from fig. 6.2(a), just with a different sign and a reduced effect due to the introduced scaling for  $c_{4B}$ .

As soon as we use higher values for the cutoff, and the perturbative inclusion is not a good prediction for the full calculation anymore, the effect already differs. In case of a repulsive interaction the effect is always weaker than the perturbative calculation suggests. For an attractive interaction, we observe the opposite. The convergence deteriorates faster as well. Already at  $\mathcal{A}_{4B} = 500 \text{ MeV}$ , the results from different model-space sizes are almost equidistant. At higher cutoffs, the convergence pattern is even inverted, and the contributions to the ground-state energy increase for larger values of  $N_{\max}$ .

In both cases, the trends for the different flow parameters are very similar. For low cutoffs, we get almost the same results in both cases, only at higher cutoffs the effect of the contact interaction differs. In the repulsive case, the effects differ only slightly, while we obtain a large difference in the case of an attractive contact interaction. However, the calculations at high cutoffs are not reliable in any way and only a small change is necessary to produce completely unphysical results in this region.

Due to the convergence behavior of the interaction at higher cutoffs, we use a cutoff of  $\mathcal{A}_{4B} = 300$  MeV in the remainder of the section. Choosing the low cutoff also ensures that perturbative inclusion of the interaction is in good agreement with the full calculation. Furthermore, we choose a regulator exponent of  $n_{\text{exp}} = 2$ . We now use this interaction in various nuclei to investigate its effect on ground-state energies and charge radii for varying strength of the four-body contact interaction.

For calculating the charge radius we start with the rms radius of the protons, which is defined as

$$R_{\text{p,rms}} = \sqrt{\langle \Psi_0 | \frac{1}{Z} \sum_{i=1}^A (r_i - R)^2 P_i^{(p)} | \Psi_0 \rangle}, \quad (6.3)$$

where  $|\Psi_0\rangle$  is the ground state,  $P_i^{(p)}$  projects on protons, and  $R$  is the center of mass, which is given by

$$R = \frac{1}{A} \sum_{i=1}^A r_i, \quad (6.4)$$

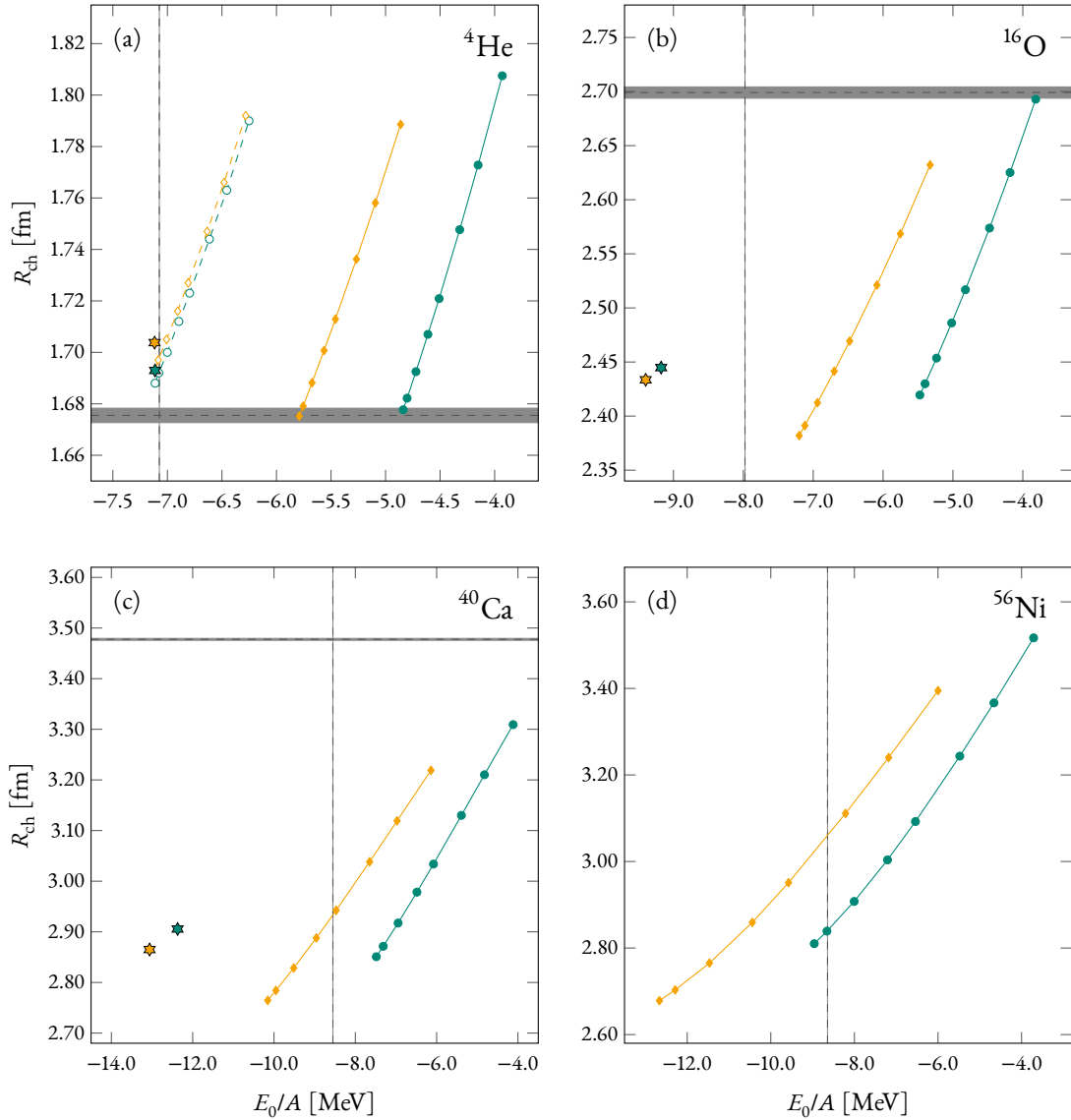
when assuming identical masses. The rms radius assumes a point-like proton, and thus it does not take the charge distribution of the proton itself into account. Therefore, the charge distribution of the proton has to be folded with the distribution of the protons in the nucleus. Furthermore, although neutrons do not carry a net charge, they do have a charge distribution that has to be included as well. From that, one can derive the following formula for the charge radius of the nucleus [117],

$$R_{\text{ch}} = \sqrt{R_{\text{p,rms}}^2 + r_{\text{p,ch}}^2 + \frac{N}{Z} r_{\text{n,ch}}^2}, \quad (6.5)$$

where  $r_{\text{p,ch}}^2$  and  $r_{\text{n,ch}}^2$  are the mean-square charge radii of the proton and neutron, respectively. We use  $r_{\text{n,ch}}^2 = -0.1161 \text{ fm}^2$  [68] and  $r_{\text{p,ch}}^2 = (0.8751 \text{ fm})^2 + \frac{3}{4m_p^2}$ , which is the proton charge radius taken from ref. [118] with the additional Darwin-Foldy term, see refs. [117, 119]. For the mass of the proton we use  $m_p = 938.272 \text{ MeV}$  [68]. Note that recent measurements of the proton charge radius in muonic hydrogen yield a much smaller charge radius [120, 121], a discrepancy that is known as the proton radius puzzle. Using the smaller value for the proton radius would reduce the charge radius of  ${}^4\text{He}$  by about 0.02 fm.

There is one additional difficulty. In case of NCSM calculations of  ${}^4\text{He}$  we always use the Jacobi NCSM variant. As it does not use a single-particle basis, calculating the proton rms radius is nontrivial. Instead we simply use the total rms radius. Full NCSM calculations with a single-particle basis yield proton rms radii that are about 0.2% larger than total rms radii. This can be traced back to the Coulomb interaction that pushes protons apart. The difference between the proton and total rms radii is about the same size as the experimental uncertainty of the charge radius in  ${}^4\text{He}$ , we therefore neglect it.

We are now in the position to investigate the effect of the 4N contact interaction on different nuclei using NCSM and HF calculations. An overview of this effort can be seen in fig. 6.3, which depicts ground-state energy per nucleon and charge radius for various strengths of the contact interaction.



**Figure 6.3:** Ground-state energy and charge radius of  ${}^4\text{He}$  (a),  ${}^{16}\text{O}$  (b),  ${}^{40}\text{Ca}$  (c), and  ${}^{56}\text{Ni}$  (d) in HF calculations at  $e_{\text{max}} = 10$ . For the two- and three body sector the EM/N500 interaction has been SRG-evolved to flow parameters of  $\alpha = 0.04 \text{ fm}^4$  ( $\color{teal}\bullet$ ), and  $\alpha = 0.08 \text{ fm}^4$  ( $\color{orange}\blacklozenge$ ). For  ${}^4\text{He}$  we also show NCSM calculations with flow parameters of  $\alpha = 0.04 \text{ fm}^4$  ( $\color{teal}\circ$ ), and  $\alpha = 0.08 \text{ fm}^4$  ( $\color{orange}\circ$ ). A repulsive contact interaction is added with a strength of  $c_{4\text{B}} = 0, 300, 1000, 2000, 3000, 5000, 7000, 10000 \text{ GeV}^{-8}$ . All calculations employ a regulator exponent of  $n_{\text{exp}} = 2$ , a cutoff of  $\mathcal{A}_{4\text{B}} = 300 \text{ MeV}$ , and a HO basis with a frequency of  $\hbar\omega = 20 \text{ MeV}$ . Dashed lines with gray bands are experimental results and uncertainties. Stars indicate the ground-state energy and charge radius from a NCSM calculation in case of  ${}^4\text{He}$  or a IMSRG calculation for  ${}^{16}\text{O}$  and  ${}^{40}\text{Ca}$ . The SRG-induced contributions to the radius are not included in any of these calculations, except for the additional NCSM calculations in  ${}^4\text{He}$ , that is, in  $\color{teal}\circ$  and  $\color{orange}\circ$ , not in the ones depicted by stars.

Let us focus on  ${}^4\text{He}$  for now, presented in fig. 6.3(a). We can see two types of NCSM calculation. Two results without any four-body force corresponding to the two flow parameters, which are depicted as stars. These calculations do not take the SRG-induced contributions to the radius operator into account. Furthermore we have NCSM calculations for various strengths of the contact interaction, which do take these contributions into account at the two-body level. These are depicted as dashed lines. Just looking at the lower left of the dashed lines, we can see the difference the SRG-induced radius contributions make. Taking them into account slightly lowers the radius and reduces the flow parameter dependence, as one would expect. Adding a repulsive contact interaction increases the ground-state energy and the radius, in fact, we observe an almost linear dependence of the radius and ground-state energy on  $c_{4B}$ .

Comparing the NCSM results to HF, we get a very similar behavior. The lines in the HF case are almost linear as well, and the direction of the lines is the same. Only the starting point, which corresponds to the calculation without four-body forces, differs drastically. If one would shift the calculation without the contact interaction to the NCSM result, the HF results are a good predictor for the NCSM results.

However, the HF calculations slightly overestimate the effect of the contact interaction. The reason is the same as for the perturbative inclusion of  $4N$  interaction in fig. 6.2, which also predicts an effect that is slightly too large. In both cases, a four-body correlation tailored to the contact interaction at hand is not accounted for in the many-body state. In the perturbative case, we do not change the ground-state at all, and in the HF case, no correlations are taken into account in the many-body calculation.

Even without shifting the HF results, they yield a charge radius close to the NCSM result. The energy is, of course, too high, while the  $\alpha = 0.08 \text{ fm}^4$  interaction does a little bit better, as the HF approximation is better suited for such a soft interaction. The trends are similar for the other nuclei, however, we do see slightly curved lines in the case of  ${}^{56}\text{Ni}$ .

For heavier nuclei, we use the IMSRG [47, 48] to calculate ground-state energies and charge radii. The IMSRG results are generally close to the NCSM calculations [48]. Even these IMSRG results without the  $4N$  interaction, depicted as stars in figs. 6.3(b) and 6.3(c), show a strong flow parameter dependence in  ${}^{16}\text{O}$  and  ${}^{40}\text{Ca}$ , as the induced many-body contributions are missing. In all heavier nuclei, the SRG-evolved interaction results in overbinding, yielding charge radii and ground-state energies that are small compared to the experimental results. These effects become more severe for heavier nuclei, and for  ${}^{56}\text{Ni}$  both HF results are already overbound. Thus, the omitted induced four-body force must be repulsive and shows strong scaling with the number of nucleons. Note that, while the ground-state energy depends strongly on the flow parameter, the effect is less severe for radii. Therefore, it seems highly unlikely that the small radii are a result of neglected SRG-induced many-body contributions. We rather conclude that the initial chiral two- and three-body forces already predict radii that are too small.

From the results we can clearly see that we cannot imitate the behavior of the missing contributions with a contact interaction. The induced contributions have almost no effect in  ${}^4\text{He}$  and grow fast with the number of nucleons, at least for the ground-state energy. We can see a scaling of the contact interaction as well, its effect does increase with the number of nucleons. However, we used a nonlocal regulator for

the contact interaction, we therefore designed the interaction to only act in the  $J^\pi T = 0^+0$  channel. For imitating the induced contributions we need the exact opposite, almost no contributions in  ${}^4\text{He}$ , while growing drastically with the number of nucleons.

Going to heavier nuclei, we also observe an increasing discrepancy between the predicted radii and experimental results for the two- and three-body interaction. In the case of radii, we also observe a scaling of the 4N contribution, but again, this scaling is too weak, if we want to employ the contact interaction to improve the prediction of charge radii. Furthermore, it seems impossible to improve the description of radii without severely deteriorating the description of binding energies. For such a task the 4N contact interaction seems to be the wrong tool. However, the prediction of radii can be fixed by modifying the two- and three-body interaction, for instance, by directly fitting the LECs to radii of nuclei, as done by Ekström *et al.* [122].

## 6.2 THE SMS/H500 INTERACTION

The second interaction we investigate is SMS/H500. It includes two- and three-body forces consistently at  $\text{N}^2\text{LO}$ , for details on this interaction see section 2.5. As it does not have a complete fit for the three-body interaction, only a correlation between  $c_D$  and  $c_E$  based on the triton ground-state energy, we simply use two values for  $c_D$  throughout this section, to be specific,  $c_D = 0$  and  $c_D = 4$ .

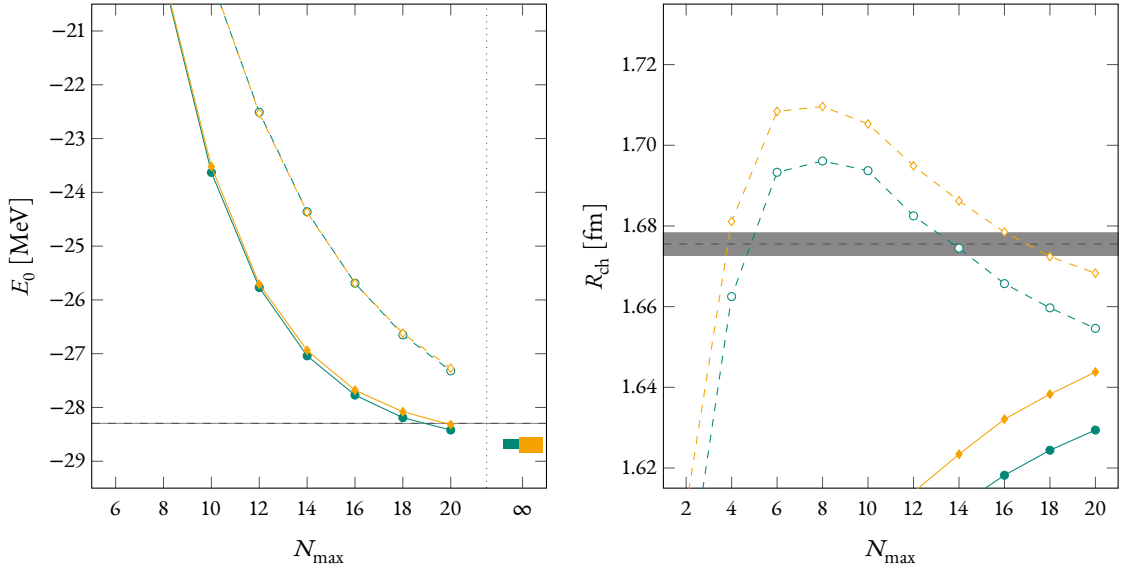
We first investigate these two interactions without any four-body force in  ${}^4\text{He}$ . For that we perform calculations with the bare interaction, as depicted in fig. 6.4. As the bare case is not converged, we have to extrapolate the ground-state energy. For that we employ the following Gaussian ansatz,

$$E(N_{\text{max}}) = E_0 + A \exp(-B N_{\text{max}} - C N_{\text{max}}^2). \quad (6.6)$$

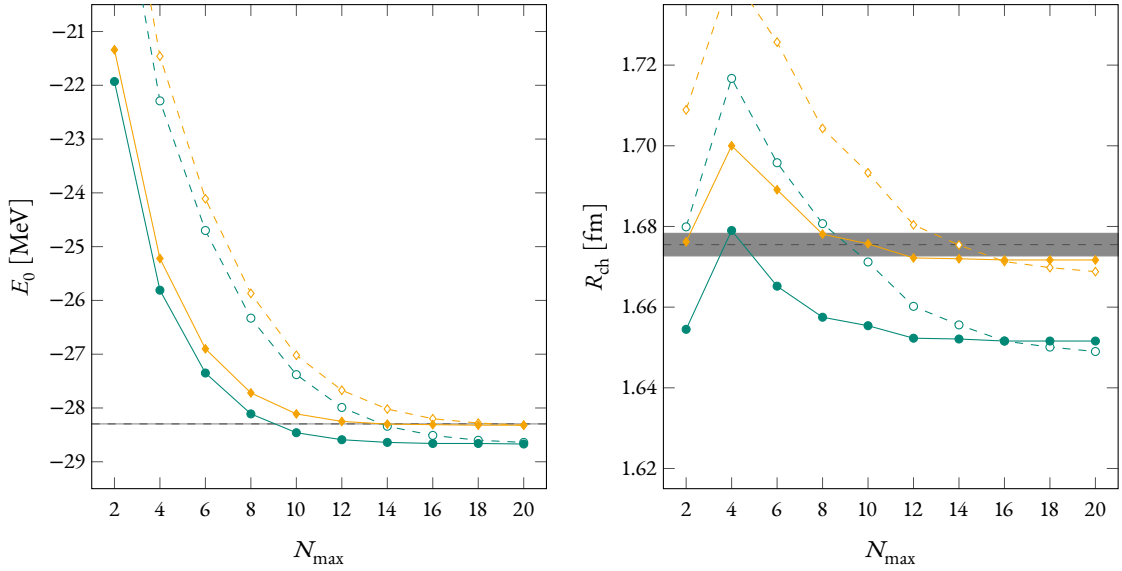
We fit the Gaussian function to the last four, five, and six data points. Furthermore, we fit an exponential function, where we simply set  $C = 0$ , to the last three to six data points. Finally, we enforce that the band spanned by these extrapolated ground-state energies is at least half of the distance between the lowest extrapolated energy and the last data point. If this condition is not fulfilled, the upper end of the band is extended towards higher energies. Note that much more sophisticated extrapolation methods exist [123–125], which allow extrapolations with less uncertainty.

Judging by the calculations employing the bare interaction, which is presented in fig. 6.4, the final ground-state energy of  ${}^4\text{He}$  and the charge radius is too low compared to experimental results. However, in both cases the discrepancy is only on the order of 1–2%. As we cannot obtain completely converged results with this interaction, we soften it using the SRG with flow parameters of  $\alpha = 0.02 \text{ fm}^4$ , and  $\alpha = 0.04 \text{ fm}^4$ . The flow parameters are chosen lower compared to the previous interaction, as the SMS/H500 interaction is already slightly softer than the EM/N500 one. Ground-state energies and charge radii of  ${}^4\text{He}$  for these two SRG-transformed interactions are shown in fig. 6.5.

Interestingly, the evolved interactions fare better in comparison with experiment, at least for  $c_D = 4$ . The



**Figure 6.4:** Ground-state energy and charge radius from NCSM calculations of  ${}^4\text{He}$  using the bare SMS/H500 interaction. The different lines correspond to  $c_D = 0.0$  ( $-\circ-$ ,  $-\bullet-$ ), and  $c_D = 4.0$  ( $-\diamond-$ ,  $-\blacklozenge-$ ), where the dashed lines correspond to a HO frequency of  $\hbar\omega = 36$  MeV, and the solid ones to  $\hbar\omega = 52$  MeV. Experimental values and uncertainties are depicted using dashed lines and gray bands, respectively. Bands at  $N_{\max} = \infty$  are spanned by extrapolations using the last three to six data points from the  $\hbar\omega = 52$  MeV calculation, see text for details.



**Figure 6.5:** Ground-state energy and charge radius of  ${}^4\text{He}$  using the SRG-evolved SMS/H500 interaction. The different lines correspond to  $c_D = 0.0$  ( $-\circ-$ ,  $-\bullet-$ ), and  $c_D = 4.0$  ( $-\diamond-$ ,  $-\blacklozenge-$ ), where the dashed lines correspond to  $\alpha = 0.02$   $\text{fm}^4$  and the solid ones to  $\alpha = 0.04$   $\text{fm}^4$ . The NCSM calculations use a HO frequency of  $\hbar\omega = 20$  MeV. SRG-induced contributions to the radius are included at the two-body level. Experimental values and uncertainties are depicted using dashed lines and gray bands, respectively.



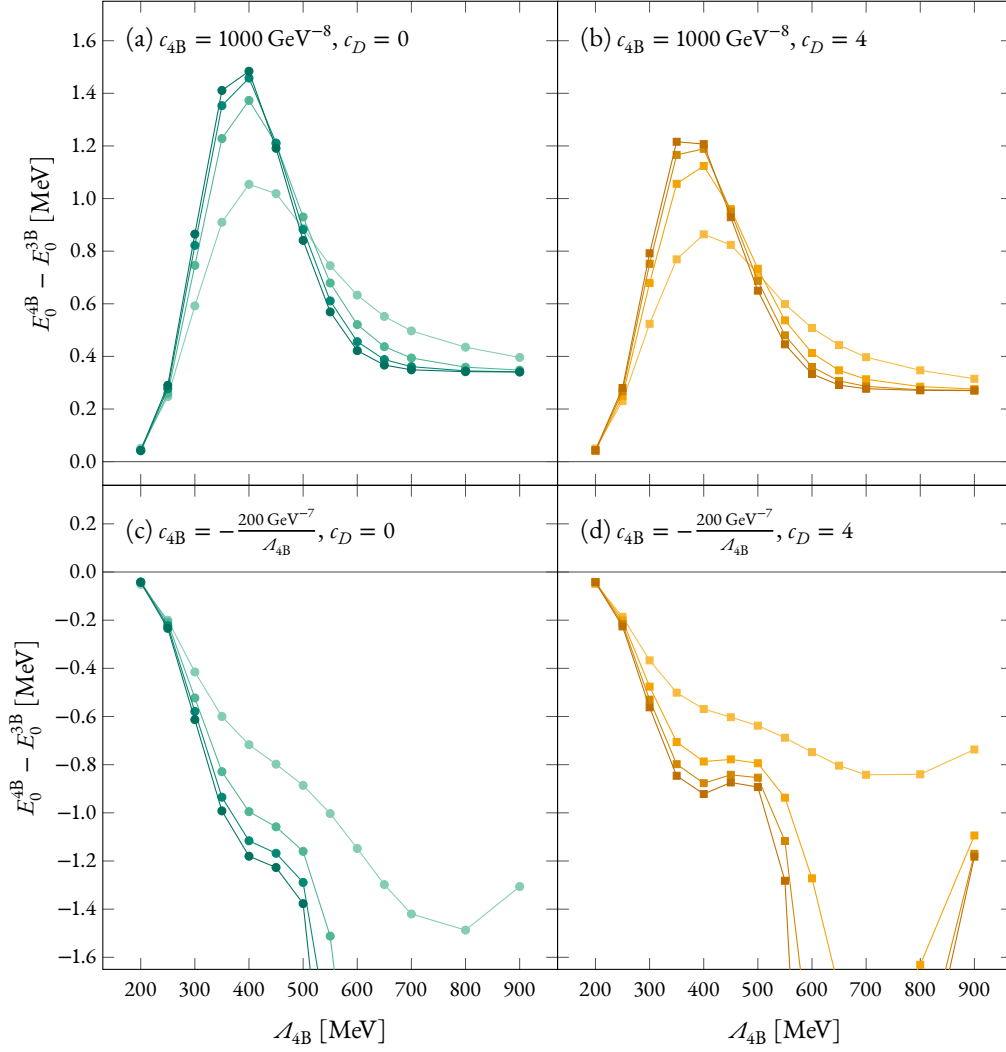
ground-state energy is on top of the experimental result for  $c_D = 4$ . For  $c_D = 0$  it is compatible with the extrapolation based on the bare interaction, yielding a value that is about 300 keV too low. The charge radii for the evolved interactions are also larger than the trend in the bare interactions suggested. Again, the result for  $c_D = 4$  is consistent with experiment and definitely higher than in the bare case. In the  $c_D = 0$  case, the charge radius is still slightly too small, but SRG-evolved result might be consistent with a converged result for the bare interaction. Note that we include the SRG-induced two-body contributions to the radius to reduce the flow parameter dependence of the result.

In case of the charge radii we see a small dependence on the flow parameter, where the smaller value of  $\alpha$  yields slightly smaller charge radii. This can be expected in a case where the charge radii are shifted upwards by the SRG transformation. However, the ground-state energy is independent of the flow parameter, even though the results for the bare interaction predict lower values for the  $c_D = 4$  interaction. In this case the missing induced contributions are clearly attractive, although the flow parameter variation does not hint at that for the ground-state energy. Neglecting the induced contributions actually improves on the overly attractive bare interaction. The effect of the SRG transformation in the  $c_D = 0$  case cannot be conclusively determined from this data, but the flow parameter dependence of the charge radius hints at an attractive effect of the neglected induced contributions.

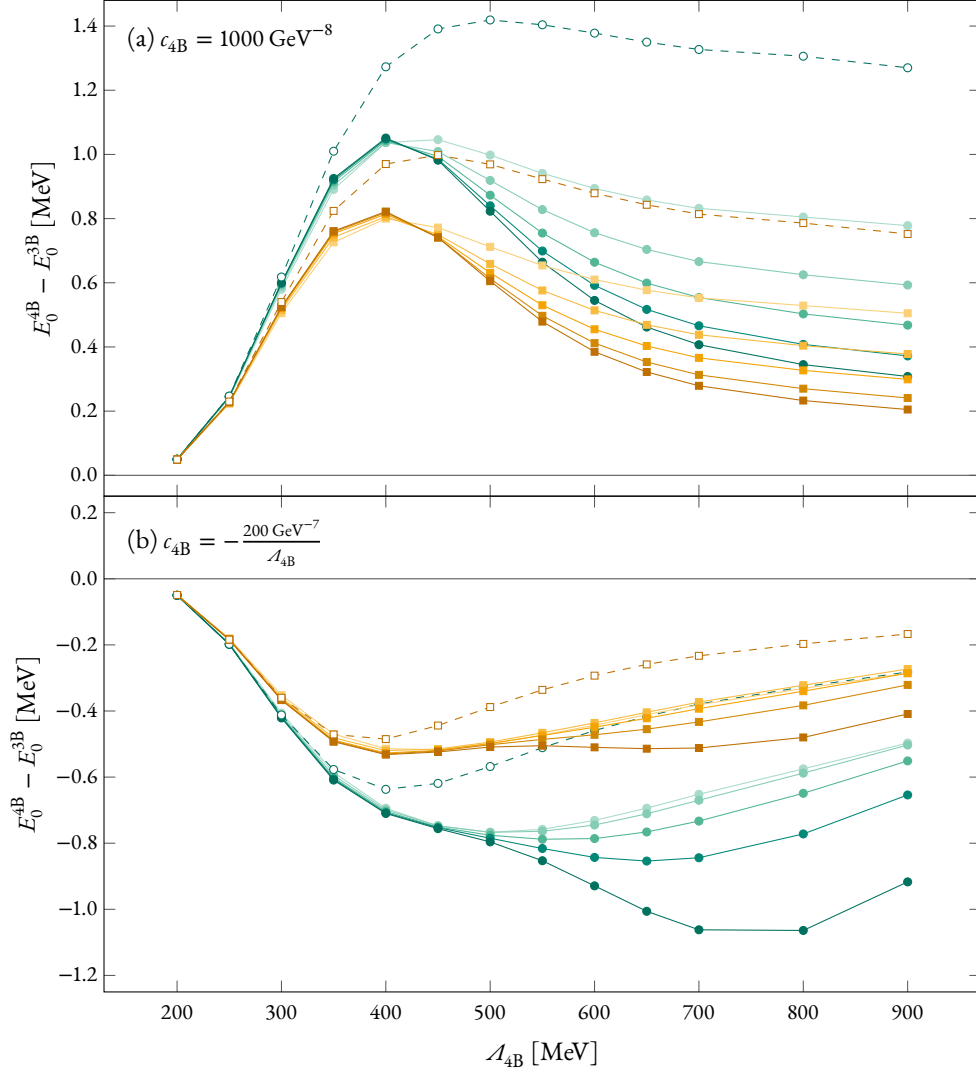
To this two- and three-body interaction we now add the contact 4N interaction. As for the EM/N500 interaction in the last section, we start by investigating the regulator dependence. To that end we varied the cutoff and regulator exponent for both values of  $c_D$  in fig. 6.6, with the same strength of the four-body interaction as in the last section. We also perform the analysis for convergence and the perturbative inclusion of the 4N interaction in exactly the same way, results are depicted in fig. 6.7.

Overall, the trends and general behavior are identical to the EM/N500 interaction. The overall effect of the 4N contact interaction is a little bit stronger and it differs between the two  $c_D$  values, yielding a stronger effect for  $c_D = 0$  than for the  $c_D = 4$  three-body interaction. The peaks in figs. 6.6(a) and 6.6(b) are a little wider and shifted to higher cutoff momenta. In fig. 6.6(d) we see relatively small effects for the  $c_D = 4$  results at very large cutoffs, however, these results are extremely far from convergence, which is apparent from fig. 6.7(b). The convergence generally seems to be slightly better in the EM/N500 case for smaller cutoffs. Nevertheless, in both cases convergence rapidly deteriorates starting from  $\mathcal{A}_{4B} = 500$  MeV.

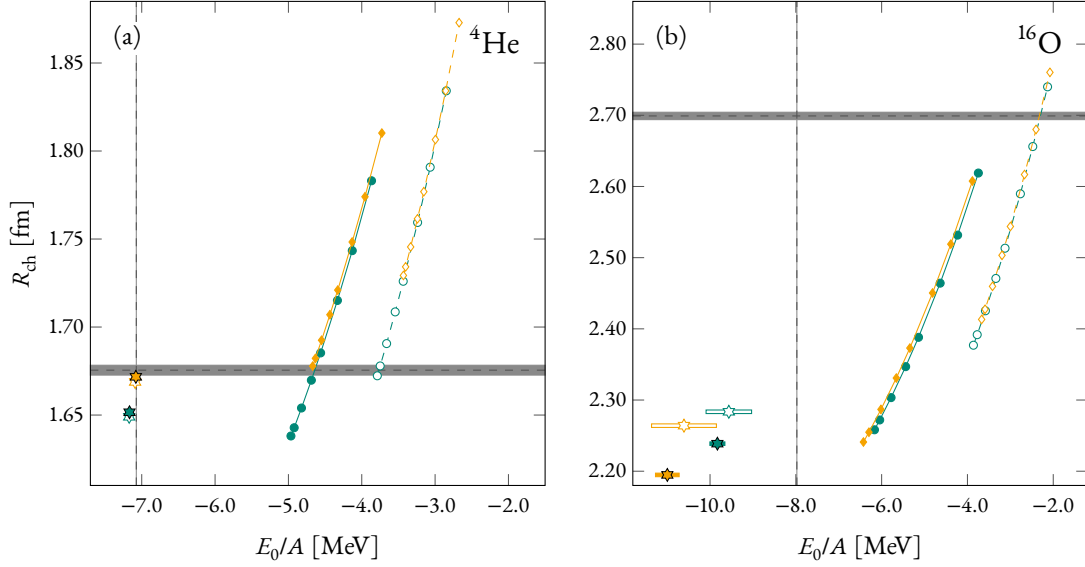
Due to the very similar behavior with respect to regulator parameters, we choose the same parameters as in the previous case, an exponent of  $n_{\text{exp}} = 2$  and a cutoff of  $\mathcal{A}_{4B} = 300$  MeV. Using this interaction, we can perform HF calculations again, focusing on  ${}^4\text{He}$  and  ${}^{16}\text{O}$ , as shown in fig. 6.8. Note that the quasi-exact results obtained with a NCSM calculation show the same trend as for EM/N500. We have almost no flow parameter dependence for  ${}^4\text{He}$ , and it is very close to the experimental value, but  ${}^{16}\text{O}$  is overbound. That is, the ground-state energy is too low and the charge radius is too small. The calculations hint at a flow parameter dependence  ${}^{16}\text{O}$ , which suggests that the induced many-body forces are repulsive in case of  ${}^{16}\text{O}$ . However, the NCSM results are far from convergence for  ${}^{16}\text{O}$ , especially for  $\alpha = 0.02 \text{ fm}^4$ . The extrapolations for the ground-state energies overlap for the different flow parameters, and the difference for the radii



**Figure 6.6:** Effect of the four-body contact interaction on the ground-state energy of  ${}^4\text{He}$  in NCSM calculations for different cutoffs and regulator exponents. The calculations employ a truncation of  $N_{\text{max}} = 20$  and a HO frequency of  $\hbar\omega = 20$  MeV. For two- and three-body sector the SMS/H500 interaction has been SRG-evolved to  $\alpha = 0.04 \text{ fm}^4$ . We show results for  $c_D = 0$  (left side) and  $c_D = 4$  (right side), with a regulator exponent  $n_{\text{exp}}$  for the contact interaction of 2 (lightest line), 4, 6, and 8 (darkest lines). Figures (a) and (b) depicts a repulsive force with  $c_{4B} = 1000 \text{ GeV}^{-8}$  and in figures (c) and (d) the attraction of the interaction is scaled by using  $c_{4B} = -\frac{200 \text{ GeV}^{-7}}{A_{4B}}$ .



**Figure 6.7:** Convergence of the ground-state energy of  ${}^4\text{He}$  in NCSM calculations with four-body contact interactions using different cutoffs. The calculations employ a regulator exponent of  $n_{\text{exp}} = 2$  and a HO basis with a frequency of  $\hbar\omega = 20$  MeV. For two- and three-body sector the SMS/H500 interaction has been SRG-evolved to  $\alpha = 0.04 \text{ fm}^4$ . We show results for  $c_D = 0$  ( $\circ$ ,  $\bullet$ ,  $\square$ ,  $\blacksquare$ ,  $\circ$ ) and  $c_D = 4$  ( $\square$ ,  $\blacksquare$ ,  $\square$ ,  $\blacksquare$ ,  $\square$ ) at  $N_{\text{max}}$  of 12 (lightest solid line), 14, 16, 18, and 20 (darkest solid line). Additionally, calculations without four-body interaction at  $N_{\text{max}} = 20$  are included, estimating the four-body contribution using first-order perturbation theory (dashed lines). Figure (a) depicts a repulsive force with  $c_{4B} = 1000 \text{ GeV}^{-8}$  and in figure (b) the attraction of the interaction is scaled by using  $c_{4B} = -\frac{200 \text{ GeV}^{-7}}{\Lambda_{4B}}$ .

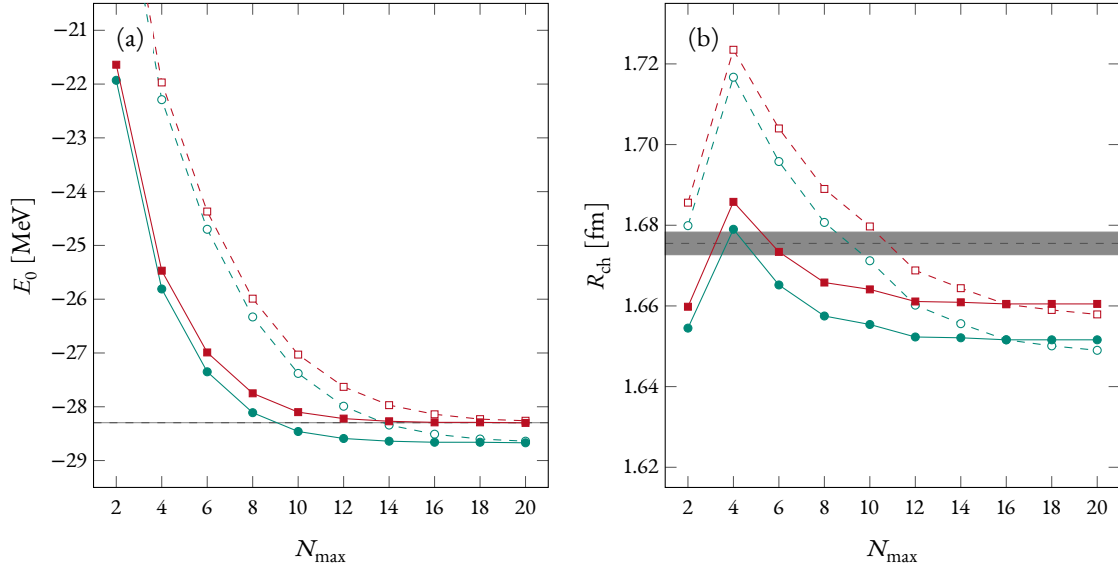


**Figure 6.8:** Ground-state energy and radius of  ${}^4\text{He}$  (a), and  ${}^{16}\text{O}$  (b), in HF calculations at  $\ell_{\text{max}} = 10$ . For the two- and three-body sector the SMS/H500 interaction has been SRG-evolved to flow parameters of  $\alpha = 0.02 \text{ fm}^4$  ( $-\circ-$ ,  $-\diamond-$ ), and  $\alpha = 0.04 \text{ fm}^4$  ( $-\bullet-$ ,  $-\blacklozenge-$ ). For the three-body interaction we show results for  $c_D = 0.0$  ( $-\bullet-$ ,  $-\circ-$ ) and  $c_D = 4.0$  ( $-\blacklozenge-$ ,  $-\diamond-$ ). A repulsive contact interaction is added with a strength of  $c_{4B} = 0, 300, 1000, 2000, 3000, 5000, 7000, 10000 \text{ GeV}^{-8}$ . All calculations employ a regulator exponent of  $n_{\text{exp}} = 2$ , a cutoff of  $\mathcal{A}_{4B} = 300 \text{ MeV}$ , and a HO basis with a frequency of  $\hbar\omega = 20 \text{ MeV}$ . Dashed lines with gray bands are experimental results and uncertainties. Stars correspond to NCSM calculations, with  $\alpha = 0.02 \text{ fm}^4$  for open stars and  $\alpha = 0.04 \text{ fm}^4$  for filled ones. Bands in the  ${}^{16}\text{O}$  case are spanned by extrapolations of the ground-state energy, see text for details. SRG-induced contributions to the radius are included at the two-body level for the NCSM calculations.

is small. We therefore cannot reliably extract the effect of the neglected induced contributions, in fact, the flow parameter dependence may change or even disappear for larger model spaces. For investigating  ${}^{16}\text{O}$ , larger flow parameters might be necessary. Note that in comparison to experiment, the  $c_D = 0$  interaction seems to fare better for  ${}^{16}\text{O}$ , exactly the opposite when compared to the  ${}^4\text{He}$  case. However, judging from the charge radii, the flow parameter dependence is stronger for the  $c_D = 0$  interaction, which might explain the additional overbinding compared to the  $c_D = 4$  case.

For HF calculations performed for  ${}^4\text{He}$ , we see an almost linear trend again, which is not completely true for  ${}^{16}\text{O}$ . The trends for different values of  $\alpha$  or  $c_D$  are similar, except for their starting point, of course. However, for  ${}^{16}\text{O}$ , the  $\alpha = 0.04 \text{ fm}^4$  lines are slightly more curved than the  $\alpha = 0.02 \text{ fm}^4$  ones and for weak contact interactions, we obtain a stronger effect on the ground-state energy in the  $\alpha = 0.04 \text{ fm}^4$  case compared to  $\alpha = 0.02 \text{ fm}^4$ .

Although the contact interaction would slightly reduce the flow parameter dependence in  ${}^{16}\text{O}$ , due to the different behavior for  $\alpha = 0.04 \text{ fm}^4$  and  $\alpha = 0.02 \text{ fm}^4$ , we cannot use the four-body interaction to imitate the induced four-body contributions. The effect on  ${}^{16}\text{O}$  is obviously too weak, and fitting different interactions for different flow parameters fails, as  ${}^4\text{He}$  is almost independent of the flow parameter. This is the same situation as in the case for the EM/N500 interaction. However, in the  $c_D = 0$  case, ground-state



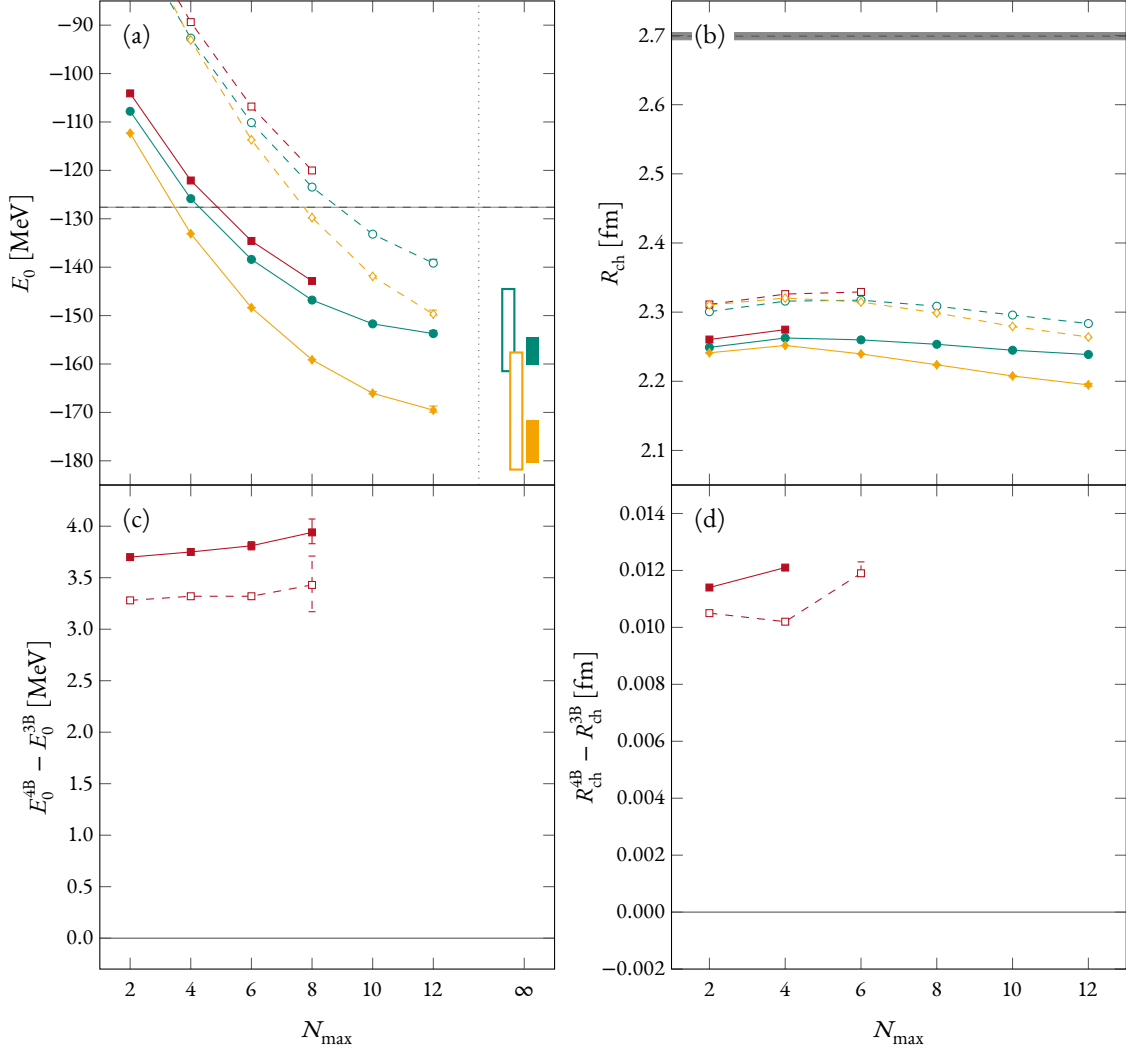
**Figure 6.9:** Ground-state energy (a) and charge radius (b) of  ${}^4\text{He}$  using the SRG-evolved SMS/H500 interaction at  $c_D = 0.0$  and a contact interaction at  $c_{4B} = 618 \text{ GeV}^{-8}$ . We show results for calculations without the contact interaction ( $-\circ-$ ,  $-\bullet-$ ) and with the four-body interaction added ( $-\square-$ ,  $-\blacksquare-$ ), where the dashed lines correspond to  $\alpha = 0.02 \text{ fm}^4$  and the solid ones to  $\alpha = 0.04 \text{ fm}^4$ . All calculations use a HO basis with a frequency of  $\hbar\omega = 20 \text{ MeV}$ . SRG-induced contributions to the radius are included at the two-body level. Experimental values and uncertainties are depicted using dashed lines and gray bands, respectively.

energy and charge radius are slightly too low. We can try to remedy that by fitting the strength of the 4N contact interaction to the experimental ground-state energy of  ${}^4\text{He}$ . As the dependence on  $\alpha$  is minimal, we do not differentiate between the two  $\alpha$  values and use  $\alpha = 0.04 \text{ fm}^4$  for the fitting procedure. The resulting strength is  $c_{4B} = 618 \text{ GeV}^{-8}$ .

Using the fitted contact interaction, we investigate it using NCSM calculations for  ${}^4\text{He}$  and  ${}^{16}\text{O}$ . We first verify that our choice indeed performs as expected in  ${}^4\text{He}$ , which is shown in fig. 6.9. The ground-state energy is depicted in fig. 6.9(a), which now yields exactly the experimental result. As expected, we also shifted the charge radius, which is closer to the experimental value, as seen in fig. 6.9(b). However, it is still below the results for  $c_D = 4$ . The net effect for the  $c_D = 0$  case is the removal of the one-pion exchange in the chiral three-body force at  $\text{N}^2\text{LO}$  and its replacement with a 4N contact interaction. Even though we used a low cutoff, effectively smearing out the contact interaction, the three-body one-pion exchange seems to have a larger effect on the radius for the same effect on the ground-state energy.

The general convergence behavior is not changed when adding the contact interaction, however the repulsive effect of the interaction increases slightly for larger values of  $N_{\text{max}}$ . When interested in the difference between a calculation with and without the four-body contact interaction, even lower values of  $N_{\text{max}}$  give a reasonable result.

As predicted from the HF calculation, different  $\alpha$  values do not change the effect of the contact interaction in  ${}^4\text{He}$ . The energies are still independent of  $\alpha$ , and the difference between  $\alpha = 0.02 \text{ fm}^4$  and



**Figure 6.10:** Ground-state energy (a) and charge radius (b) of  $^{16}\text{O}$ , as well as differences between a calculation with and without the four-body contact interaction for the energy (c) and charge radii (d). For the two- and three-body sector the SMS/H500 interaction has been SRG-evolved to  $\alpha = 0.02 \text{ fm}^4$  (dashed lines) and to  $\alpha = 0.04 \text{ fm}^4$  (solid lines). We show results without four-body interaction at  $c_D = 0$  ( $-\circ-$ ,  $-\bullet-$ ), and at  $c_D = 4$  ( $-\diamond-$ ,  $-\blacklozenge-$ ), as well as results with the contact interaction at  $c_{4B} = 618 \text{ GeV}^{-8}$  and  $c_D = 0$  ( $-\square-$ ,  $-\blacksquare-$ ). All calculations use a HO basis with a frequency of  $\hbar\omega = 20 \text{ MeV}$ . Uncertainties of individual calculations stem from the extrapolation to vanishing importance threshold. SRG-induced contributions to the radius are included at the two-body level. Experimental values and uncertainties are depicted using dashed lines and gray bands, respectively. Bands at  $N_{\text{max}} = \infty$  are spanned by extrapolations using the last three to six data points, see text for details. Open bars correspond to  $\alpha = 0.02 \text{ fm}^4$ , filled ones to  $\alpha = 0.04 \text{ fm}^4$ .

$\alpha = 0.04 \text{ fm}^4$  for the charge radii is unchanged when adding the contact interaction.

The results obtained for  $^{16}\text{O}$  from NCSM calculations are shown in fig. 6.10. Note that including a 4N interaction reduces the maximum  $N_{\text{max}}$  we can calculate, which is limited by the memory required to store the 4N interaction. However, the difference between a calculation with and one without 4N forces is sufficient to estimate the effect.

As expected from the HF calculations, the flow parameter dependence can only be slightly reduced by adding a weak contact interaction. Nonetheless, we do achieve a repulsive effect that pushes the energy and charge radius in the right direction, although the effect on the charge radius is extremely small. However, we still obtain an overbound  $^{16}\text{O}$  nucleus, the effect of the contact interaction is much too weak to change that. This is not surprising, as the HF calculation already predicts that the contact interaction does not scale strongly with the number of nucleons, even though we do see a larger effect in terms of binding energy per nucleon for  $^{16}\text{O}$  compared to  $^4\text{He}$ .

While the contact interaction is obviously unfit to reproduce effects of an SRG-induced four-body interaction, it might be used to improve shortcomings of the initial interaction. However, in the  $^{16}\text{O}$  case the effect of the induced contributions is difficult to estimate, as we are not able to obtain fully converged results. The relatively small  $\alpha$  dependence of the radii suggest that even the initial interaction would yield charge radii that are too small. Nevertheless, the contact interaction we employ here is too weak to remedy that. Note that using a four-body contact interaction breaks with the prescription of chiral EFT, which predicts the four-body contact term to be at  $N^5\text{LO}$ , which should only yield a very weak effect. Furthermore, for such a case, it might be more practical to modify the two- or three-body interaction, as the inclusion of 4N contributions in a many-body calculation is not always possible and generally requires more computational effort.

A four-body interaction that has small or no contributions in the  $J^\pi = 0^+$  channel and scales strongly with the number of nucleons might be able to mimic the omitted four-body contributions. Of course, this warrants the use of four-body forces again, and a computationally more efficient approach might be the use of different generators that yield less induced many-body contributions in the first place. However, if no such generator can be found, the use of a simple 4N interaction might be a viable alternative to a computationally demanding SRG evolution in four-body space.





# 7

## Effects of the Chiral 4N Interaction

After deriving and implementing the PWD of the chiral 4N interaction, we are now in the position to investigate its effects on nuclei. There has already been work done with chiral 4N forces, for instance by Nogga *et al.* [36], investigating its effect on  ${}^4\text{He}$ . In this case two- and three-body interactions were used to obtain the  ${}^4\text{He}$  ground state by solving Faddeev-Yakubovsky equations. Then the effect of the 4N interaction is estimated by using first-order perturbation theory. The evaluation of the expectation value includes the transformation from the partial-wave basis to a single-particle basis, which is done by using Monte Carlo integration. Furthermore, the chiral 4N interaction has been studied by Tews *et al.* [32], Krüger *et al.* [33], and Kaiser *et al.* [34], who have applied it to neutron and symmetric nuclear matter. The effect of the 4N contributions has been evaluated at the HF level using single-particle coordinates in these cases. In all these investigations the effect of the chiral 4N interaction turned out to be very small. However, previous investigations of the SRG-induced four-body force [60, 126] show a strong scaling with the number of nucleons and so far, the effect of the initial chiral 4N interaction has not been investigated in heavier nuclei. Thus, the main question for this chapter is the scaling behavior and the relevance of the 4N interaction in nuclei heavier than  ${}^4\text{He}$ .

Before we can discuss this question, we first have to investigate the effect of various parameters on the 4N interaction. We start with purely technical aspects in section 7.1, namely the parameters of the momentum grids we introduced in section 4.4.3. Furthermore, we investigate the convergence of the many-body methods in section 7.2. Afterwards, we have a closer look at the different classes that constitute the 4N interaction in section 7.3 and we vary the four-body regulator we use in section 7.4. The behavior of the 4N

interaction for different cutoffs is also investigated using a perturbative inclusion of the 4N contributions, which is discussed in section 7.5.

After these sections, we use the four-body force for nuclear structure investigations. We start by analyzing the four-body angular-momentum channels in section 7.6 and continue with a HO frequency variation in section 7.7. Both of these sections yield valuable insights on the convergence behavior of the interaction and allow us to analyze its relevance in section 7.8.

Note that the calculations performed throughout this chapter have a harsh limit on the four-body model-space size, that is, the maximum HO energy  $E_{4,\max}$  is typically limited to 2 or 4. The only exception are a few  ${}^4\text{He}$  results with a truncation of  $E_{4,\max} = 6$ , which is possible because we only need one four-body channel in this case. The reason for this truncation is the complexity and computational cost of the four-body PWD. Even though we use such a low truncation, the calculations presented in this chapter take well over a million core-hours of computing time on the Lichtenberg high performance computer at the TU Darmstadt, which is a state-of-the-art computer cluster. Most of the computing time has been spent constructing the interaction for the various parameters we investigate throughout this chapter.

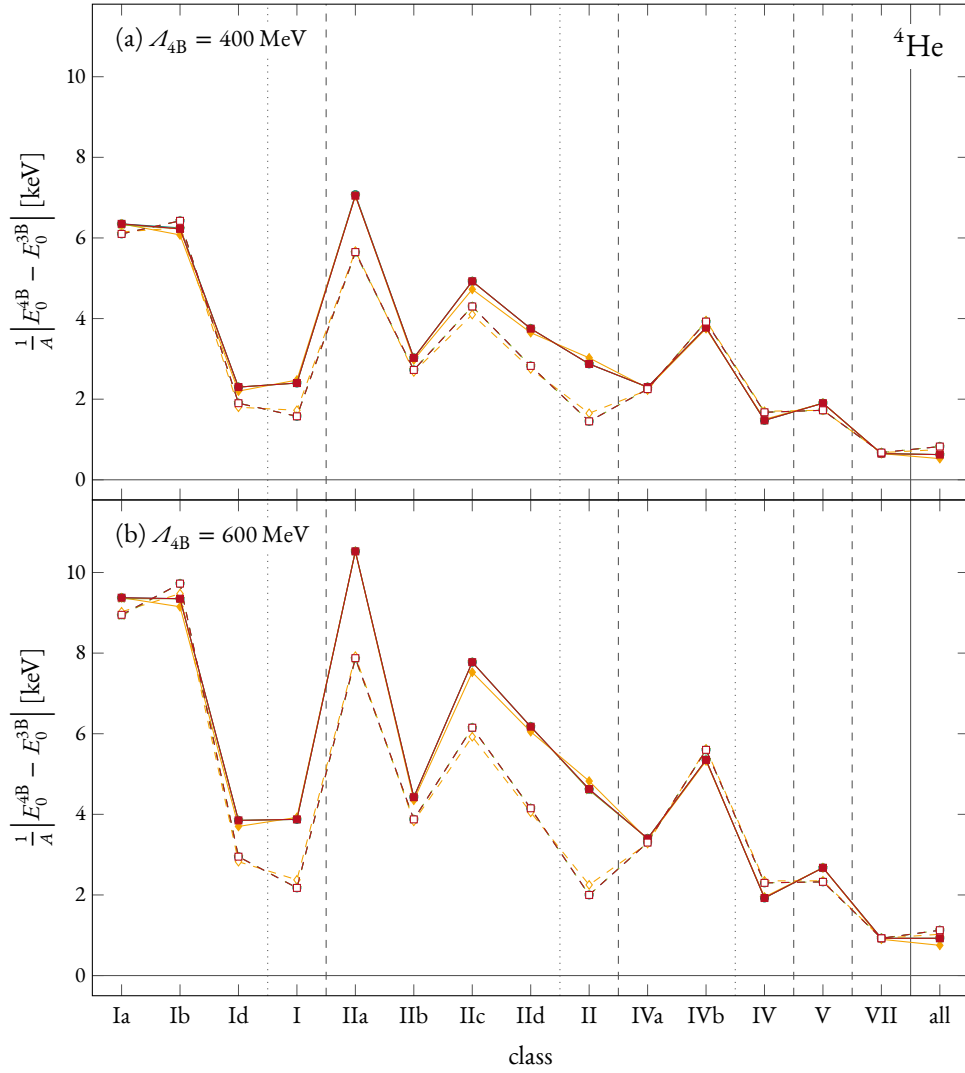
All calculations performed in this chapter use the EM/N400 interaction for the two- and three-body sector, for details on the interaction see section 2.5. This interaction has been softened using the SRG, where we fully include all bare and induced contributions up to the three-body level, with flow parameters of  $\alpha = 0.04 \text{ fm}^4$  and  $\alpha = 0.08 \text{ fm}^4$ . Note that the chiral 4N interaction has not been transformed.

## 7.1 MOMENTUM GRIDS

As we are using precalculated grids to perform the PWD, as described in section 4.4.3, we have a set of purely technical parameters, namely the number of grid points and the interpolation scheme for both, the interaction and the basis grid. Throughout this section we investigate the effect of these parameters on the calculated ground-state energy of various nuclei. From the results presented in this section we can argue that  $20^3$  grid points with cubic interpolation for the interaction part and 250 grid points with linear interpolation for the basis part yields a highly accurate discretization of the momentum expressions.

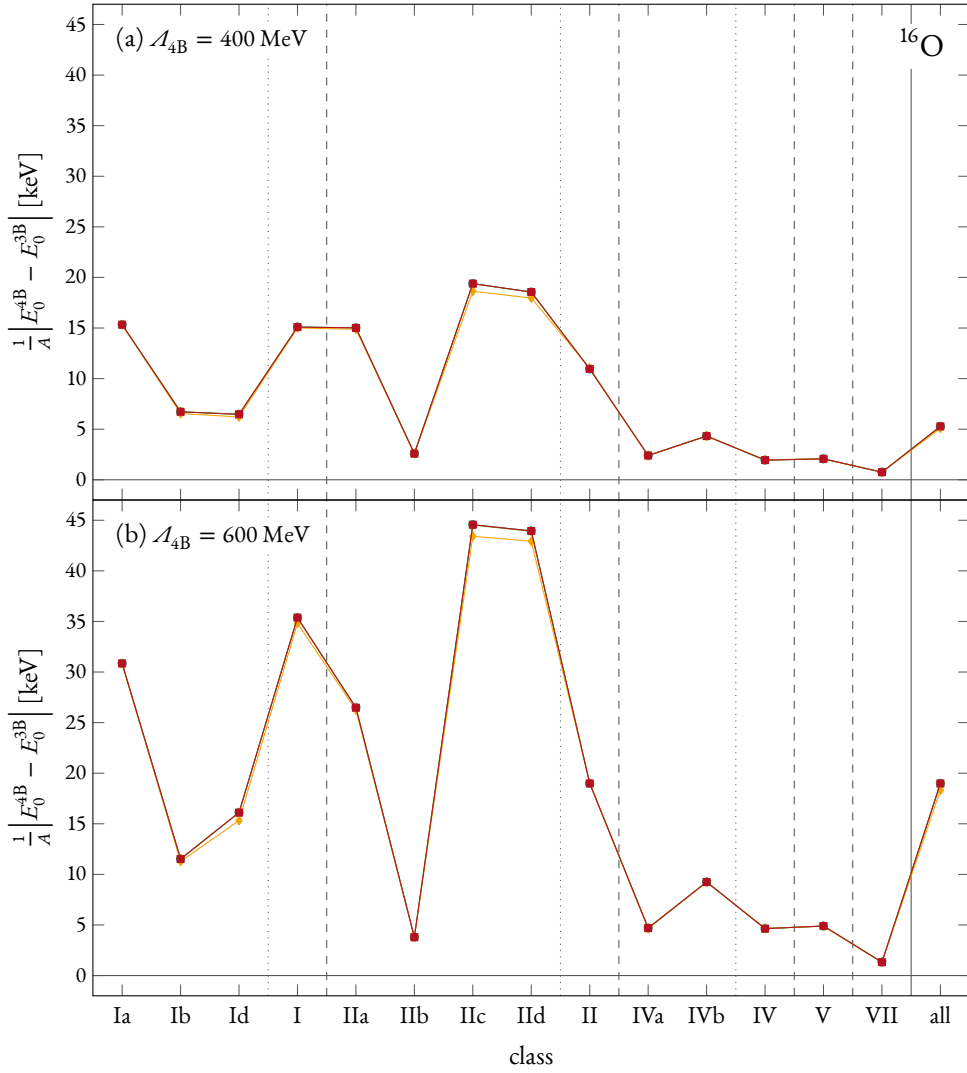
To test these grids we have performed many-body calculations yielding ground-state energies of different nuclei for various grid sizes and interpolation schemes and plot the effect of the 4N interaction for the various classes and substructures in figs. 7.1 to 7.4. In all cases we have performed HF calculations, in the case of  ${}^4\text{He}$  in fig. 7.1, we have also performed NCSM calculations, which directly show that HF calculations yield similar results. Note that each point is a separate calculation, for example, the result for class I is obtained by summing up the matrix elements and then performing a HF or NCSM calculation. In each figure, we have varied the technical parameters used in the discretization and find that the deviations between these parameter sets is minimal.

When increasing the number of grid points for the interaction part from  $20^3$  to  $30^3$ , no difference in



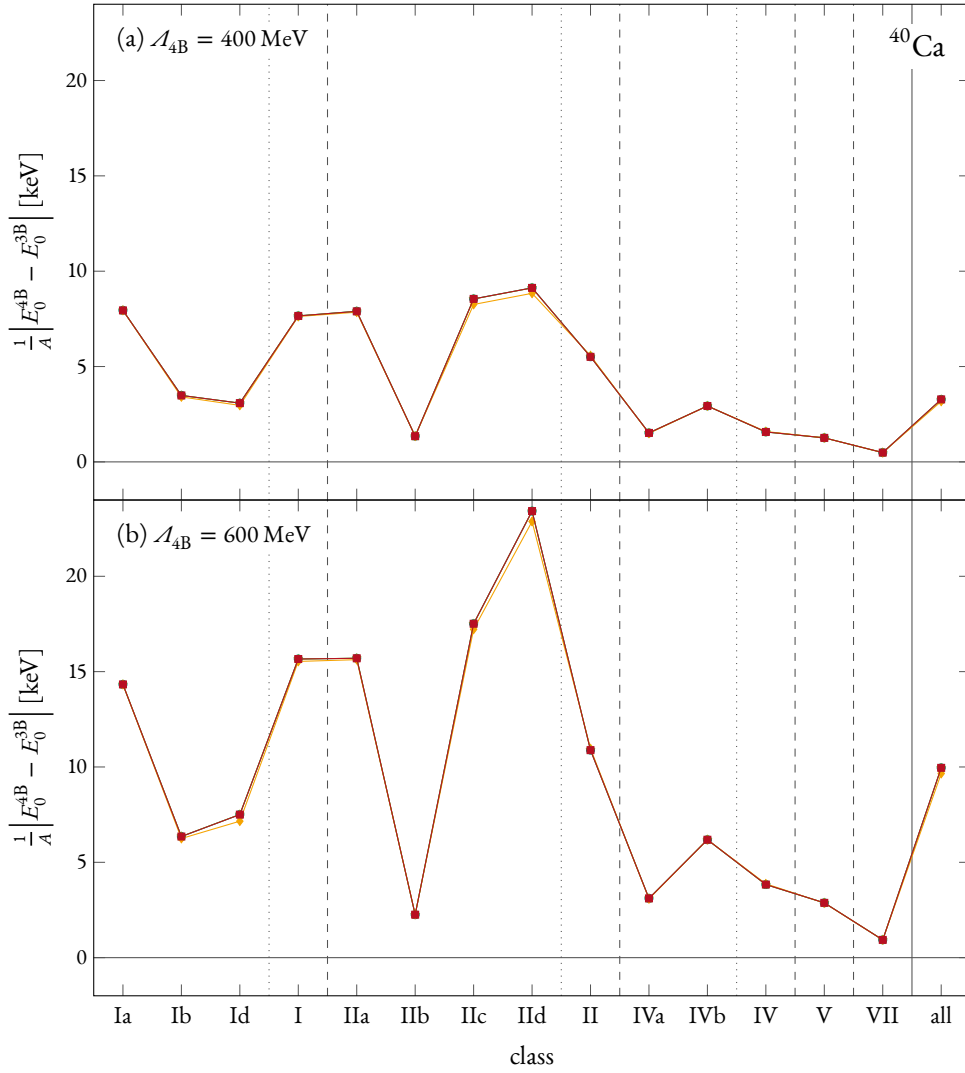
**Figure 7.1:** Absolute effect of the chiral four-body interaction on the ground-state energy for different classes and varying grid parameters in  ${}^4\text{He}$ . Solid lines are NCSM calculations at  $N_{\text{max}} = 20$  and dashed lines are HF calculations at  $e_{\text{max}} = 10$ . All calculations employ a HO basis with a frequency of  $\hbar\omega = 24$  MeV. In the two- and three-body sector the EM/N400 interaction has been SRG-evolved to a flow parameter of  $\alpha = 0.08 \text{ fm}^4$ . The four-body force uses  $C_T = 0.21 \text{ fm}^2$ , a regulator exponent of  $n_{\text{exp}} = 4$  and it is truncated at  $E_{4,\text{max}} = 2$ . The cutoff is fixed to  $\mathcal{A}_{4B} = 400$  MeV in (a) and  $\mathcal{A}_{4B} = 600$  MeV in (b). Different colors and symbols correspond to different parameters of the basis and interaction grid, which are:

- ( $\bullet$ ,  $\circ$ ) Interaction grid:  $20^3$  points, cubic interpolation. Basis grid: 200 points, linear interpolation.
- ( $\blacksquare$ ,  $\square$ ) Interaction grid:  $20^3$  points, cubic interpolation. Basis grid: 250 points, linear interpolation.
- ( $\blacklozenge$ ,  $\lozenge$ ) Interaction grid:  $20^3$  points, linear interpolation. Basis grid: 250 points, linear interpolation.
- ( $\blackstar$ ,  $\star$ ) Interaction grid:  $30^3$  points, cubic interpolation. Basis grid: 250 points, linear interpolation.



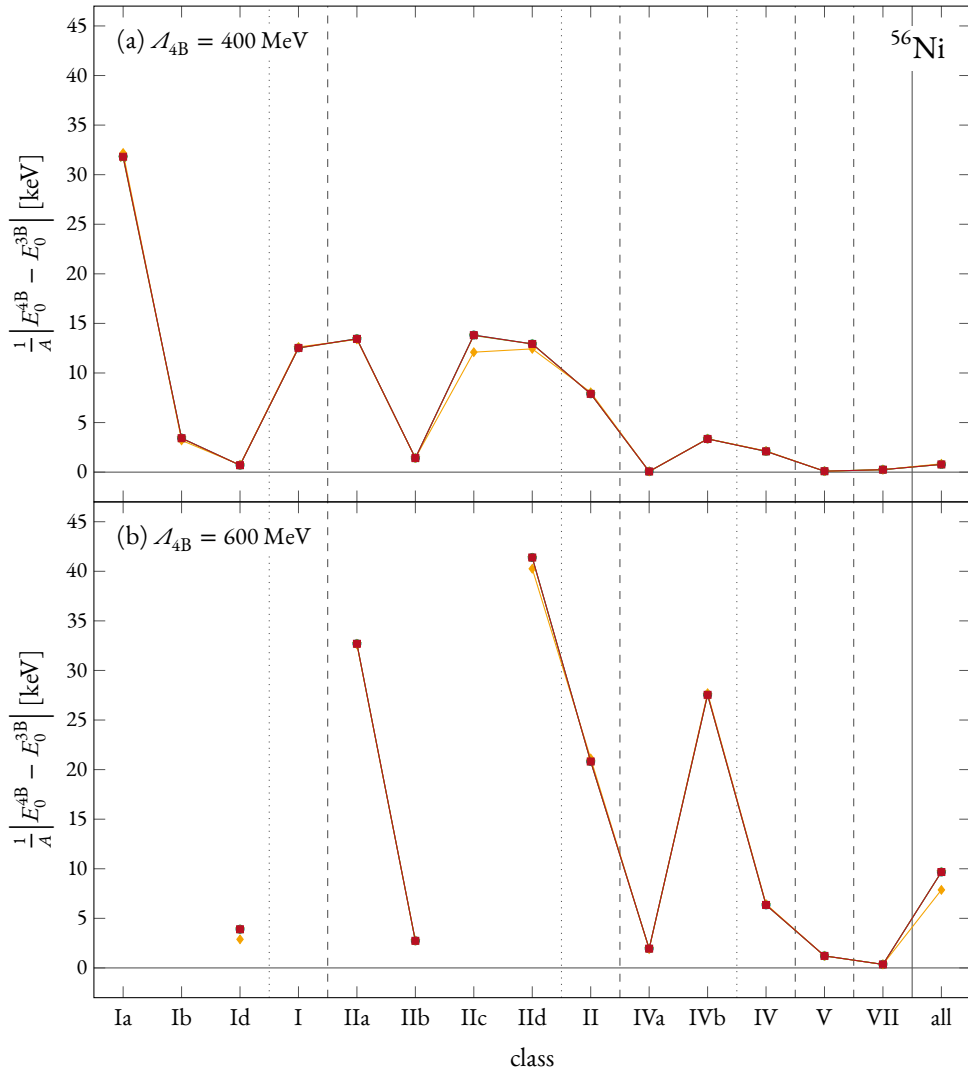
**Figure 7.2:** Absolute effect of the chiral four-body interaction on the ground-state energy for different classes and varying grid parameters in  $^{16}\text{O}$ . All results are HF calculations at  $e_{\max} = 10$  employing a HO basis with a frequency of  $\hbar\omega = 24$  MeV. In the two- and three-body sector the EM/N400 interaction has been SRG-evolved to a flow parameter of  $\alpha = 0.08$  fm $^4$ . The four-body force uses  $C_T = 0.21$  fm $^2$ , a regulator exponent of  $n_{\text{exp}} = 4$  and it is truncated at  $E_{4,\text{max}} = 2$ . The cutoff is fixed to  $\mathcal{A}_{4B} = 400$  MeV in (a) and  $\mathcal{A}_{4B} = 600$  MeV in (b). Different colors and symbols correspond to the same grid parameters as in fig. 7.1, which are:

- (—●—) Interaction grid:  $20^3$  points, cubic interpolation. Basis grid: 200 points, linear interpolation.
- (—■—) Interaction grid:  $20^3$  points, cubic interpolation. Basis grid: 250 points, linear interpolation.
- (—♦—) Interaction grid:  $20^3$  points, linear interpolation. Basis grid: 250 points, linear interpolation.
- (—★—) Interaction grid:  $30^3$  points, cubic interpolation. Basis grid: 250 points, linear interpolation.



**Figure 7.3:** Absolute effect of the chiral four-body interaction on the ground-state energy for different classes and varying grid parameters in  $^{40}\text{Ca}$ . All results are HF calculations at  $\epsilon_{\max} = 10$  employing a HO basis with a frequency of  $\hbar\omega = 24$  MeV. In the two- and three-body sector the EM/N400 interaction has been SRG-evolved to a flow parameter of  $\alpha = 0.08 \text{ fm}^4$ . The four-body force uses  $C_T = 0.21 \text{ fm}^2$ , a regulator exponent of  $n_{\text{exp}} = 4$  and it is truncated at  $E_{4,\text{max}} = 2$ . The cutoff is fixed to  $A_{4B} = 400$  MeV in (a) and  $A_{4B} = 600$  MeV in (b). Different colors and symbols correspond to the same grid parameters as in fig. 7.1, which are:

- (—●—) Interaction grid:  $20^3$  points, cubic interpolation. Basis grid: 200 points, linear interpolation.
- (—■—) Interaction grid:  $20^3$  points, cubic interpolation. Basis grid: 250 points, linear interpolation.
- (—◆—) Interaction grid:  $20^3$  points, linear interpolation. Basis grid: 250 points, linear interpolation.
- (—★—) Interaction grid:  $30^3$  points, cubic interpolation. Basis grid: 250 points, linear interpolation.



**Figure 7.4:** Absolute effect of the chiral four-body interaction on the ground-state energy for different classes and varying grid parameters in  $^{56}\text{Ni}$ . All results are HF calculations at  $e_{\max} = 10$  employing a HO basis with a frequency of  $\hbar\omega = 24$  MeV. In the two-and three-body sector the EM/N400 interaction has been SRG-evolved to a flow parameter of  $\alpha = 0.08$  fm $^4$ . The four-body force uses  $C_T = 0.21$  fm $^2$ , a regulator exponent of  $n_{\text{exp}} = 4$  and it is truncated at  $E_{4,\text{max}} = 2$ . The cutoff is fixed to  $\mathcal{A}_{4B} = 400$  MeV in (a) and  $\mathcal{A}_{4B} = 600$  MeV in (b). Different colors and symbols correspond to the same grid parameters as in fig. 7.1, which are:

- ( $\color{red}\blacktriangleleft$ ) Interaction grid:  $20^3$  points, cubic interpolation. Basis grid: 200 points, linear interpolation.
- ( $\color{red}\blacksquare$ ) Interaction grid:  $20^3$  points, cubic interpolation. Basis grid: 250 points, linear interpolation.
- ( $\color{orange}\blacktriangleright$ ) Interaction grid:  $20^3$  points, linear interpolation. Basis grid: 250 points, linear interpolation.
- ( $\color{green}\blacktriangleright$ ) Interaction grid:  $30^3$  points, cubic interpolation. Basis grid: 250 points, linear interpolation.

Using a cutoff of  $\mathcal{A}_{4B} = 600$  MeV, for some of the classes the HF calculation fails to find a bound state, thus, these results are not included in the figure.

the results can be found. However, there is a small deviation when changing the interpolation to a linear scheme in the interaction part, which indicates that the cubic interpolation converges faster with respect to the number of grid points, as one would expect. In principle, we could also use the linear interpolation for the interaction part, but this would require more grid points for the same level of accuracy. The calculation of the interaction part is the computationally most demanding step in the PWD, therefore, we exploit the cubic interpolation.

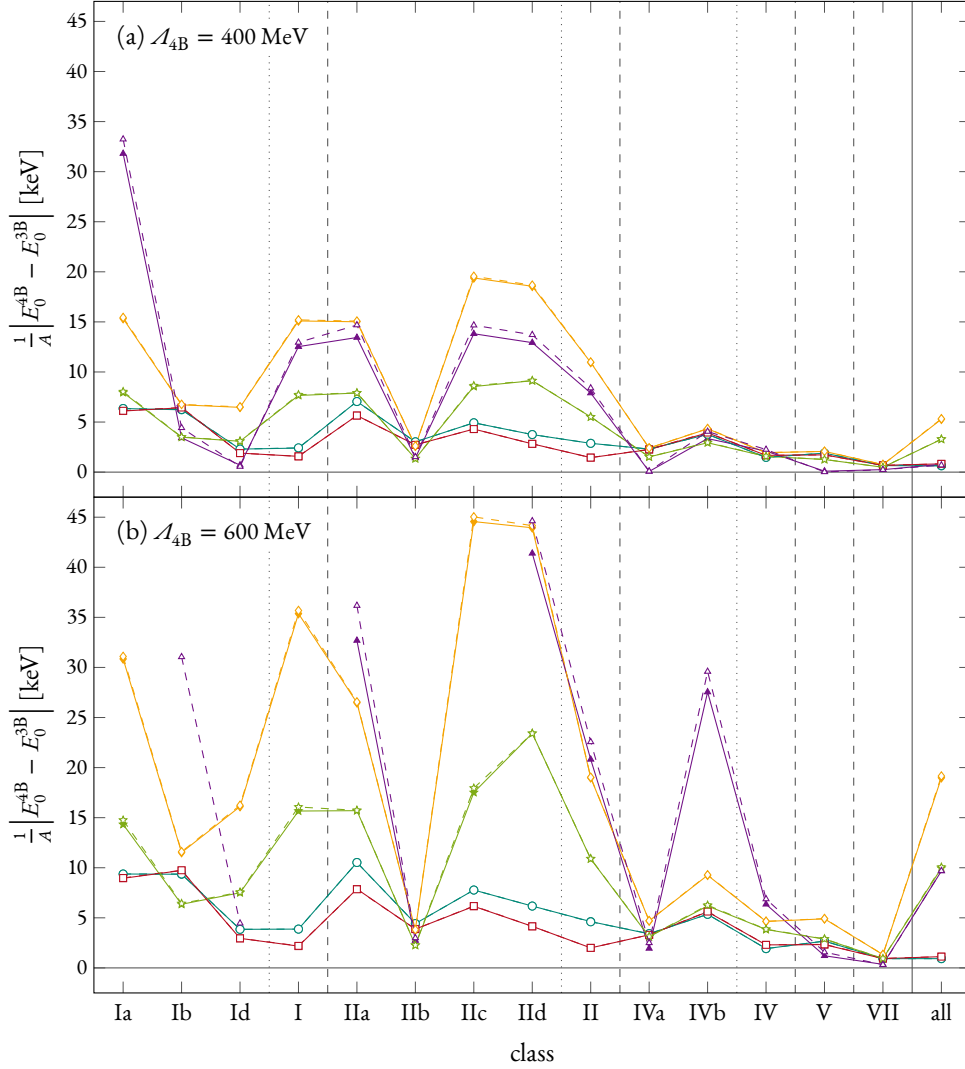
Reducing the number of grid points for the basis part or using the cubic interpolation does not change the results at all. In this case, we are well converged at 250 grid points, even with the linear interpolation. For the basis part, computational efficiency warrants the use of the linear interpolation, as the construction of the basis grids is cheap and the cubic interpolation would slow down the integration over the momenta. We therefore simply use a very high number of grid points.

Note that the analysis is true for all four figures, that is figs. 7.1 to 7.4. The nuclei, cutoffs, regulator exponent and the value for  $C_T$  is chosen to match calculations performed throughout the remainder of this chapter. In case of  $C_T$  we use the value from the two-body interaction. Note that this analysis only includes four-body forces up to  $E_{4,\max} = 2$ , as the construction of multiple interactions at higher  $E_{4,\max}$  requires too much computing time.

In fig. 7.4 we can observe an instability of the HF calculations, as for some classes the HF calculation fails to find a bound state. This only occurs in case of  $^{56}\text{Ni}$ . Calculating this nucleus without 4N contributions already results in an almost degenerate spectrum of the single-particle energies during the iteration procedure. Judging by these energies, it does not behave like a closed-shell nucleus, which is problematic for the HF approximation. Even the extremely small 4N interaction can push the spectrum to an unphysical state, where unoccupied single-particle states have an energy that is lower than some of the occupied states. In such a case the iterative solution of the HF equations may fail completely, and it does not produce a bound state. Note that this is a technical issue and might be circumvented by using a different scheme for solving the HF equations or even by using a different starting point for the iteration.

## 7.2 MODEL SPACE CONVERGENCE

Throughout this chapter we use HF calculations with  $e_{\max} = 10$  and Jacobi NCSM calculations for  $^4\text{He}$  with  $N_{\max} = 20$ . To check if the chosen model spaces are sufficient for the calculation of the effect of the 4N interaction, we investigate the model-space convergence. To that end we compare calculations in the chosen model space with calculations in slightly smaller model spaces, that is  $e_{\max} = 8$  for the HF calculations and  $N_{\max} = 18$  for the NCSM calculations. The results are summarized in fig. 7.5. The calculations have been performed for two cutoffs and all different classes, as well as for the combined interaction. In almost all cases we see no difference between the two model-space sizes. Only the  $^{56}\text{Ni}$  calculations is not completely converged with respect to the model-space size. However, the deviation is small, which indicated that the



**Figure 7.5:** Convergence of many-body methods with respect to the absolute effect of the chiral 4N interaction on the ground-state energy for different classes. The figure includes HF calculations at  $e_{max} = 8$  (dashed lines) and  $e_{max} = 10$  (solid lines) for  ${}^4\text{He}$  ( $-\square, -\blacksquare$ ),  ${}^{16}\text{O}$  ( $-\diamond, -\blacklozenge$ ),  ${}^{40}\text{Ca}$  ( $-\star, -\blackstar$ ), and  ${}^{56}\text{Ni}$  ( $-\triangle, -\blacktriangle$ ), as well as  ${}^4\text{He}$  NCSM calculations at  $N_{max} = 18$  ( $-\circ$ ) and  $N_{max} = 20$  ( $-\bullet$ ). All calculations employ a HO frequency of  $\hbar\omega = 24$  MeV and the included EM/N400 interaction has been SRG-evolved to a flow parameter of  $\alpha = 0.08$  fm $^4$ . The four-body force uses  $C_T = 0.21$  fm $^2$ , a regulator exponent of  $n_{exp} = 4$  and it is truncated at  $E_{4,max} = 2$ . The cutoff is fixed to  $\mathcal{A}_{4B} = 400$  MeV in (a) and  $\mathcal{A}_{4B} = 600$  MeV in (b). For  ${}^{56}\text{Ni}$  and  $\mathcal{A}_{4B} = 600$  MeV, the HF calculation fails to find a bound state for some of the classes, thus, these results are not included in the figure.



calculation is almost converged, and therefore, results for  $^{56}\text{Ni}$  are considered reliable. To be precise, we can assume the uncertainty from the convergence of the many-body method to be smaller than 1 % for all nuclei up to  $^{40}\text{Ca}$ , and up to 10 % in the  $^{56}\text{Ni}$  case.

Note that the instability of the HF solution depends on the actual value of  $e_{\text{max}}$ , as can be seen for class I in fig. 7.5. In cases where we observe the instability, the HF calculation fails completely and does not produce a ground state. We find no cases of a ground state with a binding energy that suddenly changes by a few MeV. This is also apparent from the convergence pattern in fig. 7.5, as calculations for  $e_{\text{max}} = 8$  and  $e_{\text{max}} = 10$  always agree, if a bound state is found for both truncations.

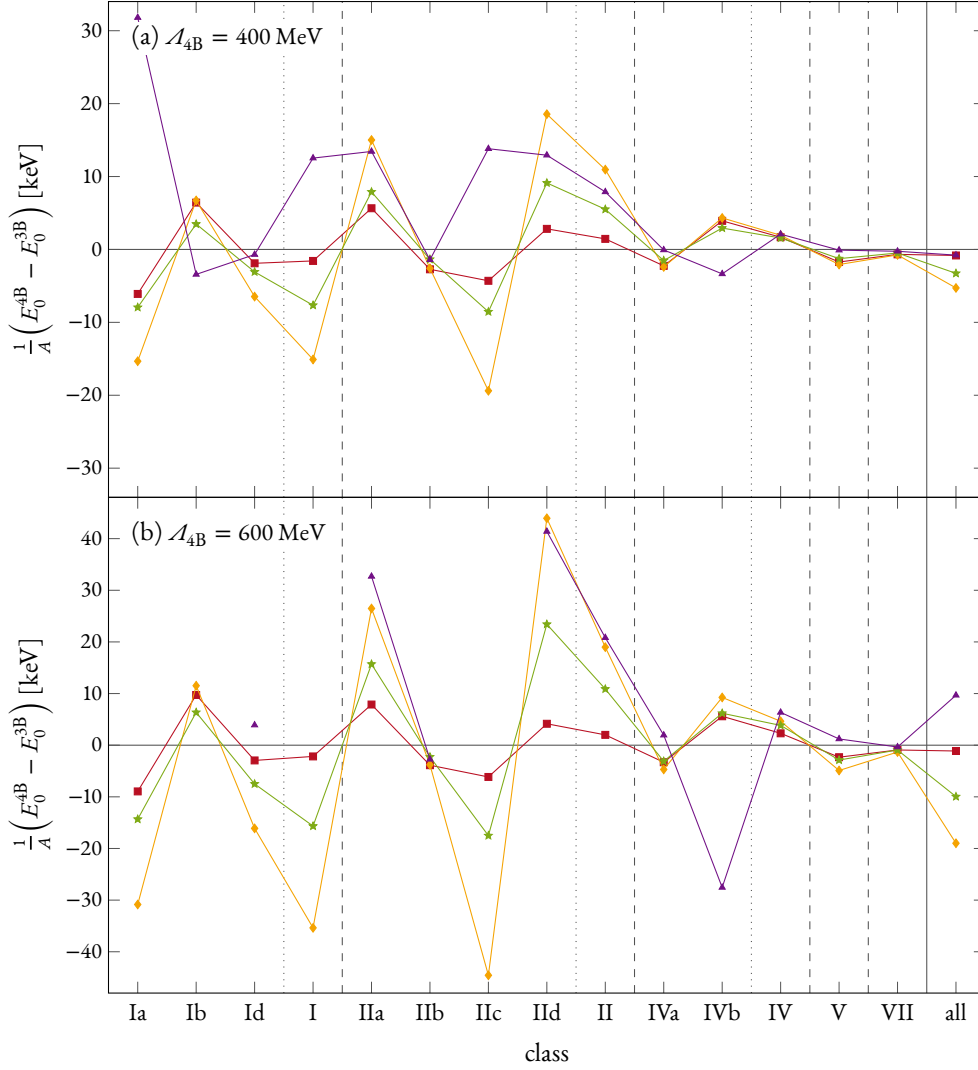
In all cases throughout this chapter we consider only the contribution from the four-body interaction, that is, the difference between a calculation with and without four-body forces, as done in fig. 7.5. In fact, the uncertainty of the ground-state energy due to the limited model-space size of the many-body calculation is much larger. The difference between a HF calculation at  $e_{\text{max}} = 8$  and  $e_{\text{max}} = 10$  usually is of the order of 1 – 50 keV per nucleon, which is on the same order as the contribution from the chiral 4N interaction. Luckily, the addition of the four-body interaction does not change the convergence pattern, resulting in the observed small uncertainties for the effect of the four-body contribution.

### 7.3 INTERACTION CLASSES

From the previous calculations we already see that the chiral four-body force has a rather weak effect, at least at the truncation of  $E_{4,\text{max}} = 2$ . In fact, the overall contribution is much smaller than contributions from the individual classes. This cancellation effect is depicted in fig. 7.6, where the different contributions are presented. In fact, multiple cancellation effects can be observed. First of all, the different substructures within a class tend to have different signs. Additionally, the resulting contributions for the five relevant classes also differ in sign and partly cancel each other, leading to a total effect that is much weaker than just the effect from a single class or substructure. These effects are especially pronounced for  $^4\text{He}$ , but exist in all nuclei shown in fig. 7.6.

Note that we perform a separate calculation for each class and substructure. This becomes apparent in the case of  $^{56}\text{Ni}$ , where summing up the individual contributions of the substructures does not yield the total contribution obtained from combining the matrix elements first and then performing the HF calculation. This already hints at the fact that a perturbative inclusion of the 4N contributions is insufficient in the case of  $^{56}\text{Ni}$ , which we discuss further in section 7.5. We will, therefore, exclude  $^{56}\text{Ni}$  from the analysis in this section, as reliably separating the contributions of different classes is not possible in this case.

When comparing  $^4\text{He}$ ,  $^{16}\text{O}$ , and  $^{40}\text{Ca}$ , we observe that the signs of the different contributions are identical in all cases. This is slightly surprising, as different nuclei contain different angular momentum and isospin structures, which could lead to a different behavior of the same class in different nuclei. Especially so, as  $^4\text{He}$  only probes one of the many four-body channels. Note that the calculations in fig. 7.6 include all



**Figure 7.6:** Contributions of different classes of the chiral four-body interaction to the ground-state energy of different nuclei. The figure includes HF calculations at  $e_{max} = 10$  for  ${}^4\text{He}$  ( $\blacksquare$ ),  ${}^{16}\text{O}$  ( $\blacklozenge$ ),  ${}^{40}\text{Ca}$  ( $\blacklozenge$ ), and  ${}^{56}\text{Ni}$  ( $\blacktriangle$ ). All calculations employ a HO basis with a frequency of  $\hbar\omega = 24$  MeV and the EM/N400 interaction for the two- and three-body sector has been SRG-evolved to a flow parameter of  $\alpha = 0.08$  fm $^4$ . The four-body force uses  $C_T = 0.21$  fm $^2$ , a regulator exponent of  $n_{exp} = 4$  and it is truncated at  $E_{4,max} = 2$ . The cutoff is fixed to  $\mathcal{A}_{4B} = 400$  MeV in (a) and  $\mathcal{A}_{4B} = 600$  MeV in (b).

possible channels at the  $E_{4,\max} = 2$  truncation. However, all these nuclei are closed-shell nuclei with the same number of protons and neutrons calculated in the HF approximation. This behavior might very well change for other cases.

The general trend shows opposite signs and similar size of the contributions from classes I and II, which are both completely independent from  $C_T$ . Contributions from classes IV and V are typically weaker than the first two classes, but they both depend on  $C_T$ , and therefore, their behavior depends on the value of  $C_T$ . However, they do have a different sign, which leads to an almost complete cancellation between these two classes. The contributions from class VII are small and attractive, and depend on  $C_T^2$ .

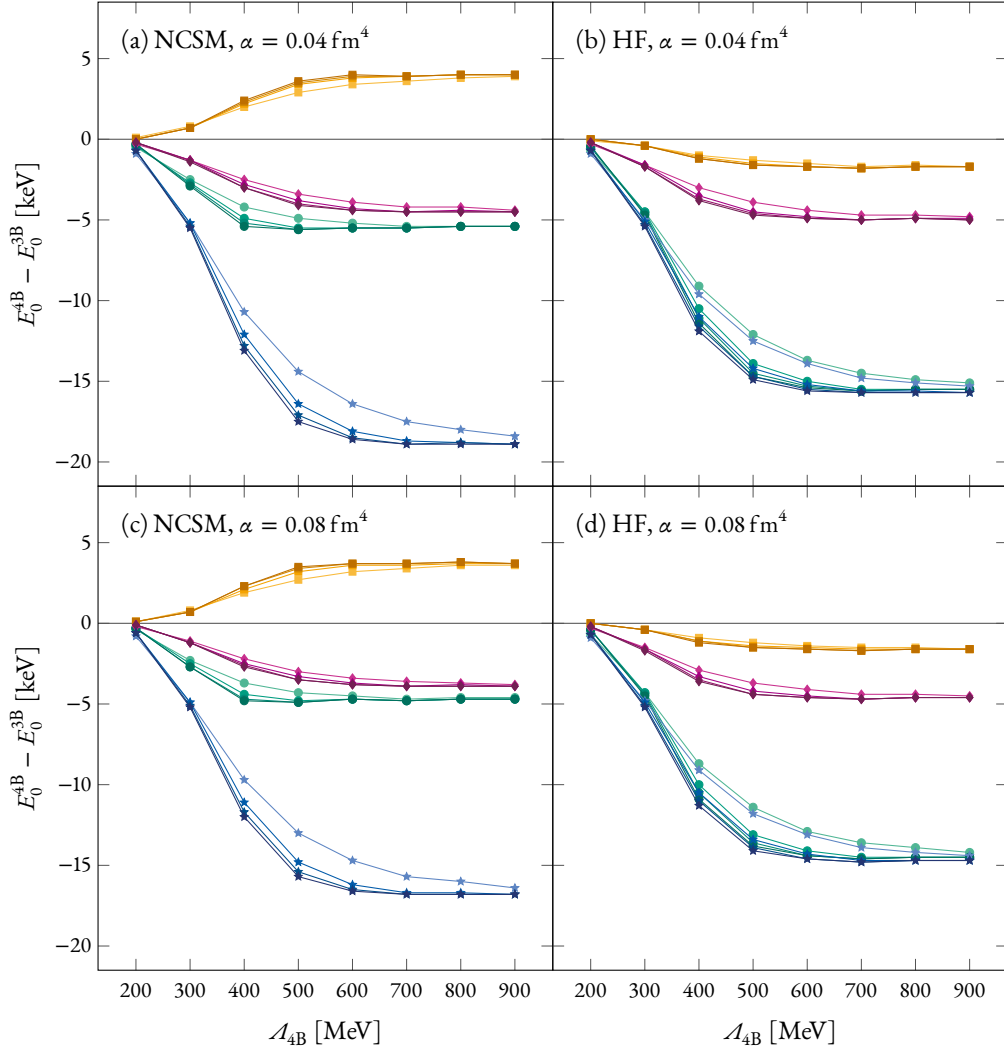
Previous calculations found similar trends in  ${}^4\text{He}$  [36] and symmetric nuclear matter [33]. The symmetric nuclear matter calculations by Krüger *et al.* [33] employ a range of NN interactions and the interaction by Entem and Machleidt [84], which we use here, is among them. Employing this interaction, the symmetric nuclear matter calculations show exactly the same trend we observe. The signs for all classes and the cancellation scheme between the classes match our calculations. Classes IV and V are also smaller than I and II in nuclear matter calculation and class VII yields the smallest results. The estimates for  ${}^4\text{He}$  by Nogga *et al.* [36] also show a weaker effect of classes IV, V, and VII compared to I and II. Furthermore, there is a cancellation between the different classes. However, the signs do not match the results presented here and, overall, our calculations yield much weaker effects of the chiral 4N interaction than the  ${}^4\text{He}$  estimates. Note that the calculations by Nogga *et al.* [36] differ from the ones presented here in various aspects, that is, the applied two- and three-body forces, the chosen regulator for the four-body force, and the many-body method, and therefore, truncations.

## 7.4 REGULATOR DEPENDENCE

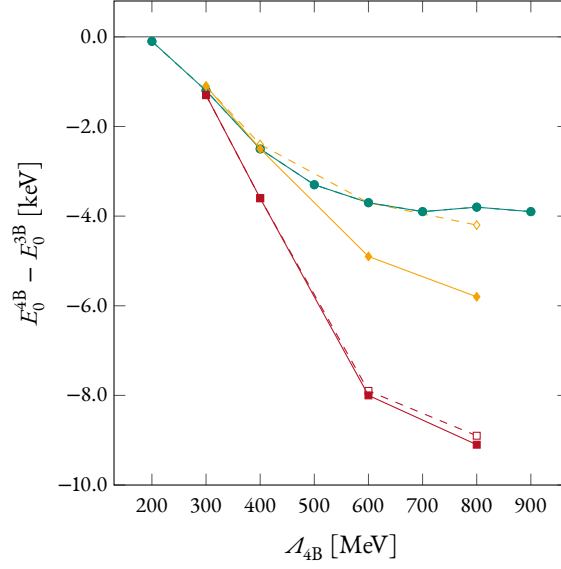
So far, we have only seen results at two fixed values for the cutoff and one specific value for the regulator exponent. To investigate the regulator behavior, HF and NCSM calculations have been performed for different regulator parameters. An overview is given in fig. 7.7 for  ${}^4\text{He}$  at  $E_{4,\max} = 2$ .

In all cases, the behavior is similar when changing the cutoff  $\mathcal{A}_{4B}$ . At a very low cutoff, the effect of the four-body force vanishes. In this case, the regulator removes contributions from the interaction at the relevant momentum scale, after all, lowering the cutoff only reduces the range of the momentum integration. Increasing the cutoff leads to a monotonic increase in the four-body contributions, with a steep increase at low cutoffs, which flattens out at higher cutoffs. This behavior is tied to the HO basis and the truncation we use. A representation of the HO states in momentum space has a Gaussian tail that acts as a built-in cutoff. Therefore all higher momenta included in the integration are irrelevant at this specific truncation.

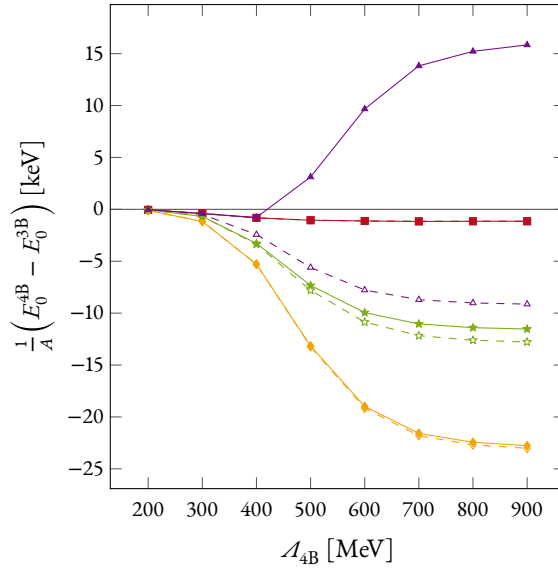
For higher values of  $E_{4,\max}$ , we cannot observe a flattening behavior up to  $\mathcal{A}_{4B} = 800$  MeV, as depicted in fig. 7.8. The HO wave functions simply extend to higher momenta in these cases, reducing the effect of the HO cutoff. This figure also nicely shows that convergence with respect to the four-body model-space



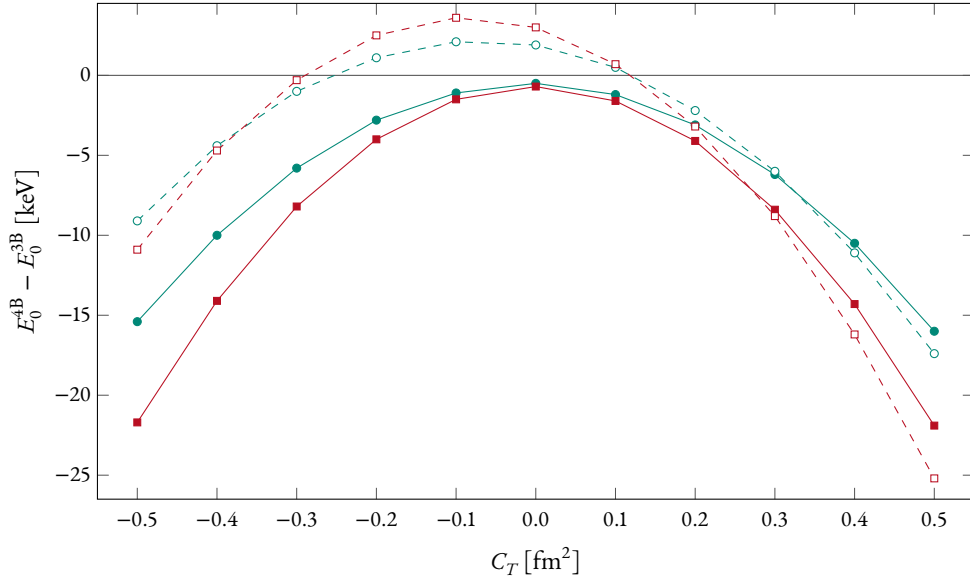
**Figure 7.7:** Contribution of the chiral 4N interaction to the ground-state energy of  ${}^4\text{He}$  for different four-body regulator parameters. For the two- and three-body sector, the SRG-evolved EM/N400 interaction is employed. Calculations are performed using the NCSM at  $N_{\text{max}} = 20$  with two flow parameters of  $\alpha = 0.04 \text{ fm}^4$  in (a), and  $\alpha = 0.08 \text{ fm}^4$  in (c). Additionally, HF calculations at  $e_{\text{max}} = 10$  are shown, again with flow parameters of  $\alpha = 0.04 \text{ fm}^4$  in (b), and  $\alpha = 0.08 \text{ fm}^4$  in (d). The four-body interactions are constructed with  $C_T = -0.4 \text{ fm}^2$  ( $\circ, \square, \diamond, \star$ ),  $C_T = -0.1 \text{ fm}^2$  ( $\circ, \square, \diamond, \star$ ),  $C_T = 0.21 \text{ fm}^2$  ( $\circ, \square, \diamond, \star$ ), and  $C_T = 0.4 \text{ fm}^2$  ( $\circ, \square, \diamond, \star$ ). Furthermore, the regulator exponent is varied using an exponent  $n_{\text{exp}}$  of 2 (lightest lines), 4, 6, and 8 (darkest lines). All calculations employ a HO basis with a frequency of  $\hbar\omega = 24 \text{ MeV}$ , and the four-body interaction is truncated at  $E_{4,\text{max}} = 2$ .



**Figure 7.8:** Contribution of the chiral 4N interaction to the ground-state energy of  ${}^4\text{He}$  for different four-body cutoffs and truncations. All calculations are performed using the NCSM at  $\mathcal{N}_{\text{max}} = 20$  with the EM/N400 interaction SRG-evolved to a flow parameter of  $\alpha = 0.08 \text{ fm}^4$ . The four-body interaction uses  $C_T = 0.21 \text{ fm}^2$  and a regulator exponent of  $n_{\text{exp}} = 4$ . Truncations of  $E_{4,\text{max}} = 2$  ( $\circ$ ,  $\bullet$ ),  $E_{4,\text{max}} = 4$  ( $\square$ ,  $\blacksquare$ ), and  $E_{4,\text{max}} = 6$  ( $\diamond$ ,  $\blacklozenge$ ) for the four-body interaction are shown. All calculations employ a HO basis with a frequency of  $\hbar\omega = 24 \text{ MeV}$ . Furthermore, all calculations are obtained using a full diagonalization (solid lines), and a diagonalization with two- and three-body forces only, approximating the four-body contribution using first-order perturbation theory (dashed lines).



**Figure 7.9:** Contribution of the chiral 4N interaction to the ground-state energy of  ${}^4\text{He}$  ( $\square$ ,  $\blacksquare$ ),  ${}^{16}\text{O}$  ( $\diamond$ ,  $\blacklozenge$ ),  ${}^{40}\text{Ca}$  ( $\star$ ,  $\blackstar$ ), and  ${}^{56}\text{Ni}$  ( $\triangle$ ,  $\blacktriangle$ ) for different four-body cutoffs. All calculations are performed using HF at  $e_{\text{max}} = 10$  with the EM/N400 interaction SRG-evolved to a flow parameter of  $\alpha = 0.08 \text{ fm}^4$ . In all cases a HO basis with a frequency of  $\hbar\omega = 24 \text{ MeV}$  is employed. The four-body interaction uses  $C_T = 0.21 \text{ fm}^2$ , a truncation of  $E_{4,\text{max}} = 2$ , and a regulator exponent of  $n_{\text{exp}} = 4$ . All results are obtained using a full HF calculation (solid lines), and a calculation with two- and three-body forces only, approximating the four-body contribution by first-order perturbation theory (dashed lines).



**Figure 7.10:** Contribution of the chiral 4N interaction to the ground-state energy of  ${}^4\text{He}$  depending on  $C_T$ . Calculations are performed using the NCSM at  $N_{\text{max}} = 20$  with the EM/N400 interaction SRG-evolved to a flow parameter of  $\alpha = 0.08 \text{ fm}^4$  at cutoffs of  $\mathcal{A}_{4B} = 400 \text{ MeV}$  ( $-\circ-$ ), and  $\mathcal{A}_{4B} = 600 \text{ MeV}$  ( $-\square-$ ). Furthermore, calculations for the same interactions are shown using HF at  $\mathcal{A}_{4B} = 400 \text{ MeV}$  ( $-\bullet-$ ), and  $\mathcal{A}_{4B} = 600 \text{ MeV}$  ( $-\blacksquare-$ ). All calculations employ a HO basis with a frequency of  $\hbar\omega = 24 \text{ MeV}$ , a four-body regulator exponent of  $n_{\text{exp}} = 4$ , and a four-body model-space truncation of  $E_{4,\text{max}} = 2$ .

size need not be monotonic. However, we can only perform  $E_{4,\text{max}} = 6$  calculations for  ${}^4\text{He}$ , as the other channels are computationally far too expensive.

Note that in some cases the effect of the 4N interaction does not behave completely monotonically when changing the cutoff. For instance, in the NCSM calculation for  $C_T = 0.21 \text{ fm}^2$  at  $\alpha = 0.08 \text{ fm}^4$  and  $E_{4,\text{max}} = 2$  in fig. 7.8 we observe a slight increase at cutoffs larger than 500 MeV. However, these increases are at the order of 0.2 keV, at such small differences, these effects might be due to numerical inaccuracies.

The cutoff dependence at  $E_{4,\text{max}} = 2$  is also similar in heavier nuclei, as depicted in fig. 7.9. For heavier nuclei, the whole curve seems to be slightly shifted. Changing the cutoff from 200 MeV to 300 MeV has only a minimal impact, but we still get the steep increase at slightly higher cutoff momenta. Thus the flattening is shifted to a higher cutoff as well. In general, heavier nuclei are expected to probe higher momenta, resulting in the shifted curve.

Note that, apart from  ${}^{56}\text{Ni}$ , we still get a monotonic increase when increasing the cutoff. Again,  ${}^{56}\text{Ni}$  does not follow this trend. Up to  $\mathcal{A}_{4B} = 400 \text{ MeV}$ , the 4N interaction acts attractive and afterwards it has a repulsive effect. This repulsion can only be found for  $E_{4,\text{max}} = 2$ , we can observe an attractive effect at  $\mathcal{A}_{4B} = 600 \text{ MeV}$  for  ${}^{56}\text{Ni}$  at  $E_{4,\text{max}} = 4$ , which is discussed in section 7.6.

So far, we have focused on the variation of the cutoff momentum, but we also have the regulator exponent left to choose. Increasing the regulator exponent does not change the observed behavior, it only results in a steeper increase at low cutoffs and the curve also flattens out at lower cutoffs. For higher exponents, the

regulator becomes more like a step function, therefore, it includes less of the contributions at momenta beyond the cutoff and more of the ones at lower momenta. As high momenta are irrelevant due the built-in cutoff of the HO basis, we only increase the contribution, when increasing the exponent while keeping the cutoff at the same level. This results in the observed differences, where some fixed  $4N$  contribution is reached at lower cutoffs for higher regulator exponents.

However, overall the behavior of the different exponents is quite similar and we simply select  $n_{\text{exp}} = 4$  for the remaining calculations. Furthermore, we use two cutoffs,  $\mathcal{A}_{4B} = 400$  MeV, and  $\mathcal{A}_{4B} = 600$  MeV. The lower one is still within the steep increase, while the regulator is already flattening at the higher one.

In fig. 7.7 calculations for different values of  $C_T$  are included. While the results almost match at  $C_T = 0.21$  fm<sup>2</sup>, this seems to be accidental. To investigate the effect, we have performed calculations for a whole set of  $C_T$  values, as shown in fig. 7.10. As we have classes with no, linear, and quadratic dependence on  $C_T$ , we obtain a parabola. In the HF case the linear contributions seem to cancel almost exactly, resulting in the maximum of the curve at  $C_T = 0$  fm<sup>2</sup>. The NCSM case yields a slightly shifted version of the parabola. For both cutoffs investigated here, the intersection between the HF and the NCSM parabola is close to  $C_T = 0.21$  fm<sup>2</sup>.

## 7.5 PERTURBATIVE INCLUSION

We have already seen that the effect of the chiral  $4N$  interaction is extremely small. Therefore, we should be able to include the effect in a calculation using first-order perturbation theory. To investigate the perturbative inclusion of the interaction we calculate the  $4N$  contribution to the ground-state energy in the same way as for the four-body contact interaction in section 6.1. In this chapter we also use the same method for HF calculations, we simply use the approximate HF ground state calculated without any four-body forces. We estimate the effect of the  $4N$  interaction by calculating the expectation value of the interaction with respect to that ground state. The result is compared to a full calculation, as done for  ${}^4\text{He}$  with different truncations in fig. 7.8 and for different nuclei in fig. 7.9.

In case of  ${}^4\text{He}$  for the HF as well as for the NCSM calculation, we see no difference between the full calculation and the perturbative inclusion at  $E_{4,\text{max}} = 2$ . At higher values of  $E_{4,\text{max}}$  we can observe differences in fig. 7.8. They are very small in case of  $E_{4,\text{max}} = 4$ , but they increase drastically for  $E_{4,\text{max}} = 6$ . In these cases, the agreement between a full calculation and the perturbative one depends on the cutoff momentum. At  $\mathcal{A}_{4B} = 400$  MeV, we see no differences between the two for any value of  $E_{4,\text{max}}$ , but for  $\mathcal{A}_{4B} = 600$  MeV and higher cutoffs, the perturbative calculation clearly differs from the full one. This is consistent with the expectation that lower cutoffs result in softer interactions that are better suited for a perturbative inclusion. We can therefore attribute the excellent agreement of the perturbative inclusion at large cutoffs  $\mathcal{A}_{4B}$  in the  $E_{4,\text{max}} = 2$  case to the built-in HO cutoff. In case of heavier nuclei, we can discern small differences that increase with larger values of the cutoff even for  $E_{4,\text{max}} = 2$ .

Again, the calculations for  $^{56}\text{Ni}$  break the pattern. In this case the perturbative inclusion and the full HF calculation do not match at all. In fact, the perturbative result is even attractive. This ties in with the almost degenerate single-particle spectrum of  $^{56}\text{Ni}$ . The perturbative inclusion of the 4N interaction follows the same trend as the other nuclei. Small changes due to the four-body interaction, however, can effect a change that is much larger than expected from such a weak force. This discrepancy should, therefore, be seen as a special case that is rooted in a combination of the HF approximation, the chosen two- and three-body interaction, and the structure of this specific nucleus.

For the remainder of this chapter we only employ full calculations. However, this analysis indicates that a perturbative inclusion of the chiral 4N interaction is sufficient at low cutoffs. This is relevant for the inclusion of the interaction in other many-body methods, as the simple evaluation of an expectation value is generally simpler and computationally less expensive than the complete inclusion of a four-body force.

## 7.6 CHANNEL STRUCTURE

As we use a PWD for including the 4N interaction, we can separate the contributions of different four-body channels. An overview of the effect is shown in fig. 7.II, where we have only included the 4N interaction up to a given four-body angular momentum. In general, we get the largest contributions when adding the channels with a four-body angular momentum of  $J_4 \leq 4$ . For the heavier nuclei,  $^{40}\text{Ca}$  and  $^{56}\text{Ni}$ , the channels with a higher angular momentum have larger contributions than in the  $^{16}\text{O}$  case. Especially the  $J_{4,\text{max}} = 4$  and  $J_{4,\text{max}} = 5$  results are identical in  $^{16}\text{O}$ , but we find contributions in the other two nuclei.

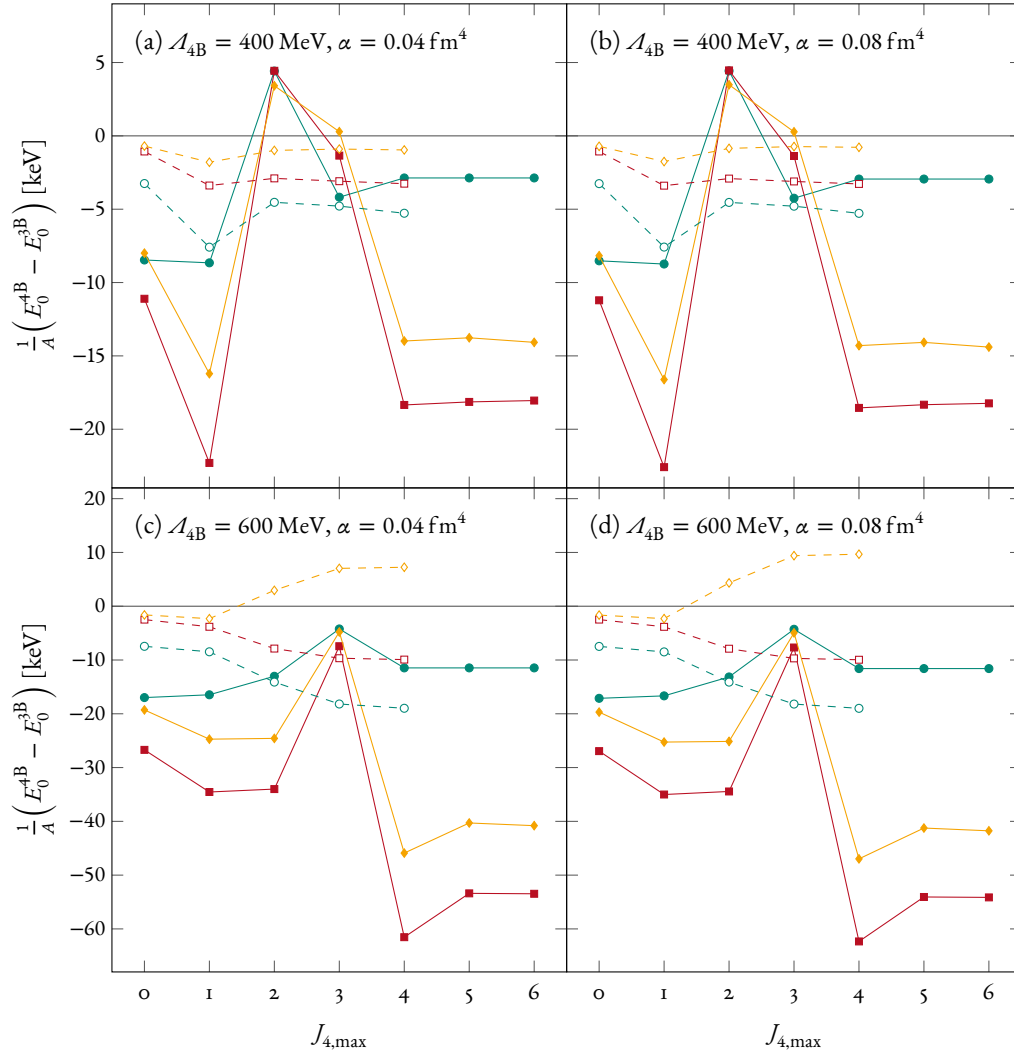
To discern the different factors that lead to the channel structure, we can employ two comparisons. First of all, fig. 7.II includes calculations for two different four-body cutoffs. As already discussed, the  $\mathcal{A}_{4\text{B}} = 600 \text{ MeV}$  cutoff leads to a larger four-body contribution than the  $\mathcal{A}_{4\text{B}} = 400 \text{ MeV}$  one. It is not surprising that the cutoff acts differently depending on the angular momentum channel, as each channel probes different length scales. We can very clearly see a very strong contribution of the  $J_4 = 2$  channels for the lower cutoff, while there is only a small contribution when using the larger cutoff.

Furthermore, the contributions of the different channels also depend on the wave-function of the nucleus in question. We already know that the effect of 4N interaction can be calculated using a perturbative inclusion. We can, therefore, use the ground state from a calculation without four-body forces as an excellent approximation to the ground state calculated with four-body forces. Note that this is not quite true for the  $^{56}\text{Ni}$  case, as discussed in section 7.5. We use the ground state  $|\Psi_0\rangle$  to calculate

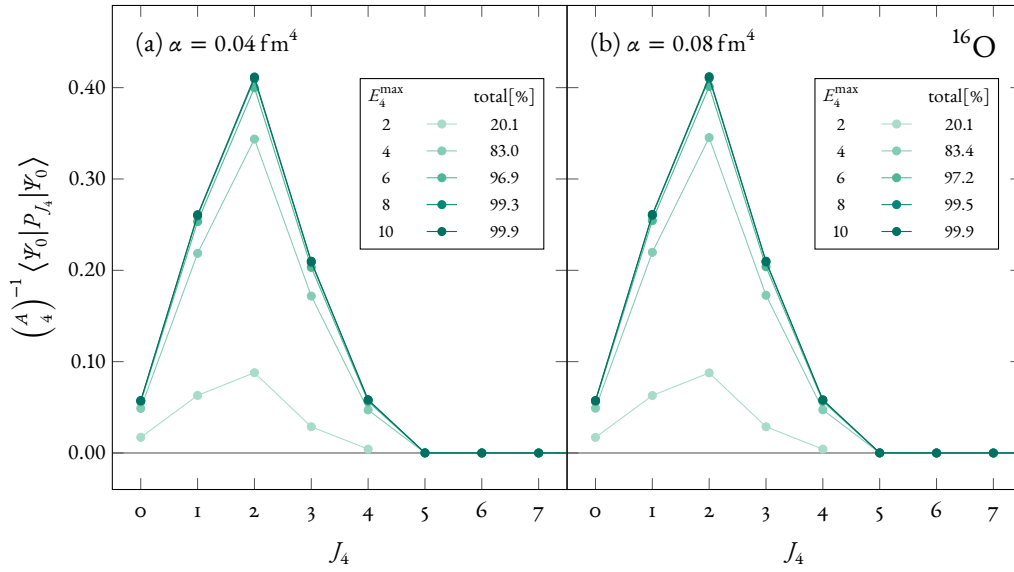
$$\binom{A}{4}^{-1} \langle \Psi_0 | P_{J_4} | \Psi_0 \rangle, \quad (7.1)$$

where  $P_{J_4}$  is the projection operator on a specific four-body angular momentum, and the expectation value is normalized in such a way that the maximum value for the given nucleus is one. This allows us to obtain the relevance of the different angular momentum channels in the ground-state.

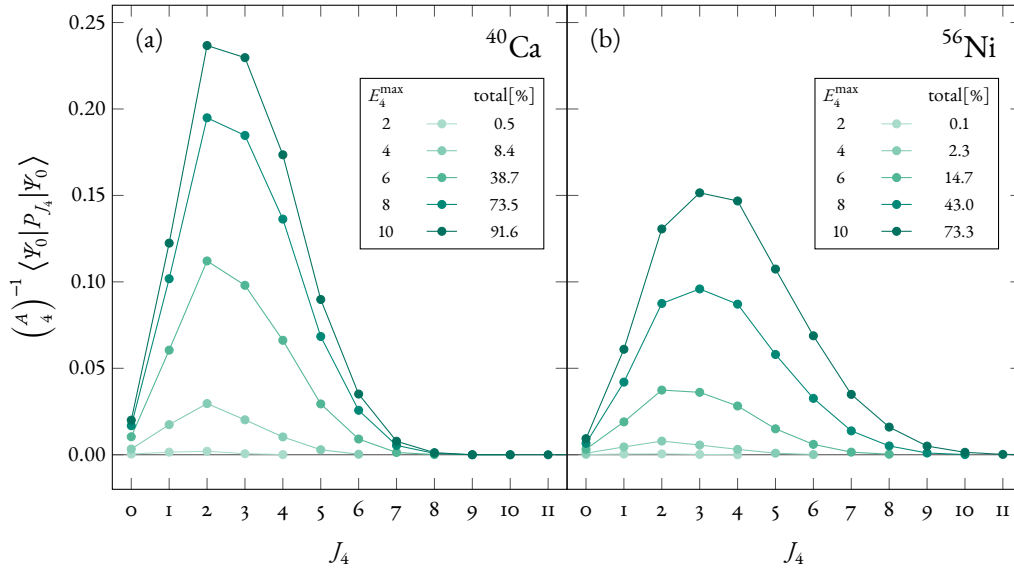




**Figure 7.11:** Effect of the chiral 4N interaction on the ground-state energy of <sup>16</sup>O (○, ●), <sup>40</sup>Ca (□, ■), and <sup>56</sup>Ni (◇, ◇) in HF calculations with a limit on the maximum four-body angular momentum,  $J_{4,\max}$ , which limits the included four-body channels. The results are obtained with the SRG-evolved EM/N400 interaction SRG-evolved to a flow parameter of  $\alpha = 0.04$  fm<sup>4</sup> in (a) and (c), and to a flow parameter of  $\alpha = 0.08$  fm<sup>4</sup> in (b) and (d). The four-body cutoff is  $\mathcal{A}_{4B} = 400$  MeV for (a) and (b), and it is  $\mathcal{A}_{4B} = 600$  MeV for (c) and (d). The dashed lines indicate an  $E_{4,\max} = 2$  truncation, and solid lines represent calculations using  $E_{4,\max} = 4$ . All results are obtained at  $e_{\max} = 10$ , employ a HO basis with a frequency of  $\hbar\omega = 24$  MeV, and use  $C_T = 0.21$  fm<sup>2</sup>.



**Figure 7.12:** Expectation value of the projection on a specific four-body angular momentum with respect to the  $^{16}\text{O}$  ground state. The ground state is obtained from a HF calculation at  $e_{\text{max}} = 10$  with the EM/N400 interaction SRG-evolved to a flow parameter of  $\alpha = 0.04 \text{ fm}^4$  (a) and  $\alpha = 0.08 \text{ fm}^4$  (b). All calculations employ a HO basis with a frequency of  $\hbar\omega = 24 \text{ MeV}$ . Different line colors correspond to a truncation of  $E_{4,\text{max}}$  to 2 (—), 4 (—), 6 (—), 8 (—), and 10 (—). The total values are calculated by summing up all expectation values at a specific truncation.



**Figure 7.13:** Expectation value of the projection on a specific four-body angular momentum with respect to the  $^{40}\text{Ca}$  (a) and  $^{56}\text{Ni}$  (b) ground state. The ground state is obtained from a HF calculation at  $e_{\text{max}} = 10$  with the EM/N400 interaction SRG-evolved to a flow parameter of  $\alpha = 0.08 \text{ fm}^4$ . All calculations employ a HO basis with a frequency of  $\hbar\omega = 24 \text{ MeV}$ . Different line colors correspond to a truncation of  $E_{4,\text{max}}$  to 2 (—), 4 (—), 6 (—), 8 (—), and 10 (—). The total values are calculated by summing up all expectation values at a specific truncation.

On a technical level, the construction can easily be done by reusing the four-body framework we have available. Instead of constructing an interaction in Jacobi momenta, we simply use the identity operator in that channel and then convert it to the single-particle basis, see section 5.2. Normalization requires dividing by the factor  $\binom{A}{4}$ , which comes in when embedding the matrix elements of the four-body projector in  $A$ -body space, see section 4.1 for details.

The results of this calculation are shown in figs. 7.12 and 7.13. Lets focus on the first figure, that is  $^{16}\text{O}$ . Note that we can clearly see a peak at  $J_4 = 2$ , which means, that this channel is expected to be important when including four-body forces. Channels with lower and higher angular momentum are less important and at  $J_4 = 5$ , no contributions can be found, which explains why the  $^{16}\text{O}$  results in fig. 7.11 do not change anymore at this level. While the size of the contributions to the ground-state energy in fig. 7.11 loosely follow the trend of fig. 7.12, they do not match completely. Obviously, the strength of the interaction itself also differs between channels. This is also apparent from the differences between the  $\mathcal{A}_{4\text{B}} = 400$  MeV and  $\mathcal{A}_{4\text{B}} = 600$  MeV calculations in fig. 7.11, which are based on the same two- and three-body interactions, and therefore, on a similar ground state.

We have already seen that the cutoff dependence does not change for different values of the flow parameter in the two- and three-body sector. The same is true for the channel structure in fig. 7.11. Both observations can be explained by the comparison in fig. 7.12. The expectation value of the four-body projection operator is almost identical for the two flow parameters, from which we can conclude that the four-body structure of these two ground states is almost identical. As the effect of the four-body interaction can be predicted using a perturbative inclusion, the differences of the ground state between a calculation with and without 4N forces should be small. Therefore, we would not expect different results for different flow parameters.

As the projection operator is treated in exactly the same way as the four-body interaction, it is also truncated at some four-body energy  $E_{4,\text{max}}$ . Constructing the projection operator is, of course, simpler, that is, it requires very little computing time, therefore, we can use much larger model spaces. In principle, if the applied truncation of the four-body space covers the ground-state wave function, we should get one when summing up the expectation values of the different channels. For low truncations, we get considerably less than one. In case of  $^{16}\text{O}$  and  $E_{4,\text{max}} = 4$ , we are already at 0.8. From this analysis we can be confident that calculations at such a low truncation are nevertheless sufficient. At the very least, the full calculations in fig. 7.11 should be of the right order of magnitude, even if we cannot see much of a convergence in fig. 7.11 on its own.

We can repeat this analysis for  $^{40}\text{Ca}$  and  $^{56}\text{Ni}$ , as shown in fig. 7.13. In these cases, we can see that the ground state also contains contributions from higher angular momenta, which is consistent with results shown fig. 7.11. In fact, for higher values of  $E_{4,\text{max}}$ , we can even expect contributions from  $J_4 = 6$  in the  $^{40}\text{Ca}$  case or even beyond that for  $^{56}\text{Ni}$ . Note that for these heavier nuclei,  $E_{4,\text{max}} = 4$  is not a sufficient truncation, as the sum of the channels yields values below 0.1 in both cases.

## 7.7 FREQUENCY VARIATION

We have already seen that we do not reach convergence with calculations performed at a truncation of  $E_{4,\max} = 4$ . For this reason, we investigate different HO frequencies using NCSM and HF calculations, as shown in fig. 7.14. Note that both the many-body calculations are converged, with uncertainties below 1% for nuclei up to  $^{40}\text{Ca}$  using  $\hbar\omega = 24$  MeV, at least when only investigating the difference between a calculation with and one without 4N forces, as discussed in section 7.2. The uncertainties due to the many-body calculation can be a little larger for other frequencies, but up to  $^{40}\text{Ca}$  they are always below 5%, they can be up to 20% in the  $^{56}\text{Ni}$  case, the exception is the calculation at  $\mathcal{A}_{4\text{B}} = 600$  MeV with  $E_{4,\max} = 2$  and  $\hbar\omega = 28$  MeV for  $^{56}\text{Ni}$ , which exhibits considerable convergence issues. However, all other calculations are reliable, and therefore, the dependence on the frequency only exists due to the truncation of the 4N interaction at such low values for  $E_{4,\max}$ .

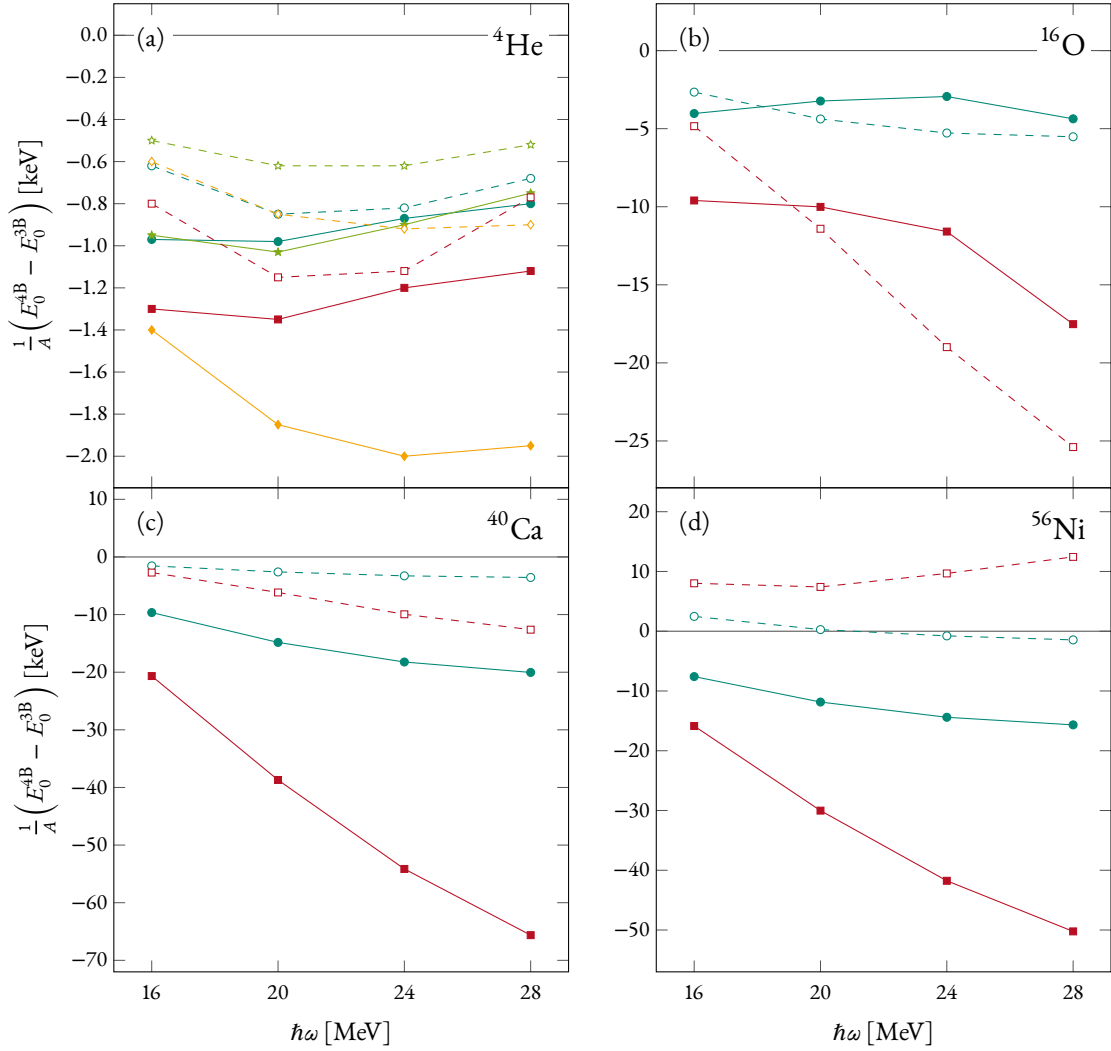
As one would expect, we do see a frequency dependence for all nuclei, as we have not reached convergence in any of the cases. The trend is flatter in case of HF calculations of  $^4\text{He}$  and  $^{16}\text{O}$ , at least for frequencies of  $\hbar\omega \leq 24$  and a truncation  $E_{4,\max} = 4$  in the latter case. This can be interpreted as an indication of convergence, which is consistent with the analysis in the last chapter, suggesting that the  $^4\text{He}$  and  $^{16}\text{O}$  results are in the right ballpark. However, we observe larger gaps between  $E_{4,\max} = 2$  and  $E_{4,\max} = 4$  results in the NCSM calculation compared to the HF calculations, which indicates that the HF calculations are missing significant contributions due to their mean-field approximation.

We can also observe that the difference between the two cutoff values becomes smaller at lower frequencies, especially for the  $E_{4,\max} = 2$  calculations. This ties in to the HO wave functions again. The HO wave functions already have a built-in cutoff, which is lowered by reducing the HO frequency. For some low value of the frequency, the two contributions from the two four-body cutoffs must be indistinguishable. We already encountered this phenomenon in section 7.4.

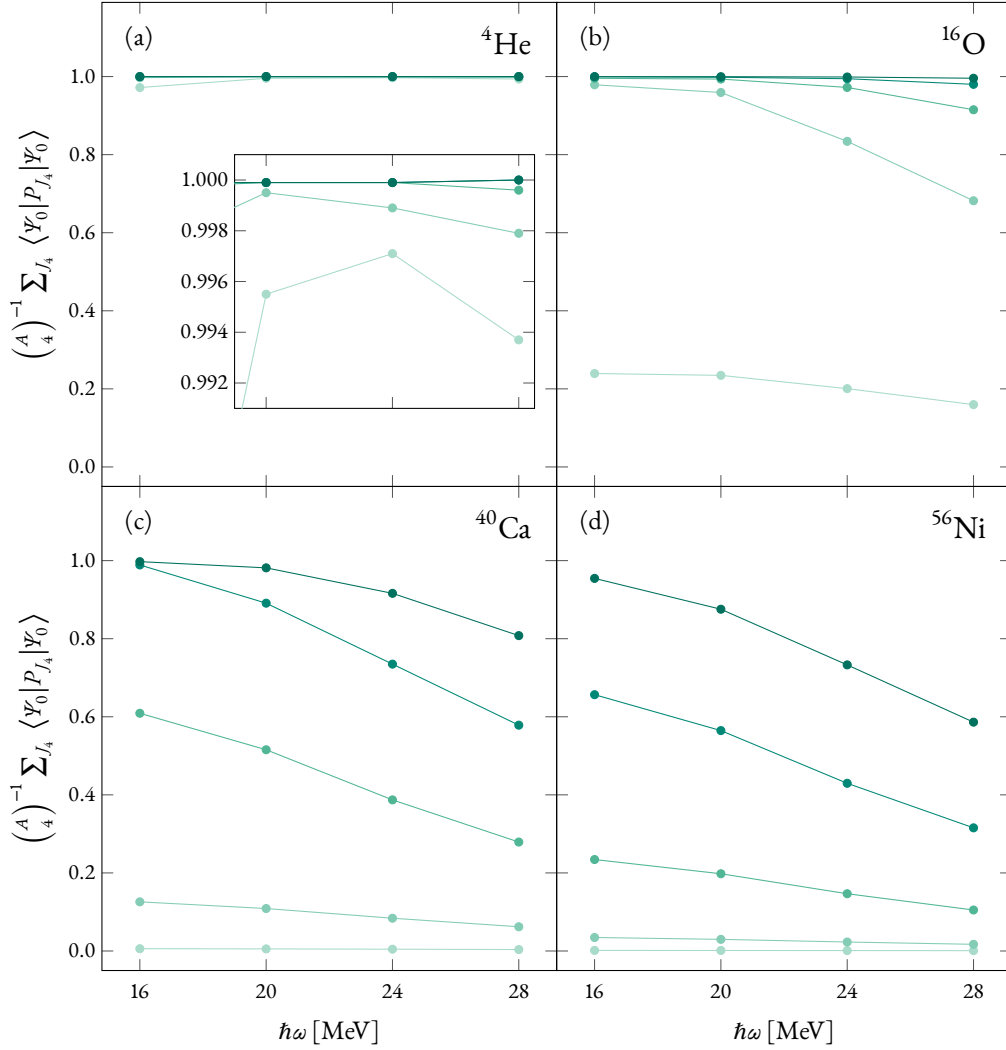
To further investigate the convergence, we can use the projection operators again. We simply sum up all angular momentum channels for each frequency, which allows us to gain insight in the four-body structure of the nuclei and separating the trends that are related to the structure. The calculations are shown in fig. 7.15.

Comparing the  $^4\text{He}$  HF calculations of the ground-state contributions with the total expectation value at the same truncation yields a remarkable resemblance. In both cases, we have the smallest distance between  $E_{4,\max} = 2$  and  $E_{4,\max} = 4$  results at  $\hbar\omega = 24$  MeV, and the largest at  $\hbar\omega = 16$  MeV. However, from fig. 7.15 we would expect to gain 99% of the contribution already at  $E_{4,\max} = 2$ , which is clearly not the case.

For all heavier nuclei, we obtain a clear trend in fig. 7.15. In all cases convergence is expected to be better at lower frequencies. As these nuclei are all larger than  $^4\text{He}$ , and as a HF calculation does not take any correlations into account, especially not clustering effects, we expect wave functions that match the size of nucleus to yield the highest expectation values for low truncations. Note that the peak can shift when the truncation is close to convergence, as apparent from the  $^4\text{He}$  case.



**Figure 7.14:** Effect of the chiral 4N interaction on the ground-state energy of  ${}^4\text{He}$  (a),  ${}^{16}\text{O}$  (b),  ${}^{40}\text{Ca}$  (c), and  ${}^{56}\text{Ni}$  (d). For all nuclei HF calculations are performed at  $e_{\text{max}} = 10$  with cutoffs of  $\mathcal{A}_{4B} = 400$  MeV ( $\bullet$ ,  $\circ$ ), and  $\mathcal{A}_{4B} = 600$  MeV ( $\blacksquare$ ,  $\square$ ). Furthermore, NCSM calculations at  $N_{\text{max}} = 20$  are shown for  ${}^4\text{He}$  with the same cutoffs of  $\mathcal{A}_{4B} = 400$  MeV ( $\star$ ,  $\diamond$ ), and  $\mathcal{A}_{4B} = 600$  MeV ( $\blacklozenge$ ,  $\blacklozenge$ ). All results are obtained with a four-body truncation of  $E_{4,\text{max}} = 2$  (dashed lines), and  $E_{4,\text{max}} = 4$  (solid lines). For the two- and three-body sector the EM/N400 interaction has been SRG-evolved to a flow parameter of  $\alpha = 0.08 \text{ fm}^4$ . For all calculations a HO basis with a frequency of  $\hbar\omega = 24 \text{ MeV}$  is employed, and the four-body interaction uses  $C_T = 0.21 \text{ fm}^2$ , as well as a regulator exponent of  $n_{\text{exp}} = 4$ .



**Figure 7.15:** Sum of the expectation value of the projection on a specific four-body angular momentum with respect to the  ${}^4\text{He}$  (a),  ${}^{16}\text{O}$  (b),  ${}^{40}\text{Ca}$  (c), and  ${}^{56}\text{Ni}$  (d) ground state. The ground state is calculated using HF at  $e_{\text{max}} = 10$  with the EM/N400 interaction SRG-evolved to a flow parameter of  $\alpha = 0.08 \text{ fm}^4$ . Different line colors correspond to a truncation of  $E_{4,\text{max}}$  to 2 (—○—), 4 (—○—), 6 (—●—), 8 (—●—), and 10 (—●—) for the projection operator.

At first sight this seems to disagree with the calculation of  $^{40}\text{Ca}$  and  $^{56}\text{Ni}$  in fig. 7.14, as the contributions grow with larger values for the HO frequency. However, there is no indication that these larger values are any closer to convergence. In fact, we expect large changes when increasing  $E_{4,\text{max}}$  and this might result in a larger effect at low frequencies. Furthermore, the convergence does not have to be monotonic, it is quite possible that the contribution at high frequencies is reduced when increasing the model space. We have explicitly seen a non-monotonic convergence pattern in case of  $^4\text{He}$  in fig. 7.8.

For  $^{16}\text{O}$ , the expectation values and the actual contributions agree with each other. From the expectation values we expect convergence at  $E_{4,\text{max}} = 4$  and lower frequencies and, indeed, the frequency dependence in fig. 7.14(b) is reduced.

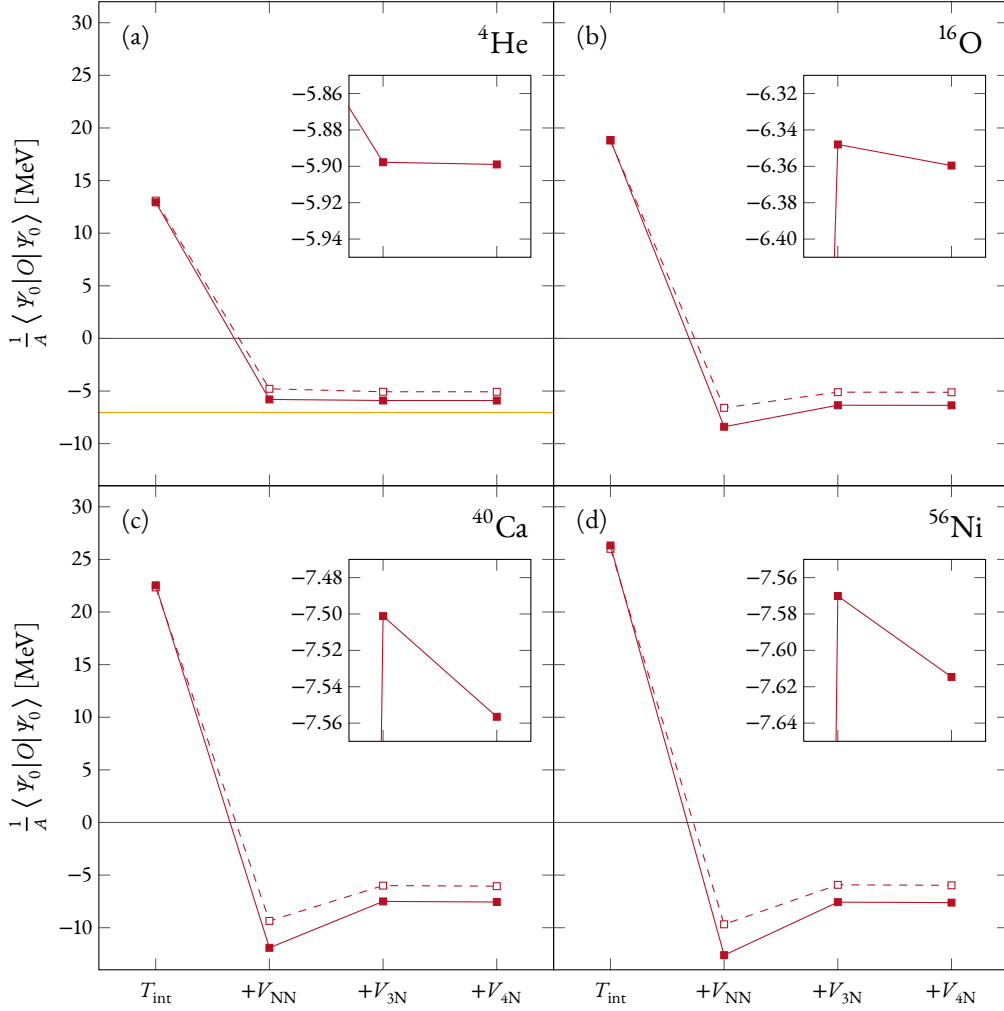
## 7.8 RELEVANCE OF THE FOUR-NUCLEON FORCE

Throughout this chapter we have investigated the effect of the four-body contribution quite thoroughly. We have seen that we are independent of the technical parameters, like the size of the momentum grids, and we know that the many-body methods are converged. We have investigated the dependence on physical parameters and we have investigated the convergence with respect to the four-body model space size, that is,  $E_{4,\text{max}}$ . Although we are quite obviously not converged with respect to  $E_{4,\text{max}}$ , we deem calculations up to  $^{16}\text{O}$  as trustworthy enough, at least to estimate the size of the total effect of the chiral 4N interaction.

This leads us to the central question of this section: Are the four-body forces even relevant? Judging from the calculations we have analyzed, there is a clear answer to this question: No, the 4N force is not relevant. To illustrate just how small the effect really is, we can have a look at the expectation value of intrinsic kinetic energy, the NN, the 3N, and the 4N interaction in fig. 7.16.

The figure clearly shows the many-body hierarchy, which is predicted by chiral EFT. We can immediately see that 3N contributions are smaller than the NN ones, but they obviously have a relevant effect. The 4N contributions, however, are completely negligible on this scale. To emphasize this point, we have a look at the  $\alpha$  dependence of the interaction. The EM/N400 interaction is known to be almost independent of the flow parameter  $\alpha$ , and we can see that in fig. 7.16(a), where the two NCSM calculations for the two flow parameters are not distinguishable. Note that the HF calculations have a larger separation, as a mean field method is better suited for the softer interaction at  $\alpha = 0.08 \text{ fm}^4$ . Nevertheless, a fully converged NCSM calculation yields a separation of only  $\sim 10 \text{ keV}$  per nucleon. However, this is still an order of magnitude larger than the effect of the initial 4N contributions.

The effect of the 4N interaction does scale with the number of nucleons, so  $^4\text{He}$  might be an extreme example. But even at  $^{16}\text{O}$  we are only at  $\sim 10 \text{ keV}$  per nucleon, which is still two orders of magnitude below the 3N contribution. We obtain slightly larger contributions for the heavier nuclei. Additionally, we cannot exclude the possibility that the effect of the 4N interaction increases by an order of magnitude for  $^{40}\text{Ca}$  or  $^{56}\text{Ni}$  when fully converged. However, it does not seem likely that the initial four-body force can have a



**Figure 7.16:** Expectation value of the intrinsic kinetic energy and sums of the kinetic energy and the different nuclear forces with respect to the HF ground state. For example, the third data point corresponds to  $1/A \langle \Psi_0 | T_{\text{int}} + V_{\text{NN}} + V_{3\text{N}} | \Psi_0 \rangle$ . The ground state is obtained using a HF calculation at  $e_{\text{max}} = 10$  with the EM/N400 interaction SRG-evolved to a flow parameter of  $\alpha = 0.04 \text{ fm}^4$  ( $\square$ ) and  $\alpha = 0.08 \text{ fm}^4$  ( $\blacksquare$ ). Furthermore, the chiral four-body interaction is included with a cutoff of  $\mathcal{A}_{4\text{B}} = 600 \text{ MeV}$ , a regulator exponent of  $n_{\text{exp}} = 4$ , a truncation of  $E_{4,\text{max}} = 4$ , and  $C_T = 0.21 \text{ fm}^2$ . All calculations employ a HO basis with a frequency of  $\hbar\omega = 24 \text{ MeV}$ . The results are shown for  ${}^4\text{He}$  (a),  ${}^{16}\text{O}$  (b),  ${}^{40}\text{Ca}$  (c), and  ${}^{56}\text{Ni}$  (d). The yellow line in (a) is the ground-state energy per nucleon obtained with a NCSM calculation at  $N_{\text{max}} = 20$  with the same interactions. Note that the two different flow parameters only differ by 10 keV in a NCSM calculation.



significant impact on the heavier nuclei, and it definitely has none on the lighter ones.

Currently, differences between variants of the chiral interactions and other uncertainties throughout a many-body calculation, for instance induced 4N interactions, seem to be much more important and should all be addressed before considering the initial chiral 4N force relevant. Even small changes to the regulator of the three-body interaction can have a significant impact on state-of-the-art calculations [126]. Furthermore, the calculation of medium-mass nuclei often yield overbound nuclei, with ground-state energies and radii that are both too small. From these difficulties it seems highly unlikely that one can perform a many-body calculation with an uncertainty that is small enough to warrant the inclusion of chiral 4N forces. Generally, we can expect ab initio description of nuclei based on chiral forces to achieve an accuracy of about 1 % of the ground-state energy in the foreseeable future. The 4N forces are smaller than that and, therefore, not relevant.



# 8

## Conclusions

Recent years brought major advances in the construction of nuclear interactions from chiral EFT, which includes the derivation and construction of chiral two-body forces up to  $N^4\text{LO}$  and beyond [22–26] and the PWD of the chiral 3N interaction at  $N^3\text{LO}$  [29]. Prompted by these developments, the current focus is on the reliable uncertainty quantification of observables calculated with chiral interactions, and on consistent order-by-order calculations. In light of the above, the incorporation of chiral 4N interactions at  $N^3\text{LO}$  is a necessary step.

This work investigates the inclusion of 4N forces in many-body calculations. Due to the formulation of the chiral interaction in single-particle momenta, the main obstacle that was overcome is the PWD of the chiral 4N interaction. The solution presented in this work is a computationally feasible approach, however, it requires a substantial analytic derivation. We include all operator structures in the leading order of the chiral 4N interaction, and for each structure we separately performed the PWD. That is, for each structure we handled coordinate transformations analytically, and evaluated as many angular integrals as possible. From the resulting formulae we separated parts that can be reused and stored them as momentum grids to reduce the computational workload. Despite the endeavor to reduce the computational effort, the PWD remains the limiting factor.

However, we are now in the position to perform the PWD in a limited model space and include the resulting interaction in many-body calculations. Variation of the grid sizes and interpolation scheme show that the construction of the interaction is reliable. To be precise, the choice of the momentum grids does not influence the calculated ground-state energies. We presented results gauging the effect of the 4N con-

tributions on a series of nuclei, from the very light  ${}^4\text{He}$  up to  ${}^{56}\text{Ni}$ . All considered cases exhibit extremely weak effects of the chiral 4N interaction. While we cannot achieve convergence with respect to the model-space size, the presented analysis strongly indicates that the order of magnitude of the effect of the chiral 4N interaction is correct, at least up to  ${}^{16}\text{O}$ . Although we do observe a scaling with the number of nucleons, we find no evidence in any of the performed interactions that the 4N interaction becomes important for heavier nuclei.

In an investigation of the different contributions we find that the overall effect of the chiral 4N interaction is weaker than individual contributions, that is, we have strong cancellations between different classes of the interaction. As expected from such a weak interaction, we find that a perturbative inclusion of the 4N contributions is sufficient, especially so for lower cutoffs.

Even compared to previous estimates of the effect in  ${}^4\text{He}$  [36], we obtain a very weak effect, and the generally small contributions from the chiral 4N interaction is also apparent from neutron and nuclear matter calculations [32–35]. However, comparing the effect of the 4N to the one of the 3N interaction at  $\text{N}^3\text{LO}$  [29, 32, 33] we generally see a much stronger effect of the 3N contributions, even though they belong to the same chiral order.

Especially compared to uncertainties in many-body calculations or the discrepancies between different variants of the two- and three-body force, the chiral 4N interactions are small. We conclude that, in the foreseeable future, the inclusion of chiral 4N forces is not relevant for ab initio descriptions of nuclei based on typical chiral two- and three-body interactions. For the future of many-body calculations this result is an excellent outcome, as many-body calculations without four-body forces are generally simpler and computationally cheaper. Neglecting the four-body forces, consistent order-by-order calculations with a matching regulator in the two- and three-body sector are already possible today.

Apart from chiral EFT, there exists another source of four-body forces relevant to nuclear structure. Any transformation of the interaction using the SRG yields induced many-body contributions, which can be sizable and show a strong scaling with the number of nucleons. It is possible to obtain these induced 4N forces and include them directly in the many-body calculation, but this approach is computationally expensive [60, 61]. While a SRG generator that minimizes these induced forces would be the optimal solution, one can try to imitate these contributions with a simpler four-body force. Additionally, the employed chiral two- and three-body interactions result in radii that are much too small for heavier nuclei, which is in all likelihood not a result of the SRG transformation. The effect might be mitigated by using a simple four-body force.

To this end we have investigated a contact interaction, which does not pose computational challenges when performing the PWD. This interaction has been designed to only act in the  $J^\pi = 0^+$  channel, and the PWD, as well as the inclusion of such an interaction in a many-body method, is simple compared to the full chiral 4N interaction. To facilitate the model-space convergence of the many-body calculation, we used a low cutoff. We have analyzed the effect of the four-body contact interaction in conjunction with the EM/N500 and the SMS/H500 interactions. In both cases we find similar results, and while we observe a

scaling of the effect of the contact interaction with the number of nucleons, it is much too weak to mimic the SRG-induced contributions. However, reducing the strong flow-parameter dependence by using a simple four-body interaction that is computationally feasible might be possible and may be investigated in future work. From the analysis done in this work such an interaction should be weak in the  $J^\pi = 0^+$  channel and feature contributions in higher partial waves. We find an effect of the contact interaction on the radius, but it is not possible to improve agreement of charge radii with experiment without obtaining unphysical binding energies.

If the inclusion of four-body forces proves to be inevitable, extending other many-body methods to include these four-body contributions will become relevant. An easy solution would be the implementation of a normal-ordering scheme, which is able to reduce the four-body force to a lower particle rank, that is, up to a two- or three-body space. This scheme has shown excellent results for reducing three-body interactions [58, 59, 127], and would directly enable the use of four-body interactions in a wide range of many-body methods.



# Appendices





# A

## Partial-Wave Decomposition of the Chiral Four-Nucleon Interaction

In this chapter, we discuss the derivation of the ten operator structures that have not been discussed when constructing the spatial part of the chiral 4N force in section 4.4.2. Note that more details are given throughout section 4.4.2, as the approach here is completely identical to the one discussed in that chapter.

### A.1 CLASS I - SUBSTRUCTURE B/C

We start by expressing the operator structure with diagrams and reduce the number of coordinate lines, in the same way as done for structure (Ia). We have already included a factor of two to account for structure (Ic) as well. Note that we have a cross product in this case, which is represented diagrammatically using eq. (3.17), yielding

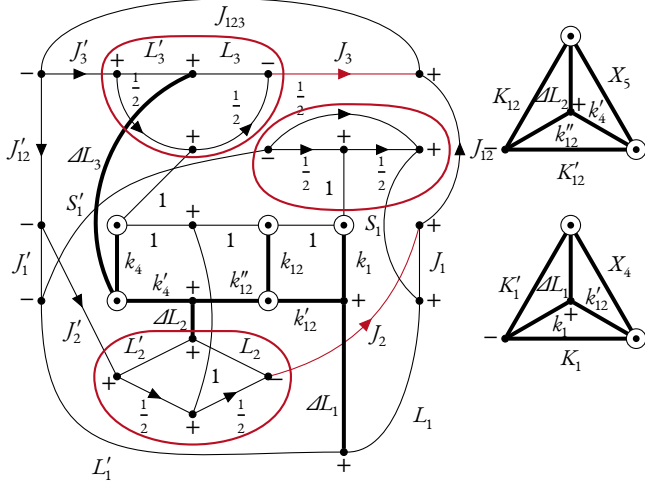
$$\begin{aligned} & \left\langle m'_{s_a} m'_{s_b} m'_{s_c} m'_{s_d}, \pi'_1 \pi'_2 \pi'_3 \left| V_{\text{Ib}}^{(s)} \right| m_{s_a} m_{s_b} m_{s_c} m_{s_d}, \pi_1 \pi_2 \pi_3 \right\rangle \\ &= \left\langle m'_{s_a} m'_{s_b} m'_{s_c} m'_{s_d} \left| -\frac{4g_A^6}{(2F_\pi)^6} \frac{\boldsymbol{\sigma}_1 \cdot \mathbf{q}_1 \boldsymbol{\sigma}_4 \cdot \mathbf{q}_4 \mathbf{q}_1 \cdot \mathbf{q}_{12} (\mathbf{q}_{12} \times \mathbf{q}_4) \cdot \boldsymbol{\sigma}_3}{[q_1^2 + M_\pi^2] [q_{12}^2 + M_\pi^2]^2 [q_4^2 + M_\pi^2]} \right| m_{s_a} m_{s_b} m_{s_c} m_{s_d} \right\rangle \end{aligned}$$

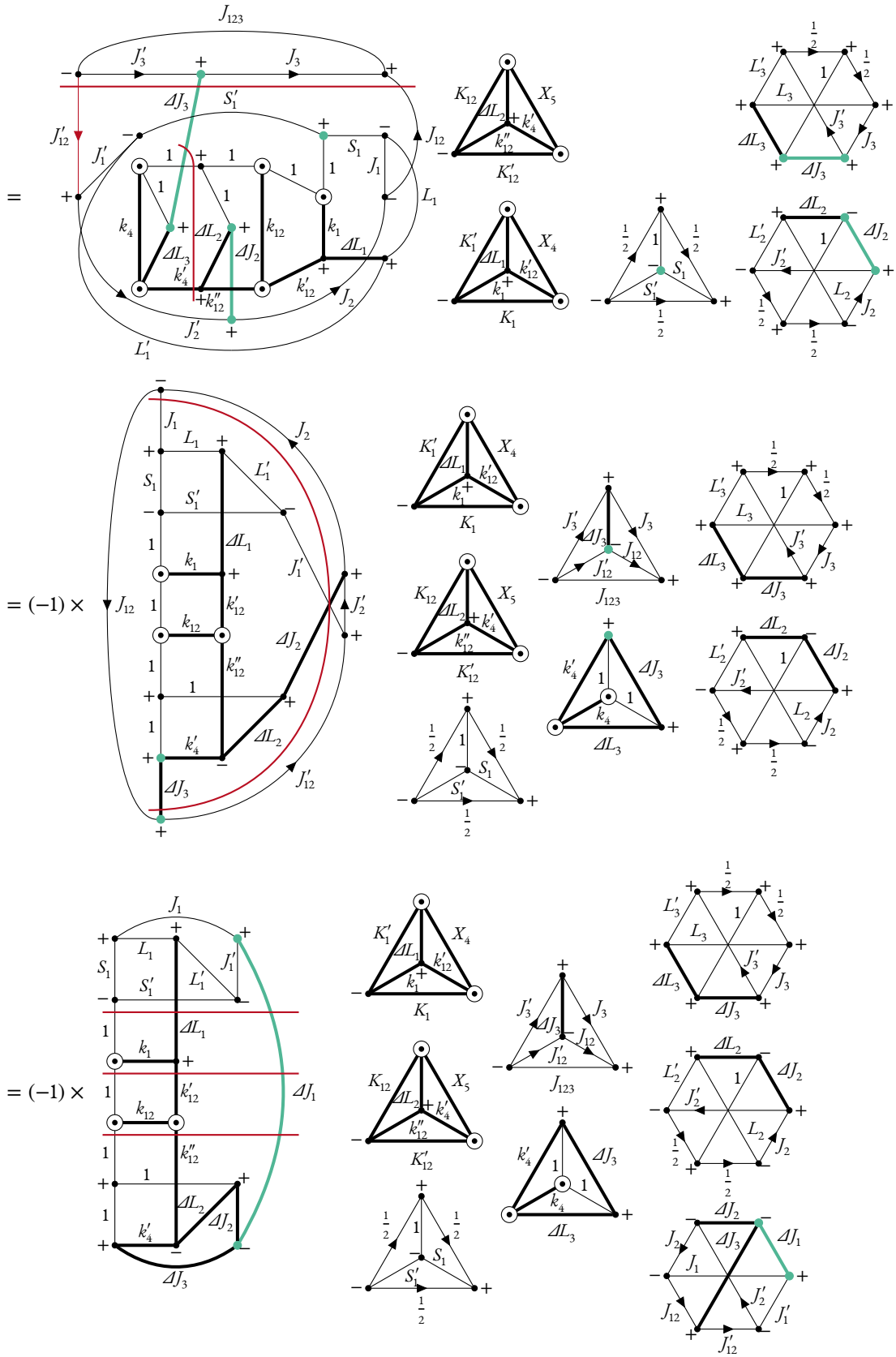
$$\begin{aligned}
 &= \text{Diagram 1} \times \delta_{m_b, m'_b} \frac{144ig_A^6}{(2F_\pi)^6} \frac{q_1^2}{q_1^2 + M_\pi^2} \frac{q_4^2}{q_4^2 + M_\pi^2} \frac{q_{12}^2}{[q_{12}^2 + M_\pi^2]^2} \\
 &= \text{Diagram 2} \times \delta_{m_b, m'_b} \frac{-144ig_A^6}{(2F_\pi)^6} \frac{q_1^2}{q_1^2 + M_\pi^2} \frac{q_4^2}{q_4^2 + M_\pi^2} \frac{q_{12}^2}{[q_{12}^2 + M_\pi^2]^2}.
 \end{aligned}$$

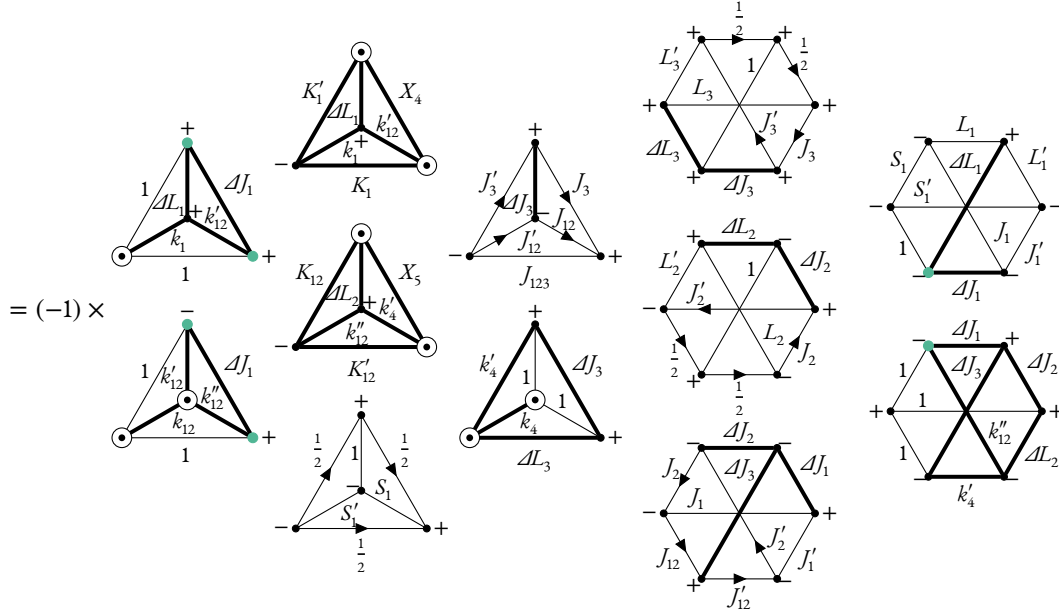
From here on, the derivation is done exactly as in the previous case, expressing all momentum transfers in terms of Jacobi momenta and reducing coordinate lines as much as possible. We therefore directly give the result in terms of Jacobi coordinates,

$$\begin{aligned}
 &= \text{Diagram 3} \times \delta_{m_b, m'_b} \int du_4 P_{X_4}(u_4) \int du_5 P_{X_5}(u_5) D_{K_1, K'_1}^{k_1} D_{K_{12}, K'_{12}}^{k'_{12}} \\
 &\quad \times \sqrt{2}^{K_{12}-2K_1-K'_1} \sqrt{3}^{-K_{12}-K'_{12}} (-1)^{1+X_4+X_5+k_{12}+k_4+k'_4} \\
 &\quad \times \frac{36ig_A^6}{(2F_\pi)^6} \frac{q_1(\mathcal{A}_1, q_{12}(\mathcal{A}_2, \mathcal{A}_3, u_5), u_4)^{2-k_1}}{q_1(\mathcal{A}_1, q_{12}(\mathcal{A}_2, \mathcal{A}_3, u_5), u_4)^2 + M_\pi^2} \\
 &\quad \times \frac{\frac{3}{4}\mathcal{A}_3^{2+K'_{12}}}{\frac{3}{4}\mathcal{A}_3^2 + M_\pi^2} \frac{q_{12}(\mathcal{A}_2, \mathcal{A}_3, u_5)^{2+K_1-k'_{12}}}{[q_{12}(\mathcal{A}_2, \mathcal{A}_3, u_5)^2 + M_\pi^2]^2} \mathcal{A}_1^{K'_1} \mathcal{A}_2^{K_{12}}
 \end{aligned}$$

At this point we can insert the expression in eq. (4.11) again and start by simplifying the diagrammatic part,







Representing the diagrammatic expression in a traditional form and adding the suppressed parts of the formulae, we obtain a formula exactly like eq. (4.16), just the interaction part needs to be exchanged for

$$\begin{aligned}
 & I_{\text{Ib}}^{L_1, L_2, L_3, S_1, J_1, J_2, J_3, J_{12}, J_{123}; \Delta L_1, \Delta L_2, \Delta L_3}(\mathcal{A}_1, \mathcal{A}_2, \mathcal{A}_3) \\
 &= \int d\mathbf{u}_4 P_{X_4}(\mathbf{u}_4) \int d\mathbf{u}_5 P_{X_5}(\mathbf{u}_5) \sum_{X_4, X_5} \sum_{K_1, K_{12}} \sum_{k_1, k_{12}} \sum_{k_4, k'_4} D_{K_1, K_1}^{k_1} D_{K_{12}, K_{12}}^{k_{12}''} \sqrt{2^{K_{12}-2K_1-K_1'}} \sqrt{3^{-K_{12}-K_{12}'}} \\
 & \quad (-1)^{1+S_1'+J_3+J_{12}'+J_{123}'+\mathcal{A}_1+\mathcal{A}_2+\mathcal{A}_3+X_4+X_5} \hat{S}_1 \hat{S}_1' \hat{J}_1 \hat{J}_1' \hat{J}_2 \hat{J}_2' \hat{J}_3 \hat{J}_3' \hat{J}_{12} \hat{J}_{12}' \hat{\Delta}_1^2 \hat{\Delta}_2^2 \hat{\Delta}_3^2 \hat{k}_1 \hat{k}_1' \hat{k}_2 \hat{k}_2' \hat{k}_3 \hat{k}_3' \hat{k}_4 \hat{k}_4' \hat{k}_{12} \hat{k}_{12}' \hat{k}_{12}'' \hat{K}_1 \hat{K}_1' \hat{K}_{12} \hat{K}_{12}' \hat{X}_4 \hat{X}_5 \\
 & \quad \begin{pmatrix} 1 & 1 & k_1 \\ 0 & 0 & 0 \end{pmatrix} \begin{pmatrix} 1 & 1 & k_4 \\ 0 & 0 & 0 \end{pmatrix} \begin{pmatrix} 1 & 1 & k_{12} \\ 0 & 0 & 0 \end{pmatrix} \begin{pmatrix} k_4 & k_4' & \Delta L_3 \\ 0 & 0 & 0 \end{pmatrix} \begin{pmatrix} k_{12} & k_{12}' & k_{12}'' \\ 0 & 0 & 0 \end{pmatrix} \begin{pmatrix} K_1 & X_4 & k_{12}' \\ 0 & 0 & 0 \end{pmatrix} \begin{pmatrix} K_1' & X_4 & \Delta L_1 \\ 0 & 0 & 0 \end{pmatrix} \\
 & \quad \begin{pmatrix} K_{12} & X_5 & \Delta L_2 \\ 0 & 0 & 0 \end{pmatrix} \begin{pmatrix} K_{12}' & X_5 & k_4' \\ 0 & 0 & 0 \end{pmatrix} \begin{Bmatrix} k_4' & \Delta L_2 & k_{12}'' \\ K_{12} & K_{12}' & X_5 \end{Bmatrix} \begin{Bmatrix} k_{12} & k_{12}' & k_{12}'' \\ \Delta J_1 & 1 & 1 \end{Bmatrix} \begin{Bmatrix} k_{12}' & \Delta L_1 & k_1 \\ K_1' & K_1 & X_4 \end{Bmatrix} \begin{Bmatrix} S_1 & S_1' & 1 \\ \frac{1}{2} & \frac{1}{2} & \frac{1}{2} \end{Bmatrix} \\
 & \quad \begin{Bmatrix} 1 & 1 & k_1 \\ k_{12}' & \Delta L_1 & \Delta J_1 \end{Bmatrix} \begin{Bmatrix} 1 & 1 & k_4 \\ k_4' & \Delta L_3 & \Delta J_3 \end{Bmatrix} \begin{Bmatrix} J_{12} & J_{12}' & \Delta J_3 \\ J_3' & J_3 & J_{123} \end{Bmatrix} \\
 & \quad \begin{Bmatrix} L_1 & S_1 & J_1 \\ L_1' & S_1' & J_1' \\ \Delta L_1 & 1 & \Delta J_1 \end{Bmatrix} \begin{Bmatrix} L_2 & \frac{1}{2} & J_2 \\ L_2' & \frac{1}{2} & J_2' \\ \Delta L_2 & 1 & \Delta J_2 \end{Bmatrix} \begin{Bmatrix} L_3 & \frac{1}{2} & J_3 \\ L_3' & \frac{1}{2} & J_3' \\ \Delta L_3 & 1 & \Delta J_3 \end{Bmatrix} \begin{Bmatrix} J_1 & J_2 & J_{12} \\ J_1' & J_2' & J_{12}' \\ \Delta J_1 & \Delta J_2 & \Delta J_3 \end{Bmatrix} \begin{Bmatrix} 1 & k_{12}'' & \Delta J_1 \\ 1 & \Delta L_2 & \Delta J_2 \\ 1 & k_4' & \Delta J_3 \end{Bmatrix} \frac{36i g_A^6}{(2F_\pi)^6} \mathcal{A}_1^{K_1'} \mathcal{A}_2^{K_{12}} \\
 & \quad \frac{q_1(\mathcal{A}_1, q_{12}(\mathcal{A}_2, \mathcal{A}_3, u_5), u_4)^{2-k_1} \frac{3}{4} \mathcal{A}_3^{2+K_{12}'}}{q_1(\mathcal{A}_1, q_{12}(\mathcal{A}_2, \mathcal{A}_3, u_5), u_4)^2 + M_\pi^2 \frac{3}{4} \mathcal{A}_3^2 + M_\pi^2} \frac{q_{12}(\mathcal{A}_2, \mathcal{A}_3, u_5)^{2+K_1-k_{12}''}}{[q_{12}(\mathcal{A}_2, \mathcal{A}_3, u_5)^2 + M_\pi^2]^2}.
 \end{aligned}$$

## A.2 CLASS I - SUBSTRUCTURE D

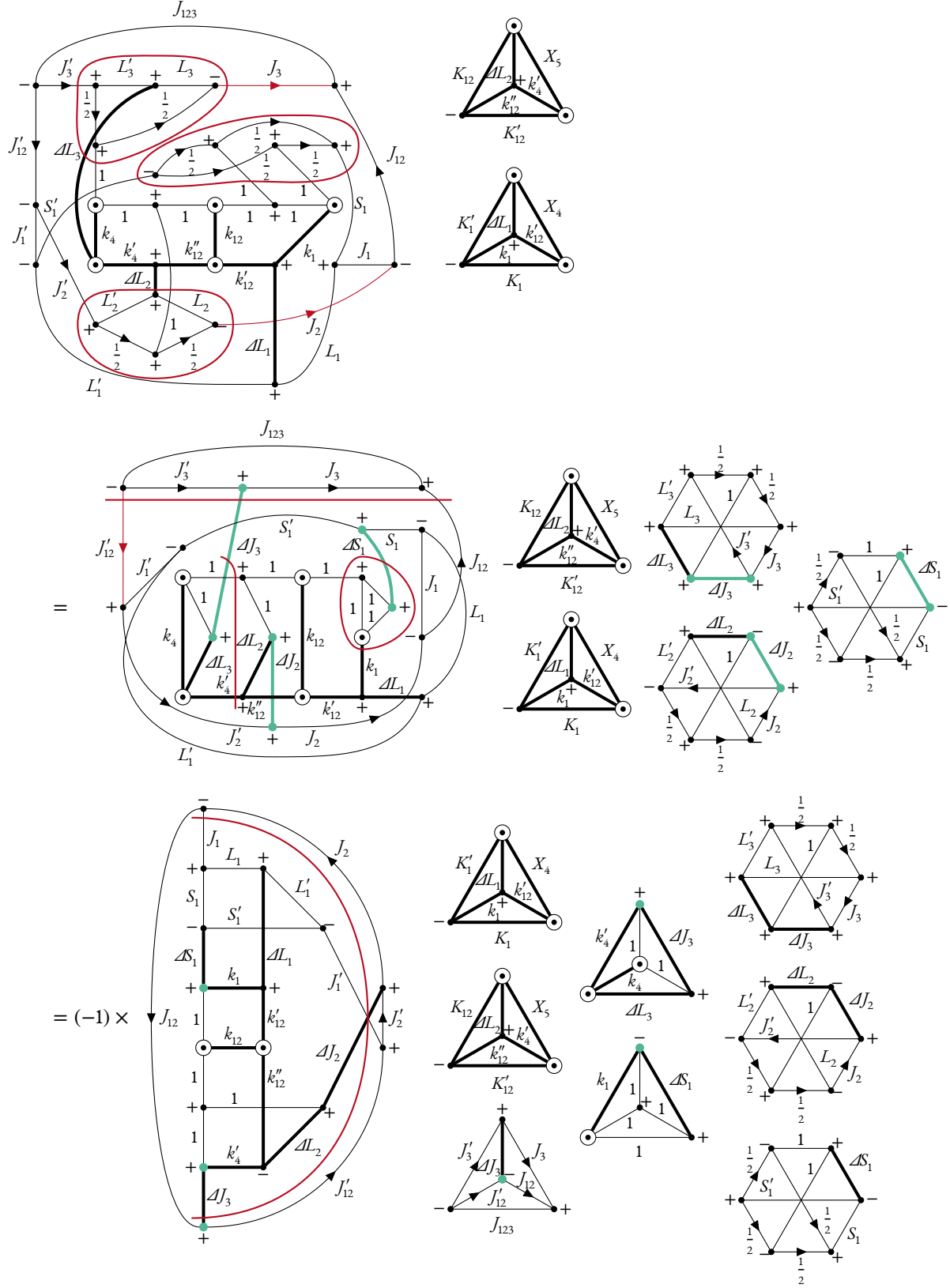
The derivation for structure (Id) works in the same way as the previous ones. First we obtain a diagrammatic expression and join coordinate lines as much as possible,

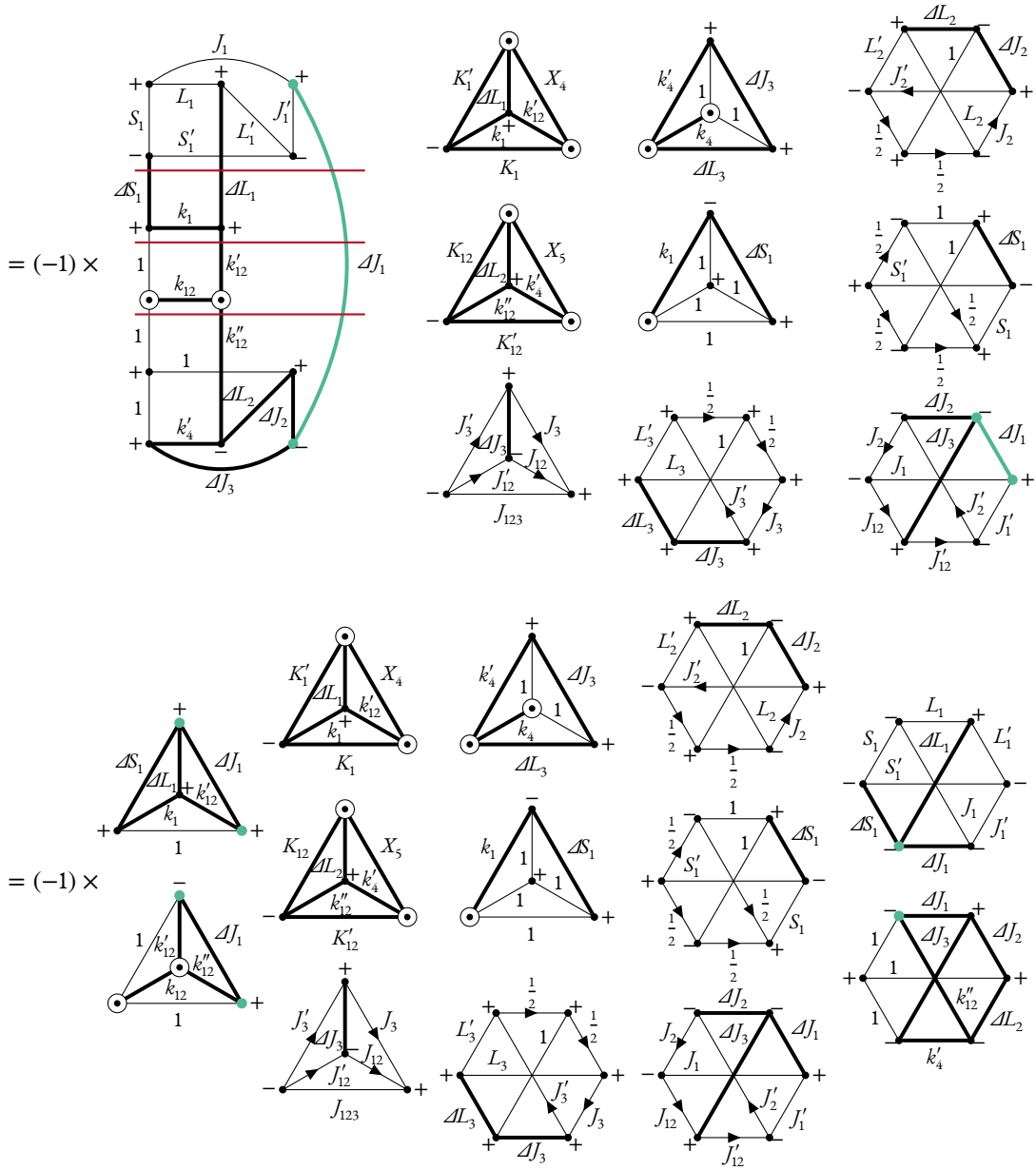
$$\begin{aligned}
& \left\langle m'_{s_a} m'_{s_b} m'_{s_c} m'_{s_d}, \pi'_1 \pi'_2 \pi'_3 \left| V_{\text{Id}}^{(c)} \right| m_{s_a} m_{s_b} m_{s_c} m_{s_d}, \pi_1 \pi_2 \pi_3 \right\rangle \\
&= \left\langle m'_{s_a} m'_{s_b} m'_{s_c} m'_{s_d} \left| -\frac{2g_A^6}{(2F_\pi)^6} \frac{\sigma_1 \cdot q_1 \sigma_4 \cdot q_4 q_{12} \times q_1 \cdot \sigma_2 (q_{12} \times q_4) \cdot \sigma_3}{[q_1^2 + M_\pi^2][q_{12}^2 + M_\pi^2][q_4^2 + M_\pi^2]} \right| m_{s_a} m_{s_b} m_{s_c} m_{s_d} \right\rangle \\
&= \begin{array}{c} \text{Diagram 1: } \left[ \begin{array}{c} \text{Two vertices } \oplus \text{ with } \frac{1}{2}m'_{s_a} \text{ and } \frac{1}{2}m'_{s_d} \text{ lines.} \\ \text{Two vertices } \oplus \text{ with } \frac{1}{2}m'_{s_b} \text{ and } \frac{1}{2}m'_{s_c} \text{ lines.} \\ \text{Two vertices } \oplus \text{ with } \frac{1}{2}m_{s_a} \text{ and } \frac{1}{2}m_{s_d} \text{ lines.} \\ \text{Two vertices } \oplus \text{ with } \frac{1}{2}m_{s_b} \text{ and } \frac{1}{2}m_{s_c} \text{ lines.} \end{array} \right] \\ \times \frac{432g_A^6}{(2F_\pi)^6} \frac{q_1^2}{q_1^2 + M_\pi^2} \frac{q_4^2}{q_4^2 + M_\pi^2} \frac{q_{12}^2}{[q_{12}^2 + M_\pi^2]^2} \\ \text{Diagram 2: } \left[ \begin{array}{c} \text{Four vertices } \oplus \text{ connected in a chain.} \\ \text{Internal lines labeled } k_1, k_{12}, k_4. \\ \text{External lines labeled } \hat{q}_1, \hat{q}_{12}, \hat{q}_4. \end{array} \right] \times \frac{72g_A^6}{(2F_\pi)^6} \frac{q_1^2}{q_1^2 + M_\pi^2} \frac{q_4^2}{q_4^2 + M_\pi^2} \frac{q_{12}^2}{[q_{12}^2 + M_\pi^2]^2}, \\ \text{Diagram 3: } \left[ \begin{array}{c} \text{Four vertices } \oplus \text{ in a vertical chain.} \\ \text{Internal lines labeled } k_1, k_{12}, k_4. \\ \text{External lines labeled } \hat{q}_1, \hat{q}_{12}, \hat{q}_4. \end{array} \right]
\end{array}
\end{aligned}$$

afterwards we transform to Jacobi coordinates. This part is identical to the previous derivations, yielding

$$\begin{aligned}
&= \begin{array}{c} \text{Diagram 4: } \left[ \begin{array}{c} \text{Four vertices } \oplus \text{ in a vertical chain.} \\ \text{Internal lines labeled } k_1, k_{12}, k_4. \\ \text{External lines labeled } \hat{A}_1, \hat{A}_2, \hat{A}_3. \end{array} \right] \\ \times \int du_4 P_{X_4}(u_4) \int du_5 P_{X_5}(u_5) D_{K_1, K'_1}^{k_1} D_{K_{12}, K'_{12}}^{k'_{12}} \\ \times \sqrt{2}^{-K_{12}-2K_1-K'_1} \sqrt{3}^{-K_{12}-K'_{12}} (-1)^{X_4+X_5+k_{12}+k_4+k'_4} \\ \times \frac{108g_A^6}{(2F_\pi)^6} \frac{q_1(\mathcal{A}_1, q_{12}(\mathcal{A}_2, \mathcal{A}_3, u_5), u_4)^{2-k_1}}{q_1(\mathcal{A}_1, q_{12}(\mathcal{A}_2, \mathcal{A}_3, u_5), u_4)^2 + M_\pi^2} \\ \times \frac{\frac{3}{4}\mathcal{A}_3^{2+K'_{12}}}{\frac{3}{4}\mathcal{A}_3^2 + M_\pi^2} \frac{q_{12}(\mathcal{A}_2, \mathcal{A}_3, u_5)^{2+K_1-k'_{12}}}{[q_{12}(\mathcal{A}_2, \mathcal{A}_3, u_5)^2 + M_\pi^2]^2} \mathcal{A}_1^{K'_1} \mathcal{A}_2^{K_{12}}. \\ \text{Diagram 5: } \left[ \begin{array}{c} \text{Two triangles } X_4 \text{ and } X_5. \\ \text{Triangle } X_4 \text{ has vertices } K_1, K'_1 \text{ and internal lines } \mathcal{A}_1, \mathcal{A}_2, \mathcal{A}_3. \\ \text{Triangle } X_5 \text{ has vertices } K_{12}, K'_{12} \text{ and internal lines } \mathcal{A}_1, \mathcal{A}_2, \mathcal{A}_3. \end{array} \right]
\end{array}
\end{aligned}$$

At this point we can insert the expression in eq. (4.11) again and start by simplifying the diagrammatic part,





Using a traditional notation, we obtain an interaction part of

$$\begin{aligned}
 & I_{\text{Id}_{L_1, L_2, L_3, S_1, J_1, J_2, J_3, J_{12}, J_{123}; \Delta L_1, \Delta L_2, \Delta L_3}}^{L_1, L_2, L_3, S_1, J_1, J_2, J_3, J_{12}, J_{123}}(\Delta_1, \Delta_2, \Delta_3) \\
 &= \int du_4 P_{X_4}(u_4) \int du_5 P_{X_5}(u_5) \sum_{X_4, X_5, \Delta S_1} \sum_{K_1, K_{12}} \sum_{k_1, k_{12}} \sum_{k_4, k'_4} D_{K_1, K'_1}^{k_1} D_{K_{12}, K'_{12}}^{k_{12}} \sqrt{2^{-K_{12}-2K_1-K'_1}} \sqrt{3^{-K_{12}-K'_{12}}} \\
 & \quad (-1)^{J_3+J'_{12}+J_{123}+\Delta J_1+\Delta J_2+\Delta J_3+\Delta S_1+X_4+X_5} \hat{S}_1 \hat{S}'_1 \hat{J}_1 \hat{J}'_1 \hat{J}_2 \hat{J}'_2 \hat{J}_3 \hat{J}'_3 \hat{J}_{12} \hat{J}'_{12} \hat{\Delta S}_1^2 \hat{\Delta J}_1^2 \hat{\Delta J}_2^2 \hat{\Delta J}_3^2 \hat{k}_1^2 \hat{k}_2^2 \hat{k}_{12}^2 \hat{k}'_1{}^2 \hat{k}'_2{}^2 \hat{k}'_{12}{}^2 \hat{k}_4^2 \hat{k}'_4{}^2 \hat{K}_1^2 \hat{K}'_1{}^2 \hat{K}_{12}^2 \hat{K}'_{12}{}^2 \\
 & \hat{X}_4^2 \hat{X}_5^2 \begin{pmatrix} 1 & 1 & k_1 \\ 0 & 0 & 0 \end{pmatrix} \begin{pmatrix} 1 & 1 & k_4 \\ 0 & 0 & 0 \end{pmatrix} \begin{pmatrix} 1 & 1 & k_{12} \\ 0 & 0 & 0 \end{pmatrix} \begin{pmatrix} k_4 & k'_4 & \Delta L_3 \\ 0 & 0 & 0 \end{pmatrix} \begin{pmatrix} k_{12} & k'_{12} & k''_{12} \\ 0 & 0 & 0 \end{pmatrix} \begin{pmatrix} K_1 & X_4 & k'_{12} \\ 0 & 0 & 0 \end{pmatrix} \begin{pmatrix} K'_1 & X_4 & \Delta L_1 \\ 0 & 0 & 0 \end{pmatrix} \\
 & \begin{pmatrix} K_{12} & X_5 & \Delta L_2 \\ 0 & 0 & 0 \end{pmatrix} \begin{pmatrix} K'_{12} & X_5 & k'_4 \\ 0 & 0 & 0 \end{pmatrix} \left\{ \begin{matrix} k'_4 & \Delta L_2 & k''_{12} \\ K_{12} & K'_{12} & X_5 \end{matrix} \right\} \left\{ \begin{matrix} k_{12} & k'_{12} & k''_{12} \\ \Delta J_1 & 1 & 1 \end{matrix} \right\} \left\{ \begin{matrix} k'_{12} & \Delta L_1 & k_1 \\ K'_1 & K_1 & X_4 \end{matrix} \right\}
 \end{aligned}$$

$$\begin{aligned}
 & \left\{ \begin{array}{ccc} \mathcal{A}_1 & 1 & k_1 \\ k'_{12} & \mathcal{A}L_1 & \mathcal{A}J_1 \end{array} \right\} \left\{ \begin{array}{ccc} 1 & 1 & k_4 \\ k'_4 & \mathcal{A}L_3 & \mathcal{A}J_3 \end{array} \right\} \left\{ \begin{array}{ccc} J_{12} & J'_{12} & \mathcal{A}J_3 \\ J'_3 & J_3 & J_{123} \end{array} \right\} \left\{ \begin{array}{ccc} 1 & 1 & 1 \\ 1 & k_1 & \mathcal{A}_1 \end{array} \right\} \\
 & \left\{ \begin{array}{ccc} \frac{1}{2} & \frac{1}{2} & 1 \\ \frac{1}{2} & \frac{1}{2} & 1 \\ S_1 & S'_1 & \mathcal{A}_1 \end{array} \right\} \left\{ \begin{array}{ccc} L_1 & S_1 & J_1 \\ L'_1 & S'_1 & J'_1 \\ \mathcal{A}L_1 & \mathcal{A}S_1 & \mathcal{A}J_1 \end{array} \right\} \left\{ \begin{array}{ccc} L_2 & \frac{1}{2} & J_2 \\ L'_2 & \frac{1}{2} & J'_2 \\ \mathcal{A}L_2 & 1 & \mathcal{A}J_2 \end{array} \right\} \left\{ \begin{array}{ccc} L_3 & \frac{1}{2} & J_3 \\ L'_3 & \frac{1}{2} & J'_3 \\ \mathcal{A}L_3 & 1 & \mathcal{A}J_3 \end{array} \right\} \left\{ \begin{array}{ccc} J_1 & J_2 & J_{12} \\ J'_1 & J'_2 & J'_{12} \\ \mathcal{A}J_1 & \mathcal{A}J_2 & \mathcal{A}J_3 \end{array} \right\} \left\{ \begin{array}{ccc} 1 & k'_{12} & \mathcal{A}J_1 \\ 1 & \mathcal{A}L_2 & \mathcal{A}J_2 \\ 1 & k'_4 & \mathcal{A}J_3 \end{array} \right\} \frac{108g_A^6}{(2F_\pi)^6} \\
 & \mathcal{A}_1^{K'_1} \mathcal{A}_2^{K'_{12}} \frac{q_1(\mathcal{A}_1, q_{12}(\mathcal{A}_2, \mathcal{A}_3, u_5), u_4)^{2-k_1}}{q_1(\mathcal{A}_1, q_{12}(\mathcal{A}_2, \mathcal{A}_3, u_5), u_4)^2 + M_\pi^2} \frac{\frac{3}{4}\mathcal{A}_3^{2+K'_{12}} q_{12}(\mathcal{A}_2, \mathcal{A}_3, u_5)^{2+K_1-k'_{12}}}{\frac{3}{4}\mathcal{A}_3^2 + M_\pi^2} \frac{q_{12}(\mathcal{A}_2, \mathcal{A}_3, u_5)^{2+K_1-k'_{12}}}{q_{12}(\mathcal{A}_2, \mathcal{A}_3, u_5)^2 + M_\pi^2}.
 \end{aligned}$$

### A.3 CLASS II - SUBSTRUCTURE A

As in the previous cases, we start by expressing structure (IIa) diagrammatically,

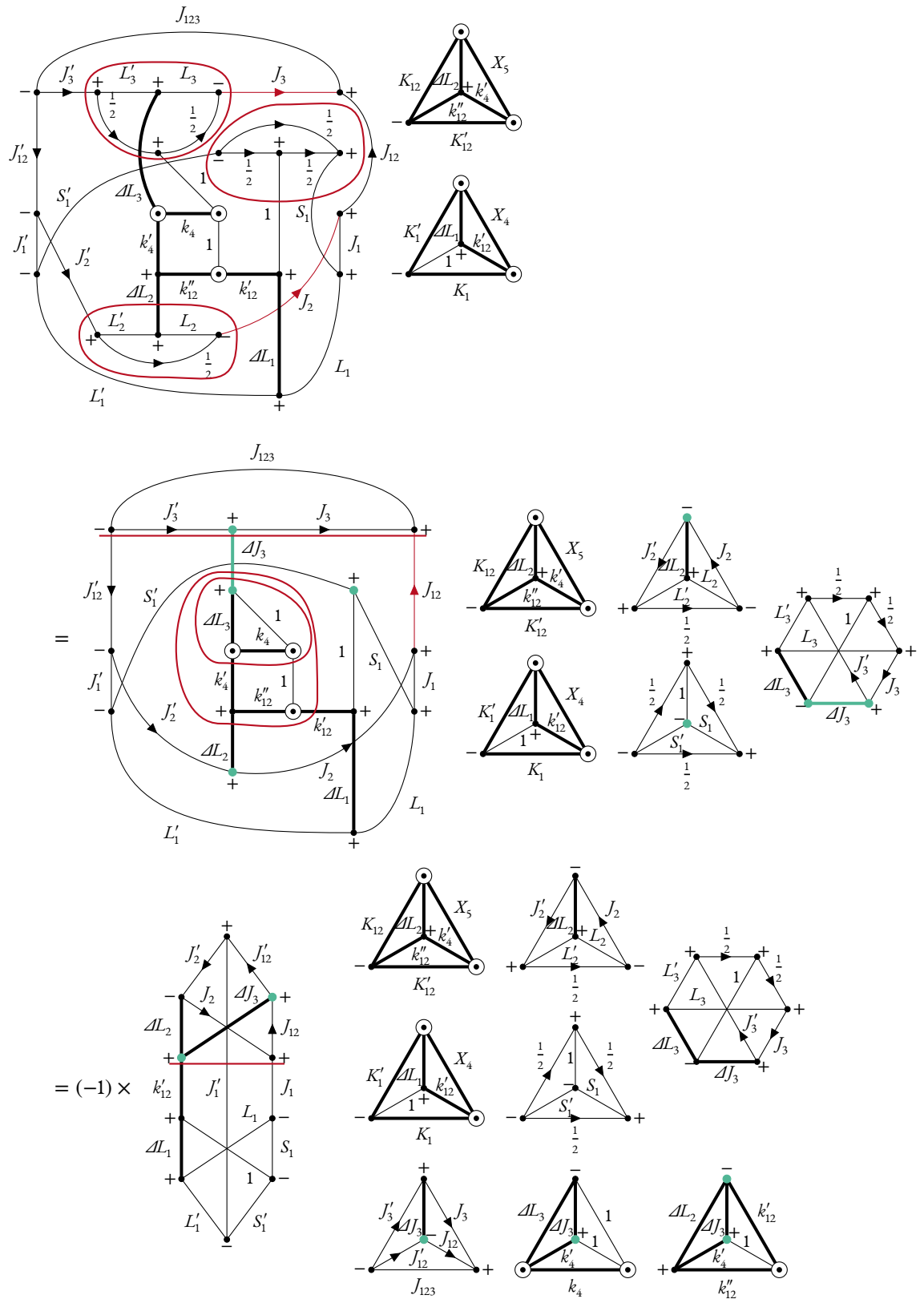
$$\begin{aligned}
 & \left\langle m'_{s_a} m'_{s_b} m'_{s_c} m'_{s_d}, \pi'_1 \pi'_2 \pi'_3 \left| V_{\text{Ia}}^{(s)} \right| m_{s_a} m_{s_b} m_{s_c} m_{s_d}, \pi_1 \pi_2 \pi_3 \right\rangle \\
 & = \left\langle m'_{s_a} m'_{s_b} m'_{s_c} m'_{s_d} \left| \frac{2g_A^4}{(2F_\pi)^6} \frac{\sigma_1 \cdot q_1 \sigma_4 \cdot q_4 q_4 \cdot q_{12}}{[q_1^2 + M_\pi^2][q_{12}^2 + M_\pi^2][q_4^2 + M_\pi^2]} \right| m_{s_a} m_{s_b} m_{s_c} m_{s_d} \right\rangle \\
 & = \begin{array}{c} \begin{array}{c} \frac{1}{2} m'_{s_a} \\ \downarrow \\ + \\ \frac{1}{2} m_{s_a} \end{array} \quad 1 \quad \hat{q}_1 \quad \begin{array}{c} \frac{1}{2} m'_{s_d} \\ \downarrow \\ + \\ \frac{1}{2} m_{s_d} \end{array} \quad 1 \quad \hat{q}_4 \quad \begin{array}{c} \hat{q}_4 \\ \rightarrow \\ \circ \end{array} \quad 1 \quad \begin{array}{c} \hat{q}_{12} \\ \rightarrow \\ \circ \end{array} \\
 \times \delta_{m_{s_b}, m'_{s_b}} \delta_{m_{s_c}, m'_{s_c}} \frac{12g_A^4}{(2F_\pi)^6} \frac{q_1}{q_1^2 + M_\pi^2} \frac{q_4^2}{q_4^2 + M_\pi^2} \frac{q_{12}}{q_{12}^2 + M_\pi^2} \\
 \begin{array}{c} \frac{1}{2} m'_{s_a} \\ \downarrow \\ + \\ \frac{1}{2} m_{s_a} \end{array} \quad 1 \quad \begin{array}{c} \hat{q}_1 \\ \rightarrow \\ \circ \end{array} \\
 = \begin{array}{c} \begin{array}{c} \frac{1}{2} m'_{s_d} \\ \downarrow \\ + \\ \frac{1}{2} m_{s_d} \end{array} \quad 1 \quad \begin{array}{c} \hat{q}_{12} \\ \rightarrow \\ \circ \end{array} \\
 \begin{array}{c} \frac{1}{2} m'_{s_d} \\ \downarrow \\ + \\ \frac{1}{2} m_{s_d} \end{array} \quad 1 \quad \begin{array}{c} \hat{q}_4 \\ \rightarrow \\ \circ \end{array} \end{array} \times \delta_{m_{s_b}, m'_{s_b}} \delta_{m_{s_c}, m'_{s_c}} \frac{-12g_A^4}{(2F_\pi)^6} \frac{q_1}{q_1^2 + M_\pi^2} \frac{q_4^2}{q_4^2 + M_\pi^2} \frac{q_{12}}{q_{12}^2 + M_\pi^2}.
 \end{array}$$

The conversion to Jacobi coordinates is exactly the same as in the previous cases, yielding

$$\begin{aligned}
 & \begin{array}{c} \frac{1}{2} m'_{s_a} \\ \downarrow \\ + \\ \frac{1}{2} m_{s_a} \end{array} \quad 1 \quad \begin{array}{c} \mathcal{A}L'_1 \\ \rightarrow \\ \circ \end{array} \quad \hat{\Delta}_1 \\
 & \begin{array}{c} \frac{1}{2} m'_{s_d} \\ \downarrow \\ + \\ \frac{1}{2} m_{s_d} \end{array} \quad 1 \quad \begin{array}{c} k'_{12} \\ \rightarrow \\ \circ \end{array} \quad \begin{array}{c} \mathcal{A}L'_2 \\ \rightarrow \\ \circ \end{array} \quad \hat{\Delta}_2 \\
 & \begin{array}{c} \frac{1}{2} m'_{s_d} \\ \downarrow \\ + \\ \frac{1}{2} m_{s_d} \end{array} \quad 1 \quad \begin{array}{c} k_4 \\ \rightarrow \\ \circ \end{array} \quad \begin{array}{c} k'_4 \\ \rightarrow \\ \circ \end{array} \quad \begin{array}{c} \mathcal{A}L'_3 \\ \rightarrow \\ \circ \end{array} \quad \hat{\Delta}_3 \\
 & \times \delta_{m_b, m'_b} \delta_{m_c, m'_c} \int du_4 P_{X_4}(u_4) \int du_5 P_{X_5}(u_5) D_{K_1, K'_1}^1 D_{K'_{12}, K'_{12}}^{k'_{12}} \\
 & \times \sqrt{2^{K_{12}-2K_1-K'_1}} \sqrt{3^{-K_{12}-K'_{12}}} (-1)^{X_4+X_5+k_4+k'_4} \\
 & \times \frac{3g_A^4}{(2F_\pi)^6} \frac{1}{q_1(\mathcal{A}_1, q_{12}(\mathcal{A}_2, \mathcal{A}_3, u_5), u_4)^2 + M_\pi^2} \\
 & \times \frac{\frac{3}{4}\mathcal{A}_3^{2+K'_{12}} q_{12}(\mathcal{A}_2, \mathcal{A}_3, u_5)^{1+K_1-k'_{12}}}{\frac{3}{4}\mathcal{A}_3^2 + M_\pi^2} \frac{q_{12}(\mathcal{A}_2, \mathcal{A}_3, u_5)^{2+K_1-k'_{12}}}{q_{12}(\mathcal{A}_2, \mathcal{A}_3, u_5)^2 + M_\pi^2} \mathcal{A}_1^{K'_1} \mathcal{A}_2^{K'_{12}}. \\
 & \begin{array}{c} \text{Diagram 1: Triangle with vertices } K_1, K'_1, X_4 \text{ and lines } \mathcal{A}L'_1, k'_{12}, 1. \\ \text{Diagram 2: Triangle with vertices } K'_{12}, K'_1, X_5 \text{ and lines } \mathcal{A}L'_2, k'_4, 1. \end{array}
 \end{array}$$



Again we insert the expression in eq. (4.II) and simplify the diagrammatic part, which results in



Adding the non-diagrammatic part of the expression and using a traditional representation for the 6j-symbols and 9j-symbols, we obtain

$$\begin{aligned}
 & I_{\text{IIa}}^{L'_1, L'_2, L'_3, S'_1, J'_1, J'_2, J'_3, J'_{12}, J'_{123}} \\
 & = \int du_4 P_{X_4}(u_4) \int du_5 P_{X_5}(u_5) \sum_{X_4, X_5} \sum_{K_1, K_{12}} \sum_{k_4, k'_4} \sum_{J_3} \sum_{K'_1, K'_{12}} \sum_{k'_{12}, k''_{12}} D_{K_1, K'_1}^1 D_{K_{12}, K'_{12}}^{k''_{12}} \sqrt{2}^{K_{12}-2K_1-K'_1} \sqrt{3}^{-K_{12}-K'_{12}} \\
 & (-1)^{\frac{1}{2}+X_4+X_5+k'_4+\Delta L_1+L_2+J'_2+J_3+J'_{12}+S'_1+J_{123}} \hat{S}_1 \hat{S}'_1 \hat{J}_1 \hat{J}'_1 \hat{J}_2 \hat{J}'_2 \hat{J}_3 \hat{J}'_3 \hat{J}_{12} \hat{J}'_{12} \hat{\Delta J}_3 \hat{k}_{12} \hat{k}'_{12} \hat{k}_4 \hat{k}'_4 \hat{K}_1 \hat{K}'_1 \hat{K}_{12} \hat{K}'_{12} \hat{X}_4 \hat{X}'_4 \hat{X}_5 \\
 & \begin{pmatrix} 1 & 1 & k_4 \\ 0 & 0 & 0 \end{pmatrix} \begin{pmatrix} k_4 & k'_4 & \Delta L_3 \\ 0 & 0 & 0 \end{pmatrix} \begin{pmatrix} 1 & k'_{12} & k''_{12} \\ 0 & 0 & 0 \end{pmatrix} \begin{pmatrix} K_1 & X_4 & k'_{12} \\ 0 & 0 & 0 \end{pmatrix} \begin{pmatrix} K'_1 & X_4 & \Delta L_1 \\ 0 & 0 & 0 \end{pmatrix} \begin{pmatrix} K_{12} & X_5 & \Delta L_2 \\ 0 & 0 & 0 \end{pmatrix} \\
 & \begin{pmatrix} K'_{12} & X_5 & k'_4 \\ 0 & 0 & 0 \end{pmatrix} \begin{Bmatrix} k'_4 & \Delta L_2 & k''_{12} \\ K_{12} & K'_{12} & X_5 \end{Bmatrix} \begin{Bmatrix} k'_{12} & \Delta L_1 & 1 \\ K'_1 & K_1 & X_4 \end{Bmatrix} \begin{Bmatrix} 1 & 1 & k_4 \\ k'_4 & \Delta L_3 & \Delta J_3 \end{Bmatrix} \begin{Bmatrix} J_{12} & J'_{12} & \Delta J_3 \\ J'_3 & J_3 & J_{123} \end{Bmatrix} \\
 & \begin{Bmatrix} S_1 & S'_1 & 1 \\ \frac{1}{2} & \frac{1}{2} & \frac{1}{2} \end{Bmatrix} \begin{Bmatrix} L_2 & L'_2 & \Delta L_2 \\ J'_2 & J_2 & \frac{1}{2} \end{Bmatrix} \begin{Bmatrix} 1 & \Delta J_3 & k'_4 \\ \Delta L_2 & k''_{12} & k'_{12} \end{Bmatrix} \begin{Bmatrix} L_1 & S_1 & J_1 \\ L'_1 & S'_1 & J'_1 \\ \Delta L_1 & 1 & k'_{12} \end{Bmatrix} \begin{Bmatrix} L_3 & \frac{1}{2} & J_3 \\ L'_3 & \frac{1}{2} & J'_3 \\ \Delta L_3 & 1 & \Delta J_3 \end{Bmatrix} \begin{Bmatrix} J_1 & J_2 & J_{12} \\ J'_1 & J'_2 & J'_{12} \\ k'_{12} & \Delta L_2 & \Delta J_3 \end{Bmatrix} \\
 & \frac{3g_A^4}{(2F_\pi)^6} \Delta_1^{K'_1} \Delta_2^{K_{12}} \frac{1}{q_1(\Delta_1, q_{12}(\Delta_2, \Delta_3, u_5), u_4)^2 + M_\pi^2} \frac{\frac{3}{4} \Delta_3^{2+K'_{12}}}{q_1(\Delta_2, \Delta_3, u_5)^2 + M_\pi^2} \frac{q_{12}(\Delta_2, \Delta_3, u_5)^{1+K_1-k'_{12}}}{q_1(\Delta_2, \Delta_3, u_5)^2 + M_\pi^2}.
 \end{aligned}$$

#### A.4 CLASS II - SUBSTRUCTURE B

Expressing the operator structure (IIb) with diagrams yields

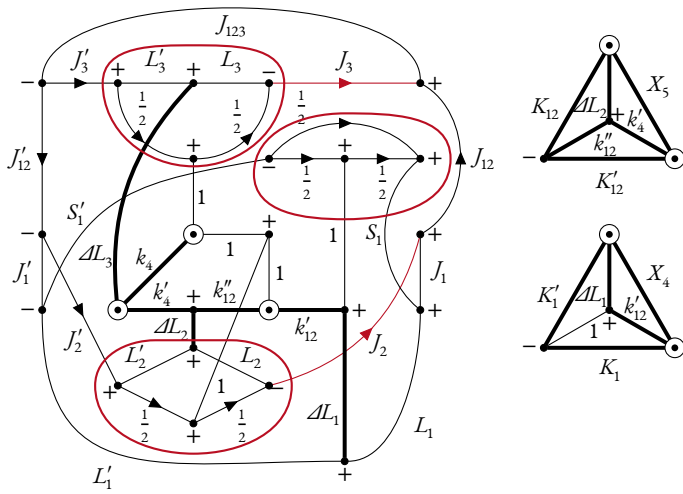
$$\begin{aligned}
 & \left\langle m'_{s_a} m'_{s_b} m'_{s_c} m'_{s_d} \left| V_{\text{IIb}}^{(9)} \right| m_{s_a} m_{s_b} m_{s_c} m_{s_d}, \boldsymbol{\pi}_1 \boldsymbol{\pi}_2 \boldsymbol{\pi}_3 \right\rangle \\
 & = \left\langle m'_{s_a} m'_{s_b} m'_{s_c} m'_{s_d} \left| \frac{2g_A^4}{(2F_\pi)^6} \frac{\boldsymbol{\sigma}_1 \cdot \mathbf{q}_1 \boldsymbol{\sigma}_4 \cdot \mathbf{q}_4 (q_{12} \times \mathbf{q}_4) \cdot \boldsymbol{\sigma}_3}{[q_1^2 + M_\pi^2][q_{12}^2 + M_\pi^2][q_4^2 + M_\pi^2]} \right| m_{s_a} m_{s_b} m_{s_c} m_{s_d} \right\rangle
 \end{aligned}$$

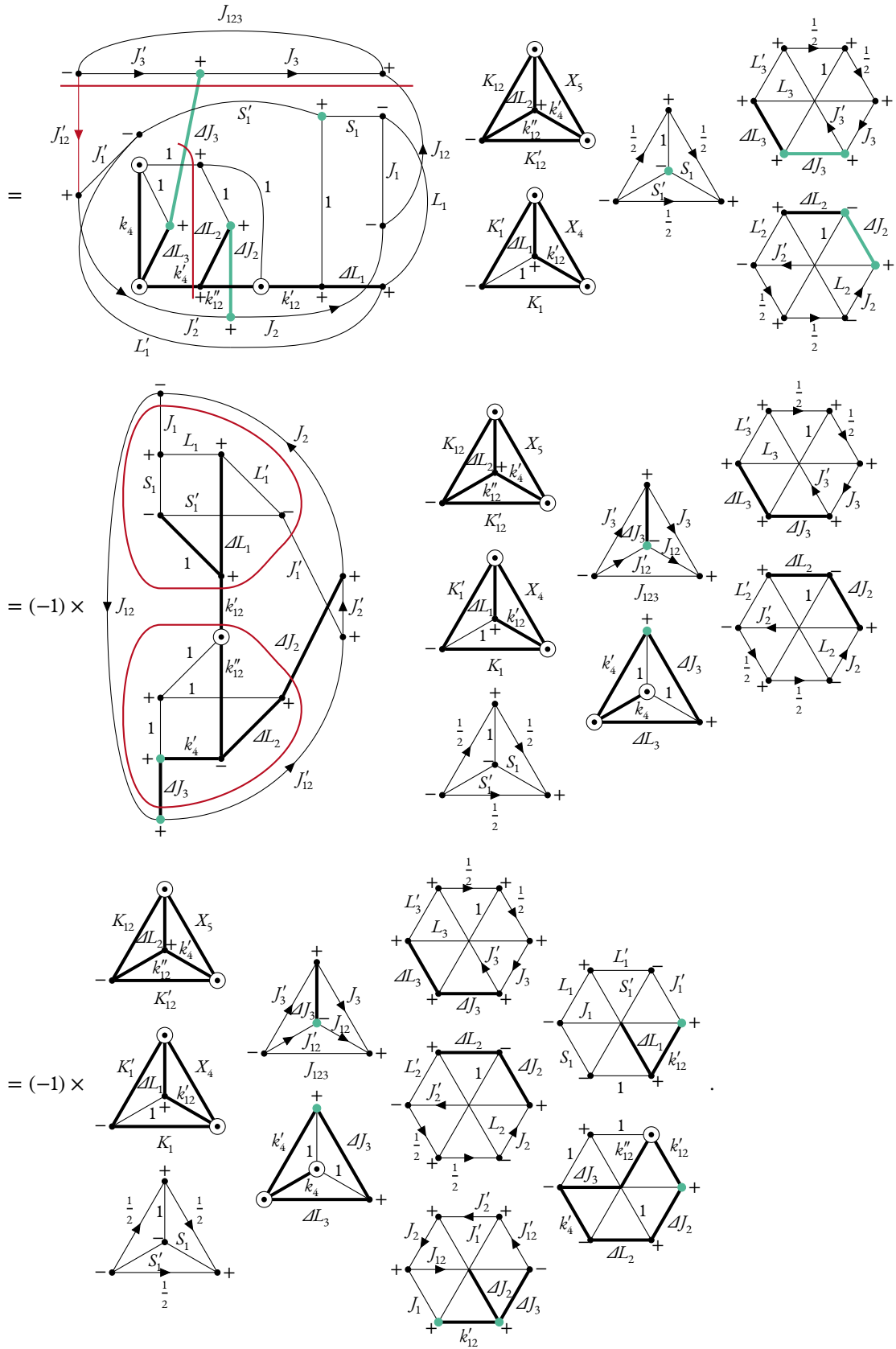
$$\begin{aligned}
 &= \text{Diagram 1} \times \delta_{m_b, m'_b} \frac{-72ig_A^4}{(2F_\pi)^6} \frac{q_1}{q_1^2 + M_\pi^2} \frac{q_4^2}{q_4^2 + M_\pi^2} \frac{q_{12}}{q_{12}^2 + M_\pi^2} \\
 &= \text{Diagram 2} \times \delta_{m_b, m'_b} \frac{-72ig_A^4}{(2F_\pi)^6} \frac{q_1}{q_1^2 + M_\pi^2} \frac{q_4^2}{q_4^2 + M_\pi^2} \frac{q_{12}}{q_{12}^2 + M_\pi^2}.
 \end{aligned}$$

The coordinate transformation is identical to the previous derivations, yielding

$$\begin{aligned}
 &= \text{Diagram 3} \times \delta_{m_b, m'_b} \int du_4 P_{X_4}(u_4) \int du_5 P_{X_5}(u_5) D_{K_1, K'_1}^1 D_{K_{12}, K'_{12}}^{k''_{12}} \\
 &\quad \times \sqrt{2}^{K_{12}-2K_1-K'_1} \sqrt{3}^{-K_{12}-K'_{12}} (-1)^{X_4+X_5+k_4+k'_4} \\
 &\quad \times \frac{18ig_A^4}{(2F_\pi)^6} \frac{1}{q_1(\Delta_1, q_{12}(\Delta_2, \Delta_3, u_5), u_4)^2 + M_\pi^2} \\
 &\quad \times \frac{\frac{3}{4}\Delta_3^{2+K'_{12}}}{\frac{3}{4}\Delta_3^2 + M_\pi^2} \frac{q_{12}(\Delta_2, \Delta_3, u_5)^{1+K_1-k''_{12}}}{q_{12}(\Delta_2, \Delta_3, u_5)^2 + M_\pi^2} \Delta_1^{K'_1} \Delta_2^{K_{12}}.
 \end{aligned}$$

At this point we can insert the expression in eq. (4.11) again and start by simplifying the diagrammatic part,





Combining the diagrammatic part with the remaining parts of the formulae, we obtain

$$\begin{aligned}
& I_{\text{Ib}}^{L'_1, L'_2, L'_3, S'_1, J'_1, J'_2, J'_3, J'_{12}, J'_{123}} \\
&= \int d u_4 P_{X_4}(u_4) \int d u_5 P_{X_5}(u_5) \sum_{X_4, X_5} \sum_{K_1, K_{12}} \sum_{k_4, k'_4} D_{K_1, K'_1}^1 D_{K_{12}, K'_{12}}^{k''_{12}} \sqrt{2^{K_{12}-2K_1-K'_1}} \sqrt{3^{-K_{12}-K'_1}} \\
& \quad (-1)^{1+S'_1+\Delta L_1+J_3+\Delta J_2+\Delta J_3+J'_{12}+J_{123}+X_4+X_5} \hat{S}_1 \hat{S}'_1 \hat{J}_1 \hat{J}'_1 \hat{J}_2 \hat{J}'_2 \hat{J}_3 \hat{J}'_3 \hat{J}_{12} \hat{J}'_{12} \hat{\Delta} \hat{J}_2^2 \hat{\Delta} \hat{J}_3^2 \hat{k}_{12}^2 \hat{k}'_{12} \hat{k}_4^2 \hat{k}'_4 \hat{K}_1^2 \hat{K}'_1 \hat{K}_{12}^2 \hat{K}'_{12} \hat{X}_4^2 \hat{X}_5^2 \\
& \quad \begin{pmatrix} 1 & 1 & k_4 \\ 0 & 0 & 0 \end{pmatrix} \begin{pmatrix} k_4 & k'_4 & \Delta L_3 \\ 0 & 0 & 0 \end{pmatrix} \begin{pmatrix} 1 & k'_{12} & k''_{12} \\ 0 & 0 & 0 \end{pmatrix} \begin{pmatrix} K_1 & X_4 & k'_{12} \\ 0 & 0 & 0 \end{pmatrix} \begin{pmatrix} K'_1 & X_4 & \Delta L_1 \\ 0 & 0 & 0 \end{pmatrix} \begin{pmatrix} K_{12} & X_5 & \Delta L_2 \\ 0 & 0 & 0 \end{pmatrix} \\
& \quad \begin{pmatrix} K'_{12} & X_5 & k'_4 \\ 0 & 0 & 0 \end{pmatrix} \begin{Bmatrix} k'_4 & \Delta L_2 & k''_{12} \\ K_{12} & K'_{12} & X_5 \end{Bmatrix} \begin{Bmatrix} k'_{12} & \Delta L_1 & 1 \\ K'_1 & K_1 & X_4 \end{Bmatrix} \begin{Bmatrix} S_1 & S'_1 & 1 \\ \frac{1}{2} & \frac{1}{2} & \frac{1}{2} \end{Bmatrix} \begin{Bmatrix} J_{12} & J'_{12} & \Delta J_3 \\ J_3 & J_3 & J_{123} \end{Bmatrix} \begin{Bmatrix} 1 & 1 & k_4 \\ k'_4 & \Delta L_3 & \Delta J_3 \end{Bmatrix} \\
& \quad \begin{Bmatrix} L_1 & S_1 & J_1 \\ L'_1 & S'_1 & J'_1 \\ \Delta L_1 & 1 & k'_{12} \end{Bmatrix} \begin{Bmatrix} L_2 & \frac{1}{2} & J_2 \\ L'_2 & \frac{1}{2} & J'_2 \\ \Delta L_2 & 1 & \Delta J_2 \end{Bmatrix} \begin{Bmatrix} L_3 & \frac{1}{2} & J_3 \\ L'_3 & \frac{1}{2} & J'_3 \\ \Delta L_3 & 1 & \Delta J_3 \end{Bmatrix} \begin{Bmatrix} J_1 & J_2 & J_{12} \\ J'_1 & J'_2 & J'_{12} \\ k'_{12} & \Delta J_2 & \Delta J_3 \end{Bmatrix} \begin{Bmatrix} 1 & 1 & 1 \\ k''_{12} & \Delta L_2 & k'_4 \\ k'_{12} & \Delta J_2 & \Delta J_3 \end{Bmatrix} \\
& \quad \frac{18 i g_A^4}{(2F_\pi)^6} \frac{1}{q_1(\Delta_1, q_{12}(\Delta_2, \Delta_3, u_5), u_4)^2 + M_\pi^2} \frac{\frac{3}{4} \Delta_3^{2+K'_{12}}}{\Delta_3^2 + M_\pi^2} \frac{q_{12}(\Delta_2, \Delta_3, u_5)^{1+K_1-k''_{12}}}{q_{12}(\Delta_2, \Delta_3, u_5)^2 + M_\pi^2} \Delta_1^{K'_1} \Delta_2^{K'_{12}}.
\end{aligned}$$

## A.5 CLASS II - SUBSTRUCTURE C

Again, we start by expressing the operator structure (IIc) with diagrams and reduce the number of coordinate lines. As the coordinates in this expression differ, we have to perform the coordinate change again,

$$\begin{aligned}
& \left\langle m'_{s_a} m'_{s_b} m'_{s_c} m'_{s_d}, \pi'_1 \pi'_2 \pi'_3 \left| V_{\text{IIc}}^{(6)} \right| m_{s_a} m_{s_b} m_{s_c} m_{s_d}, \pi_1 \pi_2 \pi_3 \right\rangle \\
&= \left\langle m'_{s_a} m'_{s_b} m'_{s_c} m'_{s_d} \left| -\frac{g_A^4}{(2F_\pi)^6} \frac{\sigma_1 \cdot q_{12} \sigma_2 \cdot q_2 \sigma_3 \cdot q_3 \sigma_4 \cdot q_4}{[q_2^2 + M_\pi^2][q_3^2 + M_\pi^2][q_4^2 + M_\pi^2]} \right| m_{s_a} m_{s_b} m_{s_c} m_{s_d} \right\rangle \\
&= \begin{array}{cccc} \begin{array}{c} \frac{1}{2} m'_{s_a} \\ \downarrow \\ + \\ \uparrow \\ \frac{1}{2} m_{s_a} \end{array} & \begin{array}{c} \frac{1}{2} m'_{s_b} \\ \downarrow \\ + \\ \uparrow \\ \frac{1}{2} m_{s_b} \end{array} & \begin{array}{c} \frac{1}{2} m'_{s_c} \\ \downarrow \\ + \\ \uparrow \\ \frac{1}{2} m_{s_c} \end{array} & \begin{array}{c} \frac{1}{2} m'_{s_d} \\ \downarrow \\ + \\ \uparrow \\ \frac{1}{2} m_{s_d} \end{array} \\ \hline & \begin{array}{cccc} 1 & \hat{q}_{12} & 1 & \hat{q}_2 & 1 & \hat{q}_3 & 1 & \hat{q}_4 \end{array} \end{array} \\
& \times \frac{-36 g_A^4}{(2F_\pi)^6} \frac{q_{12}}{q_2^2 + M_\pi^2} \frac{q_3}{q_3^2 + M_\pi^2} \frac{q_4}{q_4^2 + M_\pi^2}.
\end{aligned}$$

We first transform  $q_2$  to  $q_{12}$  and  $\Delta_1$ , introducing an integral over  $u_4$ , which corresponds to the angle  $\hat{q}_{12} \cdot \hat{\Delta}_1$ . Note that the coordinate transformation has a minus sign, which results in a phase factor,

$$\times \int du_4 P_{X_4}(u_4) D_{K_2, K'_2}^1 \sqrt{2^{-1-K_2}} (-1)^{K'_2+1} \frac{18g_A^4}{(2F_\pi)^6} q_{12}^{1+K_2} \frac{\mathcal{A}_1^{K'_2}}{q_2(\mathcal{A}_1, q_{12}, u_4)^2 + M_\pi^2 q_3^2 + M_\pi^2 q_4^2 + M_\pi^2}.$$

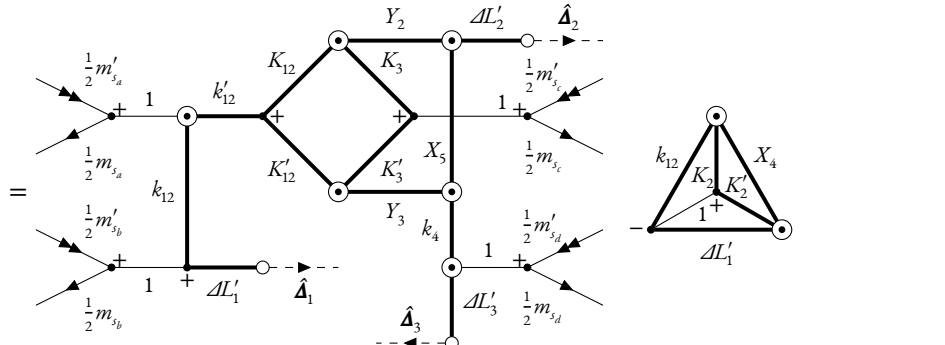
Combining the coordinate lines exactly cancels the phase factor and leads to

$$\times \int du_4 P_{X_4}(u_4) D_{K_2, K'_2}^1 \sqrt{2^{-1-K_2}} \frac{18g_A^4}{(2F_\pi)^6} q_{12}^{1+K_2} \frac{\mathcal{A}_1^{K'_2}}{q_2(\mathcal{A}_1, q_{12}, u_4)^2 + M_\pi^2 q_3^2 + M_\pi^2 q_4^2 + M_\pi^2}.$$

At this point, we can separate a 6j-symbol and transform the remaining coordinates. Again, a phase factor is introduced due to the coordinate transformation. Furthermore we obtain an integral over  $u_5$ , which corresponds to the angle  $\hat{\Delta}_2 \cdot \hat{\Delta}_3$ , yielding

$$\times \int du_4 P_{X_4}(u_4) \int du_5 P_{X_5}(u_5) D_{K_2, K'_2}^1 D_{K_3, K'_3}^1 D_{K_{12}, K'_{12}}^{k'_{12}} \sqrt{2^{-1-K_2+K_3-2K'_3+K_{12}}} \sqrt{3^{-k'_{12}}} (-1)^{K_3+1} \frac{9g_A^4}{2(2F_\pi)^6} \frac{q_{12}(\mathcal{A}_2, \mathcal{A}_3, u_5)^{1+K_2-k'_{12}} \mathcal{A}_1^{K'_2} \mathcal{A}_2^{K_3+K_{12}}}{q_2(\mathcal{A}_1, q_{12}(\mathcal{A}_2, \mathcal{A}_3, u_5), u_4)^2 + M_\pi^2 q_3(\mathcal{A}_2, \mathcal{A}_3, u_5)^2 + M_\pi^2 \frac{3}{4} \mathcal{A}_3^2 + M_\pi^2} \frac{1}{\mathcal{A}_3^{1+K'_3+K'_{12}}}.$$

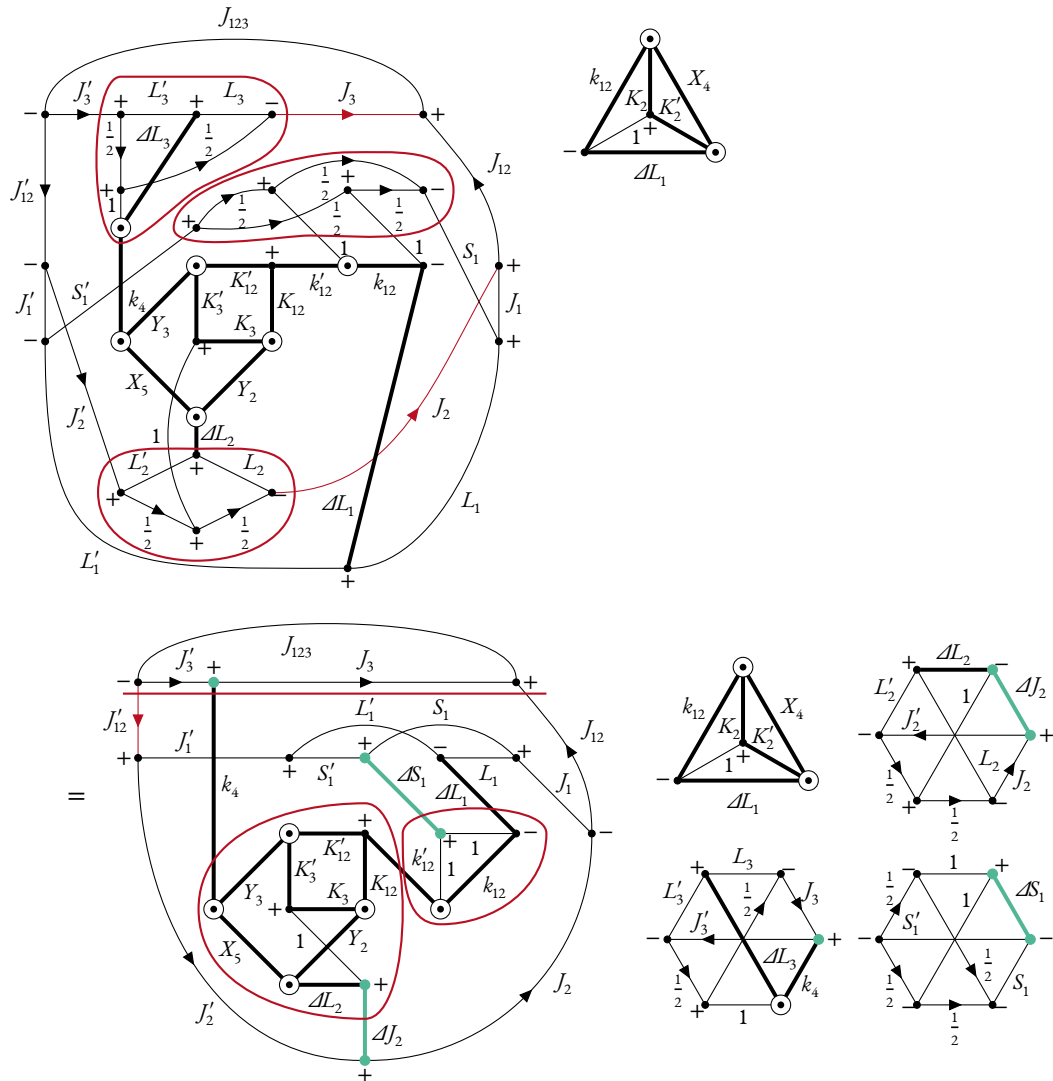
Simplifying the expression by combining coordinate lines, we obtain

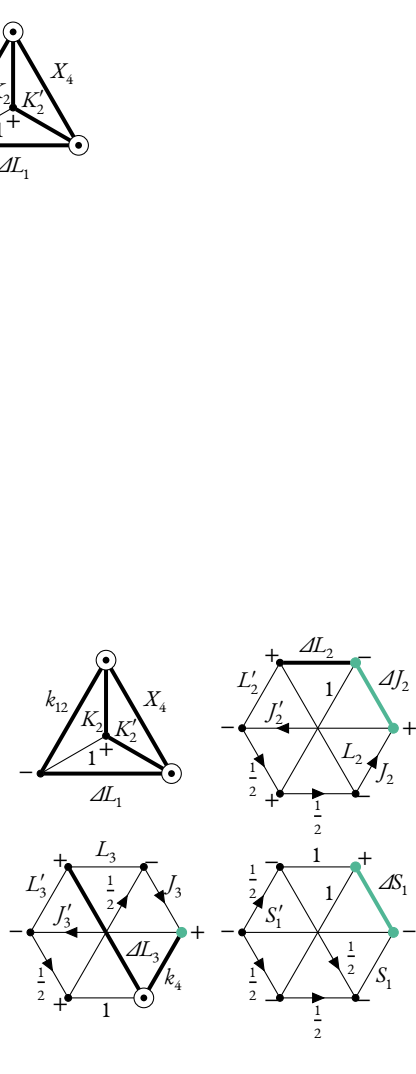


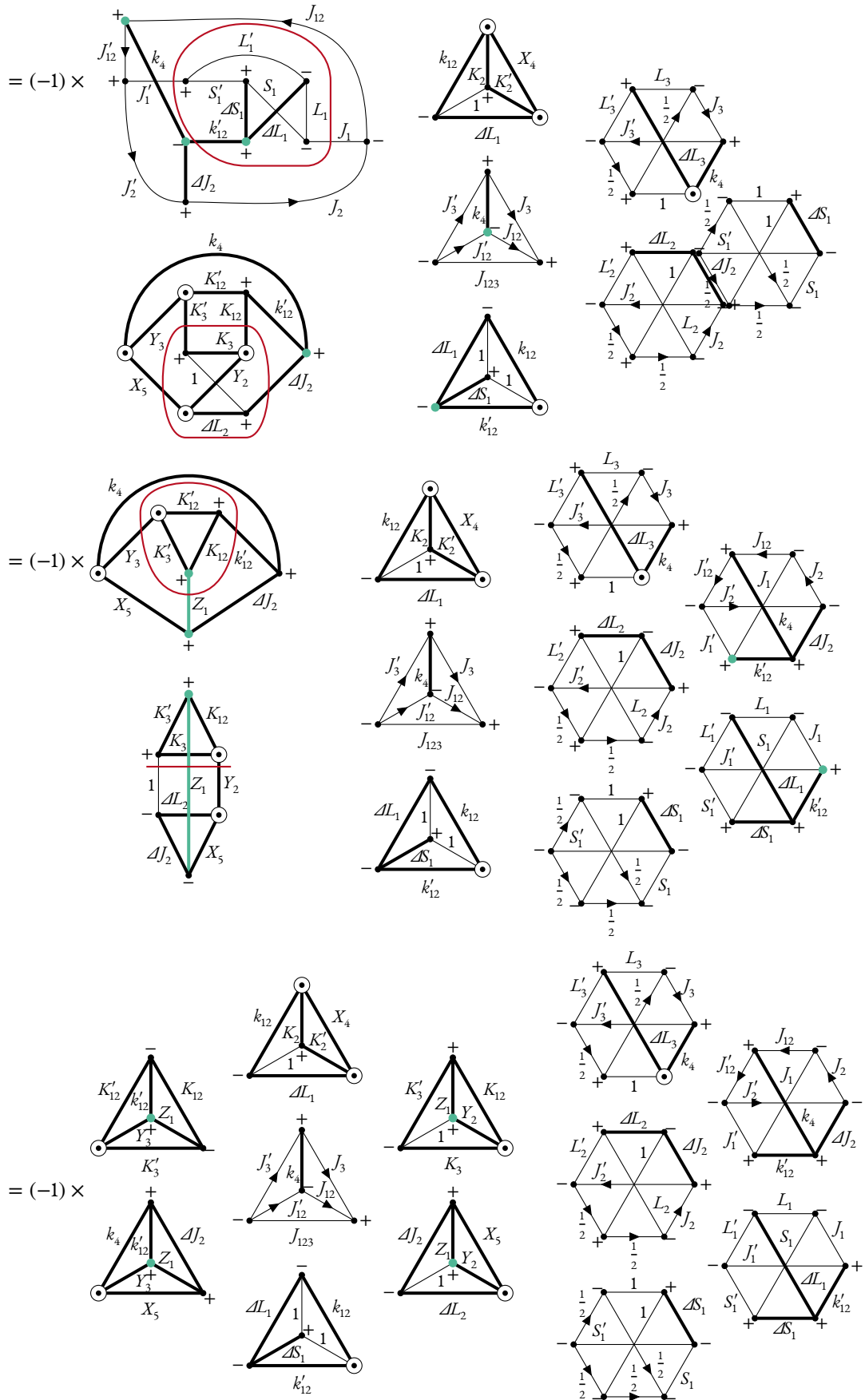
$$\times \int du_4 P_{X_4}(u_4) \int du_5 P_{X_5}(u_5) D_{K_2, K'_2}^1 D_{K_3, K'_3}^1 D_{K_{12}, K'_{12}}^{k_{12}} \sqrt{2}^{-1-K_2+K_3-2K'_3+K_{12}} \sqrt{3}^{-k_{12}} (-1)^{K'_3+X_5+\Delta L'_3}$$

$$\frac{\vartheta g_A^4}{2(2F_\pi)^6} \frac{q_{12}(\Delta_2, \Delta_3, u_5)^{1+K_2-k'_{12}} \Delta_1^{K'_2} \Delta_2^{K_3+K_{12}}}{q_2(\Delta_1, q_{12}(\Delta_2, \Delta_3, u_5), u_4)^2 + M_\pi^2} \frac{1}{q_3(\Delta_2, \Delta_3, u_5)^2 + M_\pi^2} \frac{\Delta_3^{1+K'_3+K'_{12}}}{\Delta_3^{\frac{3}{4}} + M_\pi^2}$$

Inserting the expression in eq. (4.11) again and simplifying the diagrammatic part yields



$$=$$






In traditional form and combined with the non-diagrammatic part of the formulae, we obtain an interaction part of

$$\begin{aligned}
& I_{\text{IIc}}^{L'_1, L'_2, L'_3, S'_1, J'_1, J'_2, J'_3, J'_{12}, J'_{123}}(\mathcal{A}_1, \mathcal{A}_2, \mathcal{A}_3) \\
&= \int d u_4 P_{X_4}(u_4) \int d u_5 P_{X_5}(u_5) \sum_{\substack{X_4, X_5 \\ \mathcal{A}_1, \mathcal{A}_2}} \sum_{\substack{K_2, K_3, K_{12} \\ K'_2, K'_3, K'_{12}}} \sum_{\substack{k_4, k_{12} \\ k'_4, k'_{12}}} \sum_{\substack{Y_2, Y_3 \\ Z_1}} D_{K_2, K_2}^1 D_{K_3, K_3}^1 D_{K_{12}, K_{12}}^{k'_{12}} \sqrt{2}^{-1-K_2+K_3-2K'_3+K_{12}} \sqrt{3}^{-k'_{12}} \\
& (-1)^{k'_{12}+K_{12}+X_5+Z_1+\mathcal{A}_1+\mathcal{A}_2+\mathcal{A}_3+J_3+J'_{12}+J_{123}} \hat{S}_1 \hat{S}'_1 \hat{J}_1 \hat{J}'_1 \hat{J}_2 \hat{J}'_2 \hat{J}_3 \hat{J}'_3 \hat{J}_{12} \hat{J}'_{12} \widehat{\mathcal{A}}_1 \widehat{\mathcal{A}}_2 \widehat{k}_4 \widehat{k}'_4 \widehat{k}_{12} \widehat{k}'_{12} \widehat{Y}_2 \widehat{Y}_3 \widehat{Z}_1 \widehat{K}_2 \widehat{K}'_2 \widehat{K}_3 \widehat{K}'_3 \widehat{K}_{12} \widehat{K}'_{12} \\
& \mathcal{X}_4^2 \mathcal{X}_5^2 \begin{pmatrix} 1 & \mathcal{A}L_3 & k_4 \\ 0 & 0 & 0 \end{pmatrix} \begin{pmatrix} 1 & k_{12} & k'_{12} \\ 0 & 0 & 0 \end{pmatrix} \begin{pmatrix} Y_2 & K_3 & K_{12} \\ 0 & 0 & 0 \end{pmatrix} \begin{pmatrix} Y_3 & K'_3 & K'_{12} \\ 0 & 0 & 0 \end{pmatrix} \begin{pmatrix} K_2 & X_4 & k_{12} \\ 0 & 0 & 0 \end{pmatrix} \\
& \begin{pmatrix} K'_2 & X_4 & \mathcal{A}L_1 \\ 0 & 0 & 0 \end{pmatrix} \begin{pmatrix} Y_2 & X_5 & \mathcal{A}L_2 \\ 0 & 0 & 0 \end{pmatrix} \begin{pmatrix} Y_3 & X_5 & k_4 \\ 0 & 0 & 0 \end{pmatrix} \left\{ \begin{matrix} k'_{12} & Y_3 & Z_1 \\ K'_3 & K_{12} & K'_{12} \end{matrix} \right\} \left\{ \begin{matrix} k'_{12} & Y_3 & Z_1 \\ X_5 & \mathcal{A}J_2 & k_4 \end{matrix} \right\} \\
& \left\{ \begin{matrix} 1 & Z_1 & Y_2 \\ K_{12} & K_3 & K'_3 \end{matrix} \right\} \left\{ \begin{matrix} 1 & Z_1 & Y_2 \\ X_5 & \mathcal{A}L_2 & \mathcal{A}J_2 \end{matrix} \right\} \left\{ \begin{matrix} 1 & K_2 & K'_2 \\ X_4 & \mathcal{A}L_1 & k_{12} \end{matrix} \right\} \left\{ \begin{matrix} k_4 & J_{12} & J'_{12} \\ J_{123} & J'_3 & J_3 \end{matrix} \right\} \left\{ \begin{matrix} \mathcal{A}S_1 & 1 & 1 \\ k_{12} & k'_{12} & \mathcal{A}L_1 \end{matrix} \right\} \\
& \left\{ \begin{matrix} \frac{1}{2} & \frac{1}{2} & 1 \\ \frac{1}{2} & \frac{1}{2} & 1 \end{matrix} \right\} \left\{ \begin{matrix} L_1 & S_1 & J_1 \\ L'_1 & S'_1 & J'_1 \end{matrix} \right\} \left\{ \begin{matrix} L_2 & \frac{1}{2} & J_2 \\ L'_2 & \frac{1}{2} & J'_2 \end{matrix} \right\} \left\{ \begin{matrix} L_3 & \frac{1}{2} & J_3 \\ L'_3 & \frac{1}{2} & J'_3 \end{matrix} \right\} \left\{ \begin{matrix} J_1 & J_2 & J_{12} \\ J'_1 & J'_2 & J'_{12} \end{matrix} \right\} \\
& \left\{ \begin{matrix} S_1 & S'_1 & \mathcal{A}S_1 \\ \mathcal{A}L_1 & \mathcal{A}S_1 & k'_{12} \end{matrix} \right\} \left\{ \begin{matrix} \mathcal{A}L_2 & 1 & \mathcal{A}J_2 \\ \mathcal{A}L_3 & 1 & k_4 \end{matrix} \right\} \left\{ \begin{matrix} k'_{12} & \mathcal{A}J_2 & k_4 \end{matrix} \right\} \\
& \frac{9g_A^4}{2(2F_\pi)^6} \frac{q_{12}(\mathcal{A}_2, \mathcal{A}_3, u_5)^{1+K_2-k'_{12}} \mathcal{A}_1^{K'_2} \mathcal{A}_2^{K_3+K_{12}}}{q_2(\mathcal{A}_1, q_{12}(\mathcal{A}_2, \mathcal{A}_3, u_5), u_4)^2 + M_\pi^2} \frac{1}{q_3(\mathcal{A}_2, \mathcal{A}_3, u_5)^2 + M_\pi^2} \frac{\mathcal{A}_3^{1+K'_3+K'_{12}}}{\mathcal{A}_3^{\frac{3}{4}} + M_\pi^2}.
\end{aligned}$$

## A.6 CLASS II - SUBSTRUCTURE D

We start by expressing the operator structure (IIId) with diagrams and perform the coordinate transformation again. This will result in one of the most complicated expressions, as it depends on all four single-particle momenta.

$$\begin{aligned}
& \left\langle m'_a m'_b m'_c m'_d, \pi'_1 \pi'_2 \pi'_3 \left| V_{\text{IIId}}^{(6)} \right| m_a m_b m_c m_d, \pi_1 \pi_2 \pi_3 \right\rangle \\
&= \left\langle m'_a m'_b m'_c m'_d \left| -\frac{g_A^4}{2(2F_\pi)^6} \frac{\sigma_1 \cdot q_1 \sigma_2 \cdot q_2 \sigma_3 \cdot q_3 \sigma_4 \cdot q_4 [q_{12}^2 + M_\pi^2]}{[q_1^2 + M_\pi^2][q_2^2 + M_\pi^2][q_3^2 + M_\pi^2][q_4^2 + M_\pi^2]} \right| m_a m_b m_c m_d \right\rangle \\
&= \begin{array}{cccc} \begin{array}{c} \frac{1}{2} m'_a \\ \downarrow \\ \bullet \\ \uparrow \\ \frac{1}{2} m_a \end{array} & \begin{array}{c} \frac{1}{2} m'_b \\ \downarrow \\ \bullet \\ \uparrow \\ \frac{1}{2} m_b \end{array} & \begin{array}{c} \frac{1}{2} m'_c \\ \downarrow \\ \bullet \\ \uparrow \\ \frac{1}{2} m_c \end{array} & \begin{array}{c} \frac{1}{2} m'_d \\ \downarrow \\ \bullet \\ \uparrow \\ \frac{1}{2} m_d \end{array} \\ \hline & \xrightarrow{1} \hat{q}_1 & \xrightarrow{1} \hat{q}_2 & \xrightarrow{1} \hat{q}_3 & \xrightarrow{1} \hat{q}_4 \end{array} \\
& \times \frac{-18g_A^4}{(2F_\pi)^6} \frac{q_1}{q_1^2 + M_\pi^2} \frac{q_2}{q_2^2 + M_\pi^2} \frac{q_3}{q_3^2 + M_\pi^2} \frac{q_4}{q_4^2 + M_\pi^2} [q_{12}^2 + M_\pi^2].
\end{aligned}$$

This time we have to replace  $q_1$  and  $q_2$  in the first step using the replacements from eq. (4.13), yielding

$$\times \int du_4 P_{X_4}(u_4) D_{K_1, K'_1}^1 D_{K_2, K'_2}^1 \sqrt{2^{-2-K_1-K_2}} (-1)^{1+K'_2} \frac{g_A^4}{(2F_\pi)^6} \mathcal{A}_1^{K'_1+K'_2} \frac{1}{q_1(\mathcal{A}_1, q_{12}, u_4)^2 + M_\pi^2}$$

$$\frac{1}{q_2(\mathcal{A}_1, q_{12}, u_4)^2 + M_\pi^2} \frac{q_3}{q_3^2 + M_\pi^2} \frac{q_4}{q_4^2 + M_\pi^2} q_{12}^{K_1+K_2} [q_{12}^2 + M_\pi^2].$$

Note that the expression for  $q_2$  contains a minus sign, which results in an additional phase factor. As usual, an integral was introduced over  $u_4$ , which corresponds to the angle  $\hat{q}_{12} \cdot \hat{\Delta}_1$ . Reducing the coordinate lines of  $q_{12}$  and  $\Delta_1$  results in

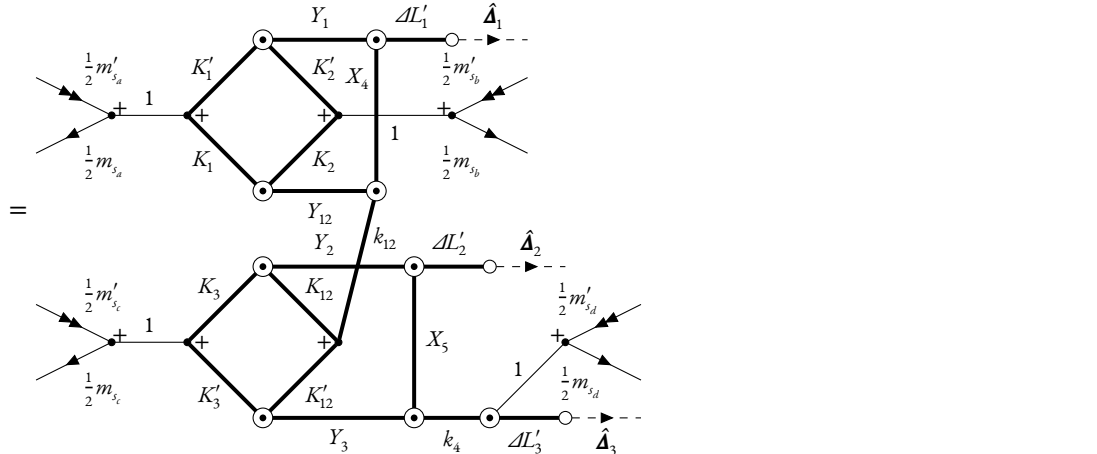
$$\times \int du_4 P_{X_4}(u_4) D_{K_1, K'_1}^1 D_{K_2, K'_2}^1 \sqrt{2^{-2-K_1-K_2}} (-1)^{1+K'_2+X_4} \frac{g_A^4}{(2F_\pi)^6} \mathcal{A}_1^{K'_1+K'_2} \frac{1}{q_1(\mathcal{A}_1, q_{12}, u_4)^2 + M_\pi^2}$$

$$\frac{1}{q_2(\mathcal{A}_1, q_{12}, u_4)^2 + M_\pi^2} \frac{q_3}{q_3^2 + M_\pi^2} \frac{q_4}{q_4^2 + M_\pi^2} q_{12}^{K_1+K_2} [q_{12}^2 + M_\pi^2].$$

We transform all three remaining coordinates in the next step, as shown in eq. (4.14), which results in

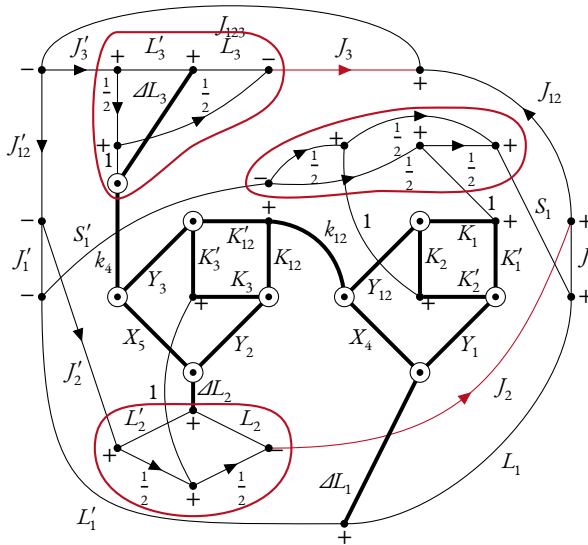
$$\begin{aligned} & \times \int du_4 P_{X_4}(u_4) \int du_5 P_{X_5}(u_5) D_{K_1, K'_1}^1 D_{K_2, K'_2}^1 D_{K_3, K'_3}^1 D_{K_{12}, K'_{12}}^{k_{12}} \sqrt{2^{-K_1-K_2+K_3-2K'_3+K_{12}}} \sqrt{3^{-k_{12}}} (-1)^{K'_2+K_3+X_4} \\ & \frac{9g_A^4}{8(2F_\pi)^6} \frac{\Delta_1^{K'_1+K'_2} \Delta_2^{K_3+K_{12}} \Delta_3^{1+K'_3+K'_{12}}}{q_1(\Delta_1, q_{12}(\Delta_2, \Delta_3, u_5), u_4)^2 + M_\pi^2} \frac{1}{q_2(\Delta_1, q_{12}(\Delta_2, \Delta_3, u_5), u_4)^2 + M_\pi^2} \\ & \frac{1}{q_3(\Delta_2, \Delta_3, u_5)^2 + M_\pi^2} \frac{1}{\Delta_3^{\frac{3}{4}} + M_\pi^2} q_{12}(\Delta_2, \Delta_3, u_5)^{K_1+K_2-k_{12}} [q_{12}(\Delta_2, \Delta_3, u_5)^2 + M_\pi^2]. \end{aligned}$$

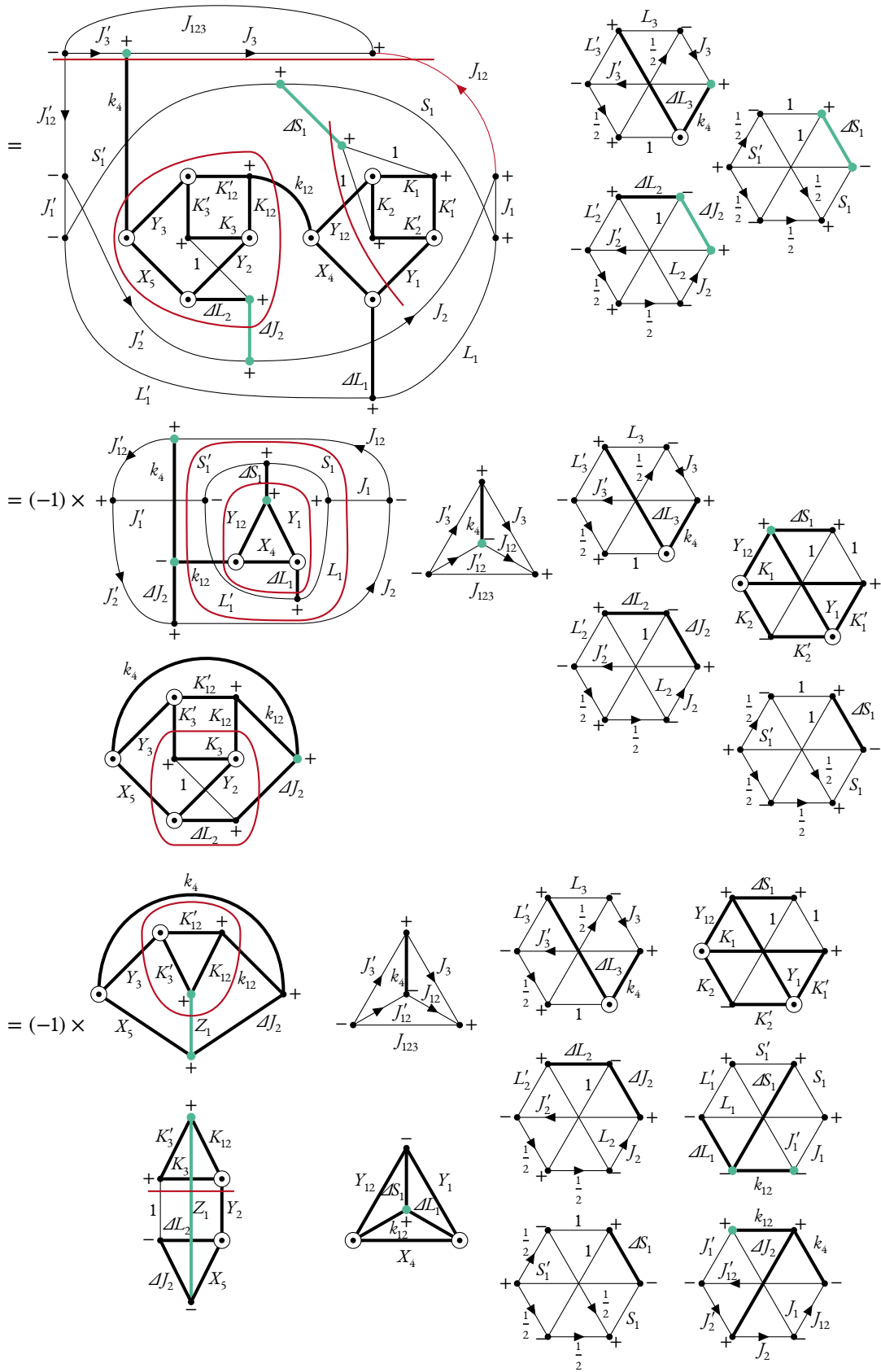
As described earlier, the integral over  $u_5$  corresponds to integration of the angle  $\hat{\Delta}_2 \cdot \hat{\Delta}_3$ . Reducing coordinate lines again yields the following expression, which is the most complicated expression so far, as all single-particle momenta are involved,

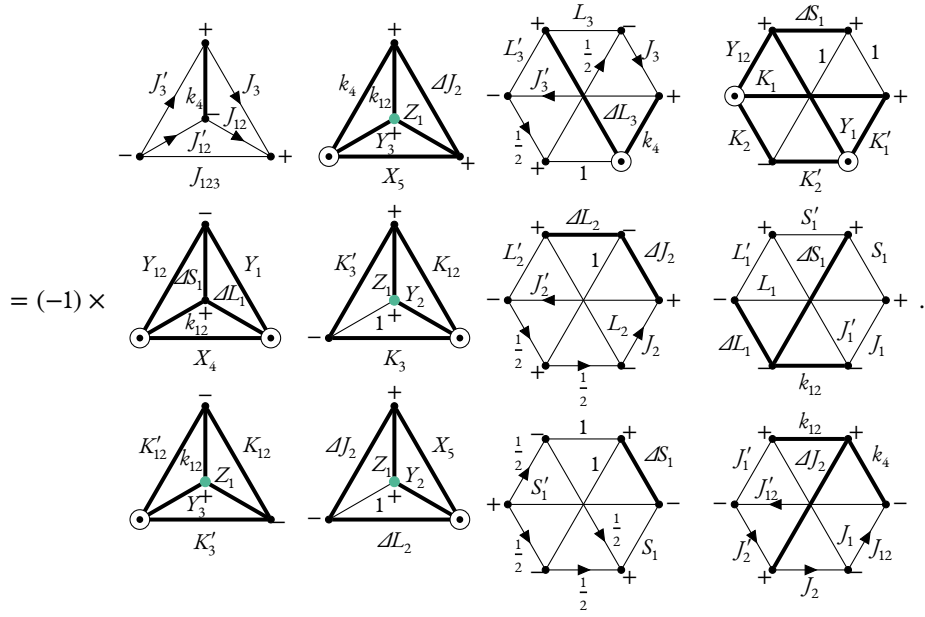


$$\begin{aligned} & \times \int du_4 P_{X_4}(u_4) \int du_5 P_{X_5}(u_5) D_{K_1, K'_1}^1 D_{K_2, K'_2}^1 D_{K_3, K'_3}^1 D_{K_{12}, K'_{12}}^{k_{12}} \sqrt{2^{-K_1-K_2+K_3-2K'_3+K_{12}}} \sqrt{3^{-k_{12}}} (-1)^{K'_2+K_3+X_4+X_5+\Delta L'_3} \\ & \frac{9g_A^4}{8(2F_\pi)^6} \frac{\Delta_1^{K'_1+K'_2} \Delta_2^{K_3+K_{12}} \Delta_3^{1+K'_3+K'_{12}}}{q_1(\Delta_1, q_{12}(\Delta_2, \Delta_3, u_5), u_4)^2 + M_\pi^2} \frac{1}{q_2(\Delta_1, q_{12}(\Delta_2, \Delta_3, u_5), u_4)^2 + M_\pi^2} \\ & \frac{1}{q_3(\Delta_2, \Delta_3, u_5)^2 + M_\pi^2} \frac{1}{\Delta_3^{\frac{3}{4}} + M_\pi^2} q_{12}(\Delta_2, \Delta_3, u_5)^{K_1+K_2-k_{12}} [q_{12}(\Delta_2, \Delta_3, u_5)^2 + M_\pi^2]. \end{aligned}$$

As done in all previous derivations, we insert the expression in eq. (4.II) and simplify the diagrammatic part,







Transforming the diagrams to a traditional form, we obtain for the interaction part:

$$\begin{aligned}
& I_{\Pi d}^{L'_1, L'_2, L'_3, S'_1, J'_1, J'_2, J'_3, J'_{12}, J'_{123}}(\mathcal{A}_1, \mathcal{A}_2, \mathcal{A}_3) \\
&= \int du_4 P_{X_4}(u_4) \int du_5 P_{X_5}(u_5) \sum_{X_4, X_5} \sum_{K_1, K_2} \sum_{K_3, K_{12}} \sum_{k_4, k_{12}} \sum_{Y_1, Y_2} D_{K_1, K'_1}^1 D_{K_2, K'_2}^1 D_{K_3, K'_3}^1 D_{K_{12}, K'_{12}}^{k_{12}} \sqrt{2^{-K_1 - K_2 + K_3 - 2K'_3 + K_{12}}} \\
& \quad \sum_{\mathcal{A}_1, \mathcal{A}_2} \sum_{K'_1, K'_2, K'_3, K'_{12}} \sum_{Z_1} \sum_{Y_3, Y_{12}} \\
& \quad \sqrt{3^{-k_{12}}} (-1)^{1+J_3+J'_{12}+J_{123}+\mathcal{A}_1+Z_1+k_4+K_1+K_{12}+Y_2} \hat{S}_1 \hat{S}'_1 \hat{J}_1 \hat{J}'_1 \hat{J}_2 \hat{J}'_2 \hat{J}_3 \hat{J}'_3 \hat{J}_{12} \hat{J}'_{12} \hat{\mathcal{A}}_1 \hat{\mathcal{A}}_2 \hat{k}_4 \hat{k}_{12} \hat{Y}_1 \hat{Y}_2 \hat{Y}_3 \hat{Y}_{12} \hat{Z}_1 \hat{K}_1 \hat{K}'_1 \hat{K}_2 \hat{K}'_2 \\
& \quad \hat{K}_3 \hat{K}'_3 \hat{K}_{12} \hat{K}'_{12} \hat{X}_4 \hat{X}_5 \begin{pmatrix} 1 & \mathcal{A}_3 & k_4 \\ 0 & 0 & 0 \end{pmatrix} \begin{pmatrix} K_1 & K_2 & Y_{12} \\ 0 & 0 & 0 \end{pmatrix} \begin{pmatrix} K'_1 & K'_2 & Y_1 \\ 0 & 0 & 0 \end{pmatrix} \begin{pmatrix} Y_2 & K_3 & K_{12} \\ 0 & 0 & 0 \end{pmatrix} \begin{pmatrix} Y_3 & K'_3 & K'_{12} \\ 0 & 0 & 0 \end{pmatrix} \\
& \quad \begin{pmatrix} Y_{12} & X_4 & k_{12} \\ 0 & 0 & 0 \end{pmatrix} \begin{pmatrix} Y_1 & X_4 & \mathcal{A}_1 \\ 0 & 0 & 0 \end{pmatrix} \begin{pmatrix} Y_2 & X_5 & \mathcal{A}_2 \\ 0 & 0 & 0 \end{pmatrix} \begin{pmatrix} Y_3 & X_5 & k_4 \\ 0 & 0 & 0 \end{pmatrix} \left\{ \begin{matrix} k_4 & J_{12} & J'_{12} \\ J_{123} & J_3 & J_3 \end{matrix} \right\} \\
& \quad \left\{ \begin{matrix} \mathcal{A}_1 & \mathcal{A}_1 & k_{12} \\ Y_{12} & X_4 & Y_1 \end{matrix} \right\} \left\{ \begin{matrix} k_{12} & Y_3 & Z_1 \\ K'_3 & K_{12} & K'_{12} \end{matrix} \right\} \left\{ \begin{matrix} k_{12} & Y_3 & Z_1 \\ X_5 & \mathcal{A}_2 & k_4 \end{matrix} \right\} \left\{ \begin{matrix} 1 & Z_1 & Y_2 \\ K_{12} & K_3 & K'_3 \end{matrix} \right\} \left\{ \begin{matrix} 1 & Z_1 & Y_2 \\ X_5 & \mathcal{A}_2 & \mathcal{A}_2 \end{matrix} \right\} \\
& \quad \left\{ \begin{matrix} \mathcal{A}_1 & Y_1 & Y_{12} \\ 1 & K'_2 & K_2 \\ 1 & K'_1 & K_1 \end{matrix} \right\} \left\{ \begin{matrix} \frac{1}{2} & \frac{1}{2} & 1 \\ \frac{1}{2} & \frac{1}{2} & 1 \\ S_1 & S'_1 & \mathcal{A}_1 \end{matrix} \right\} \left\{ \begin{matrix} L_1 & S_1 & J_1 \\ L'_1 & S'_1 & J'_1 \\ \mathcal{A}_1 & \mathcal{A}_1 & k_{12} \end{matrix} \right\} \left\{ \begin{matrix} L_2 & \frac{1}{2} & J_2 \\ L'_2 & \frac{1}{2} & J'_2 \\ \mathcal{A}_2 & 1 & \mathcal{A}_2 \end{matrix} \right\} \left\{ \begin{matrix} L_3 & \frac{1}{2} & J_3 \\ L'_3 & \frac{1}{2} & J'_3 \\ \mathcal{A}_3 & 1 & k_4 \end{matrix} \right\} \left\{ \begin{matrix} J_1 & J_2 & J_{12} \\ J'_1 & J'_2 & J'_{12} \\ k_{12} & \mathcal{A}_2 & k_4 \end{matrix} \right\} \\
& \quad \frac{9g_A^4}{8(2F_\pi)^6} \frac{\mathcal{A}_1^{K'_1+K'_2} \mathcal{A}_2^{K_3+K_{12}} \mathcal{A}_3^{1+K'_3+K'_{12}}}{q_1(\mathcal{A}_1, q_{12}(\mathcal{A}_2, \mathcal{A}_3, u_5), u_4)^2 + M_\pi^2} \frac{1}{q_2(\mathcal{A}_1, q_{12}(\mathcal{A}_2, \mathcal{A}_3, u_5), u_4)^2 + M_\pi^2} \\
& \quad \frac{1}{q_3(\mathcal{A}_2, \mathcal{A}_3, u_5)^2 + M_\pi^2} \frac{1}{q_4 \mathcal{A}_3^{\frac{3}{4}} + M_\pi^2} q_{12}(\mathcal{A}_2, \mathcal{A}_3, u_5)^{K_1+K_2-k_{12}} [q_{12}(\mathcal{A}_2, \mathcal{A}_3, u_5)^2 + M_\pi^2].
\end{aligned}$$



At this point we have to do the coordinate transformation again, starting with replacing  $q_1$  with  $q_{12}$  and  $\hat{\Delta}_1$ . Thereby we introduce an integral over  $u_4$ , which corresponds to the angle  $\hat{q}_{12} \cdot \hat{\Delta}_1$ . This results in

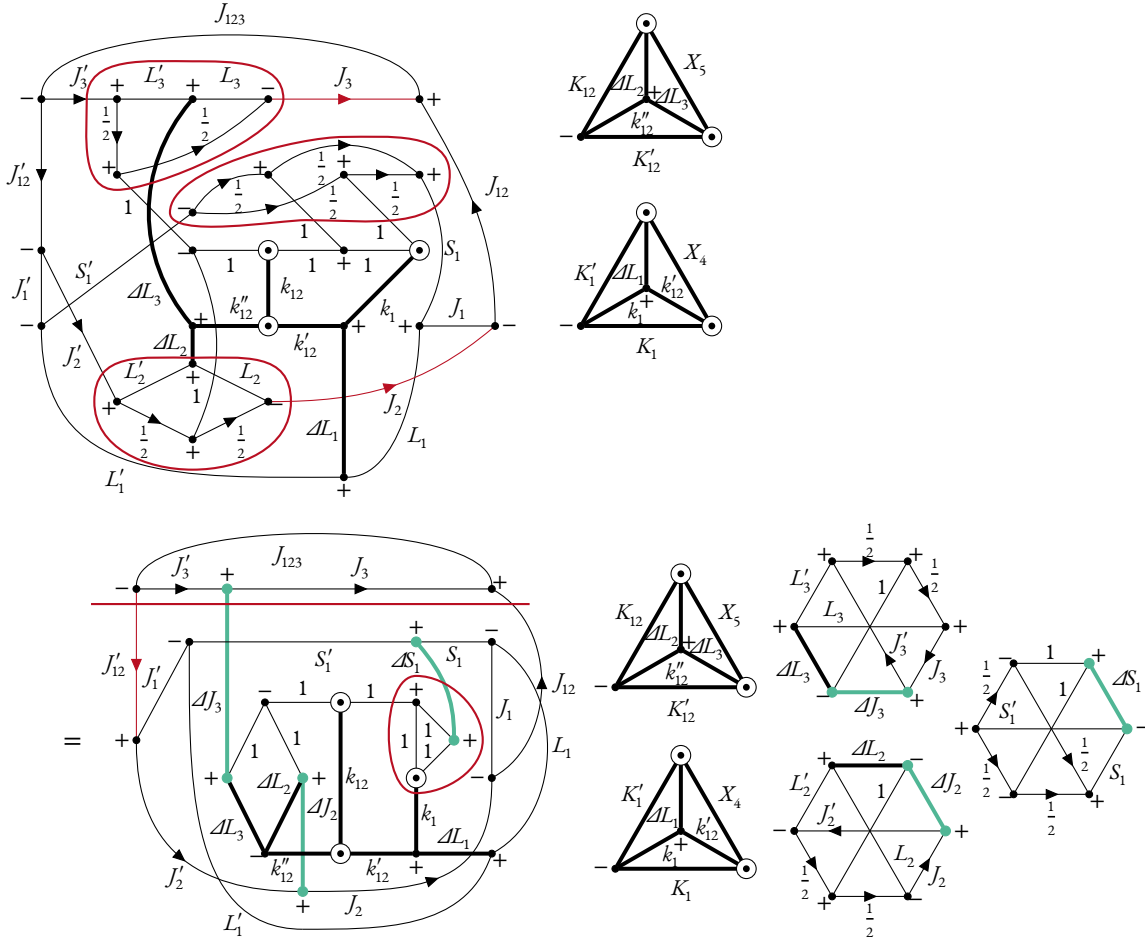
$$\begin{aligned}
 & \times \int du_4 P_{X_4}(u_4) D_{K_1, K'_1}^{k_1} \sqrt{2}^{-2K_1 - K'_1} (-1)^{1+K'_1 + k_{12}} \\
 & \times C_T \frac{432g_A^4}{(2F_\pi)^4} \frac{q_1(\Delta_1, q_{12}, u_4)^{2-k_1}}{q_1(\Delta_1, q_{12}, u_4)^2 + M_\pi^2} \frac{q_{12}^{2+K_1}}{[q_{12}^2 + M_\pi^2]^2} \Delta_1^{K'_1} \\
 & \times \int du_4 P_{X_4}(u_4) \int du_5 P_{X_5}(u_5) D_{K_1, K'_1}^{k_1} D_{K_{12}, K'_{12}}^{k''_{12}} \\
 & \times \sqrt{2}^{-2K_1 - K'_1 + K_{12}} \sqrt{3}^{-k''_{12}} (-1)^{1+K'_1 + k_{12}} C_T \frac{216g_A^4}{(2F_\pi)^4} \\
 & \times \frac{q_1(\Delta_1, q_{12}(\Delta_2, \Delta_3, u_5), u_4)^{2-k_1}}{q_1(\Delta_1, q_{12}(\Delta_2, \Delta_3, u_5), u_4)^2 + M_\pi^2} \\
 & \times \frac{q_{12}(\Delta_2, \Delta_3, u_5)^{2+K_1 - k''_{12}}}{[q_{12}(\Delta_2, \Delta_3, u_5)^2 + M_\pi^2]^2} \Delta_1^{K'_1} \Delta_2^{K_{12}} \Delta_3^{K'_{12}}.
 \end{aligned}$$

Having reduced the number of coordinate lines again, we can extract one 6j-symbol and replace  $q_{12}$  with  $\Delta_2$  and  $\Delta_3$ . Of course, this introduces an integral over  $u_5$ , which corresponds to the angle  $\hat{\Delta}_2 \cdot \hat{\Delta}_3$ . Afterwards we reduce the number of coordinate lines again, yielding

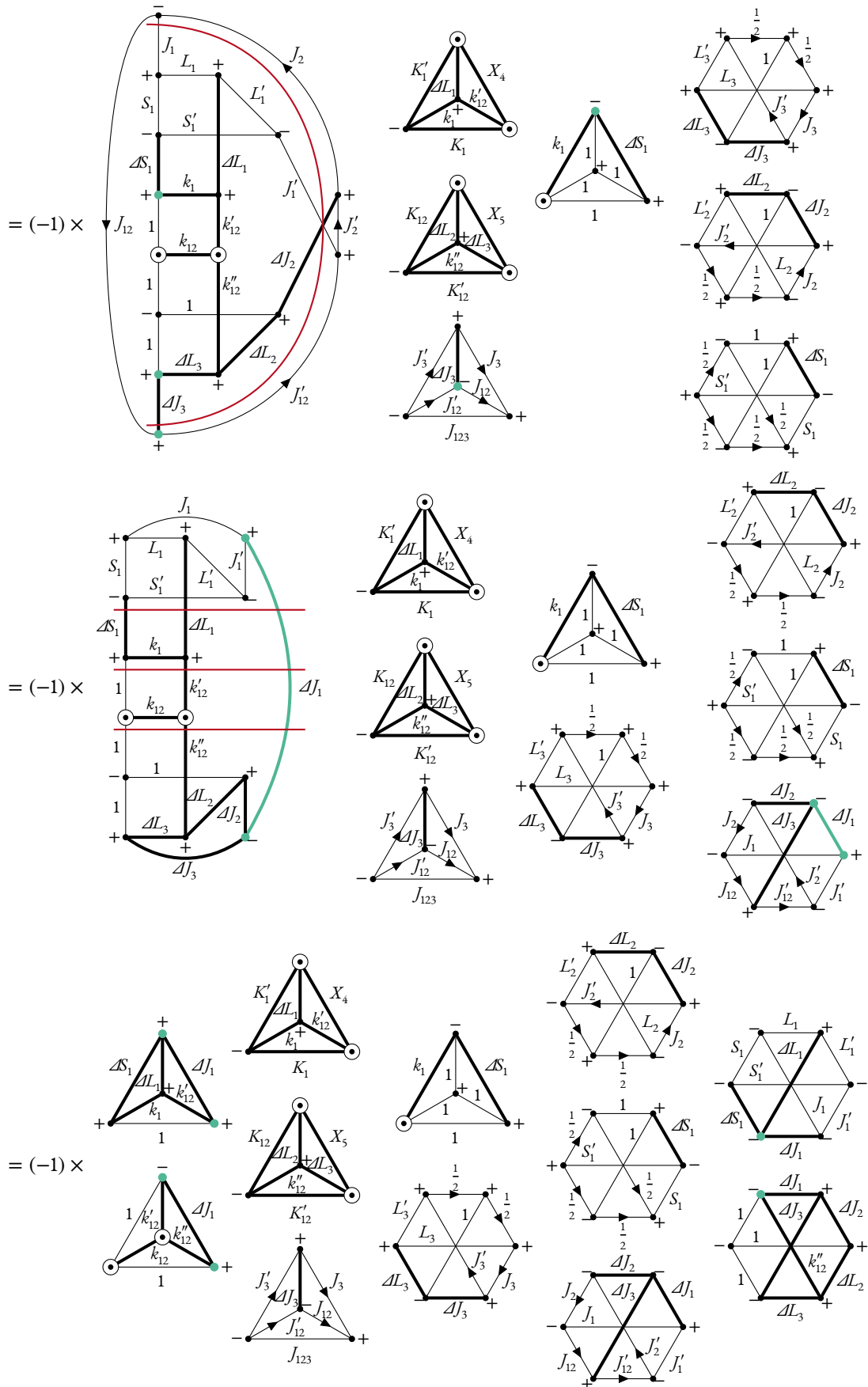
$$\begin{aligned}
 & \times \int du_4 P_{X_4}(u_4) \int du_5 P_{X_5}(u_5) D_{K_1, K'_1}^{k_1} D_{K_{12}, K'_{12}}^{k''_{12}} \\
 & \times \sqrt{2}^{-2K_1 - K'_1 + K_{12}} \sqrt{3}^{-k''_{12}} (-1)^{1+K'_1 + k_{12} + K_{12} + \Delta'_1} C_T \frac{216g_A^4}{(2F_\pi)^4} \\
 & \times \frac{q_1(\Delta_1, q_{12}(\Delta_2, \Delta_3, u_5), u_4)^{2-k_1}}{q_1(\Delta_1, q_{12}(\Delta_2, \Delta_3, u_5), u_4)^2 + M_\pi^2} \\
 & \times \frac{q_{12}(\Delta_2, \Delta_3, u_5)^{2+K_1 - k''_{12}}}{[q_{12}(\Delta_2, \Delta_3, u_5)^2 + M_\pi^2]^2} \Delta_1^{K'_1} \Delta_2^{K_{12}} \Delta_3^{K'_{12}}
 \end{aligned}$$

$$\begin{aligned}
 & \times \int du_4 P_{X_4}(u_4) \int du_5 P_{X_5}(u_5) D_{K_1, K'_1}^{k_1} D_{K_{12}, K'_{12}}^{k'_{12}} \\
 & \times \sqrt{2}^{-2K_1 - K'_1 + K_{12}} \sqrt{3}^{-k'_{12}} (-1)^{1+K'_1+k_{12}+K_{12}+\Delta L_3} C_T \frac{216g_A^4}{(2F_\pi)^4} \\
 & \times \frac{q_1(\Delta_1, q_{12}(\Delta_2, \Delta_3, u_5), u_4)^{2-k_1}}{q_1(\Delta_1, q_{12}(\Delta_2, \Delta_3, u_5), u_4)^2 + M_\pi^2} \\
 & \times \frac{q_{12}(\Delta_2, \Delta_3, u_5)^{2+K_1-k'_{12}}}{[q_{12}(\Delta_2, \Delta_3, u_5)^2 + M_\pi^2]^2} \Delta_1^{K'_1} \Delta_2^{K_{12}} \Delta_3^{K'_{12}}.
 \end{aligned}$$

At this point we can insert the expression in eq. (4.11) again and start by simplifying the diagrammatic part,







Adding the non-diagrammatic part of the expression and using a traditional representation for the 6j-symbols and 9j-symbols, we obtain

$$\begin{aligned}
 & I_{\text{IVa}}^{L'_1, L'_2, L'_3, S'_1, J'_2, J'_3, J'_{12}, J'_{123}}(\mathcal{A}_1, \mathcal{A}_2, \mathcal{A}_3) \\
 &= \int d u_4 P_{X_4}(u_4) \int d u_5 P_{X_5}(u_5) \sum_{X_4, X_5, \mathcal{A}_1} \sum_{K_1, K_2} \sum_{k_1, k_2} D_{K_1, K_1}^{k_1} D_{K_2, K_2}^{k_2} \sqrt{2^{-2K_1 - K_1 + K_2}} \sqrt{3^{-k_2}} \\
 & \quad (-1)^{J_3 + J'_2 + J_{123} + \mathcal{A}_1 + \mathcal{A}_2 + \mathcal{A}_3 + K_1 + K_2 + K'_1} \hat{S}_1 \hat{S}'_1 \hat{J}_1 \hat{J}'_1 \hat{J}_2 \hat{J}'_2 \hat{J}_3 \hat{J}'_3 \hat{J}_{12} \hat{J}'_{12} \hat{\mathcal{A}}_1^2 \hat{\mathcal{A}}_2^2 \hat{\mathcal{A}}_3^2 \hat{K}_1^2 \hat{K}_2^2 \hat{K}'_1 \hat{K}'_2 \hat{K}_{12}^2 \hat{K}'_{12} \\
 & \quad \hat{X}_4^2 \hat{X}_5^2 \begin{pmatrix} 1 & 1 & k_1 \\ 0 & 0 & 0 \end{pmatrix} \begin{pmatrix} 1 & 1 & k_2 \\ 0 & 0 & 0 \end{pmatrix} \begin{pmatrix} k_{12} & k'_{12} & k''_{12} \\ 0 & 0 & 0 \end{pmatrix} \begin{pmatrix} K_1 & X_4 & k'_{12} \\ 0 & 0 & 0 \end{pmatrix} \begin{pmatrix} K'_1 & X_4 & \mathcal{A}L_1 \\ 0 & 0 & 0 \end{pmatrix} \\
 & \quad \begin{pmatrix} K_{12} & X_5 & \mathcal{A}L_2 \\ 0 & 0 & 0 \end{pmatrix} \begin{pmatrix} K'_{12} & X_5 & \mathcal{A}L_3 \\ 0 & 0 & 0 \end{pmatrix} \begin{Bmatrix} \mathcal{A}L_3 & \mathcal{A}L_2 & k''_{12} \\ K_{12} & K'_{12} & X_5 \end{Bmatrix} \begin{Bmatrix} k_{12} & k'_{12} & k''_{12} \\ \mathcal{A}J_1 & 1 & 1 \end{Bmatrix} \begin{Bmatrix} k'_{12} & \mathcal{A}L_1 & k_1 \\ K'_1 & K_1 & X_4 \end{Bmatrix} \\
 & \quad \begin{Bmatrix} \mathcal{A}S_1 & 1 & k_1 \\ k'_{12} & \mathcal{A}L_1 & \mathcal{A}J_1 \end{Bmatrix} \begin{Bmatrix} J_{12} & J'_{12} & \mathcal{A}J_3 \\ J'_3 & J_3 & J_{123} \end{Bmatrix} \begin{Bmatrix} 1 & 1 & 1 \\ 1 & k_1 & \mathcal{A}S_1 \end{Bmatrix} \\
 & \quad \begin{Bmatrix} \frac{1}{2} & \frac{1}{2} & 1 \\ \frac{1}{2} & \frac{1}{2} & 1 \\ S_1 & S'_1 & \mathcal{A}S_1 \end{Bmatrix} \begin{Bmatrix} L_1 & S_1 & J_1 \\ L'_1 & S'_1 & J'_1 \\ \mathcal{A}L_1 & \mathcal{A}S_1 & \mathcal{A}J_1 \end{Bmatrix} \begin{Bmatrix} L_2 & \frac{1}{2} & J_2 \\ L'_2 & \frac{1}{2} & J'_2 \\ \mathcal{A}L_2 & 1 & \mathcal{A}J_2 \end{Bmatrix} \begin{Bmatrix} L_3 & \frac{1}{2} & J_3 \\ L'_3 & \frac{1}{2} & J'_3 \\ \mathcal{A}L_3 & 1 & \mathcal{A}J_3 \end{Bmatrix} \begin{Bmatrix} J_1 & J_2 & J_{12} \\ J'_1 & J'_2 & J'_{12} \\ \mathcal{A}J_1 & \mathcal{A}J_2 & \mathcal{A}J_3 \end{Bmatrix} \begin{Bmatrix} 1 & k''_{12} & \mathcal{A}J_1 \\ 1 & \mathcal{A}L_2 & \mathcal{A}J_2 \\ 1 & \mathcal{A}L_3 & \mathcal{A}J_3 \end{Bmatrix} \\
 & \quad C_T \frac{216g_A^4}{(2F_\pi)^4} \frac{q_1(\mathcal{A}_1, q_{12}(\mathcal{A}_2, \mathcal{A}_3, u_5), u_4)^{2-k_1}}{q_1(\mathcal{A}_1, q_{12}(\mathcal{A}_2, \mathcal{A}_3, u_5), u_4)^2 + \mathcal{M}_\pi^2} \frac{q_{12}(\mathcal{A}_2, \mathcal{A}_3, u_5)^{2+K_1-k_2}}{[q_{12}(\mathcal{A}_2, \mathcal{A}_3, u_5)^2 + \mathcal{M}_\pi^2]^2} \mathcal{A}_1^{K'_1} \mathcal{A}_2^{K_{12}} \mathcal{A}_3^{K'_{12}}.
 \end{aligned}$$

## A.8 CLASS IV - SUBSTRUCTURE B

Representing structure (IVb) diagrammatically yields

$$\begin{aligned}
 & \left\langle m'_{s_a} m'_{s_b} m'_{s_c} m'_{s_d}, \pi'_1 \pi'_2 \pi'_3 \left| V_{\text{IVb}}^{(6)} \right| m_{s_a} m_{s_b} m_{s_c} m_{s_d}, \pi_1 \pi_2 \pi_3 \right\rangle \\
 &= \left\langle m'_{s_a} m'_{s_b} m'_{s_c} m'_{s_d} \left| -C_T \frac{4g_A^4}{(2F_\pi)^4} \frac{\sigma_1 \cdot q_1 (\sigma_3 \times \sigma_4) \cdot q_{12} q_1 \cdot q_{12}}{[q_1^2 + \mathcal{M}_\pi^2] [q_{12}^2 + \mathcal{M}_\pi^2]^2} \right| m_{s_a} m_{s_b} m_{s_c} m_{s_d} \right\rangle \\
 &= \begin{array}{c} \begin{array}{c} \frac{1}{2} m'_{s_a} \\ \frac{1}{2} m'_{s_b} \end{array} \begin{array}{c} \frac{1}{2} m'_{s_c} \\ \frac{1}{2} m'_{s_d} \end{array} \begin{array}{c} 1 \\ 1 \end{array} \begin{array}{c} \hat{q}_1 \\ \hat{q}_1 \end{array} \begin{array}{c} 1 \\ 1 \end{array} \begin{array}{c} \hat{q}_{12} \\ \hat{q}_{12} \end{array} \\ \begin{array}{c} \frac{1}{2} m'_{s_c} \\ \frac{1}{2} m'_{s_d} \end{array} \begin{array}{c} 1 \\ 1 \end{array} \begin{array}{c} \hat{q}_{12} \\ \hat{q}_{12} \end{array} \end{array} \\
 & \quad \times \delta_{m_b, m'_b} C_T \frac{144ig_A^4}{(2F_\pi)^4} \frac{q_1^2}{q_1^2 + \mathcal{M}_\pi^2} \frac{q_{12}^2}{[q_{12}^2 + \mathcal{M}_\pi^2]^2}.
 \end{aligned}$$

Reducing the number of coordinate lines results in the following expression

$$= \dots \times \delta_{m_{s_b}, m'_{s_b}} \frac{144 i g_A^4}{(2F_\pi)^4} \frac{q_1^2}{q_1^2 + M_\pi^2} \frac{q_{12}^2}{[q_{12}^2 + M_\pi^2]^2}.$$

At this point we need to transform the coordinates again. However, the derivation is identical to structure (IVa) therefore we simply get the result

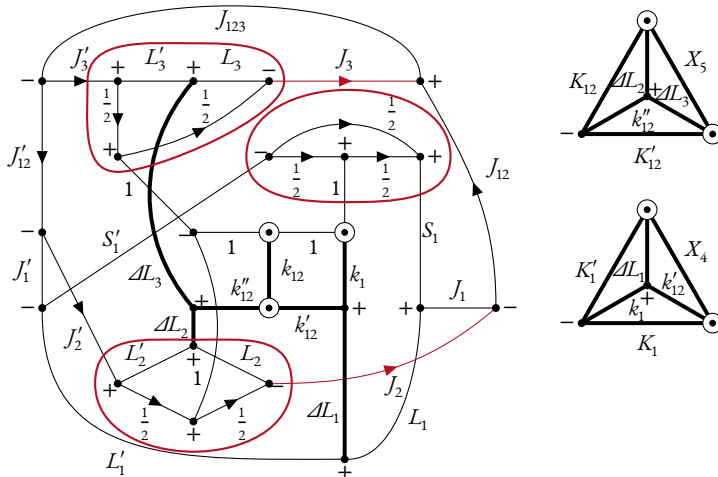
$$= \dots \times \delta_{m_{s_b}, m'_{s_b}} \int du_4 P_{X_4}(u_4) \int du_5 P_{X_5}(u_5) D_{K_1, K'_1}^{k_1} D_{K_{12}, K'_{12}}^{k'_{12}}$$

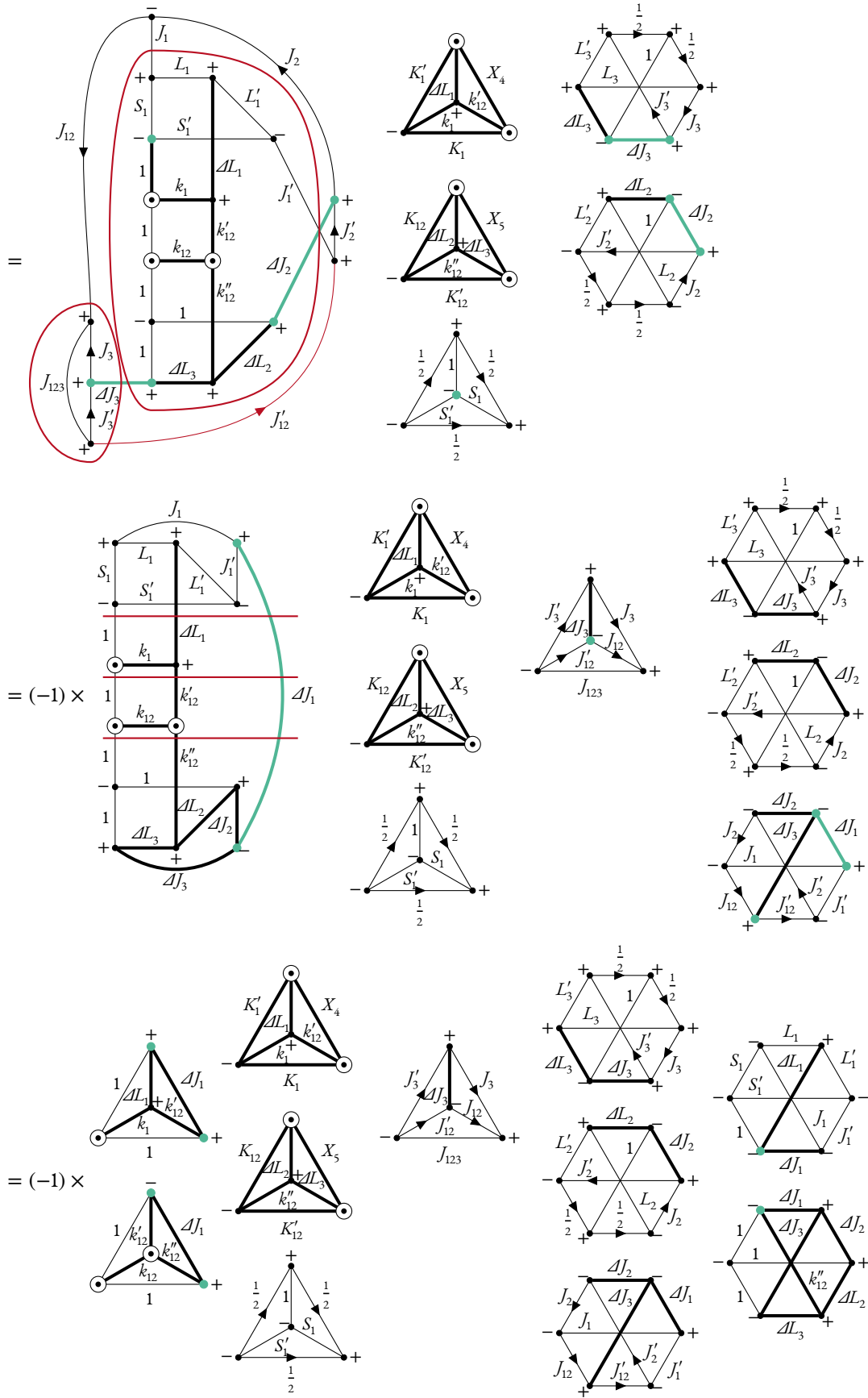
$$\times \sqrt{2^{-2K_1 - K'_1 + K_{12}}} \sqrt{3^{-k'_{12}}} (-1)^{K'_1 + k_{12} + K_{12} + \Delta L'_3} C_T \frac{36 i g_A^4}{(2F_\pi)^4}$$

$$\times \frac{q_1(\Delta_1, q_{12}(\Delta_2, \Delta_3, u_5), u_4)^{2-k_1}}{q_1(\Delta_1, q_{12}(\Delta_2, \Delta_3, u_5), u_4)^2 + M_\pi^2}$$

$$\times \frac{q_{12}(\Delta_2, \Delta_3, u_5)^{2+K_1 - k'_{12}}}{[q_{12}(\Delta_2, \Delta_3, u_5)^2 + M_\pi^2]^2} \Delta_1^{K'_1} \Delta_2^{K_{12}} \Delta_3^{K'_{12}}.$$

At this point we can insert the expression in eq. (4.ii) again and start by simplifying the diagrammatic part,





The interaction part in traditional form, combined with the remaining part of the formulae, reads

$$\begin{aligned}
& I_{\text{IVb}}^{L'_1, L'_2, L'_3, S'_1, J'_1, J'_2, J'_3, J'_{123}; \mathcal{A}_1, \mathcal{A}_2, \mathcal{A}_3}(\mathcal{A}_1, \mathcal{A}_2, \mathcal{A}_3) \\
&= \int du_4 P_{X_4}(u_4) \int du_5 P_{X_5}(u_5) \sum_{X_4, X_5} \sum_{K_1, K_2} \sum_{k_1, k_2} D_{K_1, K_1}^{k_1} D_{K_2, K_2}^{k_2} \sqrt{2}^{-2K_1 - K_1 + K_2} \sqrt{3}^{-k_2''} \\
&\quad (-1)^{S'_1 + J_3 + J'_{12} + J_{123} + \mathcal{A}_2 + \mathcal{A}_1 + \mathcal{A}_2 + k_{12} + K_{12} + K_1'} \hat{S}_1 \hat{S}'_1 \hat{J}_1 \hat{J}'_1 \hat{J}_2 \hat{J}'_2 \hat{J}_3 \hat{J}'_3 \hat{J}_{12} \hat{J}'_{12} \hat{\mathcal{A}}_1^2 \hat{\mathcal{A}}_2^2 \hat{\mathcal{A}}_3^2 \hat{k}_1^2 \hat{k}_2^2 \hat{k}_{12}^2 \hat{k}_{12}^{\prime 2} \hat{K}_1^2 \hat{K}_2^2 \hat{K}_{12}^2 \hat{X}_4^2 \hat{X}_5^2 \\
&\quad \begin{pmatrix} 1 & 1 & k_1 \\ 0 & 0 & 0 \end{pmatrix} \begin{pmatrix} 1 & 1 & k_{12} \\ 0 & 0 & 0 \end{pmatrix} \begin{pmatrix} k_{12} & k'_{12} & k''_{12} \\ 0 & 0 & 0 \end{pmatrix} \begin{pmatrix} K_1 & X_4 & k'_{12} \\ 0 & 0 & 0 \end{pmatrix} \begin{pmatrix} K'_1 & X_4 & \mathcal{A}L_1 \\ 0 & 0 & 0 \end{pmatrix} \begin{pmatrix} K_{12} & X_5 & \mathcal{A}L_2 \\ 0 & 0 & 0 \end{pmatrix} \\
&\quad \begin{pmatrix} K'_{12} & X_5 & \mathcal{A}L_3 \\ 0 & 0 & 0 \end{pmatrix} \begin{Bmatrix} \mathcal{A}L_3 & \mathcal{A}L_2 & k''_{12} \\ K_{12} & K'_{12} & X_5 \end{Bmatrix} \begin{Bmatrix} k_{12} & k'_{12} & k''_{12} \\ \mathcal{A}J_1 & 1 & 1 \end{Bmatrix} \begin{Bmatrix} k'_{12} & \mathcal{A}L_1 & k_1 \\ K'_1 & K_1 & X_4 \end{Bmatrix} \begin{Bmatrix} 1 & 1 & k_1 \\ k'_{12} & \mathcal{A}L_1 & \mathcal{A}J_1 \end{Bmatrix} \begin{Bmatrix} S_1 & S'_1 & 1 \\ \frac{1}{2} & \frac{1}{2} & \frac{1}{2} \end{Bmatrix} \\
&\quad \begin{Bmatrix} J_{12} & J'_{12} & \mathcal{A}J_3 \\ J'_3 & J_3 & J_{123} \end{Bmatrix} \begin{Bmatrix} L_1 & S_1 & J_1 \\ L'_1 & S'_1 & J'_1 \\ \mathcal{A}L_1 & 1 & \mathcal{A}J_1 \end{Bmatrix} \begin{Bmatrix} L_2 & \frac{1}{2} & J_2 \\ L'_2 & \frac{1}{2} & J'_2 \\ \mathcal{A}L_2 & 1 & \mathcal{A}J_2 \end{Bmatrix} \begin{Bmatrix} L_3 & \frac{1}{2} & J_3 \\ L'_3 & \frac{1}{2} & J'_3 \\ \mathcal{A}L_3 & 1 & \mathcal{A}J_3 \end{Bmatrix} \begin{Bmatrix} J_1 & J_2 & J_{12} \\ J'_1 & J'_2 & J'_{12} \\ \mathcal{A}J_1 & \mathcal{A}J_2 & \mathcal{A}J_3 \end{Bmatrix} \begin{Bmatrix} 1 & k''_{12} & \mathcal{A}J_1 \\ 1 & \mathcal{A}L_2 & \mathcal{A}J_2 \\ 1 & \mathcal{A}L_3 & \mathcal{A}J_3 \end{Bmatrix} \\
&\quad C_T \frac{36ig_A^4}{(2F_\pi)^4} \frac{q_1(\mathcal{A}_1, q_{12}(\mathcal{A}_2, \mathcal{A}_3, u_5), u_4)^{2-k_1}}{q_1(\mathcal{A}_1, q_{12}(\mathcal{A}_2, \mathcal{A}_3, u_5), u_4)^2 + M_\pi^2} \frac{q_{12}(\mathcal{A}_2, \mathcal{A}_3, u_5)^{2+K_1-k''_{12}}}{[q_{12}(\mathcal{A}_2, \mathcal{A}_3, u_5)^2 + M_\pi^2]^2} \mathcal{A}_1^{K'_1} \mathcal{A}_2^{K_{12}} \mathcal{A}_3^{K'_{12}}.
\end{aligned}$$

## A.9 CLASS V

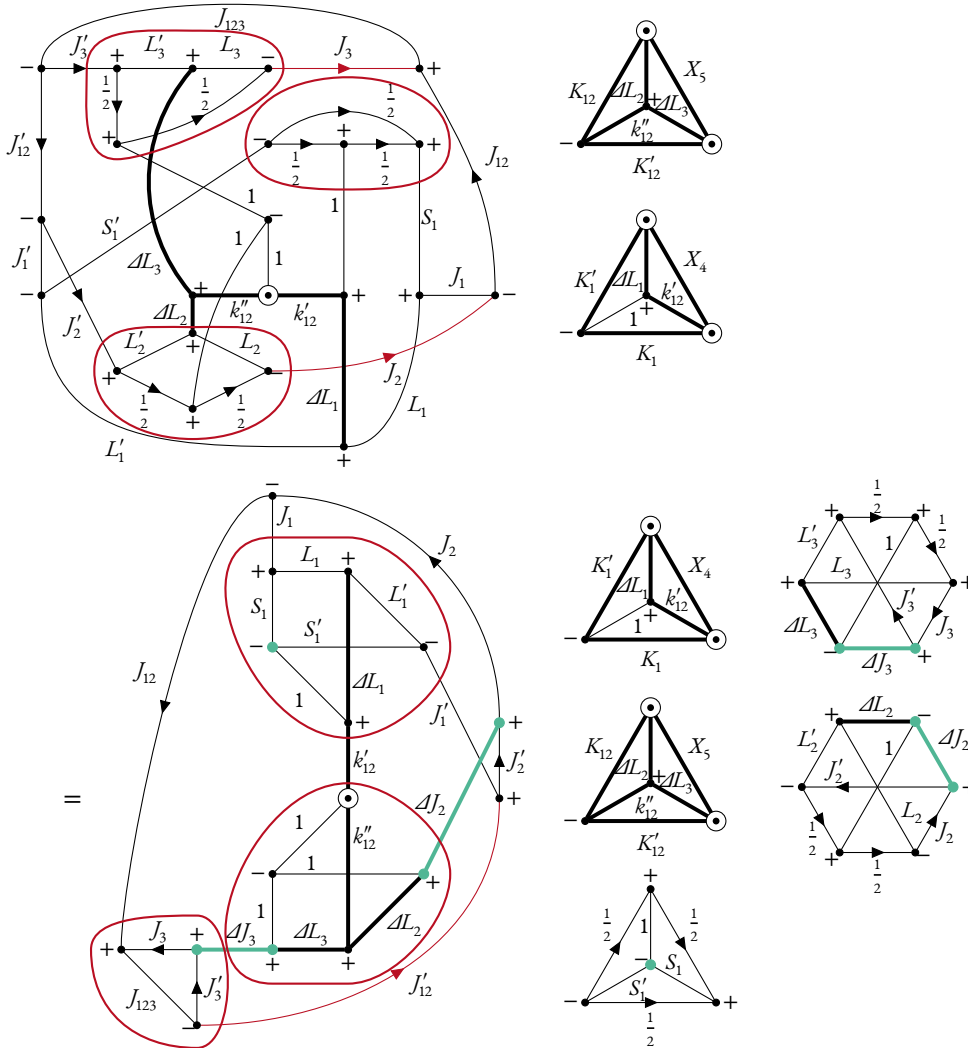
Again we start by representing structure (V) diagrammatically,

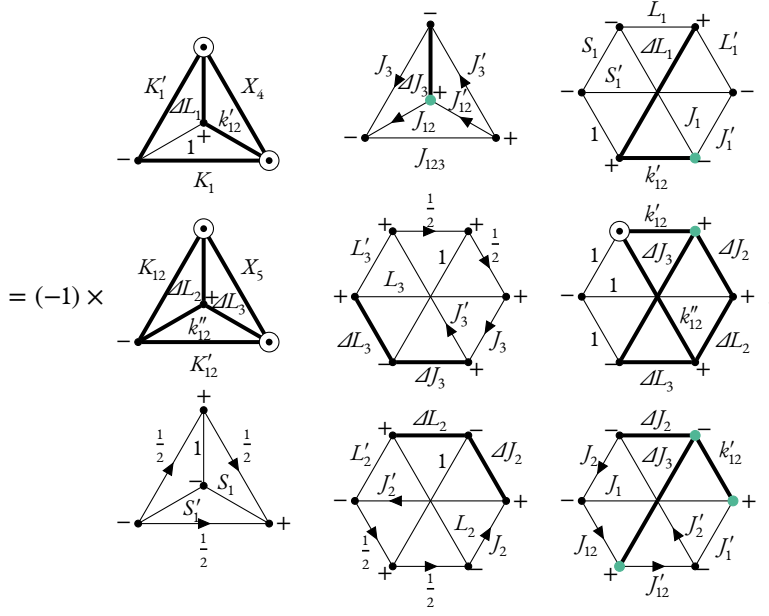
$$\begin{aligned}
& \left\langle m'_{s_a} m'_{s_b} m'_{s_c} m'_{s_d}, \pi'_1 \pi'_2 \pi'_3 \left| V_V^{(s)} \right| m_{s_a} m_{s_b} m_{s_c} m_{s_d}, \pi_1 \pi_2 \pi_3 \right\rangle \\
&= \left\langle m'_{s_a} m'_{s_b} m'_{s_c} m'_{s_d} \left| C_T \frac{2g_A^2}{(2F_\pi)^4} \frac{\sigma_1 \cdot q_1 (\sigma_3 \times \sigma_4) \cdot q_{12}}{[q_1^2 + M_\pi^2][q_{12}^2 + M_\pi^2]} \right| m_{s_a} m_{s_b} m_{s_c} m_{s_d} \right\rangle \\
&= \begin{array}{c} \begin{array}{c} \frac{1}{2} m'_{s_a} \\ \downarrow \\ \oplus \\ \uparrow \\ \frac{1}{2} m_{s_a} \end{array} \xrightarrow{1} \text{---} \hat{q}_1 \text{---} \\ \oplus \\ \begin{array}{c} \frac{1}{2} m'_{s_b} \\ \downarrow \\ \oplus \\ \uparrow \\ \frac{1}{2} m_{s_b} \end{array} \end{array} \begin{array}{c} \frac{1}{2} m'_{s_c} \\ \downarrow \\ \oplus \\ \uparrow \\ \frac{1}{2} m_{s_c} \end{array} \xrightarrow{1} \begin{array}{c} \frac{1}{2} m'_{s_d} \\ \downarrow \\ \oplus \\ \uparrow \\ \frac{1}{2} m_{s_d} \end{array} \xrightarrow{1} \text{---} \hat{q}_{12} \text{---} \end{array} \\
&\quad \times \delta_{m_{s_b}, m'_{s_b}} C_T \frac{72ig_A^2}{(2F_\pi)^4} \frac{q_1}{q_1^2 + M_\pi^2} \frac{q_{12}}{q_{12}^2 + M_\pi^2},
\end{aligned}$$

and transforming the coordinates works in exactly the same way as in the previous cases, yielding

$$\begin{aligned}
 & \begin{array}{c} \frac{1}{2}m'_{s_a} \\ \frac{1}{2}m_{s_a} \\ \frac{1}{2}m'_{s_c} \\ \frac{1}{2}m_{s_c} \\ \frac{1}{2}m'_{s_d} \\ \frac{1}{2}m_{s_d} \end{array} \begin{array}{c} \text{---} \\ \text{---} \\ \text{---} \\ \text{---} \\ \text{---} \\ \text{---} \end{array} \begin{array}{c} 1 \\ 1 \\ 1 \\ 1 \\ 1 \\ 1 \end{array} \begin{array}{c} \text{---} \\ \text{---} \\ \text{---} \\ \text{---} \\ \text{---} \\ \text{---} \end{array} \\
 & \begin{array}{c} \Delta L'_1 \\ k'_{12} \\ \Delta L'_2 \\ \Delta L'_3 \end{array} \begin{array}{c} \hat{\Delta}_1 \\ \hat{\Delta}_2 \\ \hat{\Delta}_3 \end{array} \times \delta_{m_{i_b}, m'_{i_b}} \int du_4 P_{X_4}(u_4) \int du_5 P_{X_5}(u_5) D_{K_1, K'_1}^1 D_{K_{12}, K''_{12}}^{k'_{12}} \\
 & \times \sqrt{2}^{-2K_1 - K'_1 + K_{12}} \sqrt{3}^{-k'_{12}} (-1)^{1+K'_1 + K_{12} + \Delta L'_3} C_T \frac{18ig_A^2}{(2F_\pi)^4} \\
 & \times \frac{1}{q_1(\Delta_1, q_{12}(\Delta_2, \Delta_3, u_5), u_4)^2 + M_\pi^2} \\
 & \times \frac{q_{12}(\Delta_2, \Delta_3, u_5)^{1+K_1 - k'_{12}}}{q_{12}(\Delta_2, \Delta_3, u_5)^2 + M_\pi^2} \Delta_1^{K'_1} \Delta_2^{K_{12}} \Delta_3^{K'_{12}}.
 \end{aligned}$$

At this point we can insert the expression in eq. (4.11) again and start by simplifying the diagrammatic part,





Finally, we obtain an interaction part in traditional form,

$$\begin{aligned}
& I_{\sqrt{L_1, L_2, L_3, S_1, J_1, J_2, J_3, J_{12}, J_{123}; \Delta L_1, \Delta L_2, \Delta L_3}}^{L'_1, L'_2, L'_3, S'_1, J'_1, J'_2, J'_3, J'_{12}, J'_{123}}(\Delta_1, \Delta_2, \Delta_3) \\
&= \int du_4 P_{X_4}(u_4) \int du_5 P_{X_5}(u_5) \sum_{X_4, X_5} \sum_{K_1, K'_1} \sum_{K_{12}, K'_{12}} D_{K_1, K'_1}^1 D_{K_{12}, K'_{12}}^{k''_{12}} \sqrt{2}^{-2K_1 - K'_1 + K_{12}} \sqrt{3}^{-k''_{12}} \\
& \quad (-1)^{1+S'_1+J_3+J'_{12}+J_{123}+\Delta L_2+\Delta J_2+K_1+K_{12}} \hat{S}_1 \hat{S}'_1 \hat{J}_1 \hat{J}'_1 \hat{J}_2 \hat{J}'_2 \hat{J}_3 \hat{J}'_3 \hat{J}_{12} \hat{J}'_{12} \hat{\Delta J}_2^2 \hat{\Delta J}_3^2 \hat{k}_{12}^{\prime 2} \hat{k}_{12}^{\prime \prime 2} \hat{K}_1^2 \hat{K}'_1{}^2 \hat{K}_{12}^2 \hat{K}'_{12}{}^2 \hat{X}_4^2 \hat{X}_5^2 \\
& \quad \begin{pmatrix} 1 & k'_{12} & k''_{12} \\ 0 & 0 & 0 \end{pmatrix} \begin{pmatrix} K_1 & X_4 & k'_{12} \\ 0 & 0 & 0 \end{pmatrix} \begin{pmatrix} K'_1 & X_4 & \Delta L_1 \\ 0 & 0 & 0 \end{pmatrix} \begin{pmatrix} K_{12} & X_5 & \Delta L_2 \\ 0 & 0 & 0 \end{pmatrix} \begin{pmatrix} K'_{12} & X_5 & \Delta L_3 \\ 0 & 0 & 0 \end{pmatrix} \\
& \quad \left\{ \begin{matrix} \Delta L_3 & \Delta L_2 & k''_{12} \\ K_{12} & K'_{12} & X_5 \end{matrix} \right\} \left\{ \begin{matrix} k'_{12} & \Delta L_1 & 1 \\ K'_1 & K_1 & X_4 \end{matrix} \right\} \left\{ \begin{matrix} S_1 & S'_1 & 1 \\ \frac{1}{2} & \frac{1}{2} & \frac{1}{2} \end{matrix} \right\} \left\{ \begin{matrix} J_{12} & J'_{12} & \Delta J_3 \\ J'_3 & J_3 & J_{123} \end{matrix} \right\} \\
& \quad \left\{ \begin{matrix} L_1 & S_1 & J_1 \\ L'_1 & S'_1 & J'_1 \\ \Delta L_1 & 1 & k'_{12} \end{matrix} \right\} \left\{ \begin{matrix} L_2 & \frac{1}{2} & J_2 \\ L'_2 & \frac{1}{2} & J'_2 \\ \Delta L_2 & 1 & \Delta J_2 \end{matrix} \right\} \left\{ \begin{matrix} L_3 & \frac{1}{2} & J_3 \\ L'_3 & \frac{1}{2} & J'_3 \\ \Delta L_3 & 1 & \Delta J_3 \end{matrix} \right\} \left\{ \begin{matrix} J_1 & J_2 & J_{12} \\ J'_1 & J'_2 & J'_{12} \\ k'_{12} & \Delta J_2 & \Delta J_3 \end{matrix} \right\} \left\{ \begin{matrix} 1 & k''_{12} & k'_{12} \\ 1 & \Delta L_2 & \Delta J_2 \\ 1 & \Delta L_3 & \Delta J_3 \end{matrix} \right\} \\
& \quad C_T \frac{18ig_A^2}{(2F_\pi)^4} \frac{1}{q_1(\Delta_1, q_{12}(\Delta_2, \Delta_3, u_5), u_4)^2 + M_\pi^2} \frac{q_{12}(\Delta_2, \Delta_3, u_5)^{1+K_1-k''_{12}}}{q_{12}(\Delta_2, \Delta_3, u_5)^2 + M_\pi^2} \Delta_1^{K'_1} \Delta_2^{K_{12}} \Delta_3^{K'_{12}}.
\end{aligned}$$

## A.IO CLASS VII

We start by representing structure (VII) diagrammatically and reducing the number of coordinate lines,

$$\begin{aligned}
& \left\langle m'_{s_a} m'_{s_b} m'_{s_c} m'_{s_d} \left| \pi'_1 \pi'_2 \pi'_3 \right| V_{\text{VII}}^{(s)} \left| m_{s_a} m_{s_b} m_{s_c} m_{s_d}, \pi_1 \pi_2 \pi_3 \right\rangle \\
&= \left\langle m'_{s_a} m'_{s_b} m'_{s_c} m'_{s_d} \left| C_T \frac{2g_A^2}{(2F_\pi)^2} \frac{(\sigma_1 \times \sigma_2) \cdot q_{12} (\sigma_3 \times \sigma_4) \cdot q_{12}}{[q_{12}^2 + M_\pi^2]^2} \right| m_{s_a} m_{s_b} m_{s_c} m_{s_d} \right\rangle
\end{aligned}$$

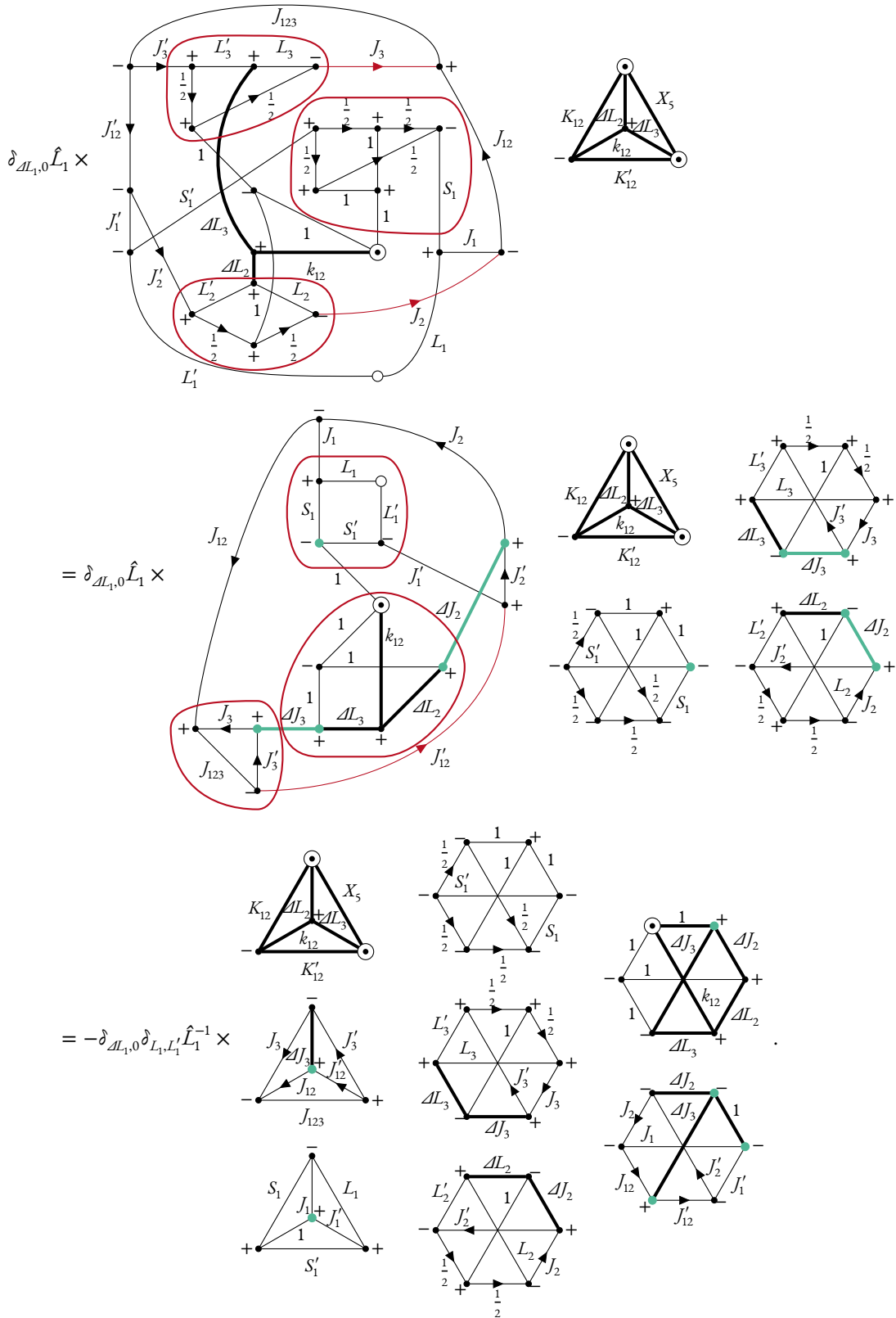
$$\begin{aligned}
 &= \text{Diagram 1} \times C_T^2 \frac{-432g_A^2}{(2F_\pi)^2} \frac{q_{12}^2}{[q_{12}^2 + M_\pi^2]^2} \\
 &= \text{Diagram 2} \times C_T^2 \frac{-432g_A^2}{(2F_\pi)^2} \frac{q_{12}^2}{[q_{12}^2 + M_\pi^2]^2} \\
 &= \text{Diagram 3} \times \int du_5 P_{X_5}(u_5) D_{K_{12}, K'_{12}}^{k_{12}} \sqrt{2}^{K_{12}} \sqrt{3}^{-k_{12}} \\
 &\quad \times C_T^2 \frac{-216g_A^2}{(2F_\pi)^2} \frac{q_{12}(\mathcal{A}_2, \mathcal{A}_3, u_5)^{2-k_{12}}}{[q_{12}(\mathcal{A}_2, \mathcal{A}_3, u_5)^2 + M_\pi^2]^2} \\
 &\quad \times \mathcal{A}_2^{K_{12}} \mathcal{A}_3^{K'_{12}}.
 \end{aligned}$$

We can now change the momentum dependence from  $q_{12}$  to  $\mathcal{A}_2$  and  $\mathcal{A}_3$ , which introduces an integral over  $u_5$ , which corresponds to the angle  $\hat{\Delta}_2 \cdot \hat{\Delta}_3$ . Note that this is the only class that does not have an integral over  $u_4$  and is independent of  $\mathcal{A}_1$ , resulting in a much simpler expression. We obtain

$$\begin{aligned}
 &= \text{Diagram 4} \times \int du_5 P_{X_5}(u_5) D_{K_{12}, K'_{12}}^{k_{12}} \sqrt{2}^{K_{12}} \sqrt{3}^{-k_{12}} (-1)^{1+K_{12}+\mathcal{A}L_3} \\
 &\quad \times C_T^2 \frac{216g_A^2}{(2F_\pi)^2} \frac{q_{12}(\mathcal{A}_2, \mathcal{A}_3, u_5)^{2-k_{12}}}{[q_{12}(\mathcal{A}_2, \mathcal{A}_3, u_5)^2 + M_\pi^2]^2} \mathcal{A}_2^{K_{12}} \mathcal{A}_3^{K'_{12}} \\
 &= \text{Diagram 5} \times \int du_5 P_{X_5}(u_5) D_{K_{12}, K'_{12}}^{k_{12}} \sqrt{2}^{K_{12}} \sqrt{3}^{-k_{12}} (-1)^{1+K_{12}+\mathcal{A}L'_3} \\
 &\quad \times C_T^2 \frac{216g_A^2}{(2F_\pi)^2} \frac{q_{12}(\mathcal{A}_2, \mathcal{A}_3, u_5)^{2-k_{12}}}{[q_{12}(\mathcal{A}_2, \mathcal{A}_3, u_5)^2 + M_\pi^2]^2} \mathcal{A}_2^{K_{12}} \mathcal{A}_3^{K'_{12}}.
 \end{aligned}$$



The next step is to insert the expression in eq. (4.11) again and start by simplifying the diagrammatic part,



Expressing the diagrams in a traditional form and combining the formulae yields an interaction part of

$$\begin{aligned}
& I_{\text{VIII}}^{L_1, L_2, L_3, S_1, J_1, J_2, J_3, J_{123}; \mathcal{A}_1, \mathcal{A}_2, \mathcal{A}_3}(\mathcal{A}_1, \mathcal{A}_2, \mathcal{A}_3) \\
&= \delta_{\mathcal{A}_1, 0} \delta_{L_1, L_1'} \int d\mu_5 P_{X_5}(u_5) \sum_{X_5, \mathcal{A}J_2, \mathcal{A}J_3} \sum_{K_{12}, K_{12}'} \sum_{k_{12}} D_{K_{12}, K_{12}'}^{k_{12}} \sqrt{2}^{K_{12}} \sqrt{3}^{-k_{12}} (-1)^{S_1+L_1+J_1+J_3+J_{12}'+J_{123}+\mathcal{A}L_2+\mathcal{A}J_2+K_{12}} \\
& \hat{L}_1^{-1} \hat{S}_1 \hat{S}_1' \hat{J}_1 \hat{J}_1' \hat{J}_2 \hat{J}_2' \hat{J}_3 \hat{J}_3' \hat{J}_{12} \hat{J}_{12}' \hat{\mathcal{A}}J_2^2 \hat{\mathcal{A}}J_3^2 \hat{k}_{12}^2 \hat{K}_{12}^2 \hat{K}_{12}'^2 \hat{X}_5^2 \begin{pmatrix} 1 & 1 & k_{12} \\ 0 & 0 & 0 \end{pmatrix} \begin{pmatrix} K_{12} & X_5 & \mathcal{A}L_2 \\ 0 & 0 & 0 \end{pmatrix} \\
& \begin{pmatrix} K_{12}' & X_5 & \mathcal{A}L_3 \\ 0 & 0 & 0 \end{pmatrix} \begin{pmatrix} \mathcal{A}L_3 & \mathcal{A}L_2 & k_{12} \\ K_{12} & K_{12}' & X_5 \end{pmatrix} \begin{pmatrix} J_{12} & J_{12}' & \mathcal{A}J_3 \\ J_3' & J_3 & J_{123} \end{pmatrix} \begin{pmatrix} 1 & J_1 & J_1' \\ L_1 & S_1' & S_1 \end{pmatrix} \\
& \left\{ \begin{matrix} \frac{1}{2} & \frac{1}{2} & 1 \\ \frac{1}{2} & \frac{1}{2} & 1 \\ S_1 & S_1' & 1 \end{matrix} \right\} \left\{ \begin{matrix} L_2 & \frac{1}{2} & J_2 \\ L_2' & \frac{1}{2} & J_2' \\ \mathcal{A}L_2 & 1 & \mathcal{A}J_2 \end{matrix} \right\} \left\{ \begin{matrix} L_3 & \frac{1}{2} & J_3 \\ L_3' & \frac{1}{2} & J_3' \\ \mathcal{A}L_3 & 1 & \mathcal{A}J_3 \end{matrix} \right\} \left\{ \begin{matrix} J_1 & J_2 & J_{12} \\ J_1' & J_2' & J_{12}' \\ 1 & \mathcal{A}J_2 & \mathcal{A}J_3 \end{matrix} \right\} \left\{ \begin{matrix} 1 & k_{12} & 1 \\ 1 & \mathcal{A}L_2 & \mathcal{A}J_2 \\ 1 & \mathcal{A}L_3 & \mathcal{A}J_3 \end{matrix} \right\} \\
& C_T^2 \frac{216g_A^2}{(2F_\pi)^2} \frac{q_{12}(\mathcal{A}_2, \mathcal{A}_3, u_5)^{2-k_{12}}}{[q_{12}(\mathcal{A}_2, \mathcal{A}_3, u_5)^2 + M_\pi^2]^2} \mathcal{A}_2^{K_{12}} \mathcal{A}_3^{K_{12}'}.
\end{aligned}$$

# B

## Four-Nucleon Extension of Spherical Hartree-Fock

The evaluation of the Fock operator is the only part of the HF calculation requiring a modification for the inclusion of four-body forces. The Fock operator obtains a contribution by summing over three of the four particles multiplied with the one-body density matrix  $g$ ,

$$\langle a' | f^{[4]} | a \rangle = \frac{1}{6} \sum_{b,b'} \sum_{c,c'} \sum_{d,d'} \langle a' b' c' d' | H | a b c d \rangle_a g_{b,b'} g_{c,c'} g_{d,d'}.$$

We use that  $g$  is rotationally invariant in the spherical formulation of HF. Thus, it cannot depend on the angular momentum projection and must be diagonal in both, single-particle angular momentum and its projection, yielding

$$g_{b,b'} = \tilde{g}_{\bar{b},\bar{b}'} \delta_{j_b,j_b'} \delta_{m_{j_b},m_{j_b'}}.$$

The index  $\bar{b}$  excludes the angular momentum projection quantum number, but it includes all remaining single-particle quantum numbers represented by  $b$ . In principle, the single-particle states also contain an isospin part. However, this part must be decoupled and cannot be handled in the coupled scheme. We, therefore, suppress the isospin part in the following derivation for brevity.

Using this relation, we can express the four-body contribution to the Fock operator diagrammatically,

suppressing the dependence of the Hamilton operator on the remaining quantum numbers,

$$\langle a' | f^{[4]} | a \rangle = \frac{1}{6} \sum_{\bar{b}, \bar{b}'} \sum_{\bar{c}, \bar{c}'} \sum_{\bar{d}, \bar{d}'} \bar{\xi}_{\bar{b}, \bar{b}'}^2 \hat{j}_b^2 \bar{\xi}_{\bar{c}, \bar{c}'}^2 \hat{j}_c^2 \bar{\xi}_{\bar{d}, \bar{d}'}^2 \hat{j}_d^2 \hat{j}_a \hat{j}_a'$$

$$= \frac{1}{6} \delta_{j_a, j_a'} \delta_{m_{j_a}, m_{j_a'}} \sum_{\bar{b}, \bar{b}'} \sum_{\bar{c}, \bar{c}'} \sum_{\bar{d}, \bar{d}'} \bar{\xi}_{\bar{b}, \bar{b}'} \bar{\xi}_{\bar{c}, \bar{c}'} \bar{\xi}_{\bar{d}, \bar{d}'}$$

where we cut the two external lines and rewrote the density matrices using  $\bar{\xi}_{\bar{b}, \bar{b}'} = \tilde{\xi}_{\bar{b}, \bar{b}'} \hat{j}_b^2$ . The diagram can be interpreted as an average over all projection quantum numbers,

$$= \frac{1}{6} \delta_{j_a, j_a'} \delta_{m_{j_a}, m_{j_a'}} \sum_{\bar{b}, \bar{b}'} \sum_{\bar{c}, \bar{c}'} \sum_{\bar{d}, \bar{d}'} \bar{\xi}_{\bar{b}, \bar{b}'} \bar{\xi}_{\bar{c}, \bar{c}'} \bar{\xi}_{\bar{d}, \bar{d}'} \underbrace{\frac{1}{\hat{j}_a \hat{j}_b \hat{j}_c \hat{j}_d} \sum_{m_{j_a}, m_{j_b}, m_{j_c}, m_{j_d}} \langle a' b' c' d' | H | a b c d \rangle_a}_{\overline{\langle a' b' c' d' | H | a b c d \rangle_a}}$$

As we store matrix elements in a coupled basis, we can speed up the calculation by evaluating the averaging in a coupled basis, with one additional complication: We have a completely antisymmetric basis and only store one of the  $24^2$  permutations of the bra and ket states in the interaction matrix. Therefore a permutation of the single-particle states is necessary. We name this permutations  $\sigma'$  and  $\sigma$  for the bra and ket state, respectively,

$$\overline{\langle a' b' c' d' | H | a b c d \rangle_a} = \frac{1}{\hat{j}_a \hat{j}_b \hat{j}_c \hat{j}_d} \sum_{\substack{m_{j_a}, m_{j_b} \\ m_{j_c}, m_{j_d}}} \underbrace{\text{sgn}(\sigma) \text{sgn}(\sigma')}_{\text{sgn}(\xi)} \langle \sigma'(a') \sigma'(b') \sigma'(c') \sigma'(d') | H | \sigma(a) \sigma(b) \sigma(c) \sigma(d) \rangle_a, \quad (\text{B.1})$$

where used the relative permutation  $\xi = \sigma' \circ \sigma^{-1}$ . For brevity we use  $p, q, r, s = \sigma(a), \sigma(b), \sigma(c), \sigma(d)$  and  $p', q', r', s' = \sigma'(a'), \sigma'(b'), \sigma'(c'), \sigma'(d')$  from now on. As the prefactor and the sum over the projection quantum numbers is symmetric in all four particles, we can express them using  $p, q, r, s$  as well. However, as the permutations between both sides differ, we cannot simply connect the outgoing  $j_p$  line with the incoming  $j'_p$  line. As a first step we can obtain the coupled matrix element by inserting identities in the  $j$ -lines,

Expressing eq. (B.1) using diagrams, inserting the above relation and cutting the  $J$  line yields

$$\begin{aligned}
 \overline{\langle a'a'b'c'd'|H|abcd\rangle}_a &= \sum_{J} \sum_{\substack{J'_{pq}, J'_{pqr} \\ J''_{pq}, J''_{pqr}}} \frac{\hat{J}^2_{pq} \hat{J}^2_{pqr} \hat{J}^2_{pqr} \hat{J}^2_{pqr}}{\hat{J}^2_p \hat{J}^2_q \hat{J}^2_r \hat{J}^2_s} \left\langle \left\{ \left[ (\bar{p}' \bar{q}') J_{pq} \bar{r}' \right] J'_{pqr} \bar{s}' \right\} J | H | \left\{ \left[ (\bar{p} \bar{q}) J_{pq} \bar{r} \right] J_{pqr} \bar{s} \right\} J \right\rangle_a \\
 &= \sum_{J} \sum_{\substack{J'_{pq}, J'_{pqr} \\ J''_{pq}, J''_{pqr}}} \frac{\hat{J}^2_{pq} \hat{J}^2_{pqr} \hat{J}^2_{pqr} \hat{J}^2_{pqr}}{\hat{J}^2_p \hat{J}^2_q \hat{J}^2_r \hat{J}^2_s} \left\langle \left\{ \left[ (\bar{p}' \bar{q}') J_{pq} \bar{r}' \right] J'_{pqr} \bar{s}' \right\} J | H | \left\{ \left[ (\bar{p} \bar{q}) J_{pq} \bar{r} \right] J_{pqr} \bar{s} \right\} J \right\rangle_a \\
 &= \sum_{J} \sum_{\substack{J'_{pq}, J'_{pqr} \\ J''_{pq}, J''_{pqr}}} \frac{\hat{J}^2_{pq} \hat{J}^2_{pqr} \hat{J}^2_{pqr} \hat{J}^2_{pqr}}{\hat{J}^2_p \hat{J}^2_q \hat{J}^2_r \hat{J}^2_s} \mathcal{F}(\xi, j_p, j_q, j_r, j_s, J_{pq}, J'_{pq}, J_{pqr}, J'_{pqr}, J).
 \end{aligned}$$

Note that at this point the lines are still not connected. However, by expressing everything in a coupled basis and cutting the  $J$  line, we separated the antisymmetric matrix element from the factor  $\mathcal{F}$  that we defined in the equation above. The factor  $\mathcal{F}$  only depends on the relative permutation, which dictates how to connect the lines. From the diagrammatic expression it is easy to see that only the relative permutation is relevant, as any permutation that is applied to both, bra and ket states, would yield the same diagram. We therefore have to go through all 24 possible permutations and calculate  $\mathcal{F}$  for each one.

We start with the simplest permutation possible,

$$\begin{aligned}
 \mathcal{F}(\{1234\}, j_p, j_q, j_r, j_s, J_{pq}, J'_{pq}, J_{pqr}, J'_{pqr}, J) &= -\text{sgn}(\{1234\}) \\
 &= \delta_{J_{pq}, J'_{pq}} \delta_{J_{pqr}, J'_{pqr}} \frac{1}{\hat{J}^2_{pq} \hat{J}^2_{pqr}} \left\{ j_p, j_q, J_{pq} \right\} \left\{ J_{pq}, j_r, J_{pqr} \right\} \left\{ J_{pqr}, j_s, J \right\}.
 \end{aligned}$$

Exchanging the first two particles only changes the sign of the relative permutation and the sign of the 3j-symbol in the top left of the diagram, which results in a simple factor.

$$\begin{aligned} \mathcal{F}\left(\{2134\}, j_p, j_q, j_r, j_s, J_{pq}, J'_{pq}, J_{pqr}, J'_{pqr}, J\right) &= -\text{sgn}(\{2134\}) \\ & \begin{array}{c} \begin{array}{ccc} & j_p & \\ + & \curvearrowright & + \\ & j_q & \\ J'_{pq} & & J_{pq} \\ - & \curvearrowright & + \\ & j_r & \\ J'_{pqr} & & J_{pqr} \\ - & \curvearrowright & + \\ & j_s & \\ & J & \end{array} \\ \\ &= (-1)^{1+j_p+j_q+J_{pq}} \mathcal{F}\left(\{1234\}, j_p, j_q, j_r, j_s, J_{pq}, J'_{pq}, J_{pqr}, J'_{pqr}, J\right). \end{array} \end{aligned}$$

This is true for all permutations, effectively reducing the number of permutations we have to derive by a factor of 2. The next permutations involve the first three particles,

$$\begin{aligned} \mathcal{F}\left(\{1324\}, j_p, j_q, j_r, j_s, J_{pq}, J'_{pq}, J_{pqr}, J'_{pqr}, J\right) &= -\text{sgn}(\{1324\}) \\ & \begin{array}{c} \begin{array}{ccc} & j_p & \\ - & \curvearrowright & + \\ & j_q & \\ J'_{pq} & & J_{pq} \\ - & \curvearrowright & + \\ & j_r & \\ J'_{pqr} & & J_{pqr} \\ - & \curvearrowright & + \\ & j_s & \\ & J & \end{array} \\ \\ &= \delta_{J_{pqr}, J'_{pqr}} \frac{1}{\hat{J}_{pqr}^2} (-1)^{1+j_q+j_r+J_{pq}+J'_{pq}} \left\{ \begin{array}{ccc} j_q & j_p & J_{pq} \\ j_r & J_{pqr} & J'_{pq} \end{array} \right\} \left\{ J_{pqr}, j_s, J \right\}, \end{array} \end{aligned}$$

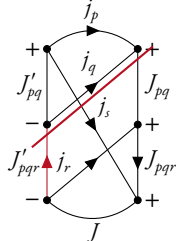
$$\mathcal{F}\left(\{3124\}, j_p, j_q, j_r, j_s, J_{pq}, J'_{pq}, J_{pqr}, J'_{pqr}, J\right) = (-1)^{1+j_p+j_r+J'_{pq}} \mathcal{F}\left(\{1324\}, j_p, j_q, j_r, j_s, J_{pq}, J'_{pq}, J_{pqr}, J'_{pqr}, J\right),$$

$$\begin{aligned} \mathcal{F}\left(\{2314\}, j_p, j_q, j_r, j_s, J_{pq}, J'_{pq}, J_{pqr}, J'_{pqr}, J\right) &= -\text{sgn}(\{2314\}) \\ & \begin{array}{c} \begin{array}{ccc} & j_q & \\ - & \curvearrowright & - \\ & j_p & \\ J'_{pq} & & J_{pq} \\ - & \curvearrowright & + \\ & j_r & \\ J'_{pqr} & & J_{pqr} \\ - & \curvearrowright & + \\ & j_s & \\ & J & \end{array} \\ \\ &= (-1)^{1+j_p+j_q+J_{pq}} \mathcal{F}\left(\{1324\}, j_q, j_p, j_r, j_s, J_{pq}, J'_{pq}, J_{pqr}, J'_{pqr}, J\right), \end{array} \end{aligned}$$

where we can see another symmetry: When exchanging the two particles that are mapped to  $j_p$  and  $j_q$ , the sign of the permutation and the sign of the 3j-symbol in the top right of the diagram are changed. Additionally, the  $j_p$  and  $j_q$  labels are exchanged. This further reduces the number of diagrams we have to evaluate. Combining both symmetries yields a fourth expression,

$$\begin{aligned} \mathcal{F}\left(\{3214\}, j_p, j_q, j_r, j_s, J_{pq}, J'_{pq}, J_{pqr}, J'_{pqr}, J\right) &= (-1)^{1+j_q+j_r+J'_{pq}} \mathcal{F}\left(\{2314\}, j_p, j_q, j_r, j_s, J_{pq}, J'_{pq}, J_{pqr}, J'_{pqr}, J\right) \\ &= (-1)^{1+j_p+j_r+J_{pq}+J'_{pq}} \mathcal{F}\left(\{1324\}, j_q, j_p, j_r, j_s, J_{pq}, J'_{pq}, J_{pqr}, J'_{pqr}, J\right). \end{aligned}$$

We now continue with permutations involving all four particles,

$$\mathcal{F}\left(\{4123\}, j_p, j_q, j_r, j_s, J_{pq}, J'_{pq}, J_{pqr}, J'_{pqr}, J\right) = -\text{sgn}(\{4123\})$$


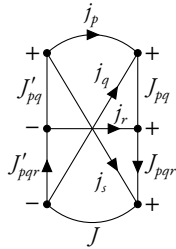
$$= (-1)^{j_p+j_q+j_r+j_s+J_{pq}+J'_{pq}+J_{pqr}+J'_{pqr}} \begin{Bmatrix} j_p & j_q & J_{pq} \\ J'_{pqr} & j_s & J'_{pq} \end{Bmatrix} \begin{Bmatrix} J_{pq} & j_r & J_{pqr} \\ J & j_s & J'_{pqr} \end{Bmatrix},$$

$$\mathcal{F}\left(\{1423\}, j_p, j_q, j_r, j_s, J_{pq}, J'_{pq}, J_{pqr}, J'_{pqr}, J\right) = (-1)^{1+j_p+j_s+J'_{pq}} \mathcal{F}\left(\{4123\}, j_p, j_q, j_r, j_s, J_{pq}, J'_{pq}, J_{pqr}, J'_{pqr}, J\right),$$

$$\mathcal{F}\left(\{4213\}, j_p, j_q, j_r, j_s, J_{pq}, J'_{pq}, J_{pqr}, J'_{pqr}, J\right) = (-1)^{1+j_p+j_q+J_{pq}} \mathcal{F}\left(\{4123\}, j_q, j_p, j_r, j_s, J_{pq}, J'_{pq}, J_{pqr}, J'_{pqr}, J\right),$$

$$\mathcal{F}\left(\{2413\}, j_p, j_q, j_r, j_s, J_{pq}, J'_{pq}, J_{pqr}, J'_{pqr}, J\right) = (-1)^{1+j_q+j_s+J'_{pq}} \mathcal{F}\left(\{4213\}, j_p, j_q, j_r, j_s, J_{pq}, J'_{pq}, J_{pqr}, J'_{pqr}, J\right)$$

$$= (-1)^{1+j_p+j_s+J_{pq}+J'_{pq}} \mathcal{F}\left(\{4123\}, j_q, j_p, j_r, j_s, J_{pq}, J'_{pq}, J_{pqr}, J'_{pqr}, J\right),$$

$$\mathcal{F}\left(\{4132\}, j_p, j_q, j_r, j_s, J_{pq}, J'_{pq}, J_{pqr}, J'_{pqr}, J\right) = -\text{sgn}(\{4132\})$$


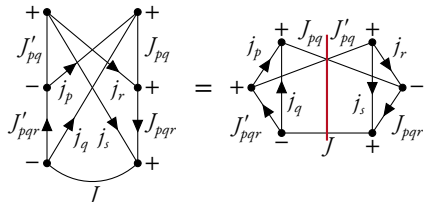
$$= (-1)^{1+j_p+j_s+J_{pq}+J_{pqr}+J'_{pqr}} \begin{Bmatrix} j_p & j_s & J'_{pq} \\ j_q & J & J'_{pqr} \\ J_{pq} & J_{pqr} & j_r \end{Bmatrix},$$

$$\mathcal{F}\left(\{1432\}, j_p, j_q, j_r, j_s, J_{pq}, J'_{pq}, J_{pqr}, J'_{pqr}, J\right) = (-1)^{1+j_p+j_s+J'_{pq}} \mathcal{F}\left(\{4132\}, j_p, j_q, j_r, j_s, J_{pq}, J'_{pq}, J_{pqr}, J'_{pqr}, J\right),$$

$$\mathcal{F}\left(\{4231\}, j_p, j_q, j_r, j_s, J_{pq}, J'_{pq}, J_{pqr}, J'_{pqr}, J\right) = (-1)^{1+j_p+j_q+J_{pq}} \mathcal{F}\left(\{4132\}, j_q, j_p, j_r, j_s, J_{pq}, J'_{pq}, J_{pqr}, J'_{pqr}, J\right),$$

$$\mathcal{F}\left(\{2431\}, j_p, j_q, j_r, j_s, J_{pq}, J'_{pq}, J_{pqr}, J'_{pqr}, J\right) = (-1)^{1+j_q+j_s+J'_{pq}} \mathcal{F}\left(\{4231\}, j_p, j_q, j_r, j_s, J_{pq}, J'_{pq}, J_{pqr}, J'_{pqr}, J\right)$$

$$= (-1)^{1+j_p+j_s+J_{pq}+J'_{pq}} \mathcal{F}\left(\{4132\}, j_q, j_p, j_r, j_s, J_{pq}, J'_{pq}, J_{pqr}, J'_{pqr}, J\right),$$

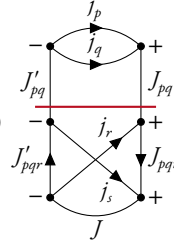
$$\mathcal{F}\left(\{4312\}, j_p, j_q, j_r, j_s, J_{pq}, J'_{pq}, J_{pqr}, J'_{pqr}, J\right) = -\text{sgn}(\{4312\})$$


$$= (-1)^{1+j_p+j_q+J'_{pq}+J} \begin{Bmatrix} j_p & j_q & J_{pq} \\ J & J'_{pq} & J'_{pqr} \end{Bmatrix} \begin{Bmatrix} j_r & j_s & J'_{pq} \\ J & J_{pq} & J_{pqr} \end{Bmatrix},$$

$$\mathcal{F}\left(\{3412\}, j_p, j_q, j_r, j_s, J_{pq}, J'_{pq}, J_{pqr}, J'_{pqr}, J\right) = (-1)^{1+j_p+j_s+J'_{pq}} \mathcal{F}\left(\{4312\}, j_p, j_q, j_r, j_s, J_{pq}, J'_{pq}, J_{pqr}, J'_{pqr}, J\right),$$

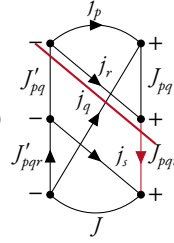
$$\begin{aligned}\mathcal{F}(\{4321\}, j_p, j_q, j_r, j_s, J_{pq}, J'_{pq}, J_{pqr}, J'_{pqr}, J) &= (-1)^{1+j_p+j_q+J_{pq}} \mathcal{F}(\{4312\}, j_q, j_p, j_r, j_s, J_{pq}, J'_{pq}, J_{pqr}, J'_{pqr}, J), \\ \mathcal{F}(\{3421\}, j_p, j_q, j_r, j_s, J_{pq}, J'_{pq}, J_{pqr}, J'_{pqr}, J) &= (-1)^{1+j_r+j_s+J'_{pq}} \mathcal{F}(\{4321\}, j_p, j_q, j_r, j_s, J_{pq}, J'_{pq}, J_{pqr}, J'_{pqr}, J) \\ &= (-1)^{j_p+j_q+j_r+j_s+J_{pq}+J'_{pq}} \mathcal{F}(\{4312\}, j_q, j_p, j_r, j_s, J_{pq}, J'_{pq}, J_{pqr}, J'_{pqr}, J),\end{aligned}$$

$$\begin{aligned}\mathcal{F}(\{1243\}, j_p, j_q, j_r, j_s, J_{pq}, J'_{pq}, J_{pqr}, J'_{pqr}, J) &= -\text{sgn}(\{1243\}) \\ &= \delta_{J_{pq}, J'_{pq}} \frac{1}{f_{pq}^2} (-1)^{1+j_r+j_s+J_{pqr}+J'_{pqr}} \begin{Bmatrix} j_r & J_{pq} & J_{pqr} \\ j_s & J & J'_{pqr} \end{Bmatrix} \begin{Bmatrix} j_p & j_q & J_{pq} \end{Bmatrix},\end{aligned}$$



$$\mathcal{F}(\{2143\}, j_p, j_q, j_r, j_s, J_{pq}, J'_{pq}, J_{pqr}, J'_{pqr}, J) = (-1)^{1+j_p+j_q+J_{pq}} \mathcal{F}(\{1243\}, j_p, j_q, j_r, j_s, J_{pq}, J'_{pq}, J_{pqr}, J'_{pqr}, J),$$

$$\begin{aligned}\mathcal{F}(\{1342\}, j_p, j_q, j_r, j_s, J_{pq}, J'_{pq}, J_{pqr}, J'_{pqr}, J) &= -\text{sgn}(\{1342\}) \\ &= (-1)^{1+j_r+j_s+J_{pq}+J'_{pq}+J_{pqr}+J'_{pqr}} \begin{Bmatrix} j_p & j_q & J_{pq} \\ J_{pqr} & j_r & J'_{pq} \end{Bmatrix} \begin{Bmatrix} j_q & J'_{pq} & J_{pqr} \\ j_s & J & J'_{pqr} \end{Bmatrix},\end{aligned}$$



$$\mathcal{F}(\{3142\}, j_p, j_q, j_r, j_s, J_{pq}, J'_{pq}, J_{pqr}, J'_{pqr}, J) = (-1)^{1+j_p+j_r+J'_{pq}} \mathcal{F}(\{1342\}, j_p, j_q, j_r, j_s, J_{pq}, J'_{pq}, J_{pqr}, J'_{pqr}, J),$$

$$\mathcal{F}(\{2341\}, j_p, j_q, j_r, j_s, J_{pq}, J'_{pq}, J_{pqr}, J'_{pqr}, J) = (-1)^{1+j_p+j_q+J_{pq}} \mathcal{F}(\{1342\}, j_q, j_p, j_r, j_s, J_{pq}, J'_{pq}, J_{pqr}, J'_{pqr}, J),$$

$$\begin{aligned}\mathcal{F}(\{3241\}, j_p, j_q, j_r, j_s, J_{pq}, J'_{pq}, J_{pqr}, J'_{pqr}, J) &= (-1)^{1+j_q+j_r+J'_{pq}} \mathcal{F}(\{2341\}, j_p, j_q, j_r, j_s, J_{pq}, J'_{pq}, J_{pqr}, J'_{pqr}, J) \\ &= (-1)^{1+j_p+j_r+J_{pq}+J'_{pq}} \mathcal{F}(\{1342\}, j_q, j_p, j_r, j_s, J_{pq}, J'_{pq}, J_{pqr}, J'_{pqr}, J).\end{aligned}$$

Evaluating the averaging in this way can speed up the calculation tremendously, as the sum over the projection quantum numbers does not have to be performed anymore and decoupling of the matrix elements is only necessary for the isospin part.



# References

- [1] J. Chadwick, **The Existence of a Neutron**, *Proceedings of the Royal Society A: Mathematical, Physical and Engineering Sciences* 136, 692 (1932), DOI: [10.1098/rspa.1932.0112](https://doi.org/10.1098/rspa.1932.0112).
- [2] H. Yukawa, **On the Interaction of Elementary Particles. I**, *Proceedings of the Physico-Mathematical Society of Japan. 3rd Series* 17, 48 (1935), DOI: [10.11429/ppmsj1919.17.0\\_48](https://doi.org/10.11429/ppmsj1919.17.0_48).
- [3] C. M. G. Lattes, H. Muirhead, G. P. S. Occhialini, *et al.*, **Processes involving Charged Mesons**, *Nature* 159, 694 (1947), DOI: [10.1038/159694a0](https://doi.org/10.1038/159694a0).
- [4] R. Machleidt, K. Holinde, and C. Elster, **The Bonn meson-exchange model for the nucleon-nucleon interaction**, *Physics Reports* 149, 1 (1987), DOI: [10.1016/S0370-1573\(87\)80002-9](https://doi.org/10.1016/S0370-1573(87)80002-9).
- [5] R. Machleidt, **High-precision, charge-dependent Bonn nucleon-nucleon potential**, *Physical Review C* 63, 024001 (2001), arXiv: [nuc1-th/0006014](https://arxiv.org/abs/nuc1-th/0006014), DOI: [10.1103/PhysRevC.63.024001](https://doi.org/10.1103/PhysRevC.63.024001).
- [6] A. Rios, A. Carbone, and A. Polls, **Comparison of nuclear Hamiltonians using spectral function sum rules**, *Physical Review C* 96, 014003 (2017), arXiv: [1702.03117](https://arxiv.org/abs/1702.03117), DOI: [10.1103/PhysRevC.96.014003](https://doi.org/10.1103/PhysRevC.96.014003).
- [7] W. E. Ormand, B. A. Brown, and M. Hjorth-Jensen, **Realistic calculations for c-coefficients of the isobaric mass multiplet equation in 1p0f shell nuclei**, *Physical Review C* 96, 024323 (2017), arXiv: [1608.08127](https://arxiv.org/abs/1608.08127), DOI: [10.1103/PhysRevC.96.024323](https://doi.org/10.1103/PhysRevC.96.024323).
- [8] L. Hlophe, J. Lei, C. Elster, *et al.*, **<sup>6</sup>Li in a Three-Body Model with Realistic Forces: Separable versus Non-separable Approach**, *Physical Review C* 96, 064003 (2017), arXiv: [1710.02602](https://arxiv.org/abs/1710.02602), DOI: [10.1103/PhysRevC.96.064003](https://doi.org/10.1103/PhysRevC.96.064003).
- [9] A. Shirokov, J. Vary, A. Mazur, *et al.*, **Realistic nuclear Hamiltonian: Ab exitu approach**, *Physics Letters B* 644, 33 (2007), arXiv: [nuc1-th/0512105](https://arxiv.org/abs/nuc1-th/0512105), DOI: [10.1016/j.physletb.2006.10.066](https://doi.org/10.1016/j.physletb.2006.10.066).
- [10] R. B. Wiringa, V. G. J. Stoks, and R. Schiavilla, **Accurate nucleon-nucleon potential with charge-independence breaking**, *Physical Review C* 51, 38 (1995), arXiv: [nuc1-th/9408016](https://arxiv.org/abs/nuc1-th/9408016), DOI: [10.1103/PhysRevC.51.38](https://doi.org/10.1103/PhysRevC.51.38).

- [11] J. Fujita and H. Miyazawa, **Pion Theory of Three-Body Forces**, *Progress of Theoretical Physics* 17, 360 (1957), DOI: [10.1143/PTP.17.360](https://doi.org/10.1143/PTP.17.360).
- [12] N. Kalantar-Nayestanaki and E. Epelbaum, **Feature Article: The Three-Nucleon System as a Laboratory for Nuclear Physics: The Need for 3N Forces**, *Nuclear Physics News* 17, 22 (2007), arXiv: [nuc1-th/0703089](https://arxiv.org/abs/nuc1-th/0703089), DOI: [10.1080/10506890701404222](https://doi.org/10.1080/10506890701404222).
- [13] S. C. Pieper, V. R. Pandharipande, R. B. Wiringa, *et al.*, **Realistic models of pion-exchange three-nucleon interactions**, *Physical Review C* 64, 014001 (2001), arXiv: [nuc1-th/0102004](https://arxiv.org/abs/nuc1-th/0102004), DOI: [10.1103/PhysRevC.64.014001](https://doi.org/10.1103/PhysRevC.64.014001).
- [14] T. Yamazaki, K.-i. Ishikawa, Y. Kuramashi, *et al.*, **Study of quark mass dependence of binding energy for light nuclei in 2 + 1 flavor lattice QCD**, *Physical Review D* 92, 014501 (2015), DOI: [10.1103/PhysRevD.92.014501](https://doi.org/10.1103/PhysRevD.92.014501).
- [15] K. Orginos, A. Parreno, M. J. Savage, *et al.*, **Two Nucleon Systems at  $m_\pi \sim 450$  MeV from Lattice QCD**, *Physical Review D* 92, 114512 (2015), arXiv: [1508.07583](https://arxiv.org/abs/1508.07583), DOI: [10.1103/PhysRevD.92.114512](https://doi.org/10.1103/PhysRevD.92.114512).
- [16] E. Chang, W. Detmold, K. Orginos, *et al.*, **Magnetic structure of light nuclei from lattice QCD**, *Physical Review D* 92, 114502 (2015), arXiv: [1506.05518](https://arxiv.org/abs/1506.05518), DOI: [10.1103/PhysRevD.92.114502](https://doi.org/10.1103/PhysRevD.92.114502).
- [17] S. Aoki, T. Doi, T. Hatsuda, *et al.*, **Lattice quantum chromodynamical approach to nuclear physics**, *Progress of Theoretical and Experimental Physics* 2012, 1A105 (2012), arXiv: [1206.5088](https://arxiv.org/abs/1206.5088), DOI: [10.1093/ptep/pts010](https://doi.org/10.1093/ptep/pts010).
- [18] S. Weinberg, **Nuclear forces from chiral lagrangians**, *Physics Letters B* 251, 288 (1990), DOI: [10.1016/0370-2693\(90\)90938-3](https://doi.org/10.1016/0370-2693(90)90938-3).
- [19] S. Weinberg, **Effective chiral lagrangians for nucleon-pion interactions and nuclear forces**, *Nuclear Physics B* 363, 3 (1991), DOI: [10.1016/0550-3213\(91\)90231-L](https://doi.org/10.1016/0550-3213(91)90231-L).
- [20] P. Boucaud, P. Dimopoulos, F. Farchioni, *et al.*, **Dynamical twisted mass fermions with light quarks**, *Physics Letters B* 650, 304 (2007), arXiv: [hep-lat/0701012](https://arxiv.org/abs/hep-lat/0701012), DOI: [10.1016/j.physletb.2007.04.054](https://doi.org/10.1016/j.physletb.2007.04.054).
- [21] R. Baron, P. Boucaud, P. Dimopoulos, *et al.*, **Light meson physics from maximally twisted mass lattice QCD**, *Journal of High Energy Physics* 2010, 97 (2010), arXiv: [0911.5061](https://arxiv.org/abs/0911.5061), DOI: [10.1007/JHEP08\(2010\)097](https://doi.org/10.1007/JHEP08(2010)097).
- [22] D. R. Entem, N. Kaiser, R. Machleidt, *et al.*, **Peripheral nucleon-nucleon scattering at fifth order of chiral perturbation theory**, *Physical Review C* 91, 014002 (2015), arXiv: [1411.5335](https://arxiv.org/abs/1411.5335), DOI: [10.1103/PhysRevC.91.014002](https://doi.org/10.1103/PhysRevC.91.014002).

- [23] D. R. Entem, N. Kaiser, R. Machleidt, *et al.*, **Dominant contributions to the nucleon-nucleon interaction at sixth order of chiral perturbation theory**, *Physical Review C* 92, 064001 (2015), arXiv: [1505.03562](#), DOI: [10.1103/PhysRevC.92.064001](#).
- [24] E. Epelbaum, H. Krebs, and U.-G. Meißner, **Precision Nucleon-Nucleon Potential at Fifth Order in the Chiral Expansion**, *Physical Review Letters* 115, 122301 (2015), arXiv: [1412.4623](#), DOI: [10.1103/PhysRevLett.115.122301](#).
- [25] D. R. Entem, R. Machleidt, and Y. Nosyk, **High-quality two-nucleon potentials up to fifth order of the chiral expansion**, *Physical Review C* 96, 024004 (2017), arXiv: [1703.05454](#), DOI: [10.1103/PhysRevC.96.024004](#).
- [26] P. Reinert, H. Krebs, and E. Epelbaum, **Semilocal momentum-space regularized chiral two-nucleon potentials up to fifth order** (2017), arXiv: [1711.08821](#).
- [27] V. Bernard, E. Epelbaum, H. Krebs, *et al.*, **Subleading contributions to the chiral three-nucleon force: Long-range terms**, *Physical Review C* 77, 064004 (2008), arXiv: [0712.1967](#), DOI: [10.1103/PhysRevC.77.064004](#).
- [28] V. Bernard, E. Epelbaum, H. Krebs, *et al.*, **Subleading contributions to the chiral three-nucleon force. II. Short-range terms and relativistic corrections**, *Physical Review C* 84, 054001 (2011), arXiv: [1108.3816](#), DOI: [10.1103/PhysRevC.84.054001](#).
- [29] K. Hebeler, H. Krebs, E. Epelbaum, *et al.*, **Efficient calculation of chiral three-nucleon forces up to N<sup>3</sup>LO for *ab initio* studies**, *Physical Review C* 91, 044001 (2015), arXiv: [1502.02977](#), DOI: [10.1103/PhysRevC.91.044001](#).
- [30] E. Epelbaum, **Four-nucleon force in chiral effective field theory**, *Physics Letters B* 639, 456 (2006), arXiv: [nucl-th/0511025](#), DOI: [10.1016/j.physletb.2006.06.046](#).
- [31] E. Epelbaum, **Four-nucleon force using the method of unitary transformation**, *The European Physical Journal A* 34, 197 (2007), arXiv: [0710.4250](#), DOI: [10.1140/epja/i2007-10496-0](#).
- [32] I. Tews, T. Krüger, K. Hebeler, *et al.*, **Neutron Matter at Next-to-Next-to-Next-to-Leading Order in Chiral Effective Field Theory**, *Physical Review Letters* 110, 032504 (2013), arXiv: [1206.0025](#), DOI: [10.1103/PhysRevLett.110.032504](#).
- [33] T. Krüger, I. Tews, K. Hebeler, *et al.*, **Neutron matter from chiral effective field theory interactions**, *Physical Review C* 88, 025802 (2013), arXiv: [1304.2212](#), DOI: [10.1103/PhysRevC.88.025802](#).
- [34] N. Kaiser and R. Millus, **Reducible chiral four-body interactions in nuclear matter**, *The European Physical Journal A* 52, 4 (2016), arXiv: [1508.07323](#), DOI: [10.1140/epja/i2016-16004-7](#).

- [35] T. Krüger, **Neutron matter, neutron pairing, and neutron drops based on chiral effective field theory interactions**, PhD thesis, TU Darmstadt (2016), <http://tuprints.ulb.tu-darmstadt.de/id/eprint/5649>.
- [36] A. Nogga, D. Rozpędzik, E. Epelbaum, *et al.*, **Four-nucleon force contribution to the binding energy of  $^4\text{He}$** , *EPJ Web of Conferences* 3, 05006 (2010), DOI: [10.1051/epjconf/20100305006](https://doi.org/10.1051/epjconf/20100305006).
- [37] A. K. Motovilov, **Progress in methods to solve the Faddeev and Yakubovsky differential equations**, *Few-Body Systems* 43, 121 (2008), arXiv: [0712.0620](https://arxiv.org/abs/0712.0620), DOI: [10.1007/s00601-008-0219-5](https://doi.org/10.1007/s00601-008-0219-5).
- [38] J. Lomnitz-Adler, V. Pandharipande, and R. Smith, **Monte Carlo calculations of triton and  $^4\text{He}$  nuclei with the Reid potential**, *Nuclear Physics A* 361, 399 (1981), DOI: [10.1016/0375-9474\(81\)90642-4](https://doi.org/10.1016/0375-9474(81)90642-4).
- [39] J. Carlson, **Alpha particle structure**, *Physical Review C* 38, 1879 (1988), DOI: [10.1103/PhysRevC.38.1879](https://doi.org/10.1103/PhysRevC.38.1879).
- [40] B. S. Pudliner, V. R. Pandharipande, J. Carlson, *et al.*, **Quantum Monte Carlo Calculations of  $A \leq 6$  Nuclei**, *Physical Review Letters* 74, 4396 (1995), arXiv: [nuc1-th/9502031](https://arxiv.org/abs/nuc1-th/9502031), DOI: [10.1103/PhysRevLett.74.4396](https://doi.org/10.1103/PhysRevLett.74.4396).
- [41] D. C. Zheng, B. R. Barrett, L. Jaqua, *et al.*, **Microscopic calculations of the spectra of light nuclei**, *Physical Review C* 48, 1083 (1993), arXiv: [nuc1-th/9304025](https://arxiv.org/abs/nuc1-th/9304025), DOI: [10.1103/PhysRevC.48.1083](https://doi.org/10.1103/PhysRevC.48.1083).
- [42] R. Roth and P. Navrátil, **Ab Initio Study of  $^{40}\text{Ca}$  with an Importance-Truncated No-Core Shell Model**, *Physical Review Letters* 99, 092501 (2007), arXiv: [0705.4069](https://arxiv.org/abs/0705.4069), DOI: [10.1103/PhysRevLett.99.092501](https://doi.org/10.1103/PhysRevLett.99.092501).
- [43] R. Roth, **Importance truncation for large-scale configuration interaction approaches**, *Physical Review C* 79, 064324 (2009), arXiv: [0903.4605](https://arxiv.org/abs/0903.4605), DOI: [10.1103/PhysRevC.79.064324](https://doi.org/10.1103/PhysRevC.79.064324).
- [44] G. Hagen, M. Hjorth-Jensen, G. R. Jansen, *et al.*, **Emergent properties of nuclei from ab initio coupled-cluster calculations**, *Physica Scripta* 91, 063006 (2016), arXiv: [1601.08203](https://arxiv.org/abs/1601.08203), DOI: [10.1088/0031-8949/91/6/063006](https://doi.org/10.1088/0031-8949/91/6/063006).
- [45] A. Cipollone, C. Barbieri, and P. Navrátil, **Isotopic Chains Around Oxygen from Evolved Chiral Two- and Three-Nucleon Interactions**, *Physical Review Letters* 111, 062501 (2013), arXiv: [1303.4900](https://arxiv.org/abs/1303.4900), DOI: [10.1103/PhysRevLett.111.062501](https://doi.org/10.1103/PhysRevLett.111.062501).
- [46] V. Somà, A. Cipollone, C. Barbieri, *et al.*, **Chiral two- and three-nucleon forces along medium-mass isotope chains**, *Physical Review C* 89, 061301 (2014), arXiv: [1312.2068](https://arxiv.org/abs/1312.2068), DOI: [10.1103/PhysRevC.89.061301](https://doi.org/10.1103/PhysRevC.89.061301).

- [47] K. Tsukiyama, S. K. Bogner, and A. Schwenk, **In-Medium Similarity Renormalization Group For Nuclei**, *Physical Review Letters* 106, 222502 (2011), arXiv: [1006.3639](#), DOI: [10.1103/PhysRevLett.106.222502](#).
- [48] H. Hergert, S. K. Bogner, T. . Morris, *et al.*, **The In-Medium Similarity Renormalization Group: A novel ab initio method for nuclei**, *Physics Reports* 621, 165 (2016), arXiv: [1512.06956](#), DOI: [10.1016/j.physrep.2015.12.007](#).
- [49] A. Tichai, J. Langhammer, S. Binder, *et al.*, **Hartree-Fock many-body perturbation theory for nuclear ground-states**, *Physics Letters B* 756, 283 (2016), arXiv: [1601.03703](#), DOI: [10.1016/j.physletb.2016.03.029](#).
- [50] M. Hjorth-Jensen, M. P. Lombardo, and U. van Kolck, Eds., **An Advanced Course in Computational Nuclear Physics**, ser. Lecture Notes in Physics. Cham: Springer International Publishing (2017), 936, ISBN: [978-3-319-53335-3](#), DOI: [10.1007/978-3-319-53336-0](#).
- [51] A. Tichai, E. Gebrerufael, and R. Roth, **Open-Shell Nuclei from No-Core Shell Model with Perturbative Improvement**, *submitted to Physical Review Letters* (2017), arXiv: [1703.05664](#).
- [52] E. Gebrerufael, K. Vobig, H. Hergert, *et al.*, **Ab Initio Description of Open-Shell Nuclei: Merging No-Core Shell Model and In-Medium Similarity Renormalization Group**, *Physical Review Letters* 118, 152503 (2017), arXiv: [1610.05254](#), DOI: [10.1103/PhysRevLett.118.152503](#).
- [53] H. Feldmeier, T. Neff, R. Roth, *et al.*, **A unitary correlation operator method**, *Nuclear Physics A* 632, 61 (1998), arXiv: [nucl-th/9709038](#), DOI: [10.1016/S0375-9474\(97\)00805-1](#).
- [54] S. D. Głazek and K. G. Wilson, **Renormalization of Hamiltonians**, *Physical Review D* 48, 5863 (1993), DOI: [10.1103/PhysRevD.48.5863](#).
- [55] F. Wegner, **Flow-equations for Hamiltonians**, *Annalen der Physik* 506, 77 (1994), DOI: [10.1002/andp.19945060203](#).
- [56] R. Furnstahl, **The Renormalization Group in Nuclear Physics**, *Nuclear Physics B - Proceedings Supplements* 228, 139 (2012), arXiv: [1203.1779](#), DOI: [10.1016/j.nuclphysbps.2012.06.005](#).
- [57] R. J. Furnstahl and K. Hebeler, **New applications of renormalization group methods in nuclear physics**, *Reports on Progress in Physics* 76, 126301 (2013), arXiv: [1305.3800](#), DOI: [10.1088/0034-4885/76/12/126301](#).
- [58] R. Roth, S. Binder, K. Vobig, *et al.*, **Medium-Mass Nuclei with Normal-Ordered Chiral NN + 3N Interactions**, *Physical Review Letters* 109, 052501 (2012), arXiv: [1112.0287](#), DOI: [10.1103/PhysRevLett.109.052501](#).

- [59] H. Hergert, S. Binder, A. Calci, *et al.*, **Ab Initio Calculations of Even Oxygen Isotopes with Chiral Two-Plus-Three-Nucleon Interactions**, *Physical Review Letters* 110, 242501 (2013), arXiv: 1302.7294, DOI: 10.1103/PhysRevLett.110.242501.
- [60] A. Calci, **Evolved Chiral Hamiltonians at the Three-Body Level and Beyond**, PhD thesis, Technische Universität Darmstadt (2014), <http://tuprints.ulb.tu-darmstadt.de/id/eprint/4069>.
- [61] S. Schulz, **SRG-Induced Four-Body Forces in Ab Initio Nuclear Structure**, Master's thesis, Technische Universität Darmstadt (2013), [http://crunch.ikp.physik.tu-darmstadt.de/tnp/pub/2013\\_schulz\\_master.pdf](http://crunch.ikp.physik.tu-darmstadt.de/tnp/pub/2013_schulz_master.pdf).
- [62] E. Anderson, S. K. Bogner, R. J. Furnstahl, *et al.*, **Block diagonalization using similarity renormalization group flow equations**, *Physical Review C* 77, 037001 (2008), arXiv: 0801.1098, DOI: 10.1103/PhysRevC.77.037001.
- [63] E. D. Jurgenson, **Applications of the Similarity Renormalization Group to the Nuclear Interaction**, PhD thesis, Ohio State University (2009), arXiv: 0912.2937.
- [64] W. Li, E. R. Anderson, and R. J. Furnstahl, **Similarity renormalization group with novel generators**, *Physical Review C* 84, 054002 (2011), arXiv: 1106.2835, DOI: 10.1103/PhysRevC.84.054002.
- [65] S. Reinhardt, **Unitary Transformations for Nuclear Structure Calculations**, PhD thesis, Technische Universität Darmstadt (2013), <http://tuprints.ulb.tu-darmstadt.de/3448/>.
- [66] N. M. Dicaire, C. Omand, and P. Navrátil, **Alternative similarity renormalization group generators in nuclear structure calculations**, *Physical Review C* 90, 034302 (2014), arXiv: 1406.1815, DOI: 10.1103/PhysRevC.90.034302.
- [67] T. Hüther, **Alternative Generators for the Similarity Renormalisation Group**, Master's thesis, Technische Universität Darmstadt (2016).
- [68] C. Patrignani, K. Agashe, G. Aielli, *et al.*, **Review of Particle Physics**, *Chinese Physics C* 40, 100001 (2016), DOI: 10.1088/1674-1137/40/10/100001.
- [69] J.-W. Chen, G. Rupak, and M. J. Savage, **Nucleon-nucleon effective field theory without pions**, *Nuclear Physics A* 653, 386 (1999), arXiv: nucl-th/9902056, DOI: 10.1016/S0375-9474(99)00298-5.
- [70] S. Weinberg, **Phenomenological Lagrangians**, *Physica A: Statistical Mechanics and its Applications* 96, 327 (1979), DOI: 10.1016/0378-4371(79)90223-1.
- [71] E. Epelbaum, H.-W. Hammer, and U.-G. Meißner, **Modern theory of nuclear forces**, *Reviews of Modern Physics* 81, 1773 (2009), arXiv: 0811.1338, DOI: 10.1103/RevModPhys.81.1773.

- [72] R. Machleidt and D. Entem, **Chiral effective field theory and nuclear forces**, *Physics Reports* 503, 1 (2011), arXiv: [1105.2919](https://arxiv.org/abs/1105.2919), DOI: [10.1016/j.physrep.2011.02.001](https://doi.org/10.1016/j.physrep.2011.02.001).
- [73] V. Koch, **Aspects of Chiral Symmetry**, *International Journal of Modern Physics E* 06, 203 (1997), arXiv: [nuc1-th/9706075](https://arxiv.org/abs/nuc1-th/9706075), DOI: [10.1142/S0218301397000147](https://doi.org/10.1142/S0218301397000147).
- [74] D. Phillips, **Building light nuclei from neutrons, protons, and pions**, *Czechoslovak Journal of Physics* 52, B49 (2002), arXiv: [nuc1-th/0203040](https://arxiv.org/abs/nuc1-th/0203040), DOI: [10.1007/s10582-002-0079-z](https://doi.org/10.1007/s10582-002-0079-z).
- [75] S. Scherer and M. R. Schindler, **A Primer for Chiral Perturbation Theory**, ser. Lecture Notes in Physics. Berlin, Heidelberg: Springer Berlin Heidelberg (2012), 830, ISBN: [978-3-642-19253-1](https://www.springer.com/978-3-642-19253-1), DOI: [10.1007/978-3-642-19254-8](https://doi.org/10.1007/978-3-642-19254-8).
- [76] E. Epelbaum, **Nuclear forces from chiral effective field theory**, *Progress in Particle and Nuclear Physics* 67, 343 (2012), arXiv: [1001.3229](https://arxiv.org/abs/1001.3229), DOI: [10.1016/j.ppnp.2011.12.041](https://doi.org/10.1016/j.ppnp.2011.12.041).
- [77] J. Goldstone, **Field theories with « Superconductor » solutions**, *Il Nuovo Cimento* 19, 154 (1961), DOI: [10.1007/BF02812722](https://doi.org/10.1007/BF02812722).
- [78] V. Bernard, N. Kaiser, J. Kambor, *et al.*, **Chiral structure of the nucleon**, *Nuclear Physics, Section B* 388, 315 (1992), DOI: [10.1016/0550-3213\(92\)90615-I](https://doi.org/10.1016/0550-3213(92)90615-I).
- [79] E. Epelbaum, W. Glöckle, and U.-G. Meißner, **Nuclear forces from chiral Lagrangians using the method of unitary transformation (I): Formalism**, *Nuclear Physics A* 637, 107 (1998), arXiv: [nuc1-th/9801064](https://arxiv.org/abs/nuc1-th/9801064), DOI: [10.1016/S0375-9474\(98\)00220-6](https://doi.org/10.1016/S0375-9474(98)00220-6).
- [80] S. Ôkubo, **Diagonalization of Hamiltonian and Tamm-Dancoff Equation**, *Progress of Theoretical Physics* 12, 603 (1954), DOI: [10.1143/PTP.12.603](https://doi.org/10.1143/PTP.12.603).
- [81] E. Epelbaum, W. Glöckle, and U.-G. Meißner, **Nuclear forces from chiral Lagrangians using the method of unitary transformation II: The two-nucleon system**, *Nuclear Physics A* 671, 295 (2000), arXiv: [nuc1-th/9910064](https://arxiv.org/abs/nuc1-th/9910064), DOI: [10.1016/S0375-9474\(99\)00821-0](https://doi.org/10.1016/S0375-9474(99)00821-0).
- [82] M. E. Peskin and D. V. Schroeder, **An Introduction to Quantum Field Theory**. Cambridge, Massachusetts: Perseus Books (1995), ISBN: [0-201-50397-2](https://www.perseusbooks.com/0-201-50397-2).
- [83] C. Ordóñez, L. Ray, and U. van Kolck, **Two-nucleon potential from chiral Lagrangians**, *Physical Review C* 53, 2086 (1996), arXiv: [hep-ph/9511380](https://arxiv.org/abs/hep-ph/9511380), DOI: [10.1103/PhysRevC.53.2086](https://doi.org/10.1103/PhysRevC.53.2086).
- [84] D. R. Entem and R. Machleidt, **Accurate charge-dependent nucleon-nucleon potential at fourth order of chiral perturbation theory**, *Physical Review C* 68, 041001 (2003), arXiv: [nuc1-th/0304018](https://arxiv.org/abs/nuc1-th/0304018), DOI: [10.1103/PhysRevC.68.041001](https://doi.org/10.1103/PhysRevC.68.041001).
- [85] D. R. Entem and R. Machleidt, **Chiral  $2\pi$  exchange at fourth order and peripheral NN scattering**, *Physical Review C* 66, 014002 (2002), arXiv: [nuc1-th/0202039](https://arxiv.org/abs/nuc1-th/0202039), DOI: [10.1103/PhysRevC.66.014002](https://doi.org/10.1103/PhysRevC.66.014002).

- [86] R. N. Pérez, J. E. Amaro, and E. R. Arriola, **Coarse-grained potential analysis of neutron-proton and proton-proton scattering below the pion production threshold**, *Physical Review C* 88, 064002 (2013), arXiv: [1310.2536](https://arxiv.org/abs/1310.2536), DOI: [10.1103/PhysRevC.88.064002](https://doi.org/10.1103/PhysRevC.88.064002).
- [87] R. Navarro Pérez, J. E. Amaro, and E. R. Arriola, **Erratum: Coarse-grained potential analysis of neutron-proton and proton-proton scattering below the pion production threshold** [*Phys. Rev. C* 88, 064002 (2013)], *Physical Review C* 91, 029901 (2015), DOI: [10.1103/PhysRevC.91.029901](https://doi.org/10.1103/PhysRevC.91.029901).
- [88] P. Navrátil, **Local three-nucleon interaction from chiral effective field theory**, *Few-Body Systems* 41, 117 (2007), arXiv: [0707.4680](https://arxiv.org/abs/0707.4680), DOI: [10.1007/s00601-007-0193-3](https://doi.org/10.1007/s00601-007-0193-3).
- [89] D. Gazit, S. Quaglioni, and P. Navrátil, **Three-Nucleon Low-Energy Constants from the Consistency of Interactions and Currents in Chiral Effective Field Theory**, *Physical Review Letters* 103, 102502 (2009), arXiv: [0812.4444](https://arxiv.org/abs/0812.4444), DOI: [10.1103/PhysRevLett.103.102502](https://doi.org/10.1103/PhysRevLett.103.102502).
- [90] K. Hebeler, *Private Communication* (2017).
- [91] T. Hüther, *Private Communication* (2017).
- [92] D. A. Varshalovich, A. N. Moskalev, and V. K. Khersonskii, **Quantum theory of angular momentum**. World Scientific Publishing (1988), ISBN: [9971501074](https://www.worldscientific.com/97898101074).
- [93] G. Kamuntavičius, R. Kalinauskas, B. Barrett, *et al.*, **The general harmonic-oscillator brackets: compact expression, symmetries, sums and Fortran code**, *Nuclear Physics A* 695, 191 (2001), arXiv: [nuc1-th/0105009](https://arxiv.org/abs/nuc1-th/0105009), DOI: [10.1016/S0375-9474\(01\)01101-0](https://doi.org/10.1016/S0375-9474(01)01101-0).
- [94] P. Navrátil, G. P. Kamuntavičius, and B. R. Barrett, **Few-nucleon systems in a translationally invariant harmonic oscillator basis**, *Physical Review C* 61, 044001 (2000), arXiv: [nuc1-th/9907054](https://arxiv.org/abs/nuc1-th/9907054), DOI: [10.1103/PhysRevC.61.044001](https://doi.org/10.1103/PhysRevC.61.044001).
- [95] S. Binder, **Angular Momentum Projection and Three-Body Forces in the No-Core Shell Model**, Master's thesis, Technische Universität Darmstadt (2010), [http://crunch.ikp.physik.tu-darmstadt.de/tnp/pub/2010\\_binder\\_master.pdf](http://crunch.ikp.physik.tu-darmstadt.de/tnp/pub/2010_binder_master.pdf).
- [96] S. G. Johnson, **Cubature - adaptive multidimensional integration**, version 1.0.1 (2013), <https://github.com/stevengj/cubature>.
- [97] S. K. Bogner, R. J. Furnstahl, and R. J. Perry, **Similarity renormalization group for nucleon-nucleon interactions**, *Physical Review C* 75, 061001 (2007), arXiv: [nuc1-th/0611045](https://arxiv.org/abs/nuc1-th/0611045), DOI: [10.1103/PhysRevC.75.061001](https://doi.org/10.1103/PhysRevC.75.061001).
- [98] F. J. Wegner, **Flow equations for Hamiltonians**, *Physics Reports* 348, 77 (2001), DOI: [10.1016/S0370-1573\(00\)00136-8](https://doi.org/10.1016/S0370-1573(00)00136-8).
- [99] J. C. Slater, **The Theory of Complex Spectra**, *Physical Review* 34, 1293 (1929), DOI: [10.1103/PhysRev.34.1293](https://doi.org/10.1103/PhysRev.34.1293).



- [100] E. U. Condon, **The Theory of Complex Spectra**, *Physical Review* 36, 1121 (1930), DOI: [10.1103/PhysRev.36.1121](https://doi.org/10.1103/PhysRev.36.1121).
- [101] A. Calci, **Ab initio nuclear structure with SRG-transformed chiral NN plus NNN interactions**, Master's thesis, Technische Universität Darmstadt (2010), [http://crunch.ikp.physik.tu-darmstadt.de/tnp/pub/2010\\_calci\\_master.pdf](http://crunch.ikp.physik.tu-darmstadt.de/tnp/pub/2010_calci_master.pdf).
- [102] D. C. Zheng, J. P. Vary, and B. R. Barrett, **Large-space shell-model calculations for light nuclei**, *Physical Review C* 50, 2841 (1994), arXiv: [nuc1-th/9405018](https://arxiv.org/abs/nuc1-th/9405018), DOI: [10.1103/PhysRevC.50.2841](https://doi.org/10.1103/PhysRevC.50.2841).
- [103] D. C. Zheng, B. R. Barrett, J. P. Vary, *et al.*, **Large-basis shell model studies of light nuclei with a multivalued G-matrix effective interaction**, *Physical Review C* 52, 2488 (1995), arXiv: [nuc1-th/9507011](https://arxiv.org/abs/nuc1-th/9507011), DOI: [10.1103/PhysRevC.52.2488](https://doi.org/10.1103/PhysRevC.52.2488).
- [104] P. Navrátil and B. R. Barrett, **No-core shell-model calculations with starting-energy-independent multivalued effective interactions**, *Physical Review C* 54, 2986 (1996), arXiv: [nuc1-th/9609046](https://arxiv.org/abs/nuc1-th/9609046), DOI: [10.1103/PhysRevC.54.2986](https://doi.org/10.1103/PhysRevC.54.2986).
- [105] C. Lanczos, **An iteration method for the solution of the eigenvalue problem of linear differential and integral operators**, *Journal of Research of the National Bureau of Standards* 45, 255 (1950), DOI: [10.6028/jres.045.026](https://doi.org/10.6028/jres.045.026).
- [106] G. Papadimitriou, J. Rotureau, N. Michel, *et al.*, **Ab initio no-core Gamow shell model calculations with realistic interactions**, *Physical Review C* 88, 044318 (2013), arXiv: [1301.7140](https://arxiv.org/abs/1301.7140), DOI: [10.1103/PhysRevC.88.044318](https://doi.org/10.1103/PhysRevC.88.044318).
- [107] S. Baroni, P. Navrátil, and S. Quaglioni, **Ab Initio Description of the Exotic Unbound  $^7\text{He}$  Nucleus**, *Physical Review Letters* 110, 022505 (2013), arXiv: [1210.1897](https://arxiv.org/abs/1210.1897), DOI: [10.1103/PhysRevLett.110.022505](https://doi.org/10.1103/PhysRevLett.110.022505).
- [108] S. Baroni, P. Navrátil, and S. Quaglioni, **Unified ab initio approach to bound and unbound states: No-core shell model with continuum and its application to  $^7\text{He}$** , *Physical Review C* 87, 034326 (2013), arXiv: [1301.3450](https://arxiv.org/abs/1301.3450), DOI: [10.1103/PhysRevC.87.034326](https://doi.org/10.1103/PhysRevC.87.034326).
- [109] C. Constantinou, M. A. Caprio, J. P. Vary, *et al.*, **Natural orbital description of the halo nucleus  $^6\text{He}$**  (2016), arXiv: [1605.04976](https://arxiv.org/abs/1605.04976).
- [110] A. Szabo and N. S. Ostlund, **Modern Quantum Chemistry: Introduction to Advanced Electronic Structure Theory**. Dover Publications (1996), ISBN: [0486691861](https://www.doverpublications.com/0486691861).
- [111] R. Wirth, **Ab-Initio Approach to Hypernuclei**, PhD thesis, Technische Universität Darmstadt (2018).

- [112] W. Huang, G. Audi, M. Wang, *et al.*, **The AME<sub>2016</sub> atomic mass evaluation (I). Evaluation of input data; and adjustment procedures**, *Chinese Physics C* 41, 030002 (2017), DOI: [10.1088/1674-1137/41/3/030002](https://doi.org/10.1088/1674-1137/41/3/030002).
- [113] M. Wang, G. Audi, F. G. Kondev, *et al.*, **The AME<sub>2016</sub> atomic mass evaluation (II). Tables, graphs and references**, *Chinese Physics C* 41, 030003 (2017), DOI: [10.1088/1674-1137/41/3/030003](https://doi.org/10.1088/1674-1137/41/3/030003).
- [114] I. Angeli and K. Marinova, **Table of experimental nuclear ground state charge radii: An update**, *Atomic Data and Nuclear Data Tables* 99, 69 (2013), DOI: [10.1016/j.adt.2011.12.006](https://doi.org/10.1016/j.adt.2011.12.006).
- [115] R. Roth, J. Langhammer, A. Calci, *et al.*, **Similarity-Transformed Chiral NN+3N Interactions for the *Ab Initio* Description of <sup>12</sup>C and <sup>16</sup>O**, *Physical Review Letters* 107, 072501 (2011), arXiv: [1105.3173](https://arxiv.org/abs/1105.3173), DOI: [10.1103/PhysRevLett.107.072501](https://doi.org/10.1103/PhysRevLett.107.072501).
- [116] R. Roth, A. Calci, J. Langhammer, *et al.*, **Evolved Chiral NN+3N Hamiltonians for *Ab Initio* Nuclear Structure Calculations**, *Physical Review C* 90, 024325 (2014), arXiv: [1311.3563](https://arxiv.org/abs/1311.3563), DOI: [10.1103/PhysRevC.90.024325](https://doi.org/10.1103/PhysRevC.90.024325).
- [117] J. L. Friar, J. Martorell, and D. W. L. Sprung, **Nuclear sizes and the isotope shift**, *Physical Review A* 56, 4579 (1997), arXiv: [nuc1-th/9707016](https://arxiv.org/abs/nuc1-th/9707016), DOI: [10.1103/PhysRevA.56.4579](https://doi.org/10.1103/PhysRevA.56.4579).
- [118] P. J. Mohr, D. B. Newell, and B. N. Taylor, **CODATA recommended values of the fundamental physical constants: 2014**, *Reviews of Modern Physics* 88, 035009 (2016), arXiv: [1507.07956](https://arxiv.org/abs/1507.07956), DOI: [10.1103/RevModPhys.88.035009](https://doi.org/10.1103/RevModPhys.88.035009).
- [119] U. D. Jentschura, **Proton radius, Darwin-Foldy term and radiative corrections**, *The European Physical Journal D* 61, 7 (2011), arXiv: [1012.4029](https://arxiv.org/abs/1012.4029), DOI: [10.1140/epjd/e2010-10414-6](https://doi.org/10.1140/epjd/e2010-10414-6).
- [120] R. Pohl, A. Antognini, F. Nez, *et al.*, **The size of the proton**, *Nature* 466, 213 (2010), DOI: [10.1038/nature09250](https://doi.org/10.1038/nature09250).
- [121] A. Antognini, F. Nez, K. Schuhmann, *et al.*, **Proton Structure from the Measurement of 2S-2P Transition Frequencies of Muonic Hydrogen**, *Science* 339, 417 (2013), DOI: [10.1126/science.1230016](https://doi.org/10.1126/science.1230016).
- [122] A. Ekström, G. R. Jansen, K. A. Wendt, *et al.*, **Accurate nuclear radii and binding energies from a chiral interaction**, *Physical Review C* 91, 051301 (2015), arXiv: [1502.04682](https://arxiv.org/abs/1502.04682), DOI: [10.1103/PhysRevC.91.051301](https://doi.org/10.1103/PhysRevC.91.051301).
- [123] R. J. Furnstahl, G. Hagen, and T. Papenbrock, **Corrections to nuclear energies and radii in finite oscillator spaces**, *Physical Review C* 86, 031301 (2012), arXiv: [1207.6100](https://arxiv.org/abs/1207.6100), DOI: [10.1103/PhysRevC.86.031301](https://doi.org/10.1103/PhysRevC.86.031301).

- [124] S. A. Coon, M. I. Avetian, M. K. G. Kruse, *et al.*, **Convergence properties of *ab initio* calculations of light nuclei in a harmonic oscillator basis**, *Physical Review C* 86, 054002 (2012), arXiv: [1205.3230](https://arxiv.org/abs/1205.3230), DOI: [10.1103/PhysRevC.86.054002](https://doi.org/10.1103/PhysRevC.86.054002).
- [125] A. Geißel, **Bayessche Extrapolation für das No-Core Schalenmodell**, Bachelor's thesis, Technische Universität Darmstadt (2017).
- [126] S. Binder, J. Langhammer, A. Calci, *et al.*, **Ab initio path to heavy nuclei**, *Physics Letters B* 736, 119 (2014), arXiv: [1312.5685](https://arxiv.org/abs/1312.5685), DOI: [10.1016/j.physletb.2014.07.010](https://doi.org/10.1016/j.physletb.2014.07.010).
- [127] S. Binder, J. Langhammer, A. Calci, *et al.*, **Ab initio calculations of medium-mass nuclei with explicit chiral 3N interactions**, *Physical Review C* 87, 021303 (2013), arXiv: [1211.4748](https://arxiv.org/abs/1211.4748), DOI: [10.1103/PhysRevC.87.021303](https://doi.org/10.1103/PhysRevC.87.021303).



# Danksagung

An erster Stelle möchte ich Prof. Robert Roth danken für die Möglichkeit diese Dissertation anzufertigen. Seine hilfreichen Ratschläge und physikalische Intuition haben wesentlich zum Gelingen dieser Arbeit beigetragen.

Für die Übernahme des Zweitgutachtens und wertvolle Diskussionen während der Promotion danke ich Prof. Hans-Werner Hammer.

Ein großer Dank geht auch an HGS-HIRe für die abwechslungsreichen und interessanten Fortbildungen im Rahmen der Graduiertenschule sowie die finanzielle Unterstützung von Konferenzbesuchen.

Ich danke meiner Arbeitsgruppe und Bürokollegen für die angenehme Arbeitsatmosphäre, sowie die reichhaltigen Diskussionen physikalischer und anderweitiger Natur. Ohne euch würde ich wohl noch heute über das eine oder andere Problem grübeln. Besonders möchte ich Roland Wirth danken, für seinen unermüdlischen Einsatz als Systemadministrator und wertvolle Hilfe bei allen technischen und physikalischen Herausforderungen.

Ganz besonderer Dank geht an Anna Eichhorn, Eskendr Gebrerufael, Alexander Tichai und Klaus Vobig für das Korrekturlesen der Arbeit und die hilfreichen Verbesserungsvorschläge.

Schließlich bedanke ich mich bei meinen Eltern, die mich während des gesamten Studiums unterstützt haben, sowie bei all den Freunden, die mich während der Promotion begleitet haben, ein offenes Ohr für meine Probleme hatten und mich immer unterstützt haben.



# Werdegang

**Name:** Stefan Schulz  
**Geburtsdatum:** 25.07.1988  
**Geburtsort:** Gießen  
**Nationalität:** deutsch

1999 - 2008 **Gymnasium Philippinum Weilburg**  
2009 - 2011 **Bachelorstudium Physik**, Technische Universität Darmstadt,  
Thesis: *Auswirkung der Form des Konkurrenzterms auf die Dynamik von  
Räuber-Beute Systemen*  
2011 - 2013 **Masterstudium Physik**, Technische Universität Darmstadt,  
Thesis: *SRG-Induced Four-Body Forces in Ab Initio Nuclear Structure*  
2014 - 2018 **Promotionsstudium**, Technische Universität Darmstadt





# Erklärung zur Dissertation

Hiermit versichere ich, die vorliegende Dissertation ohne Hilfe Dritter nur mit den angegebenen Quellen und Hilfsmitteln angefertigt zu haben. Alle Stellen, die aus Quellen entnommen wurden, sind als solche kenntlich gemacht. Diese Arbeit hat in gleicher oder ähnlicher Form noch keiner Prüfungsbehörde vorgelegen. Eine Promotion wurde bisher noch nicht versucht.

Darmstadt, den 6. Februar 2018

---

Stefan Schulz